Transceiver Architectures and Physical Layer Techniques for Unconventional Communications in the Internet of Everything

by

Meltem Civaş

Doctor of Philosophy

in

Electrical and Electronics Engineering

KOÇ ÜNİVERSİTESİ

January, 2024

Transceiver Architectures and Physical Layer Techniques for Unconventional Communications in the Internet of Everything

Koç University
Graduate School of Sciences and Engineering
This is to certify that I have examined this copy of a doctoral dissertation by

Meltem Civaş

and have found that it is complete and satisfactory in all respects,
and that any and all revisions required by the final
examining committee have been made.

Committee Members:

Prof. Özgür Barış Akan (Advisor)

Prof. Alper T. Erdoğan

Prof. Fatih Alagöz

Prof. Murat Tekalp

Prof. Özgür Gürbüz

Date: ______________________

To my father Kamuran Civaş

ABSTRACT

Transceiver Architectures and Physical Layer Techniques for Unconventional Communications in the Internet of Everything
Meltem Civaş
Doctor of Philosophy in Electrical and Electronics Engineering
January, 2024

This thesis explores the emerging Internet of Everything (IoE) framework, a transformative paradigm in Information and Communication Technologies (ICT) that extends human connectivity beyond traditional boundaries. The IoE conceptualizes a comprehensive network architecture that mirrors the complexity of interconnected systems in nature, integrating a diverse array of ICT technologies across different scales and environments. This advancement presents numerous opportunities but also poses significant challenges, particularly in aligning communication technology with the IoE's complex and dynamic nature. The thesis considers the challenges and the solutions at the physical layer/device level linked to unconventional communications essential for realizing the IoE. It focuses on two emerging communication paradigms: Molecular communications (MC) and Terahertz (THz)-band communications. These paradigms are key to expanding beyond the limitations of existing networks and are instrumental in actualizing the IoE. A comprehensive exploration is conducted into the challenges and potential solutions associated with these unconventional communications. The thesis first introduces the universal IoE transceiver, a novel device concept for integrating heterogeneous networks within the IoE framework. It discusses transceiver architectures based on graphene and related materials, which are promising for unconventional communication modalities, especially in the context of the Internet of Bio-Nano Things (IoBNT), an emerging subset of the IoE. The thesis further investigates advanced physical layer techniques for practical MC systems and explores effective solutions for facilitating THz-band communication in space. These in-depth studies aim to enhance connectivity and communication on a universal scale, shaping the future landscape of the IoE. The work presented provides pathways toward mitigating the complexities inherent in unconventional

communications, thereby contributing to the advancement of IoE technologies.

ÖZETÇE

Her Şeyin İnternetinde Geleneksel Olmayan Haberleşme için Alıcı-Verici Mimarileri ve Fiziksel Katman Teknikleri
Meltem Civaş
Elektrik ve Elektronik Mühendisliği, Doktora
Ocak, 2024

Bu tez, insan bağlantısını geleneksel sınırların ötesine taşıyan Bilgi ve İletişim Teknolojilerinde (BİT) dönüştürücü bir yaklaşım olan, gelişmekte olan Her Şeyin İnterneti (IoE) çerçevesini incelemektedir. IoE, doğadaki birbirine bağlı sistemlerin karmaşıklığını yansıtan, farklı ölçeklerde ve ortamlarda çeşitli BİT teknolojilerini entegre eden kapsamlı bir ağ mimarisini kavramsallaştırmaktadır. Bu ilerleme çok sayıda fırsat sunmakla birlikte, özellikle iletişim teknolojisini IoE'nin karmaşık ve dinamik doğasıyla uyumlu hale getirme konusunda önemli zorluklar da ortaya çıkarmaktadır. Tez, IoE'nin gerçekleştirilmesi için gerekli olan geleneksel olmayan iletişimle bağlantılı fiziksel katman ve cihaz seviyesindeki zorlukları ve olası çözümleri ele almaktadır. Gelişmekte olan iki iletişim paradigmasına odaklanmaktadır: Moleküler iletişim (MC) ve Terahertz (THz) bandı iletişimi. Bu paradigmalar, mevcut ağların sınırlamalarının ötesine geçmenin anahtarıdır ve IoE'nin hayata geçirilmesinde etkilidir. Bu geleneksel olmayan iletişimlerle ilgili zorluklar ve potansiyel çözümler hakkında kapsamlı bir araştırma yapılmıştır. Tezde ilk olarak IoE çerçevesinde heterojen ağları entegre etmek için yeni bir cihaz konsepti olan evrensel IoE alıcı-vericisi tanıtılmaktadır. Özellikle IoE'nin gelişmekte olan bir alt kümesi olan Biyo-Nano Nesnelerin İnterneti (IoBNT) bağlamında, geleneksel olmayan haberlesşme modaliteleri için umut verici olan grafen ve ilgili malzemelere dayalı alıcı-verici mimarilerini tartışmaktadır. Tez ayrıca pratik biyosensör tabanlı MC sistemleri için gelişmiş fiziksel katman tekniklerini araştırmakta ve uzayda THz-bant iletişimini kolaylaştırmak için etkili çözümler araştırmaktadır. Bu derinlemesine çalışmalar, IoE'nin gelecekteki manzarasını şekillendirerek evrensel ölçekte bağlantı ve iletişimi geliştirmeyi amaçlamaktadır. Sunulan çalışma, geleneksel olmayan iletişimin doğasında var olan karmaşıklıkları azaltmaya yönelik yollar

sunmakta ve böylece IoE teknolojilerinin ilerlemesine katkıda bulunmaktadır.

ACKNOWLEDGMENTS

I would like to express my deepest gratitude to my advisor, Prof. Özgür Barış Akan, for his constant guidance, encouragement, and patience. Without his endless support, completing this thesis would have been impossible. His mentorship extends beyond the academic realm, imparting wisdom and insights that will guide me throughout my life. I am truly honored and feel very fortunate to have been a student of Prof. Akan.

I also sincerely thank Prof. Alper Erdoğan and Prof. Fatih Alagöz for agreeing to supervise this thesis and advancing it through their valuable comments and suggestions throughout the process. My gratitude extends to Prof. Özgür Gürbüz and Prof. Murat Tekalp for taking part in my thesis committee and for their valuable comments.

I also want to sincerely thank Dr. Murat Kuşcu for his invaluable support and collaboration in numerous research efforts. He has been like a brother to me throughout this journey, offering unwavering support. My thanks also go to the members of NWCL for their support. My special thanks are to Beyza Ezgi Örtlek and Çağlar Koca, who are good friends beyond colleagues.

I also gratefully acknowledge the support of AXA Research, Huawei Türkiye, and Koç University.

Last, but not least, I am eternally grateful to my family and friends for their everlasting support and love.

TABLE OF CONTENTS

List of Tables **xiv**

List of Figures **xv**

Introduction **1**

I Transceivers Architectures for the Internet of Everything: Opportunities and Challenges **6**

Chapter 1: Universal Transceivers for the IoE **7**

1.1 Introduction 7
1.2 Universal IoE Transceiver 9
1.3 Opportunities of Universal IoE Transceivers 11
1.3.1 Heterogeneous IoE 11
1.3.2 Ubiquitous Connectivity and Continuous Operation 13
1.3.3 Increasing the Communication Performance 18
1.3.4 Increasing the Energy Harvesting Capacity 19
1.4 Challenges and Potential Research Directions 20
1.4.1 Multi-modal Communications 21
1.4.2 Multimodal Energy Harvesting 26
1.4.3 Adaptivity and Tunability 29
1.4.4 Miniaturization 34
1.5 Conclusion 39

Chapter 2: Graphene and Related Materials for the Internet of Bio-

Nano Things 40
2.1 Introduction 40
2.2 Graphene and Related Materials (GRMs) 44
2.2.1 Properties of GRMs 44
2.2.2 Synthesis of GRMs 47
2.3 GRM-based Micro/Nanoscale Transceivers 49
2.3.1 Transceivers for Molecular Communications 50
2.3.2 Transceivers for THz-band Nanocommunications 55
2.3.3 Transceivers for Ultrasonic Nanocommunications 57
2.3.4 Multi-modal Transceivers for IoBNT 60
2.4 GRM-based Bio-cyber Interfaces 62
2.4.1 GRM-based Biosensors for IoBNT 63
2.4.2 GRM-based Neural Interfaces for IoBNT 66
2.4.3 GRM-based Drug Delivery Systems for IoBNT 68
2.5 GRM-based Micro/Nanoscale Energy Harvesting and Storage 69
2.5.1 GRM-based Micro/Nanoscale Energy Harvesting for IoBNT . 69
2.5.2 GRM-based Micro/Nanoscale Energy Storage for IoBNT . . . 74
2.6 Discussion on Material Challenges 78
2.7 Conclusions and Future Outlook 82

II Physical Layer Techniques for Practical Molecular Communication Systems 85

Chapter 3: Frequency-Domain Detection for Molecular Communications 86
3.1 Introduction 86
3.2 System Model 89
3.3 Time-Domain Detection 95
3.4 Frequency-domain Detection 96

3.4.1 Theoretical Model of Binding Noise PSD 96
3.4.2 Maximum Likelihood Estimation of PSD Parameters 99
3.4.3 Symbol Detection 101
3.4.4 Asymptotic Bit Error Probability 104
3.5 Simulation of the System 105
3.5.1 Particle-based Stochastic Simulations 105
3.5.2 Simulation parameters 106
3.5.3 Monte Carlo Simulation 110
3.6 Performance Evaluation 111
3.6.1 Effect of Interference on BEP 112
3.6.2 Effect of Similarity on BEP 114
3.6.3 Effect of Number of Samples on BEP 115
3.6.4 Effect of 1/f Noise on BEP 115
3.6.5 Effect of Bit-0/Bit-1 Concentration Ratio on BEP 118
3.6.6 Effect of Transmitter-Receiver Distance on BEP 118
3.6.7 Effect of Surface Receptor Length on BEP 119
3.6.8 Effect of Multiple Types of Interferers on BEP 120
3.7 Conclusion 122

Chapter 4: Performance Analysis of Molecular Communication with Cross-Reactive Receptors 125

4.1 Introduction 125
4.2 System Model 126
4.2.1 Channel Model 127
4.2.2 Reception Model 128
4.2.3 Maximum Likelihood Estimation of Ligand Concentrations . . 130
4.3 Symbol Error Probability for M-CSK 132
4.3.1 Symbol Error Probability in M-CSK Under Stochastic Noise . 132

4.3.2 SEP in MCSK Under Intersymbol Interference and Background Interference . . . 138
4.4 Capacity Analysis . . . 139
4.4.1 CSK Modulation Under Background Noise . . . 140
4.4.2 Multi-dimensional Inputs . . . 143
4.5 Conclusion . . . 144

III Enabling Terahertz Communication in the IoE: Physical Layer Solutions and Applications 146

Chapter 5: Terahertz-Band Intersatellite Communication Links 147
5.1 Introduction . . . 147
5.2 Intersatellite Communication Links . . . 149
5.3 Terahertz Band Communications . . . 150
5.3.1 Comparison with Other Technologies . . . 152
5.4 Terahertz Band Intersatellite Links . . . 153
5.4.1 Link Budget Analysis . . . 154
5.5 Future Research Directions . . . 161
5.5.1 Terahertz Ultra-Massive Multiple Input Multiple Output . . . 161
5.5.2 5G and Beyond 5G Satellite Networks . . . 161
5.5.3 Internet of Space Things . . . 162
5.5.4 Hybrid Space-Air Network . . . 162
5.6 Challenges . . . 163
5.6.1 High Path Loss . . . 164
5.6.2 Interference . . . 164
5.6.3 Space Debris . . . 165
5.6.4 Doppler Spread . . . 165
5.6.5 Device Linearity . . . 166
5.7 Conclusions . . . 166

Chapter 6: Terahertz Wireless Communications in Space **168**

6.1 Introduction . . . 168

6.2 Applications . . . 171

6.2.1 Earth Observation . . . 171

6.2.2 Interplanetary communications by hybrid THz/FSO links . . . 172

6.3 Challenges and Solutions . . . 173

6.3.1 Molecular Absorption Loss . . . 173

6.3.2 Spreading loss . . . 175

6.3.3 Spectrum sharing . . . 177

6.4 Terahertz Mars-Space Links . . . 178

6.4.1 The Planetary Spectrum Generator . . . 178

6.4.2 Zenith transmittance . . . 179

6.5 Conclusion . . . 181

Chapter 7: Conclusion **182**

Bibliography **186**

LIST OF TABLES

1.1 Comparison of some of the key IoE communication modalities. 15

3.1 Default Values of System Parameters 112

4.1 Default Values of System Parameters 133

5.1 Comparison of Different Technologies [1] 153

5.2 GEO-to-GEO Communications Link Case for an SNR of 10 dB . . . 158

5.3 GEO-to-GEO Communications Link Budget for an SNR of 10 dB . . 158

6.1 Vertical profile of Mars atmosphere 179

LIST OF FIGURES

1.1 An example architecture for a universal IoE transceiver. 12
1.2 Remote healthcare application with continuous health monitoring enabled by universal IoE transceiver. 14
1.3 Ubiquitous connectivity enabled by the universal IoE transceivers for the underwater applications. 17
1.4 Graphene-based micro/nanoscale MC receiver [2]: (a) Conceptual drawing of MC receiver with functionalized graphene, (b) Fabricated MC receiver, (c, d) Integration of the MC receiver into a microfluidic MC channel. 37

2.1 (a) Conceptual drawing of a continuous health monitoring application of IoBNT, involving intrabody distributed MC nanonetworks of biosensors and a bio-cyber interface interconnecting the nanonetworks and conventional networks [3]. (b) MC among engineered bacteria, and between GRM-based BNTs. Reproduced with permission from Proceedings of IEEE 107, 7 (2019). Copyright 2019 IEEE. 41
2.2 Chemical structures of graphene, graphene oxide, and reduced graphene oxide. 46
2.3 GRM synthesis methods: (a) mechanical cleavage, (b) liquid-phase exfoliation, (c) chemical vapor deposition, (d) epitaxial growth on SiC substrate. Reproduced with permission Materials Today 15, 12 (2012). Copyright 2012 Elsevier. 49

2.4 Graphene bioFET-based MC receiver [4]: (a) A conceptual drawing of the MC receiver architecture. (b) Micro/nanofabricated MC receiver. (c,d) Integration of the MC receiver with a microfluidic chip. 52

2.5 Conceptual drawings of envisioned MC-Tx architectures [5]: (a) Liquid-borne MC-Tx with hydrophobic nanopore. (b) Liquid-borne MC-Tx with hydrophobic nanopore and nanoporous graphene membrane. (c) MC-Tx with hydrogel and nanoporous graphene membrane. (d) Air-borne MC-Tx with molecule wax and nanoporous graphene membrane. 54

2.6 (a) Conceptual design of a graphene nanoribbon-based plasmonic antenna for THz communication. (b, c, d) Graphene-based THz detector [6]: (b) Schematics of the bilayer graphene FET architecture used in the THz detector. (c) 3D rendering of the THz detector with a broadband bow-tie antenna and hemispherical silicon lens, enabling modulation of the gate-to-source voltage. (d) Optical micrograph of the detector. 56

2.7 Optoacoustic ultrasound transmitter based on rGO-coated PDMS film [7]: (a) Schematic representation of the film. (b) Maximum pressure of ultrasonic waves from different samples at varying fluences. (c) Frequency spectra of ultrasonic waves observed for different samples. Reproduced from S. H. Lee et al, "Reduced graphene oxide coated polydimethylsiloxane film as an optoacoustic transmitter for high pressure and high frequency ultrasound generation," Applied Physics Letters, vol. 106, no. 8, p. 081911, 2015, with the permission of AIP Publishing. 59

2.8 An IoBNT architecture with GRM-based bio-cyber interfaces facilitating bi-directional communication between intrabody nanonetworks and conventional networks: (1) GRM-based bio-cyber interface enabling bi-directional communication between the Internet and intrabody networks. (2) GRM-based high-resolution neural interface connecting to external networks via THz signals. (3) Nanosensor/actuator network monitoring and controlling gut microbiome composition, connected to a bio-cyber interface through acoustic signals. (4) GRM-based transdermal patch providing sensory feedback to (2) via the Internet by converting biochemical signals to THz signals and transmitting them to the Internet infrastructure for further processing. (5) The cyber domain of the Internet. 62
2.9 GRM-based wearable smart contact lens [8]: (a) GRM-based wearable contact lens sensor integrating a glucose sensor and an intraocular pressure sensor. (b) Illustration of the transparent glucose sensor on the contact lens. (c) GRM-based wireless sensor integrated onto a rabbit's eye. Joohee Kim, Nature communications, 8, 14997 (2017), 2017; licensed under a Creative Commons Attribution (CC BY) license. 65
2.10 Illustration of a GRM-based hybrid nanogenerator, simultaneously converting kinetic and thermal energy into electricity [9]. Reproduced with permission from Ju-Hyuck Lee et al, Advanced Materials 26, 5 (2014). Copyright 2014 Wiley Online Library. 71

2.11 Large-scale integration of fully inkjet-printed flexible MSCs on Kapton [10]: (a-b) Photographic images of MSC arrays from different perspectives. (c) Cyclic voltammetry (CV) profiles at different scan rates, captured one month post-fabrication. (f) CV profiles at various time intervals following fabrication, illustrating long-term stability. (d) Galvanostatic charge/discharge (GCD) curves, demonstrating ideal capacitive performance. (e) Areal energy density versus power density plot, demonstrating that large-scale MSCs deliver heightened power density. Reproduced with permission from ACS Nano 11, 8 (2017). Copyright 2017 American Chemical Society. 74

2.12 (a-g) Schematic illustration of the fabrication process for flexible rGO-based MSC on a PET substrate, involving plasma reduction and oxygen plasma etching [11]. (h-k) Optical images depicting (h) the rGO film on a PMMA substrate, (i) the rGO film on a PET substrate, (j) the rGO-MSC-PET device with gold current collectors, and (k) the rGO-MSC-PET device without gold current collectors, illustrating the device's flexibility. (l-n) CV curves of the rGO-MSC-PET device at various scan rates, showcasing high power performance, and areal capacitance measurements, indicating high energy performance. Zhong Shuai Wu et al, Nature Communications, 4, 2487 (2013), 2013; licensed under a Creative Commons Attribution (CC BY) license. . . 76

3.1 A three-dimensional illustration (a) the microfluidic MC channel, including the positions of the MC-Tx and MC-Rx, and (b) the detailed view of the graphene bioFET-based MC-Rx exposed to information and interferer molecules. 91

3.2 Snapshot of the Smoldyn simulation illustrating the MC system. The parameters have been adjusted for illustrative purposes. Thus, this representation is not to scale. 106

3.3 (a) Characteristic frequencies highlighted on the graph of the S multiplied by frequency f, where S is the theoretical PSD of noise. (b) Model PSD generated with estimated molecule concentrations and the observed PSD (periodogram) generated with the Smoldyn data. . 108

3.4 BEP for varying (a) information to interference ratio γ and (b) similarity η. 113

3.5 BEP for varying (a) number of samples (b) power of 1/f noise at 1 Hz. 116

3.6 BEP for varying bit-0/bit-1 concentration ratio when the MC-Rx is (a) near saturation, and (b) in a non-saturation state. 117

3.7 BEP for varying (a) transmitter-receiver distance d and (b) receptor length r. 120

3.8 BEP performance under different ligand-receptor affinities, modulated by the factor ν, in scenarios involving (i) a single interferer type (L_2) and (ii) multiple interferer types (L_2, L_3) in the channel. . . 121

4.1 A detailed view of the graphene bioFET-based MC-Rx exposed to ligands. 128

4.2 SEP in M-CSK under background interference for varying (a) ratio between interference and information ligand concentrations at sampling time γ (b) similarity in the binding affinities of information and interferer ligands (c) maximum ligand concentration $c_m^{\max}$. 136

4.3 SEP in 2-CSK, 4-CSK and 8-CSK for varying interference and similarity levels. 137

4.4 SEP performance for 2-CSK for varying symbol interval T_s/t_p with respect to peak time t_p. 138

4.5 Optimal input distribution (above) and the distribution of the estimated inputs, i.e., information-carrying ligand concentrations, corresponding to Gaussian PDFs (below) given the mean interferer ligand concentration, i.e., $\mu_{c_i}/c_m^{\max} = 0.5$. 141

4.6 Capacity for CSK under background noise for (a) varying background noise level (b) varying similarity between the binding affinities of the information and interferer molecules. 142
4.7 Capacity for multi-dimensional input, namely both concentration and type are used in the modulation. 144

5.1 Classification of THz links. 151
5.2 Minimum gain required. 159
5.3 Beamwidth required. 160
5.4 Minimum gain required for several bandwidths, $f_c = 1$ THz. 160
5.5 Hybrid space-air-sea-ground network. 163

6.1 Classification of THz links [12]. 170
6.2 Interplanetary communications: Black arrows (THz links), red arrows (FSO links). 171
6.3 The transmittance of Earth-space links at several altitudes from one of the driest locations of the Earth, i.e., ALMA, denoting the fraction of EM radiation after experiencing molecular absorption. The zenith angle is 35°. 173
6.4 Pressure vs temperature. 178
6.5 Zenith transmittance of clear Mars atmosphere for various altitudes. 180
6.6 Zenith transmittance of Mars atmosphere during a local dust storm for various altitudes ($r_{eff} = 1.5\mu m$). 180

INTRODUCTION

The digital world is advancing towards a new era extending human connectivity beyond traditional boundaries, marking the emergence of the Internet of Everything (IoE). The IoE represents an innovative paradigm in the field of Information and Communication Technologies (ICT), conceptualizing a comprehensive network architecture that mirrors the intricacy of interconnected systems observed in nature. Drawing from a diverse array of ICT technologies across different scales and environments, the IoE presents numerous opportunities. However, these opportunities also come with their challenges. Addressing these challenges requires enhancing our communication technology to align with the complex and dynamic nature of the IoE.

The present-day networking environment comprises a wide variety of communication technologies. Our relentless efforts to probe into less-explored environments, such as underwater, outer space, and within the human body, drive the continual diversification of these technologies. By analogy, the natural communication systems that have evolved over billions of years demonstrate significant variability, particularly noticeable in biological signaling pathways and entities. The IoE framework aspires to unify traditional and emerging communication mechanisms from these heterogeneous networks. This unification, melding natural and human-made networks, is a step towards optimizing our connectivity on a universal scale.

Therefore, this thesis considers the challenges and potential solutions at the physical layer/device level linked to unconventional communications that are key to realizing the IoE. It focuses on two emerging communication paradigms: Molecular communications (MC) and Terahertz (THz)-band communications. These paradigms hold the power to expand beyond the limitations of our existing communication networks, playing a significant role in making the IoE a reality.

In the subsequent chapters of this thesis, a thorough exploration will be conducted into the challenges and potential solutions associated with unconventional communications at the physical layer/device level. This level is crucial for realizing the IoE paradigm, as the most prominent challenges lie at the physical level. Extensive research and novel approaches supported by detailed analysis aim to illuminate this critical aspect, providing pathways toward mitigating the complexities inherent in unconventional communications.

The first part of the thesis introduces an innovative communication device paradigm - the universal IoE transceiver. This concept embodies the significant potential for seamlessly integrating heterogeneous networks within the framework of the IoE. The discourse will then explore transceiver architectures based on graphene and related materials. These architectures offer promising avenues for unconventional communication modalities, specifically emphasizing MC and Terahertz (THz)-band communications within the Internet of Bio-Nano Things (IoBNT), an emerging subset of the IoE. The next part will investigate advanced physical layer techniques for practical MC systems. After that, the focus will shift toward exploring effective physical layer solutions instrumental in facilitating THz-band communication. These in-depth explorations aim to pave the way for a deeper, more seamless connection and communication with the universe, sculpting the landscape of the upcoming IoE era. The thesis is organized as follows:

Part 1: Transceivers Architectures for the Internet of Everything: Opportunities and Challenges

Chapter 1: This chapter introduces a new communication device concept, i.e., *the universal IoE transceiver*. This concept encompasses transceiver architectures characterized by multi-modality in communication (with modalities such as molecular, RF/THz, optical and acoustic) and energy harvesting (with modalities such as mechanical, solar, and biochemical), along with modularity, tunability, and scalability. An overview of the opportunities micro/nanoscale universal transceiver architectures offer to realize IoE applications is provided. The most pressing challenges in implementing such transceivers and a brief review of the open research directions are also discussed. This discussion mainly focuses on the opportunities and challenges of the IoE physical layer, which can enable the efficient and effective design of higher-level techniques. It is proposed that such universal transceivers can pave the way for a deeper, seamless connection and communication with the universe and pioneer the construction of the forthcoming IoE landscape.

Chapter 2: This chapter focuses on expanding connectivity to biological networks via the Internet of Bio-Nano Things (IoBNT). The IoBNT, a transformative communication framework within the IoE, is characterized by heterogeneous networks comprising biological entities and artificial micro/nano-scale devices, referred to as Bio-Nano Things (BNTs). These BNTs interface with conventional communication networks to enable innovative biomedical and environmental applications. Realizing the potential of IoBNT necessitates the development of new and unconventional communication technologies, such as molecular communications. This development also includes corresponding transceivers, bio-cyber interfacing technologies that connect the biochemical domain of IoBNT to the electromagnetic domain of conventional networks, and miniaturized energy harvesting and storage components for the continuous power supply to BNTs. Graphene and related materials (GRMs) exhibit exceptional electrical, optical, biochemical, and mechanical properties, making them ideal candidates for addressing the challenges posed by IoBNT. This chapter highlights recent advancements in GRM-based device technologies that hold promise for implementing the core components of IoBNT. By identifying the unique opportunities offered by GRMs and aligning them with the practical challenges associated with IoBNT, particularly in the materials domain, the aim is to accelerate the transition of envisaged IoBNT applications from theoretical concepts to practical implementations while also uncovering new application areas for GRMs.

Part 2: Physical Layer Techniques for Practical Molecular Communication Systems

Chapter 3: This chapter introduces a novel detection method for graphene bioFET-based MC receivers (MC-Rxs). Practical MC-Rxs may be implemented based on field-effect transistor biosensor (bioFET) architectures, in which surface receptors reversibly react with ligands, encoding the information via their concentration. The time-varying concentration of ligand-bound receptors is translated into electrical signals via the field effect, which is then used to decode the transmitted information. However, ligand-receptor interactions often fail to provide ideal molecular selectivity since similar types of ligands, or interferers, co-existing in the MC channel can interact with the same type of receptors, resulting in cross-talk. Overcoming this molecular cross-talk with time-domain samples of the Rx's electrical output is not always achievable, especially when the Rx lacks knowledge of the interferer statistics or operates near saturation. In order to address this issue, a frequency-domain detection (FDD) technique for bioFET-based MC-Rxs is proposed in this chapter. This technique leverages the difference in binding reaction rates of different types of ligands, which is reflected in the noise spectrum of the ligand-receptor binding fluctuations. An analytical derivation of the bit error probability (BEP) of the FDD technique is presented, demonstrating its effectiveness in decoding transmitted concentration signals under stochastic molecular interference compared to a widely-used time-domain detection (TDD) technique. This analytical performance bound for the FDD is then verified through particle-based spatial stochastic simulations of the binding reactions on the MC-Rx in microfluidic channels. The proposed FDD method can be applied to any biosensor-based MC-Rxs that employ receptor molecules as the channel-Rx interface.

Chapter 4: This chapter analyze the symbol error probability (SEP) for FDD introduced in the previous chapter, and also investigate the end-to-end channel capacity of bioFET-based MC receiver with cross-reactive receptors, considering factors such as background interference and similarities in ligand affinities. The results are promising regarding the potential of bio-sensor based MC systems.

Part 3: Enabling Terahertz Communication in the IoE: Physical Layer Solutions and Applications

Chapter 5: Despite its potential viability, the Terahertz (THz) band has frequently been overlooked in discussions about inter-satellite links (ISLs). This chapter proposes a THz-band ISL system, considering recent advancements in the area from the past decade. Subsequently, link budgets for a representative usage scenario are computed to demonstrate propagation mechanisms. As the chapter concludes, it outlines avenues for future research, including exploring the Internet of Space, while acknowledging potential challenges that might emerge.

Chapter 6: This chapter proposes using Terahertz band (0.1-10 THz) wireless communications in the Internet of Space to meet the increasing demand for space links. The major challenges posed by the realization of THz band space links and potential solutions are discussed. The chapter also includes the simulation of Mars-space THz links under conditions of a clear Mars atmosphere and heavy dust storms, demonstrating that a significant bandwidth is available for Mars communication traffic even under the most challenging conditions.

Part I

Transceivers Architectures for the Internet of Everything: Opportunities and Challenges

Chapter 1

UNIVERSAL TRANSCEIVERS FOR THE IOE

1.1 Introduction

The ever-growing demand for high data rates and low latency coupled with the exponential increase in the number of interconnected devices has been met by the evolution and diversification of the conventional communication technologies, particularly moving towards higher frequency bands, e.g., mm-Wave and THz bands [13]. Likewise, the objective of extending our control and connectivity to underexplored environments, e.g., underwater, intra-body, with the ever-increasing resolution has led to the emergence of new non-conventional communication modalities, such as acoustic communications and molecular communications (MC) [14, 15]. These fast-paced developments have been further accompanied by the introduction of numerous wireless power transfer (WPT) and energy harvesting (EH) techniques that can exploit various energy sources to overcome the limitations of finite-capacity batteries and enable self-sustaining networks within the Internet of Things (IoT) framework [16, 17, 18]. Hence, the current and future landscapes of communications and networking are characterized by increasing heterogeneity of communication and power supply technologies, which are optimized only for particular scales, environments, and applications.

The recently introduced *Internet of Everything (IoE)* framework is positioned to exploit the heterogeneity of current and next-generation communication and networking technologies (both conventional and non-conventional) to extend our connectivity to the entire universe, which is itself a natural IoE, an inherently heterogeneous network of everything we perceive, whose interactions governed by the laws of physics [19]. Maximizing the connectivity to the universal scale through the integration of different communication technologies and their close interaction with the natural IoE is expected to enable novel applications. For example, control over biological communication pathways among living entities, such as biological cells, animals, plants, through the seamless interface of our communication technologies will have broad implications for biomedical, agricultural, and environmental applications [20]. As a particular example, interfacing future molecular nanosensor networks located inside the human brain to the low-latency and high-rate electromagnetic 5G wireless networks can bring the Internet of Senses to reality, enabling the nonverbal, i.e., conceptual, communication of human-body senses between individuals. The countless number of applications that can be enabled by the blend of heterogeneous technologies across different scales and environments, however, impose several fundamental challenges, such as interoperability, ubiquitous connectivity, energy efficiency, and miniaturization.

As in all networking technologies, the opportunities and limitations pertaining to the physical layer of the IoE will largely determine what we can achieve with higher-layer techniques and protocols in terms of tackling its core challenges. With this consideration, we set out to investigate the physical architecture of a universal transceiver that, we believe, can enable the efficient and effective design of higher-level techniques for the IoE. Here we coin the *universal IoE transceiver* as an umbrella term, which encompasses all transceiver devices that are characterized by the key IoE attributes, such as *multi-modality*, *modularity*, *tunability*, and *scalability*, and can be embedded into any entity or device to transform them into *IoE devices*. Although combinations of these traits have already been considered in the literature for various communication devices and networks, those studies are limited to particular communication technologies and applications, and thus, away from providing general insights into transceiver architectures that can address the IoE challenges. For example, multi-modal communications has been extensively studied in the context of underwater networks to optimize the connectivity by adaptively combining acoustic communications with optical or RF communications [21, 22, 23]. Smart gateway architectures, providing modularity and multi-modality in terms of communication technologies and protocols, have been proposed for IoT to shield the heterogeneity of the IoT sensing layer in its interaction with the network layer [24]. Cognitive radio, and in general, software-defined radio technologies consist in the dynamic tunability of the transmission and reception parameters of network nodes, which gives their flexibility in overcoming the limited spectrum challenges [25, 26, 27]. Multi-modal, bio-cyber, and macro-nano interface architectures have been proposed for MC, which transduce MC signals to different signal forms including RF and optical [28, 29, 30].

Focusing on the fundamental traits introduced above, this chapter provides an overview of the opportunities that are made possible by such universal transceiver architectures. That is performed in the context of IoE, such that the overview is not focused on particular technologies or applications. However, example scenarios of practical applications accompany the discussion to justify the need for universal transceivers combining these features. We also discuss the most important challenges in implementing such transceivers and briefly review potential research directions to practically address them. Although our discussion is focused on physical layer challenges, we occasionally extend it to higher layers to provide a broader perspective.

1.2 Universal IoE Transceiver

We envision a universal IoE transceiver as a physical device enabling the design of higher-level communication techniques and protocols that would help overcome the fundamental IoE challenges, such as interoperability, ubiquitous connectivity, energy efficiency, miniaturization, and scarcity of bandwidth. Although this work is not proposing a particular architecture, the following set of properties delineates the universal IoE transceiver, which is investigated in this chapter in terms of opportunities and challenges:

- **Multi-modality in communications:** The universal IoE transceiver is capable of transceiving communication signals in multiple forms, e.g., RF, optical, molecular, and acoustic. Supporting multiple combinations of communication modalities, the universal transceiver will bring important functionalities, such as adaptivity, multiplexing, and seamless interfacing between different modalities as discussed in Section 1.3, which will help overcome the interoperability and ubiquitous connectivity challenges of the IoE.

- **Multi-modality in EH:** The considered device has an architecture that can harvest energy from multiple energy sources, such as RF, mechanical, biochemical, and solar energy sources, as well as, utilize WPT in an hybrid manner. The adaptivity enabled by multi-modality in energy supply will effectively address the energy scarcity challenges in the IoE.

- **Modularity:** The device has a modular architecture that enables reconfigurability. This will allow the utilization of the most appropriate communication and EH modalities for particular applications and application environments, eliminating any redundancy. Future communication and EH technologies can also be integrated into the universal transceiver thanks to its modular structure.

- **Tunability:** The dynamic tunability of transmission and reception parameters for individual communication modalities, e.g., the frequency of transmit signals in RF communications or the type of carrier molecules in MC, will contribute to the adaptivity, energy efficiency, and environment-compatibility of the universal transceiver, as discussed in Section 1.3.

- **Scalability:** The device architecture is scalable to micro/nanoscales, supporting ubiquitous connectivity especially in bio-nano environments and enabling the deployment of more IoE functionalities in smaller volumes.

In the following, we address the **PHY/device** opportunities and challenges for a universal IoE transceiver defined by aforementioned properties. Extension of the investigation to upper layers (e.g., network layer) within the IoE framework can be considered as a future work.

1.3 Opportunities of Universal IoE Transceivers

The universal IoE transceivers can present unprecedented opportunities within the emerging IoE framework by supporting the interoperability of heterogeneous communication networks through seamlessly interfacing their physical layers, providing ubiquitous operation and adaptivity at diverse and dynamic environments, and enabling the opportunistic utilization of multiple communication and energy modalities. In this section, we present a detailed discussion of these opportunities along with the potential applications.

1.3.1 Heterogeneous IoE

The current landscape of networking is already characterized by heterogeneity of communication technologies. On top of that, our perennial quest to reach out to underexplored environments, such as underwater and intra-body, is pushing the diversification of the communication technologies to new levels. Besides, natural communication systems, which are optimized through billions of years of evolution, are also characterized by substantial heterogeneity, for example, in terms of biological signalling pathways and signalling entities.

IoE, which aims at integrating these conventional and unconventional communication mechanisms involved in these heterogeneous networks to merge natural and human-made networks and maximize our connectivity to the universal scale, poses a great interoperability challenge.

Nature has developed its unique and elegant ways of overcoming the interoperability challenge in interconnecting different species through inter-kingdom communication pathways which lend itself to intriguing consequences that are yet to be fully uncovered. For example, the signalling through gut-brain axis connects the nerve cells in human central nervous system and the microbes in the gastrointestinal tract, which have implications in many human-body disorders and diseases, such as depression and irritable bowel syndrome [31]. Plants and animals communicate with diverse signalling mechanisms, e.g., visual and biochemical signals released by the

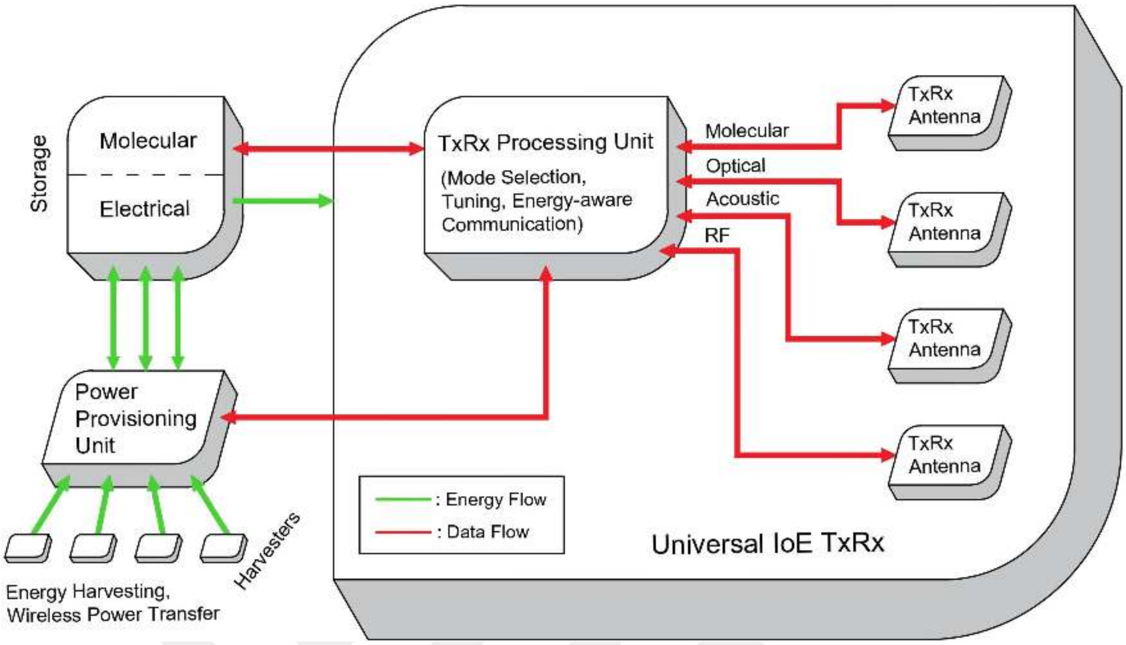

Figure 1.1: An example architecture for a universal IoE transceiver.

plants attract the animals that can disperse the seeds of the plant, or, bat-pollinated plants can communicate with the bats via acoustic signals [32]. Similarly, the plants and the microbes located at the plant's root, e.g., fungi and bacteria, communicate by means of chemical signals enabling mutual relationship for the plant and the microbes. That is, the plant releases metabolites to the soil, and the microbes provide nutrition and protection against pathogens and stress for the plant upon stimulation [33]. These inter-kingdom communication pathways are typically realized through the sharing of a common information carrier that is recognized by all involved species.

It is difficult to envision a scenario where a signal type of carriers is used to interconnect all entities, both natural and human-made, involved in a universal IoE. However, a universal transceiver supporting multi-modal communications, as shown in Fig. 1.1, can overcome the interoperability challenge of the IoE by acting as a seamless interface between different types of networks.

Interfacing various networks of heterogeneous technologies via universal transceivers, that is the underlying theme of the IoE framework, is expected to open up unprecedented opportunities. For example, reprogramming biological communication systems for smart farming, can be realized by bridging different IoE technologies. More specifically, an Internet of Bio-Nano Things (IoBNT) [20], which uses molecular communication modality to regulate the growth of certain microorganisms in soil that provide the plants with the immune response against the upcoming environmental changes, can be interconnected via an electromagnetic communication modality with an Internet of Drones (IoD) [17, 34, 35] that provides real-time feedback by monitoring the crops having disease or stress. Similarly, an IoBNT using MC to communicate with the intra-body cells can be interconnected with a bio-cyber interface via multiple communication technologies suitable for the intra-body communication, e.g., MC, THz, and acoustic, for healthcare applications such as remote healthcare with continuous monitoring as illustrated in Fig. 2.1. In particular, an IoBNT can monitor the concentrations of hormones or molecules in the blood, and transmit this information to the bio-cyber interface, which can connect to the conventional EM networks using RF modality so that the healthcare provider can remotely monitor the person's health condition [36]. Moreover, the neural interfaces and wearable sensor/actuator networks embedded with universal transceivers can be utilized in the transfer of senses, thoughts and skills non-verbally among individuals, i.e, Internet of People and Senses (IoPS) [37]. In particular, a neural interface communicating with the neurons in the human brain can be interconnected to the other neural interfaces for the transfer of thoughts via low-latency and high-data-rate communication technologies, e.g., THz and optical, that can satisfy the requirements of such applications [38]. The universal IoE transceivers can facilitate the cooperation of many other *Internet of X's (IoXs)*, such as Internet of Vehicles (IoV) and Internet of Energy (IoEn), within the IoE framework for novel applications emerging from the close interaction between the heterogeneous technologies inherent in these IoXs.

1.3.2 Ubiquitous Connectivity and Continuous Operation

Varying environmental factors and dynamically changing application requirements demand flexibility and adaptation for maintaining reliable communication and con-

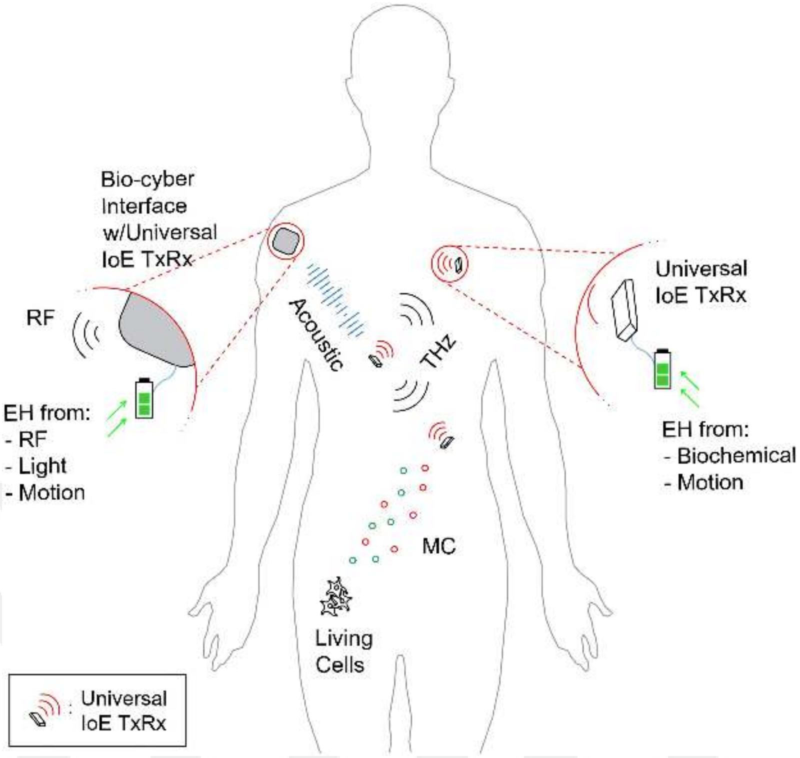

Figure 1.2: Remote healthcare application with continuous health monitoring enabled by universal IoE transceiver.

tinuous energy harvesting concurrently. The modular architecture and tunability, on which a universal IoE transceiver relies, can satisfy these requirements by enabling reconfigurability and adaptation. That is, a universal IoE transceiver either reconfigures its communication and/or energy harvesting modes to the one that is best suited for the environment and the application or opts for the most appropriate transmission/reception and energy harvesting parameters. This can provide seamless coverage and uninterrupted operation everywhere.

There exist a number of communication technologies, each of which has various advantages and disadvantages for a particular application or an environment (see Table 1.1). The multi-modality support of an IoE device for communication can eliminate the shortcomings of a particular technology by allowing the utilization of advantage of another in a flexible manner. As an example, consider free space optical (FSO) and RF communications for outdoor applications. FSO communica-

Table 1.1: Comparison of some of the key IoE communication modalities.

Communication modality	**Medium**	**Data rate**	**Communication range**
Molecular	Intrabody, Airborne, Underwater	Very low	Low
THz-*band EM*	Intrabody, Airborne	Very high	Low
Acoustic	Intrabody, Airborne, Underwater	High	Moderate
RF	Airborne, Underwater	High	High
Optical	Underwater, Intrabody	Very high	Moderate

tion can provide high data rates compared to RF communication. However, FSO communication is highly affected by the weather conditions such as fog and clouds, and atmospheric turbulence [39]. This can cause link failures or range reduction due to strong attenuation in hard weather conditions. To utilize the potentials of both technologies in the fullest extent and ensure reliability together, the IoE transceiver can employ both modalities adaptively and collaboratively using novel methods such as hybrid channel coding [40].

Similarly, a universal transceiver can incorporate the advantages of multiple communication technologies, e.g., acoustic, optical and MC using buoyancy, for continuous operation in the underwater. Acoustic communication is a well known solution for underwater applications such as underwater habitat monitoring and submarine communication due to its robustness and relatively long-range support in the underwater. However, acoustic communication cannot support the applications requiring high-data rates such as high-quality video streaming due to the limited bandwidth. On the contrary, optical communication can provide extremely high data rates but suffers from the strong underwater attenuation limiting the communication range. Moreover, the optical links may not be always available because they require line-of-sight. For instance, in an underwater surveillance scenario based on the sensor network equipped with the universal IoE transceivers, videos or images can be streamed in real-time using optical links, and when the optical links are not available videos and images can be streamed using acoustic links nevertheless with low quality. Furthermore, both optical and acoustic communication may not work for the deep sea applications such as transmission of the location of *black box* on deep ocean floor, since optical and acoustic communication suffers from high attenuation and long channel multipath limiting the reliable communication in long distances, respectively. In such a scenario, the black box with a universal transceiver can use MC via buoyancy, which is a recently introduced delay-tolerant method for the deep sea applications [41], to transmit its location to the surface buoyant machine vertically. In MC via buoyancy, the injected information-carrying liquid, which is lighter than the ambient, is propelled by the buoyancy forces after losing the initial inertia force [41]. Thus, when the buoyancy force is stronger than the horizontal ocean currents, buoyancy-based MC links are suitable. On the other hand, MC via buoyancy still requires effective coding methods to improve the low transmission rates. In addition, according to the availability of the sensor network with the universal transceivers deployed nearby, the universal transceiver of the black box can opportunistically utilize acoustic or optical communication to communicate with the sensor nodes that can relay the information to the surface buoyant machine. Then, the surface buoyant machine relays the location of the black box to the drone network that can provide the rescue team with knowledge of the disaster area, as illustrated in Fig. 1.3.

The dynamic tunability of transmission/reception parameters for a particular modality in the universal transceiver can help overcome challenges imposed by the environmental factors, affecting reliable operation. This can be exemplified by the case of MC, which uses molecules as the information carriers. The environmental factors, such as the chemical composition of the channel, dynamic flow conditions, and temperature, can affect the lifetime of the information carrying molecules and the bio-compatibility of the MC link [5]. For example, considering an intrabody IoE application, a particular type of information carrying molecules might be safe only up to a certain level of concentration in blood, beyond which it may cause

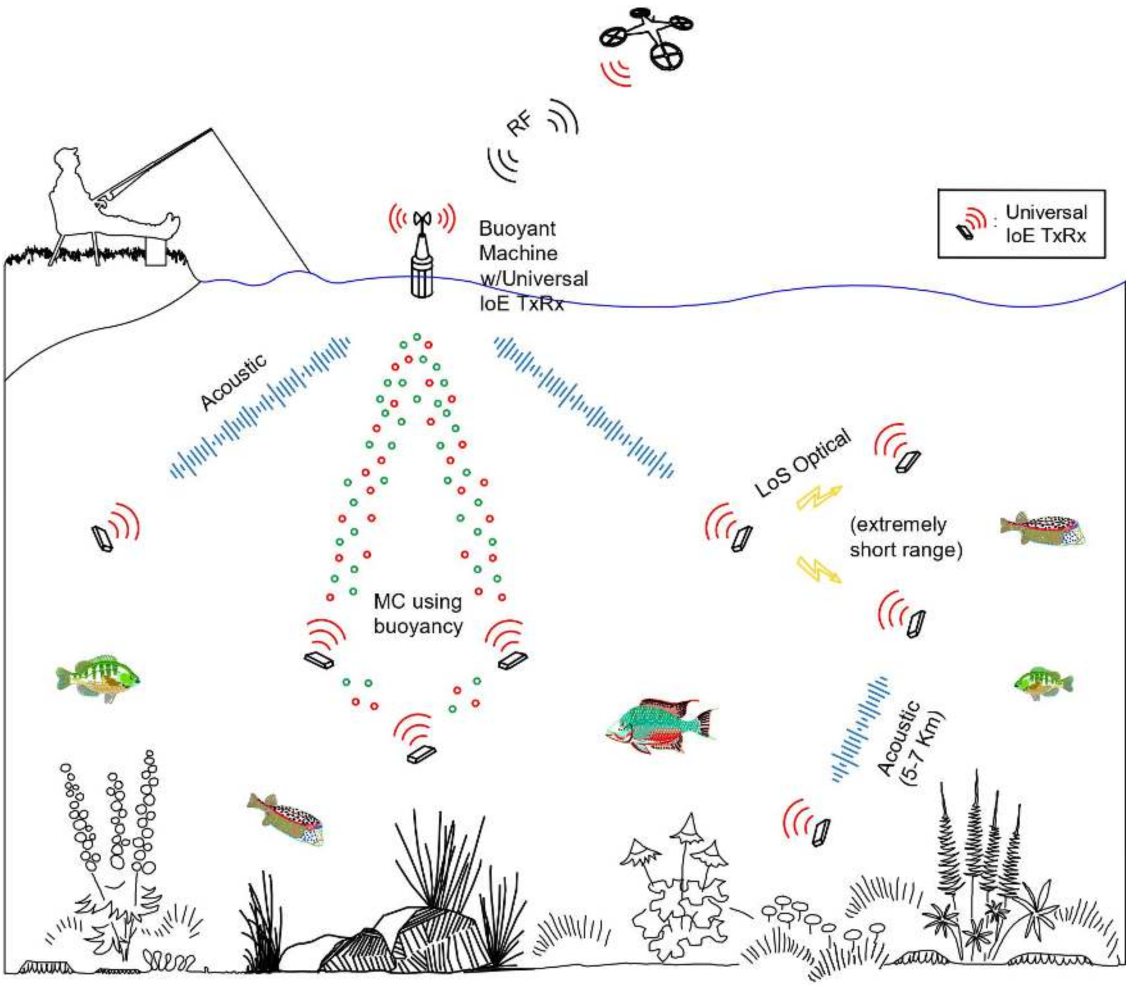

Figure 1.3: Ubiquitous connectivity enabled by the universal IoE transceivers for the underwater applications.

toxic effects for tissues and organs. A universal IoE transceiver can adapt to this condition by alternating the type of the carrier molecules within the set of molecule types harvested and stored in its molecular storage unit, as shown in Fig. 1.1.

Continuous operation also requires exploitation of multiple energy sources due to the uncertainty inherent to these energy sources. A multi-modal energy harvesting unit sensing and exploiting diverse forms of energy resources available in the environment can alleviate this problem. The multi-modal energy harvesting capability will not only provide continuous operation but also increase the energy harvesting capacity of the universal IoE transceivers as discussed in Section 1.3.4.

1.3.3 Increasing the Communication Performance

Utilizing multi-modal communications for performance improvement is a emerging research topic [42, 43].

The current approaches are based on either using a particular modality at a time or using two different communication modalities simultaneously via multiplexing. However, with only these functionalities, the adaptation to the diverse environments is not possible. A universal IoE architecture can simultaneously provide a combination of diverse functionalities including the aforementioned ones such as mode-switching, multi-modality and dynamic tuning of transmission/reception parameters, which can allow fullest adaptivity to the environment and/or application, and provide improved performance at the same time.

The functionalities of a universal IoE transceiver can pave the way for novel solutions tackling the performance impediments even in the arguably most challenging environments. For instance, there exist only a few technologies that can potentially support in-body communications, e.g., MC and Terahertz (THz)-band communications, due to the challenges imposed by the size constraints and physiological conditions. Considering an MC communication scenario involving multiple nanomachines sharing the same channel medium, multi-user interference (MUI) caused by the interfering molecules released by the other transmitters can degrade the performance significantly [44]. In case of a crowded MC network, the universal IoE transceiver can tune or reconfigure its communication mode opportunistically to minimize or avoid interference. For instance, the IoE transceiver can alternate the type of carrier molecules prior to transmission by dynamically sensing the channel in terms of concentration levels, similar to the cognitive radio methods in EM communications [45]. Alternatively, it can utilize an orthogonal communication modality, e.g., THz-band EM communications, to avoid MUI depending on the channel conditions. In addition, hybrid communication schemes multiplexing MC and THz-band communications can be devised to exploit orthogonality of these modalities collaboratively.

The functionalities of the universal IoE transceivers can also be leveraged in transmission control. For instance, in the case of MC, synchronization between the transmitter and the receiver is challenging because the feedback link from the receiver can cause huge overhead due to slow propagation of molecules [46]. An IoE transceiver can employ different types of molecules for data transmission and synchronization [47]. Similarly, an IoE transceiver can use a communication modality in transmission control to assist another modality used in data transmission. A relevant example is the hybrid underwater optical/acoustic networks for real-time video streaming [48]. The optical data transmission is only possible when the optical modems are aligned properly. Therefore, until the alignment, while the optical links are not available, acoustic links can provide backup for transmission of data, and control signals, such as acknowledgements, for the optical modems.

1.3.4 Increasing the Energy Harvesting Capacity

EH enables IoE transceivers to operate without requiring any external source of power. By assuring theoretically unlimited energy, EH aims to increase longevity and hence to replace batteries, in particular, which are not only capacity-limited but also maintenance-heavy and environmentally unfriendly. Despite its benefits, EH often fails to support periodic reporting due to the uncontrollable and unpredictable nature of the exploitable sources and the power-hungry communication capabilities of the IoE transceivers. Hence, the coexistence of different harvesting mechanisms is crucial to tackle the non-deterministic behavior of the EH, achieving reliability in IoE communications.

Hybrid EH enables us to utilize ambient sources opportunistically and thus reduce the variance in the EH output thanks to the enhanced continuity in the energy input. If the deployment environment has multiple sources available together, the IoE transceiver can harvest them simultaneously or alternately. That often increases the amount of collected energy for a given time period, which expands the feasible energy tunnel enhancing the optimal energy allocation policy [16]. If a large enough storage is employed, the optimal energy allocation policy of the hybrid EH IoE transceiver approximates to that of an unlimited battery, referring to perpetual and reliable operations at the highest transmission rate possible.

There are a plethora of studies combining different energy sources/harvesters in practice [49]. The prominent examples of this exploit either a single source (providing multiple energy streams, such as temperature gradients and vibrations generated on a pipe due to water flow) with different harvesting mechanisms, e.g., thermoelectric and piezoelectric generators, or multiple (diverse) sources, such as solar and wind power or acoustic waves and RF signals. The hybridization of sources should also increase the overall energy conversion efficiency of the system, compared to the sum of individual efficiencies, which can be achieved at the slight expanse of volume, cost, and complexity [50]. Increasing the EH capacity is particularly important for applications in which the power provisioning process is intertwined with data communication. One example is the nano-devices harvesting molecules for energy generation, where some of those molecules are then used to transmit data. Hence, the IoE transceivers with multi-modal EH capabilities will increase the likelihood of energy generation from their surroundings by accommodating the necessary components, which offers numerous benefits especially for the multi-modal communications in the IoE domain.

1.4 Challenges and Potential Research Directions

The fundamental properties of the universal IoE transceivers, i.e., multi-modality in communications and energy harvesting, modularity, tunability and scalability, bring many opportunities, some of which are discussed in the previous section; however, the realization of them poses unique challenges. In this section, some of these challenges along with the open research directions that can potentially address them are discussed. We first focus on the open problems in enabling the multi-modality in communications and energy harvesting. Our discussion is then extended to the adaptivity challenges in connection with the tunability property of the universal transceivers with regard to several aspects including channel sensing and energy awareness. We also provide an in-depth discussion on the miniaturization challenges to satisfy the scalability criterion of the universal transceivers.

1.4.1 Multi-modal Communications

Integration of multiple communication modalities is a key feature of the universal IoE transceiver architectures, providing the IoE devices with the capability of seamless interfacing between heterogeneous networks and ubiquitous operation. On the other hand, multi-modality in communication poses two fundamental challenges, namely, reliable and information-efficient inter-modality transduction, and cross-modality interference.

Inter-modality transduction is highly common in conventional communication networks. For instance, conversion between electrical and optical signals is the enabler of the global Internet through optical fiber links. Acoustic transceiver components such as acoustic signal generators and receivers also rely on transduction between acoustic and electrical signals. On the other hand, with the emergence of IoBNT, research efforts are increasingly focused on bridging conventional modalities, e.g., optical, magnetic and electrical, with the unconventional carriers of information such as molecules [51, 52, 53]. In this direction, proposed transduction methods are mainly based on synthetic biology products and tools, such as whole cell biosensors and optogenetic methods [54]. However, entirely biological nature of these transduction methods limits their application range to in vivo environments. On the other hand, the universal IoE transceiver consisting in the interface of conventional and unconventional communication modalities must be able to operate in various environments to support the universality of the IoE. To this end, investigation of novel nanomaterials which are compatible with a large range of environments and scales, and support transduction of different energy forms into each other could be a promising approach. Transduction performances of such materials in terms of information efficiency and delay also an issue requiring through investigation along with the hardware complexity burden that each modality adds. Moreover, multi-modality in communications comes with its unique challenges. For example, it is imperative to investigate cross-modality interference, which could significantly affect the communication performance, if two modalities are interlinked indirectly through their impact on communication channel or transceiver. In the following, we discuss some of these challenges and propose potential research directions.

Transduction

Inter-modality transduction can be performed in two ways, namely transduction of all modalities to and from electrical domain, and direct transduction between different modalities without conversion to electrical domain. We envision that inter-modality transduction in universal IoE transceiver architectures is based on the first one because current signal processing elements rely on electrical signals providing fast processing. Important challenges regarding the inter-modality transduction are transduction efficiency, processing delay, throughput mismatch between different modalities, and hardware complexity. Direct inter-modality transduction without conversion to electrical signal is also a potential approach that can be taken to address the aforementioned issues with the indirect transduction [55, 56].

Inter-modality transduction must be information efficient such that information loss during the transduction process should be minimized. In this direction, investigation of high-performance novel materials enabling transduction from a set of diverse modalities to electrical domain and from electrical domain to the modality of choice is crucial. Employing the same material for transduction of all modalities is also crucial for integrability. Moreover, for an efficient transduction, respective material parameters, which affect the material properties, must be optimized as well. Graphene and related materials (GRMs) are promising in this direction. Graphene is a two-dimensional carbon-based nanomaterial having unique electrical, optical, mechanical, thermal and chemical properties [57], which make it suitable for transduction of diverse modalities including acoustic, optical, RF/microwave, THz and molecular. The outstanding properties of graphene also enable sensitive and fast sensing of diverse modalities including light and molecules [57]. Moreover, as a planar material graphene provides flexibility in a way that high integrability and compactness are possible [57].

GRMs in acoustic-electrical transduction: Thanks to its high mechanical strength and ultra-thin structure, graphene is deemed promising as a wideband ultrasonic transducer as well as wide-frequency-response electrostatic acoustic transducer [58, 59]. Thin structure of graphene-based diaphragm of acoustic transducers provides the broadening in the frequency spectrum of the generated or detected acoustic waves considering conventional diaphragms, and high mechanical strength of graphene makes graphene-based diaphragms robust to deformation [59]. On the other hand, such acoustic transducers can have limitations in terms of the output quality. For instance, graphene-based acoustic wave generators provide limited output pressure density due to the loss caused by high sheet resistance of graphene [60]. In this direction, thermo-acoustic graphene acoustic wave generators using thermal variations in the air near its surface instead of mechanical vibrations to generate acoustic waves offer a great potential because of their flatter output response at wide frequency range and the output power increasing linearly with the input power [61]. In this direction, investigating the performance of graphene acoustic transducers in diverse environments, e.g., underwater, is also crucial for the IoE support.

GRMs in EM-electrical transduction: Graphene can also be used in wideband optical to electrical and electrical to optical conversion thanks to its electro-absorption and electro-refraction properties [62]. Due to its high conductivity, graphene can also be utilized in radiating and receiving RF and microwave signals. Although exfoliated and chemical vapor deposition (CVD)-based graphene sheets exhibit large surface resistance causing large losses at RF/microwave frequencies [63], it has been demonstrated that screen-printed graphene components can be utilized in RF sensing and transmission [64]. Graphene also supports the tunable propagation of *Surface Plasmon Polariton (SPP) waves* at THz band [65], which are EM waves propagating along a metal-dielectric (or semiconductor-dielectric) interface formed through the interaction of EM field with the oscillation of surface charges. This capability of graphene has opened the way for the development of tunable graphene plasmonic modulators modulating SPP waves, and tunable graphene plasmonic nano-antennas converting SPP waves to EM waves and vice versa [66, 67].

GRMs in molecular-electrical transduction: Graphene can also be utilized in molecular-to-electrical and electrical-to-molecular transduction [5]. Field-effect transistor-based biosensors (bioFETs) made of functionalized graphene have been shown to be promising in the transduction of biomolecular concentrations, e.g., present in blood, saliva and tissues [68, 69], into electrical signals. There also exist porous graphene structures, which can be utilized as a membrane in drug reservoirs that can selectively release particular types of molecules through controllable pore sizes [70, 5]. In addition to GRMs, transition metal dichalcogenides (TMDs) are also emerging 2D layered materials offering great potential for inter-modality transduction [71]. A particular member of TMDs is Molybdenum disulfide (MoS_2), which has attracted great attention because it is electrically and mechanically robust. In this direction, various applications of MoS_2 have been reported including highly sensitive molecular-to-electrical conversion [72] and optical-to-electrical conversion [73], and electro-optic modulators [74, 75]. Black phosphorus (BP), which is the another class of 2D materials with the applications in optical detection and modulation, and molecule sensing [76], can be potentially utilized in inter-modality transduction.

Cross-domain matching: The investigation of high-performance materials is also crucial to address transduction and processing delay issue. Graphene is also promising in this direction. Thanks to its exceptionally high carrier mobility (up to $\sim 10^5 \text{cm}^2/\text{V}\cdot\text{s}$ at room-temperature [77]), graphene can transform light as well as THz signals into electrical signal with ultrafast response [78, 79]. Graphene can also enable tunable ultrahigh-speed processing components for THz-band communication such as frequency converters, mixers and modulators [80]. Large surface specific area of graphene (~ 2600 m^2/g) provides rapid sensing of molecules as well [81]. It has been also demonstrated that graphene composites can be utilized in ultra-fast sensing of acoustic signals [82].

Information throughput of different communication links might be different due to the diversity in employed communication methods, bringing the challenge of throughput-mismatch in interfacing heterogeneous networks. For instance, consider a IoBNT scenario where an intra-body nanonetwork employing MC interfaces with external networks via EM communication. Due to slow molecular diffusion and reaction dynamics, MC provides very low data rates compared to conventional EM communications. In such as scenario, when the external device sends high-rate data to an intra-body nanomachine with an universal IoE transceiver, the nanomachine may not relay the external input to the other intra-body nanomachines reliably because of the limited storage capacity, i.e, buffer overflow. Thus, novel transmission rate control techniques for limited storage capacity are required in this direction.

Integration: The integration of separate transduction, processing, and memory components for multiple communication modality can increase the hardware complexity of the universal IoE transceivers. In this regard, one of the potential research directions is the direct inter-modality transduction without conversion to electrical signals, which removes the necessity of processing in electrical domain, and also improves the transduction efficiency and delay. Alternatively, materials and methods enabling multi-functional capabilities, e.g., transduction, signal processing and memory, can be investigated towards reducing the complexity.

Cross-modality Interference

As the universal IoE transceivers can use multiple communication modalities simultaneously, a novel performance limiting factor, namely the cross-modality interference emerges. For instance, when MC and EM communication are active at the same time, MC changes molecular composition of the medium, which in turn affects the propagation of EM waves in a way that molecules vibrate as a result of energy absorption from EM waves and causes the molecular absorption noise at the corresponding EM wave frequencies [83]. The impact is drastic at THz and optical frequencies. Similarly, EM radiation can affect the performance of MC because the temperature fluctuations due to molecular absorption of EM energy affect molecular dynamics [84]. Moreover, the molecular composition of the medium can change the reception/transmission performance of the transceiver components. For instance, absorption of interfering molecules on the graphene THz or optical antennas can change the refractive index of the antenna surface, which in turn affects the propagation of surface plasmonic waves [85]. A similar effect can be observed on graphene-oxide-based optical antennas, whose fluorescent properties are affected by the pH change in the medium due to the interfering chemical molecules [86]. This challenge can be addressed by identifying all the possible cross-modality interferences and developing the necessary channel and network coding methods.

1.4.2 Multimodal Energy Harvesting

Leaving aside the continuous efforts to improve simplicity and hence energy efficiency of the communication methods, such as modulation and detection techniques [5], the most promising solution to enable self-sustaining operations is the integration of EH modalities into the IoE domain. EH has recently received tremendous research interest partly due to the energy needs set by the emerging IoE applications. Different application requirements and ever-changing medium conditions have proliferated the need for EH methodologies to achieve robust, continuous, and self-sustaining operations by reducing the impact of unpredictable and uncontrollable factors, i.e., the uncertainties. These are the options that have been considered for self-sustainable communication networks; thus, they are promising for integration into the IoE transceivers in a multi-modal manner. Depending on the application environment and device architectures, various energy sources can be exploited by the IoE devices [87, 19]. For example, solar power, flow energy, vibrations, electromagnetic signals, and metabolic sources have been deemed feasible for harvesting [16]. Despite being useful, using only one harvesting mechanism may not always be enough for the continuous operation of IoE devices. Hence, the research has looked towards *hybridization* of harvesters/resources.

Hybrid Energy Harvesting Methods

An interesting research direction in parallel with the wider IoE vision is towards hybrid EH systems exploiting multiple energy sources. We have previously investigated novel EH methods based on ambient electric field [88, 89, 90], and introduced energy-neutral Internet of Drones concept under the umbrella of IoE [17]. The aim here should be to combine several EH mechanisms for designing self-sustaining battery-less universal transceivers that can support various applications from micro-nano scale in-body applications to macro-scale airborne applications. Towards this objective, total energy consumption of universal transceiver should be estimated by considering energy requirements of different communication modalities and processing units. At the end, different EH and WPT techniques can be combined to provide the energy required for node operation, i.e. sensing and processing, as well as data communication between nodes and information gateways.

Concerning the intrabody and body area applications, human body stands as a vast source of energy in the form of mechanical vibrations resulting from body movements, respiration, heartbeat, and blood flow in vessels, thermal energy resulting from varying body temperature, and biochemical energy resulting from metabolic reactions and physiological processes [91]. Literature now includes a multitude of successful applications of EH from human body to power miniature biomedical devices and implants. Some examples are thermoelectric EH from body heat for wearable devices [92], piezoelectric EH from heartbeats [93] and respiratory movements [94] for pacemakers, as well as biochemical EH from human perspiration [95]. These together with EH from chemical reactions within the body, such as glucose uptake, lactate release, and pH variations [91, 96], can be exploited to power the IoE transceivers. Among the potential EH mechanisms, mechanical EH has attracted the most interest. Research in this field has gained momentum with the use of flexible piezoelectric nanomaterials, such as ZnO nanowires and lead zirconate titanate (PZT), in nanogenerators, enabling energy extraction from natural and artificial vibrations with frequencies ranging from very low frequencies (< 1 Hz) up to several kHz [97, 98]. A hybrid EH architecture is also proposed for IoE comprising modules for EH from light, mechanical, thermal, and EM sources [16].

Wireless Power Transfer

As explained previously, the universal IoE transceivers can sustain multi-modal EH capabilities by benefiting from ambient resources that are available in their deployment environment. In some cases, some of those sources can be dedicated, i.e., external sources delivering power to the IoE transceivers remotely, which refers to WPT. WPT has seen significant advances in recent years due to increasing need for replenishing the energy reservoir of IoT devices as well as wearable and implantable devices [99]. Various forms of WPT have been considered for powering medical implants [100, 101]. For example, near-field resonant inductive coupling (NRIC)-based WPT, the oldest WPT technique, has been widely-used for cochlear implants [102, 103]. Other techniques include near-field capacitive coupling, mid- and far-field EM-based WPT, and acoustic WPT. The near-field capacitive and inductive coupling, however, is only efficient for distances on the order of transmitting and receiving device sizes, and for the right alignment of devices. Therefore, it might not be suitable for powering micro/nanoscale IoE tranceivers [102]. On the other hand, radiative mid- and far-field EM-based WPTs can have looser restrictions depending on the frequency of the EM waves.

Recent research on mmWave and THz rectennas suggests the use of high-frequency EM WPT techniques for power delivery [104]. However, for intra-body applications, the higher absorption with increasing frequency and power restrictions should be taken into account. Nonetheless, simultaneous wireless information and power transfer techniques (SWIPT) utilizing THz-band have been investigated for EM nanonetworks [105, 106]. Similar SWIPT applications have been considered for MC, where the IoE devices use the received molecules for both decoding the information and harvesting energy [107, 108]. There are also applications of acoustic WPT for biomedical implants using external ultrasonic devices [109, 110]. Although not practically implemented yet, ultrasonic EH has been also considered for powering IoE devices with piezoelectric transducers [111, 112, 113].

It should be noted that both EH and WPT are still at their infancy especially for nano-molecular communications in the IoE domain. New research efforts focus on reducing the power requirements of IoE transceivers by using energy efficient protocols, conservation schemes and novel topologies, rather than focusing on EH and WPT mechanisms or their joint utilization [114]. Therefore, it stands as a major open issue to utilize various EH and WPT mechanisms to create modular energy unit for the universal transceiver framework, such that different power extraction modalities can be configured depending on the application and medium of operation.

1.4.3 Adaptivity and Tunability

Channel Sensing and Cognitive Radio

Channel sensing is essential to enable adaptivity in universal transceiver architectures. The adaptive and opportunistic selection of the most proper communication modality and dynamic tuning of transmission and reception characteristics require dynamic channel sensing in multiple modalities and in a broadband manner. Broadband sensing refers to the sensing capability that can provide tunability property to the universal IoE transceivers in the maximum possible extent. For instance, in the case of MC, sensing as many different kinds of molecules as natural systems have is required for bio-compatibility. For EM communication, sensing at wide frequency range is needed for dynamic tunability. On the other, simultaneous channel sensing in different communication modalities may impose high complexity burden. These issues necessitate the development of low-complexity, reliable and broadband channel sensing techniques for each communication modality. Channel sensing techniques have been widely explored for RF [115, 116], optical wireless [117, 118, 119] and acoustic communications [120, 121], and similar investigations have just started for MC [45].

For the RF modality, spectrum sensing has received great attention because it is indispensable part of cognitive radio (CR) technology alleviating spectrum scarcity problem via dynamic spectrum access. CR capability can provide the universal transceivers with the adaptivity desired in a way that the universal transceivers can reconfigure their transmission parameters according to the available communication resources in the surroundings. Considering the heterogeneity of networks in the IoE environment, diverse communication technologies will utilize the RF spectrum. In this respect, one particular challenge is the identification of the signal types/transceivers occupying the bands and their corresponding transmission parameters, e.g., carrier frequency, bandwidth, modulation type, transmission protocol, number of carriers [122], which is crucial to obtain spectrum awareness. Different from the classical signal identification techniques, deep-learning based identification does not require prior knowledge about the signals such as noise statistics, demanding extensive analysis [123, 124]. Hence, deep learning-based identification techniques could be promising in this direction but the complexity burden should be further considered. Regarding spectrum sensing in RF spectrum, wideband and low-complexity compressed sensing techniques are available, thus can be utilized for the universal transceivers [125].

As the frequency usage is shifting towards mmWave and THz frequencies in EM communication, there is also need for ultra-wideband spectrum sensing techniques. Considering the high-sampling rate requirement of mmWave and THz band communication technologies, compressed sensing techniques exploiting the inherent sparsity of mmWave and THz signals can be utilized in universal transceivers [126]. Time-varying spectrum occupancy and high path losses affecting reliable sensing are the other issues relevant for channel sensing in mmWave/THz communication modalities [127].

CR has also been considered for acoustic communication systems for efficient spectrum usage. The concerted effort in *cognitive acoustic* have been focused on underwater acoustic communications [128]. The challenges identified in this direction include narrowband response of the acoustic transducers, long preamble of underwater acoustic modems, i.e., guard time or cyclic prefix signal inserted to overcome interference, and highly varying underwater channels [128]. As discussed in Section 1.4.1, graphene-based acoustic transducers, which are suitable for wideband acoustic transduction [58], offer a potential to address narrowband transduction issue.

Moreover, further investigation considering channel conditions peculiar to other application environments different than the underwater channels is needed towards realizing cognitive acoustic for the universal transceivers.

Similar to the CR technology, the universal transceivers can use the MC channels opportunistically by sensing the type and concentration of molecules in the channel dynamically. For instance, if the channel is crowded with a specific type of molecule, the transceiver can use a different type of molecule to avoid MUI. However, sensing becomes challenging as the number of communication entities using MC, including bio-entities using chemical signaling, in the medium increases because there might be many types of molecules in the medium. Thus, to maintain reliable communication and to minimize the possible harmful effects on surrounding bio-processes, novel MC wideband sensing techniques recognizing as many as molecules are needed.

In addition to the modality-specific issues in channel sensing, there are novel issues such as sampling rate adjustment. Sampling rate can be different for different modalities. For instance, MC does not require high-rate sampling as the wideband RF spectrum sensing requires. However, in dynamic environments higher sampling rates may be needed. Hence, the dynamic optimization of the sampling rate is an open problem.

Energy-aware Communications

The conventional way of ensuring the longevity for energy-constrained devices is to adopt energy-efficient communication techniques since the majority of the limited energy budget is consumed during data transmission. Radio optimization, clock synchronization, low-power sleep/wake-up, energy-efficient routing, and data reduction schemes are the main enablers of lengthened operation times [35].

Energy-aware communications can be regarded as a subset of those techniques yet they have some differences in practice. For example, the low-power operation can be achieved through aggressive duty-cycling and/or wake-up radios by turning the radio on (for idle-listening or transmission) and off (for power saving) periodically [129]. In similar, multi-path routing, data compression, and network coding schemes can be adopted during the system design stage to assure reliable communications on a budget. When the energy input is not constant, i.e., the device is creating its own energy via EH, however, energy-aware communication techniques come into prominence. In such cases, the devices adapt to energy availability by changing their transmit power and/or sampling rate dynamically, besides updating their data queue by dropping some packets based on freshness or priority. The recently emerged intermittent *or* transient computing techniques, on the other hand, can assure application execution under scarce EH conditions through an incremental process at each power cycle based on the energy input [130], [131].

On the molecular level, energy-aware algorithms can be used for efficient coordination and movement EH nanonetworks, e.g., engineered bacteria tracking and eliminating harmful targets in the human body [132]. Since the molecules harvested for energy generation can also transport information, the EH process directly governs data transmissions [133]. Other approaches, such as feedback control, are also promising for energy-aware MC, especially in diffusion-based information transfer [134]. By adopting these technologies, the IoE transceivers can achieve energy awareness in communication in concordance with the EH modality selection mechanism.

EH Modality Selection

As discussed earlier, adaptive hybridization of different energy forms is crucial for the IoE vision as it grants unique capabilities. However, the design of a hybrid EH system is not always straightforward [135] since each harvester/storage device often needs its own interface circuitry, which translates into increased cost and complexity.

Most of the communication modalities utilize electrical energy, which is stored in electrical storage shown in Fig. 1.1. To ensure the flow, the system needs an input power conditioning/management/provisioning circuit to interface with the EH sources, alternate between harvesters and energy stores (molecular or electrical), or combine them when necessary. This circuit should include a rectifier for converting the collected energy into a utilizable form and preventing its flow back to the harvester(s), besides a DC-to-DC converter for maximum power tracking and providing the stable output required by the transceiver antennas. The MC modality of the IoE transceiver can also use the electrical energy for internal operations, such as sensing and processing. However, the IoE transceiver harvesting molecules need additional components, such as a chemical bank with basic building components to convert the harvested molecules into molecular information [107], which can be attached to the molecular storage.

Once established, the IoE transceiver can harvest energy opportunistically from any source available in its vicinity, swap between (or combine) harvesters or energy stores when the primary source disappears or when it changes its application environment, and probe its proximity using different sensors enabled/disabled according to the requirements of different tasks/applications. In this way, universal, modular, and adaptive IoE systems can be devised.

As discussed, the EH modality selection can be either pre-planned or adaptive to the ambient factors. One example is swapping sunlight to wind and/or rain drops when the weather in the deployment environment changes. The other case is the change of the environment itself, i.e., the system can harvest energy from heartbeat and/or blood flow instead of lactate or glucose when it moves within the body. These approaches often refer to *online energy profiling*, in which the IoE system adapts its operation to the current channel/medium state, thereby harvesting energy opportunistically. The conventional EH transceivers, however, commonly accommodate *offline energy profiling*, i.e., the medium-specific energy availability is known prior to operation. If the IoE transceiver employs the latter, it changes its application environment as it knows that a particular source will be available/in abundance in a particular location. This availability can be either due to perpetual bio-mechanical drivers, such as heartbeat, blood pressure, and breathing, or due to recurring events, e.g., periodically released hormones [136]. Hence, the IoE system not only changes its medium but also its EH modality as a reflex to sustain reliable communications by getting the most out of the surrounding resources. That requires seamless coordination and efficient interaction of system components.

1.4.4 Miniaturization

The miniaturization trend at all levels of communication systems is being driven by the increasing number of connected devices. The miniaturization can provide key advantages including easy integrability, more functionality with lower footprint, increased performance, reduced power consumption and manufacturing cost. In the context of IoE, which aims at the ubiquitous connectivity of highly diverse entities, including bio/nanomachines, the miniaturization of transceiver components to micro/nanoscales is indispensable. The future 6G networks will also be a part of the IoE environment, for which the frequency shift towards THz band in EM communication is inevitable [137]. The usage of THz band necessitates downscaling the size of transceiver components to micro/nanoscales. Moreover, nano and bio-nano networks using unconventional communications at nanoscales, such as MC, are important components of the IoE, and interfacing these networks also requires miniaturization to micro/nanoscales. As such, universal transceivers must be integrable to a very large set of diverse devices and entities of varying scale and structures. Moreover, micro/nanoscale devices and components are known to be more energy-efficient in providing the similar functions as their macroscale counterparts. The miniaturization of the universal transceivers can also provide flexibility in their integration to various devices of different size scales to transform them into IoE devices. For example, micro/nanoscale universal transceivers can be embedded into both micro/nanoscale biosensors and macroscale bio-cyber interfaces as part of an IoBNT application such as remote healthcare with continuous health monitoring based on IoBNT as illustrated in Fig. 2.1.

In the past decades, silicon semiconductor technology has been the driving force for down-scaling the size of transistors so that they can be packed onto smaller and smaller chips. However, it is now long-evident that the silicon technology is reaching its physical limits. As silicon layers are getting thinner, electron flow through silicon channels is slowing down due to the surface imperfections that are scattering charges [138]. New novel nanomaterials with exceptional electrical, mechanical and biochemical properties, such as GRMs as discussed in Section 1.4.1, have emerged to overcome this limitation and to expand the diversity in functionalities in line with the More than Moore approach. However, there still exist substantial challenges with regard to growth and processing of these materials [139].

There also exist technical challenges to build some transceiver components with desired performances at micro/nanoscales. For instance, regarding conventional communications, e.g., RF and acoustic, shrinking the size of transceiver components such as antennas and modulators to micro/nanoscales while preserving their functions is still an issue because the operation in the micro/nanoscale limits the carrier frequency to high-frequency ranges for these technologies. On the other hand, it should be noted that realizing universal IoE transceivers requires departure from the approaches aiming to optimize the performances of the transceiver components for individual modalities. Rather, the underlying theme of universal transceivers must be the maximization of the versatility stemming from multi-modality, scalability, and tunability, which can nevertheless be obtained by transceiver components suboptimally performing in individual modalities. Accordingly, in the following, we discuss the miniaturization challenges and potential research directions in developing miniaturized IoE universal transceiver components with regard to several modalities.

With the recent paradigm shift towards the usage of THz band, EM antennas are getting shrunk down to micro/nanoscales. Due to high losses introduced at THz frequencies by spreading, molecular absorption and scattering, the THz communication range is substantially limited. To overcome this limitation, multi-input-multi-output (MIMO) array architectures enabled by graphene plasmonic nano antennas have been proposed [140, 141]. Howeover, THz wave propagation introduces novel physical phenomena that can affect the performance of MIMO arrays. For instance, a THz beam may diverge from the direction of its modulation sidebands slightly due to frequency-dependent diffraction nature of THz signals [142]. This may degrade the performance of a MIMO array in terms of bit error rate because different antennas may detect different spectral information [142]. Thus, novel detection and demodulation methods are needed to overcome this limitation. Other important challenges towards THz communications with miniaturized transceivers are the efficient signal generation and detection. In this direction, concerted effort has been dedicated to solid-state electronics and photonics approaches [143]. However, the electronics approach suffers from limited output power at THz frequencies and photonics approach based on quantum cascade lasers offers poor performance at room temperature [144]. In this direction, micro/nanoscale graphene transistors with extremely high carrier mobility can pave the way for the development of THz-based signal generation and sensitive detection components [145].

Silicon technology has achieved the miniaturization of optical communication components to microscale [146, 147]. Recently, optical components utilizing SPPs have emerged for further miniaturization that are able to confine the light into nanometer scale. In this direction, plasmonic nanoantennas [148], nanolasers [149] and modulators [150] have been developed. The most pressing challenges in this direction are tuning plasmonic resonance frequency to higher frequencies, e.g., visible and near-infrared, which could be achieved through high level of doping [151], and integration of plasmonic components into non-plasmonic structures without high insertion losses [152].

Regarding MC, the first prototype of a nanoscale MC receiver, as illustrated in Fig. 2.4, has been recently introduced in [2]. This architecture incorporates the sensing mechanisms of electrical biosensors for detecting MC signals. Regarding the miniaturized MC transmitter component of the universal transceiver, as discussed in Section 1.4.1, porous graphene structures enabling controllable permeability across pores via electric field are promising for providing selective and tunable molecule transmission. On the other hand, high surface-to-volume ratio in nanopores exhibits new physical phenomenon that is not observed at larger scales. That is, surface charges become dominant in molecular transport by introducing electrostatic forces affecting the interactions between molecules and surfaces in liquids [153]. Thus, the effect of surface charges need to be considered in MC transmitter design. Molecule storage is also an important challenge regarding the miniaturization of MC transmitters. In this direction, stimuli-responsive hydrogels, which are also envisioned for

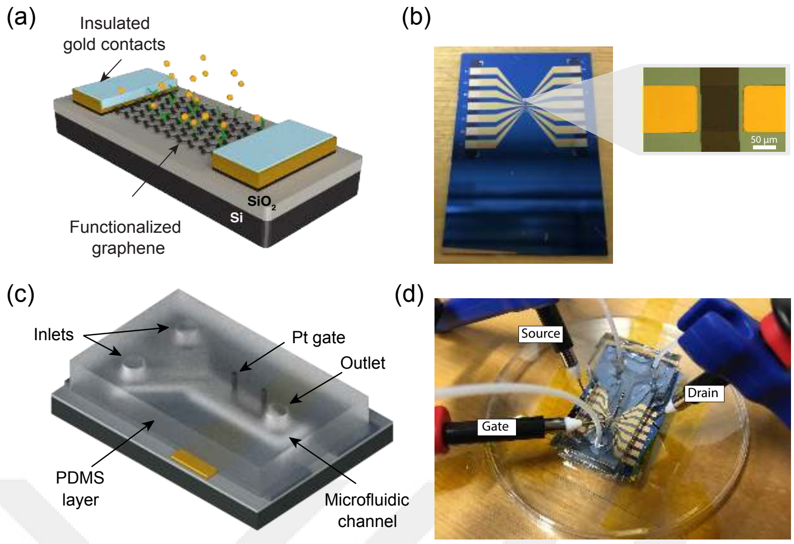

Figure 1.4: Graphene-based micro/nanoscale MC receiver [2]: (a) Conceptual drawing of MC receiver with functionalized graphene, (b) Fabricated MC receiver, (c, d) Integration of the MC receiver into a microfluidic MC channel.

smart drug delivery, are promising [154]. Various type of molecules can be harvested from a fluidic medium by triggering the deswelling state in a hydrogel reservoir and loaded molecules can be transferred to MC transmitter antenna, i.e., tunable porous graphene membrane, by activating the swelling state through the application of a stimulus such as electrical field, magnetic field or light [155] in a controllable manner.

The miniaturization efforts regarding RF applications have focused on carbon-based materials, especially carbon nanotube (CNT) in the last two decades. CNTs have material properties including high mobility and small size that are suitable for miniaturized RF applications such as modulators, mixers, amplifiers [156]. Initial demonstrations of CNTs in RF applications were nanotube radios [157, 158]. Although the AM demodulator based on a single CNT in [158] has small size, i.e., $1 \times 10^{-21}\,\text{m}^3$ of system volume, the overall volume of the system including the external antenna is of order $1 \times 10^{-3}\,\text{m}^3$ [159]. In this direction, resonant CNT antennas can further reduce the overall system size because slow propagation of the waves on CNTs compared to free space provides a reduction in the resonant antenna size up to 100 times [160]. Different from the radios in completely electrical nature, the operation of the nanotube radio implemented using a single CNT in [157] is partly mechanical. Micro/nanometers long CNTs for nanoelectromechanical-based RF applications are suitable for the operation in MHz and GHz range, respectively. On the other hand, for both nanotube radios, the sensitivity is low such that receiving weak RF signals is not possible [161]. Thus, further research is needed in this direction towards realizing micro/nanoscale RF components for the universal IoE transceivers. Alternatively, magneto-electric (ME) materials are also promising to miniaturize RF components such as antennas to micro/nanoscales [162, 163]. For instance, instead of EM wave resonance, nanomechanical ME antennas operate at the acoustic resonance frequency. Since the acoustic wave length is smaller than the EM wave length at the same frequency, ME antennas can potentially provide dramatic miniaturization, i.e., hundreds to thousands of times smaller antennas, without performance degradation [164].

Two-dimensional nanomaterial technology have also opened the way for reducing the size of acoustic transceiver components, such as microphones, loudspeakers and earphones. In particular, graphene membranes that can generate and sense acoustic waves have received great interest due to their exceptional mechanical and electrical properties [58, 59, 165]. However, downscaling the dimensions of a graphene membrane, which is a vibrating element, to micro/nanoscales limits the operation frequency range to MHz-GHz because the resonance frequency of a graphene membrane f scales as t/L^2, where t and L is the thickness and the length of the graphene membrane, respectively [166]. Thus, for the operation in the low frequency range, i.e., Hz-kHz, large membranes in millimeter scale are required [167]. Alternatively, based on the relation t/L^2, thick and small scale multilayer graphene membranes can be utilized in the low frequency range [168]. However, increased thickness may lower the sensitivity of the graphene membrane [167]. In addition, integrating graphene membrane to the universal transceivers can be challenging since it is a mechanical component. Therefore, further research is needed in this direction to realize micro/nanoscale broadband acoustic components for the universal transceivers.

1.5 Conclusion

In this chapter, we introduced the concept of universal IoE transceiver that defines the transceiver architectures, which possess multi-modality in communication and energy harvesting, modularity, tunability, and scalability. Through several practical cases involving also non-conventional communication modalities, e.g., molecular, THz-band communications, which will be relevant in the upcoming IoE landscape, we argued that such universal transceivers that can be scaled down to micro/nanoscales could address the unique IoE challenges, such as interoperability, ubiquitous connectivity, energy efficiency, and miniaturization, and could open up further opportunities in diversifying the IoE applications. Along this direction, key physical layer challenges are outlined with potential solutions, which are centered around the use of novel nanomaterials, such as graphene, that manifest unique electrical, optical, mechanical and biochemical properties.

Chapter 2

GRAPHENE AND RELATED MATERIALS FOR THE INTERNET OF BIO-NANO THINGS

2.1 Introduction

The contemporary landscape of information and communication technologies (ICT) is experiencing a rapid evolution, driven by the proliferation of Internet of Things (IoT) applications. These applications hinge on the interconnection of a vast number of heterogeneous devices that interact closely with the physical world, utilizing an array of sensing and communication technologies. Advancements in biotechnology and nanotechnology, particularly in synthetic biology and nanomaterials, pave the way for the next significant milestone: extending our control and connectivity to the universal scale, including the complex biotic world, ultimately serving the holistic *Internet of Everything (IoE)* vision [169, 19, 170].

Central to the IoE vision, which draws inspiration from the vast connectivity and diverse networking characteristics in the universe, is the emerging *Internet of Bio-Nano Things (IoBNT)* framework, which encompasses collaborative networks of *Bio-Nano Things (BNTs)* [3]. These networks consist of diverse array of context-aware entities, including biological beings and artificial micro/nanoscale devices, such as engineered bacteria and nanosensors that interact closely with their natural counterparts in complex biological environments [20]. Leveraging the power of nanotechnology and biotechnology with communication and networking tools, IoBNT is poised to seamlessly bridge the digital and biological worlds in ways and at spatio-temporal resolutions that were previously inconceivable. Therefore, towards the core IoE vision of bringing connectivity into unprecedented domains, IoBNT is expected to play a critical role in overcoming heterogeneity and scalability challenges of IoE.

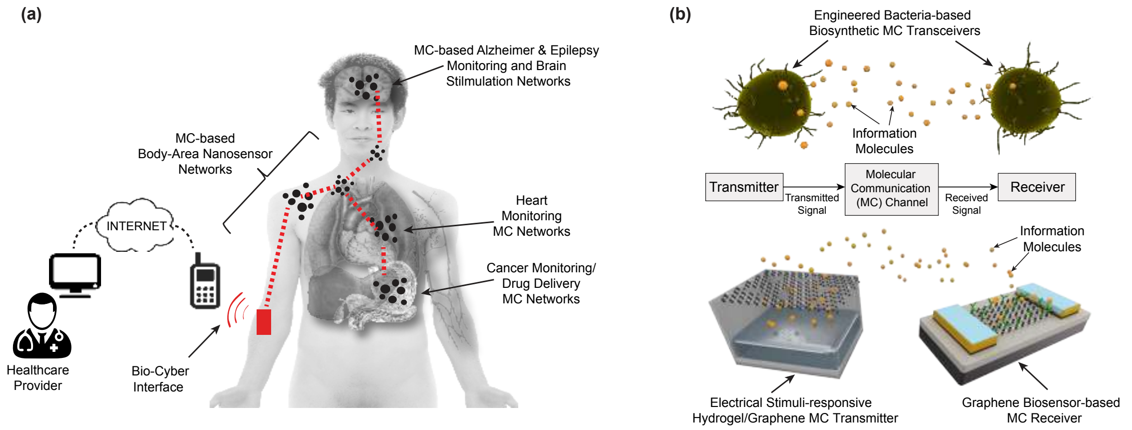

Figure 2.1: (a) Conceptual drawing of a continuous health monitoring application of IoBNT, involving intrabody distributed MC nanonetworks of biosensors and a bio-cyber interface interconnecting the nanonetworks and conventional networks [3]. (b) MC among engineered bacteria, and between GRM-based BNTs. Reproduced with permission from Proceedings of IEEE 107, 7 (2019). Copyright 2019 IEEE.

As such, BNTs and the IoBNT framework stand as a crucial piece of IoE, underpinning the expansion of our connectivity to the universal scale, and unlocking a vast array of opportunities to devise novel applications, particularly in healthcare.

The IoBNT framework envisions integrating BNTs into conventional communication networks through seamless bio-cyber interfaces, thereby enabling novel applications, such as remote and continuous health monitoring with nanobiosensor networks inside human body (Fig. 2.1(a)), theranostic smart drug delivery systems that can be remotely monitored and controlled, distributed sensing of chemical agents with engineered bacteria networks in various environments, artificial biochemical networks that replace or reinforce their natural counterparts for treatment of diseases, and many others [36, 38]. The biotic world is, however, characterized by immense heterogeneity among interacting entities, such as living cells, animals, plants, and bacterial communities, communicating across various spatio-temporal scales in challenging biological environments, such as inside human body. These natural BNTs interact through unconventional communication methods, such as exchanging biochemical and electrochemical signals, across diverse physiological environments [3]. At the fundamental level, biological interactions primarily involve micro/nanoscale components or their modular assemblies, such as ligand receptors and cargo-carrying microtubules [171], highlighting the essential role of artificial BNTs within the IoBNT framework for monitoring and controlling biological systems at single molecular resolution.

IoBNT presents numerous challenges, foremost of which is the need for innovative communication technologies that can withstand noisy and dynamic media such as biological environments. These technologies must be adaptable to micro/nano size scales and diverse biotic and abiotic characteristics of BNTs. Conventional electromagnetic (EM) communications are considered unsuitable due to size mismatch and BNTs' limited energy and computational resources. Emerging unconventional communication technologies offer potential solutions for enabling heterogeneous networks in IoBNT. Bio-inspired molecular communications (MC) stand out as a prime method for interconnecting BNTs, delivering superior biocompatibility and biotic-abiotic interoparability by harnessing nature's communication strategies. Terahertz (THz)-band EM communications and ultrasonic nanocommunications, utilizing extremely high-frequency EM waves and high-frequency acoustic waves, respectively, represent additional promising IoBNT communication technologies closely aligned with conventional ICT expertise.

Unconventional communication methods necessitate novel transceiver (Tx/Rx) architectures that are also unconventional in size, complexity, and transmission and reception functionalities. In MC, for instance, transceivers should be capable of encoding information into distinguishable molecular properties, such as molecular concentration, transmitting molecular signals into the channel, and subsequently sensing and decoding these signals [172] (Fig. 2.1(b)). The design of transceivers for THz-band EM nanocommunications necessitate revisiting the antenna theory to accommodate plasmons at the interface between solid-state materials and high-frequency airborne EM waves [66]. Fortunately, recent advancements in nanomaterials and nanofabrication techniques have facilitated significant progress in designing and fabricating practical Tx/Rxs for unconventional communication modalities. In particular, graphene and related materials (GRMs), with their exceptional electrical, optical, biochemical and mechanical properties, biocompatibility, and ease of fabrication and integration, show great potential in this area. Graphene's high surface-to-volume ratio makes it highly sensitive to biomolecules, enabling detection of a wide variety of molecular signals in biological environments. Additionally, graphene's plasmonic response supports the emission and detection of THz radiation [173, 6], while its exceptional thermo-photoacoustic properties enable wideband emission of high-frequency ultrasonic signals [174].

Interfacing BNTs and IoBNT networks, which partially or entirely rely on the exchange of molecular signals in challenging biological environments, with conventional EM-based communication networks presents another significant challenge, necessitating bio-cyber or nano-macro interfaces. These interfaces translate biochemical signals into other physical forms, such as electrical, optical, or EM, that can be processed by conventional ICT devices, vice versa. Existing neural interfaces, electrical biosensors, and drug delivery devices offer valuable insights for designing bio-cyber interfaces for IoBNT. Nanomaterials, particularly GRMs, stand out in these emerging technologies because of their exceptional ability to convert signals between various forms. Inspiring examples include graphene field-effect transistor (FET) sensors transducing biomolecular concentrations into electrical signals [175], and GRM nanocomposites releasing drug molecules upon electrical stimulation [176].

Energy self-sufficiency is crucial for most IoBNT applications, requiring BNTs to harvest energy from ambient sources and store it for continuous operation. The development of miniaturized energy harvesters and storage components relies heavily on nanomaterials and micro/nanofabrication technologies, which can also facilitate on-chip integration for IoBNT components. GRMs, with their remarkable electromechanical properties and flexibility, have found widespread use in these technologies. Their exceptional electrical and thermal conductivity, and mechanical strength make them suitable for harnessing various ambient energy sources, including mechanical vibrations, sound, heat, and light. Moreover, GRMs with large specific surface area, high electrical conductivity, and electrochemical stability exhibit great potential as high-performance active electrode materials for micro-supercapacitors (MSCs), an emerging technology for realizing integrable micro/nanoscale energy storage components for BNTs.

Therefore, GRMs with outstanding properties hold great promise in addressing the key challenges of IoBNT. In light of this, this chapter evaluates the potential of GRMs and related device technologies for the practical implementation of fundamental IoBNT components, namely micro/nanoscale transceivers, bio-cyber interfaces, and energy harvesting and storage components. By evaluating these technologies, we aim to contribute to the development and realization of the IoBNT vision, thereby fostering the emergence of groundbreaking applications at the intersection of nanotechnology, biotechnology, and ICT.

2.2 Graphene and Related Materials (GRMs)

Graphene, a two-dimensional (2D) monolayer of carbon atoms arranged in a honeycomb crystal lattice, has captivated researchers due to its extraordinary electrical, optical, thermal, mechanical, and biochemical properties. These properties make graphene an excellent alternative for existing materials in a wide range of nanotechnology applications. The first successful isolation of graphene from graphite and the subsequent groundbreaking experiments earned the researchers a Nobel Prize in 2010 [177]. In this section, we provide an overview of the fundamental properties of GRMs relevant for the fabrication of abiotic BNTs and IoBNT applications, as well as a discussion of widely-used GRM synthesis methods.

2.2.1 Properties of GRMs

Graphene is the very first example of a closely-packed 2D material isolated in nature. The sp^2 hybridization of carbon (C) atoms in graphene results in a unique honeycomb structure (Fig. 2.2), where each C atom connects to three other C atoms at a 120-degree angle and with an inter-atomic distance of 1.42 Å. This structure leaves one electron in the out-of-plane π orbital, which can move almost freely in the lattice due to the large overlap between the π orbitals of neighboring C atoms [178]. The strong in-plane σ_{C-C} bonds give rise to graphene's remarkable mechanical strength, while the out-of-plane π orbitals account for its extraordinary carrier mobility [179]. Graphene's unique structure serves as the basis for other graphitic carbon allotropes, including graphite, carbon nanotubes (CNTs), fullerene, graphyne, and related materials (e.g., charcoal, carbon fiber (CF), amorphous carbon (AC)).

Graphene is the mother of GRMs, which primarily consist of single-layer graphene (SLG), bilayer graphene (BLG), few-layer graphene (FLG), graphene oxide (GO), reduced graphene oxide (rGO), graphene nanoribbons (GNRs), graphene nanoplatelets (GNPs), and others [180]. BLG and FLG consist of two and more than two layers of hexagonal lattices, respectively, held together by weak van der Waals forces. GO shares a similar honeycomb structure with graphene (Fig. 2.2), but combines sp^2 and sp^3 hybridizations. GO can be produced through chemical oxidation of graphite, which results in functionalization with oxygen-containing functional groups [181]. Reduction of GO, either chemically or through thermal annealing, yields rGO, which resembles pristine graphene but with more defects and remnants of oxygen-groups on the surface (Fig. 2.2). Furthermore, GNRs are planar quasi-one-dimensional (1D) graphene structures, which can be further categorized into two groups based on edge termination: 1) armchair and 2) zigzag. While zigzag GNRs exhibit metallic properties, armchair GNRs can be metallic or semiconducting, depending on their width [182].

The hexagonal lattice structure of graphene, with two identical atoms in its unit cell, results in a distinct energy-momentum dispersion relation characterized by a conical energy band diagram near the Brillouin zone corners, where the valence and conduction bands touch each other. This electronic band structure, with a zero band gap, sets graphene apart from conventional semiconductors and metals, placing it in the semi-metal category. Near the band-crossing point, known as the Dirac point, the energy-momentum dispersion is linear. This characteristic causes charge carriers to behave as massless relativistic Dirac fermions with a Fermi velocity only 300 times smaller than the speed of light, drawing significant attention from physicists eager to explore relativistic physics in a solid-state material [183].

The symmetry of the valence and conduction bands around the Dirac point also

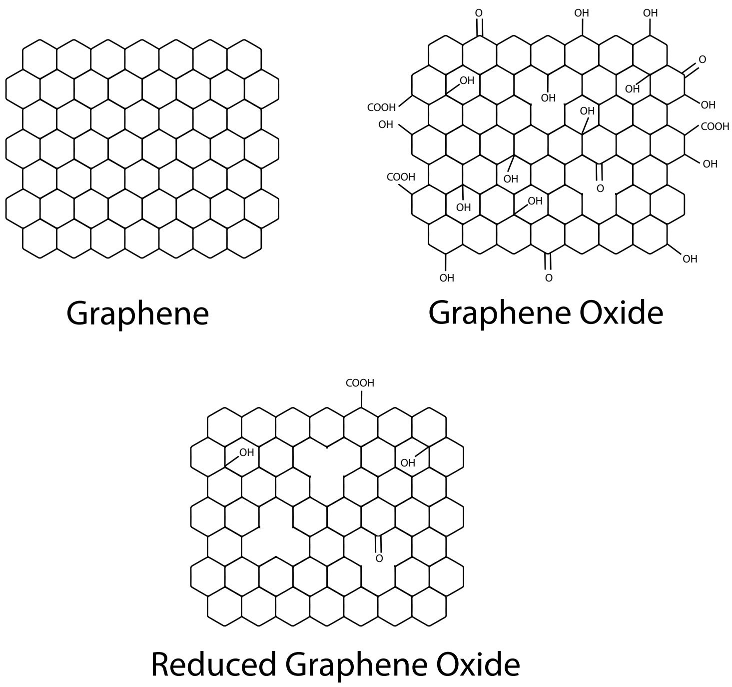

Figure 2.2: Chemical structures of graphene, graphene oxide, and reduced graphene oxide.

results in the ambipolar nature of graphene, allowing the charge carrier type to be switched by applying a slight perturbation to the Fermi level around the Dirac point, for example, via an applied electric field, without the need for chemical doping. This symmetry also leads to electrons and holes sharing the same Fermi velocity, which has significant implications for the design of graphene-based pn-junction devices in electronics applications. The absence of backscattering in the graphene lattice, which can potentially lead to ultra-high carrier mobilities, reaching up to $10,000$ cm^2/V-s in pristine samples on Si/SiO_2 substrates at room temperature, and $250,000$ cm^2/V-s when encapsulated between hexagonal boron nitride (h-BN) layers [184, 185, 186]. It is important, however, to highlight that these values represent the upper limit of graphene's mobility, typically achieved under highly controlled experimental conditions.

As the thinnest known material with single-atomic-layer thickness, graphene has an exceptional surface-to-volume ratio, with the contact area of sp^2-hybridized carbons doubled. This high surface-to-volume ratio, combined with high carrier mobility at room temperature, makes graphene highly sensitive to its surrounding environment, rendering it an excellent material for sensor applications [187]. More importantly, graphene's ability to withstand considerable mechanical stress while maintaining its single-atomic-layer thickness renders it an ideal material for wearable devices and implants, such as skin-conformable electronic tattoos [188] and neural interfaces [189], which demand ultimate flexibility to conform to soft biological tissues seamlessly [190]. Graphene's potential in wearable and implantable biomedical applications is further reinforced by its biocompatibility [191, 192, 193].

Despite being only one atom thick, SLG displays notable opacity, absorbing 2.3% of light across a wide spectrum, ranging from visible to infrared, due to its unique electronic structure [194]. Graphene's properties also lend themselves to plasmonic applications, attributable to its high carrier mobility [195], tunability [196], and strong light confinement capabilities [197]. Chemically doped graphene offers potential in THz optoelectronics, as its transparency reduction can reach up to 40% [198].

2.2.2 Synthesis of GRMs

Top-down methods

Various top-down methods have been developed to produce graphene on different scales. Mechanical cleavage, one of the simplest methods, is employed to produce single- and few-layer graphene flakes from graphite via the repeated cleavage of graphite using a scotch tape [177], as illustrated in Fig. 2.3(a). Chemical reduction of exfoliated GO is a solution-processed route for bulk-scale graphene production, commonly used for fabrication of organic devices and photovoltaic cells [199]. Another top-down method, liquid-phase exfoliation (LPE), entails exfoliating graphite in fluidic media using ultrasound waves to obtain single- or few-layer graphene (Fig. 2.3(b)). This process includes dispersion of graphite in a solvent, followed by exfoliation and purification steps [200]. A relatively marginal yet interesting approach to producing graphene is unzipping CNTs to create graphene GNRs [201] through various techniques, such as Argon plasma etching [202], unwrapping by electrical current [203], and longitudinal unzipping of multi-walled CNTs [204].

Bottom-up methods

Chemical vapor deposition (CVD) is the most prevalent method for producing graphene, as it yields high-quality, large-area monolayers. In CVD, graphene is synthesized on metallic substrates, such as copper, in vacuum chambers supplied with gaseous precursors that react with the substrate at reaction rates set by chamber pressure and temperature (Fig. 2.3(c)). Graphene produced through this method is typically polycrystalline, and the grain boundaries in polycrystalline graphene can impair its electrical, mechanical, and biochemical properties [205]. Moreover, the post-synthesis transfer of graphene from metallic substrates onto insulating surfaces, such as Si/SiO_2, required for electronic and sensing applications, introduces defects and impurities that can degrade device performance. Graphene can also be fabricated through epitaxial growth on silicon carbide (SiC) substrates (Fig. 2.3(d)). This method can produce high-quality, large-area graphene with uniform thickness, without the need for transferring it to another substrate, which is desirable for defect-free fabrication of electronic devices [206].

In summary, the choice of synthesis method can significantly impact the properties of the resulting GRMs, which, in turn, influences the performance of GRM-based devices. While mechanical cleavage can deliver the highest-quality graphene in terms of electrical and optical properties, this method is not scalable and exhibits low level of reproducibility. Conversely, CVD offers scalability for mass-producing large-area graphene; however, achieving single-crystal graphene, which is highly desired for sensing applications, is challenging with this method. Lastly, since LPE provides limited control over the quality and layer structure of the resulting graphene, its products are more suitable for use coating agents in printed electronics applications that typically do not demand high charge carrier mobilities.

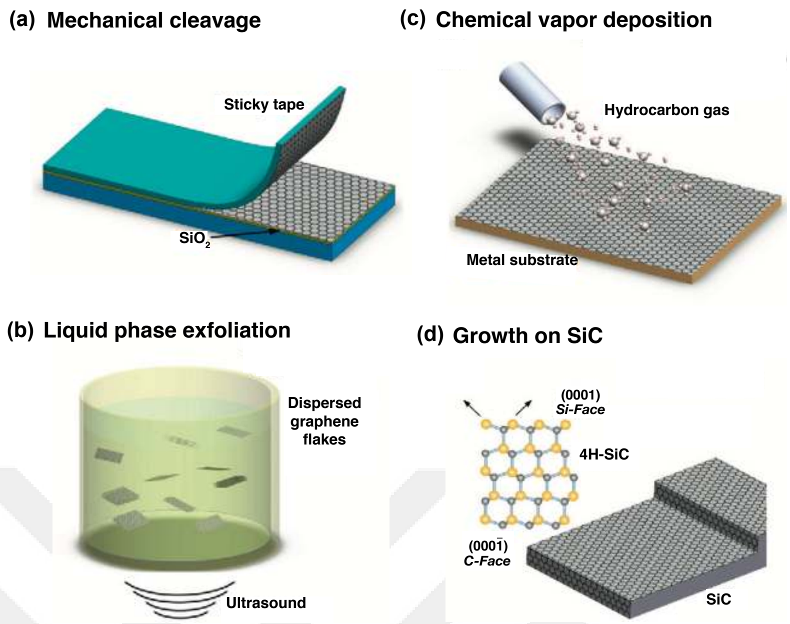

Figure 2.3: GRM synthesis methods: (a) mechanical cleavage, (b) liquid-phase exfoliation, (c) chemical vapor deposition, (d) epitaxial growth on SiC substrate. Reproduced with permission Materials Today 15, 12 (2012). Copyright 2012 Elsevier.

2.3 GRM-based Micro/Nanoscale Transceivers

The application environments of IoBNT, that primarily involve biological media, have been relatively unexplored by the ICT researchers until recently, as EM waves, which underpin conventional communication systems, are ill-suited for these settings. Hence, the exploration of unconventional communication approaches is of paramount importance to address the challenges posed by the unique characteristics of such environments. Among the emerging unconventional communication methods, MC, THz-band EM nanocommunications, and ultrasonic nanocommunications have garnered significant attention.

These communication modalities exhibit significant deviations from conventional methods with respect to the form of information carriers, noise characteristics, achievable transmission rates, and communication delays. Moreover, in the context of THz-band EM and ultrasonic nanocommunications, although these modalities rely on wave propagation similar to conventional systems, EM and acoustic waves experience distinct physical phenomena at these operating frequencies in addition to complexities introduced by the biological environments. Consequently, new design approaches are essential for the practical implementation of Tx/Rx architectures tailored to the unique features of these unconventional modalities and the intricate biological settings.

GRMs hold immense promise as a key enabler for realizing these novel communication methods. In this section, we present the state-of-the-art GRM technologies that have the potential to inspire the design of micro/nanoscale Tx/Rx components, encompassing antennas, signal sources, and detectors for MC, THz-band EM and ultrasonic nanocommunications in IoBNT applications. We highlight the key challenges in implementing full-fledged micro/nano Tx/Rxs and discuss the prospects of GRM-enabled novel Tx/Rxs in supporting multi-modal communications within the broader IoE framework.

2.3.1 Transceivers for Molecular Communications

Bio-inspired MC has emerged as the most promising communication method to realize the IoBNT. Capitalizing on molecules for information transfer, MC is inherently biocompatible, energy-efficient, and robust in physiologically-relevant environments such as within the human body. While there have been significant theoretical advances in understanding the performance limits of MC, such as channel capacity [5], practical implementations of MC-capable artificial devices remain in their infancy.The radical differences between MC and conventional communication methods necessitate novel approaches for the physical design of MC Tx/Rxs. Recent demonstrations of prototype micro/nanoscale MC systems based on GRMs have revealed the enormous potential of nanomaterials in the development of practical MC devices [4].

As IoBNT applications, such as continuous health monitoring, are expected to closely interact with biological systems and tissues, it is imperative to ensure the biocompatibility and bio-durability of the materials used. This has led to the exploration of nanomaterials-based approaches for the design of MC-Tx/Rxs, which focus on chemically stable and biocompatible materials for sensing and releasing molecules, such as GRMs, CNTs, and silicon nanowires (SiNWs) [5]. While synthetic biology provides an alternative for designing biocompatible MC-Tx/Rxs [207, 208], it faces challenges concerning applicability and integration into functional systems [209, 51]. Thus, in the following, we will review the potential of nanomaterials, particularly GRMs, in designing and implementing practical MC-Tx/Rxs within the IoBNT framework.

Molecular Communication Receiver

Drawing on the shared design principles between MC receivers (MC-Rxs) and biosensors, it is prudent to explore existing biosensor technologies, particularly those incorporating GRMs, as a foundation for designing MC-Rxs. Graphene has attracted significant attention in biosensing applications due to its remarkable properties, such as high charge mobility, chemical stability, and high sensitivity to biomolecules. Furthermore, graphene's 2D planar structure enables functionalization of its surface with an extensive array of biomolecular probes or receptors, facilitating selective sensing of various types of target molecules.

Among the diverse sensing modalities, including electrical, optical and mechanical, the FET-based biosensors (bioFETs) stand out for their ability to deliver miniaturization and high sensitivity, owing to their inherent signal amplification capability through the electrical field-effect [210]. Graphene-based bioFETs, employing graphene as the transducer channel, have been reported to exhibit high sensitivity with detection limits in the sub-femtomolar range [211], as well as rapid, real-time detection of various biomolecules [212]. Although one-dimensional (1D) nanomaterials, such as SiNWs [213] and single-walled CNTs [214], have been widely considered for the transducer channel of bioFETs due to their comparable sensing performance to graphene-based transducers, challenges in their fabrication and scalable integration into existing complementary metal-oxide-semiconductor (CMOS) fabrication processes impede the development of 1D bioFETs [215, 211].

Graphene bioFETs also enable label-free, continuous molecular detection through

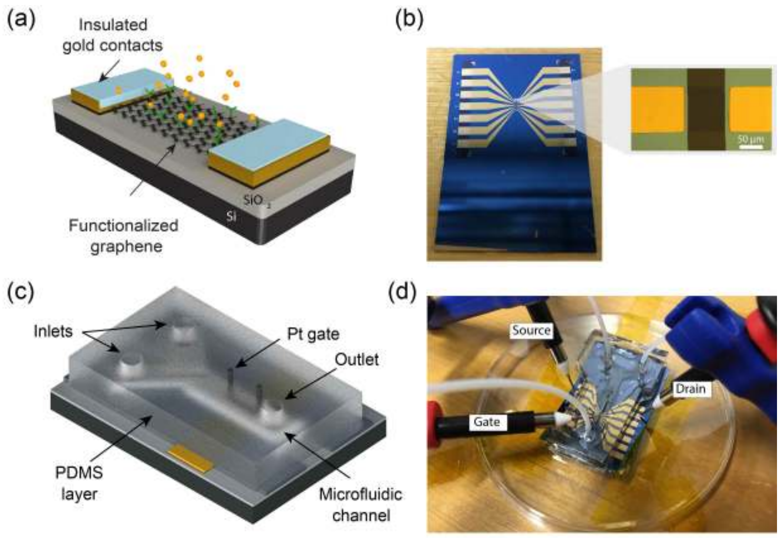

Figure 2.4: Graphene bioFET-based MC receiver [4]: (a) A conceptual drawing of the MC receiver architecture. (b) Micro/nanofabricated MC receiver. (c,d) Integration of the MC receiver with a microfluidic chip.

the non-covalent functionalization of the graphene transducer channel with biological probes that reversible bind to the corresponding target molecules, such as aptamers and proteins, [5]. This capability has been demonstrated in a variety of biosensing applications, including the detection of pathogens, such as viruses and bacteria [212, 216], disease biomarkers for cancer and Alzheimer's Disease [69, 217], and nucleic acids [218]. Inspired by the potential of graphene bioFETs, Kuscu *et al.* recently introduced the first micro/nanoscale MC-Rx based on graphene bioFETs, employing single-stranded DNA molecules as information carriers and their complementary DNA molecules as receptors on graphene transducer surface, as illustrated in Fig. 2.4 [4].

Practical applications of graphene bioFET-based MC-Rxs currently face several challenges, including issues relatd to reproducibility and reliability. CVD growth of graphene on copper substrates is the most common method, but the introduction of defects and impurities during the graphene transfer process onto another substrate for bioFET fabrication is unavoidable. Si/SiO_2 substrates are typically used in bioFETs due to their compatibility with the conventional microfabrication processes. However, these substrates can introduce charged impurities that reduce the charge carrier mobility of CVD-grown graphene in biosensing applications [185]. For instance, SLG exhibits high charge carrier mobility ($> 200,000$ cm^2 V^{-1} s^{-1}) at technologically relevant carrier densities [219], while CVD-grown graphene-based FETs typically exhibit mobility in the range of 1000–$10,000$ cm^2 V^{-1} s^{-1} [220]. Consequently, alternative substrates or growth methods, such as direct graphene growth on non-metallic substrates, such as organic flexible materials [221], [210], warrant further investigation. Moreover, previse control over the coverage, stability, and orientation of immobilized probes on the graphene transducer channel is still lacking, [222, 211], which must be addressed to resolve reproducibility concerns.

Additionally, the potential interaction of graphene with non-specific molecules present in the communication channel poses a challenge for the reliable operation of bioFET-based MC-Rxs in biological environments, where numerous types of molecules and ions can co-exist. For example, in physiological environments with high ionic concentrations, the molecular detection performance of MC-Rxs may be significantly degraded due to the Debye screening effect. Researchers are exploring novel strategies to mitigate these phenomena, such as encapsulating the bioFET with a biomolecule-permeable polymer layer to increase the effective screening length [223, 211] or employing surface passivation techniques to minimize non-specific interactions [220].

Molecular Communication Transmitter

MC transmitters (MC-Txs) encode information into various physical properties of molecules, such as concentration and type, before releasing modulated molecular signals into the MC channel. Practical implementation of MC-Txs remains an open issue, as there is a lack of literature on precise, controllable molecule delivery structures and micro/nanoscale molecule reservoirs capable of sustaining continuous molecule release. GRMs can offer significant advantages in addressing these challenges, due to their unique electronic, mechanical, and chemical properties.

Kuscu *et al.* proposed micro/nanoscale MC-Tx architectures for both liquid-

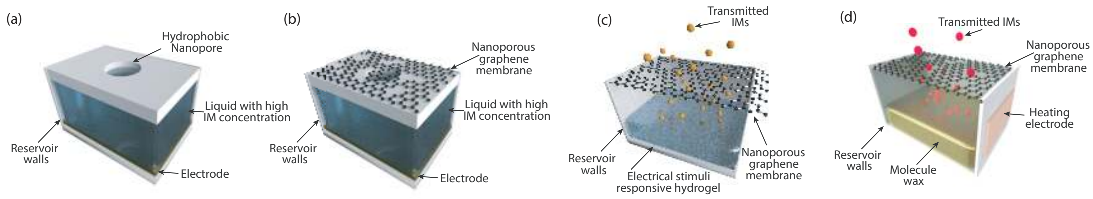

Figure 2.5: Conceptual drawings of envisioned MC-Tx architectures [5]: (a) Liquid-borne MC-Tx with hydrophobic nanopore. (b) Liquid-borne MC-Tx with hydrophobic nanopore and nanoporous graphene membrane. (c) MC-Tx with hydrogel and nanoporous graphene membrane. (d) Airborne MC-Tx with molecule wax and nanoporous graphene membrane.

borne and airborne MC communications, utilizing nanoporous graphene membranes to cap molecule reservoirs [5], as depicted in Fig 2.5. The permeability of the nanoporous graphene membrane is regulated by an electric field, facilitating selective and tunable release of information-carrying molecules (IMs) stored in the reservoir, while minimizing molecule leakage, a challenge associated with hydrophobic nanopores, as shown in Fig. 2.5(a). The use of graphene membranes offers several advantages over conventional membranes, such as high mechanical strength, large surface area, low thickness, and tunable pore size [5].

In the liquid-borne MC-Tx architecture illustrated in Fig. 2.5(b), an electrode plate at the bottom of the molecule container provides further control over molecule release by attracting or repelling charged molecules using the electric field. The architecture shown in Fig. 2.5(c) employs electrically-responsive hydrogels as molecule reservoirs, enabling modulation of molecule release through electrical stimulation. The airborne MC-Tx architecture in Fig. 2.5(d) incorporates a wax layer to store molecules, which are continuously released when heated by an electric field. Key concerns for these architectures include molecular leakage (non-negligible molecule release without electrical stimuli), and transmission delay (time required for information molecules to enter the MC channel after electric field application). GRMs can help mitigate these issues by providing a barrier layer (graphene membrane) between the reservoir and the environment, and reinforce hydrogels or polymeric waxes with improved mechanical properties and responsiveness [224].

2.3.2 Transceivers for THz-band Nanocommunications

As IoBNT applications involve biological environments such as tissues, unique challenges arise in various aspects, necessitating the transformation of material and device technologies to accommodate the unique requirements of these environments. Conventional EM communication technologies, namely radio frequency (RF) technologies, are not suitable for IoBNT due to the limited miniaturization of RF Tx/Rx components at the required operating frequencies and power levels, which exceed the capabilities of BNTs. However, the emerging field of THz-band communications, employing high-frequency EM waves in the underexplored 0.1 to 10 THz range, appears promising for IoBNT, as it facilitates micro/nanoscale miniaturization and low-power operation. Moreover, THz-band communications exhibits biocompatibilty, as THz radiation does not ionize biological tissues, lacking sufficient energy for ionization of atoms and molecules [225].

Since the THz-band lies between microwave and infrared frequencies, THz waves exhibit both photonic and electromagnetic properties, rendering electronic and photonic device technologies applicable for THz Tx/Rx design. On the other hand, THz device technology remained underdeveloped until recently, primarily due to the scarcity of practical signal generators and detectors for the so-called THz gap. More specifically, conventional solid-state electronic devices generate limited signal power at THz frequencies, while photonic devices have been constrained by the absence of materials with suitable electrical and optical properties [226]. Nonetheless, the emergence of GRMs with exceptional electronic and optical properties has significantly propelled the advancements in THz device technologies.

Graphene, with its gapless band structure, demonstrates a spectral response at THz frequencies, unlike other 2D materials with larger band gaps [227]. This attribute enables EM radiation-graphene interaction at THz frequencies, making it suitable for THz emission, modulation, and detection. Graphene's electrical, optical and plasmonic properties can be tuned through chemical doping or electrical/magnetic biasing [228], allowing the development of reconfigurable THz Tx/Rx components, such as nano-antennas with dynamic radiation patterns controlled by

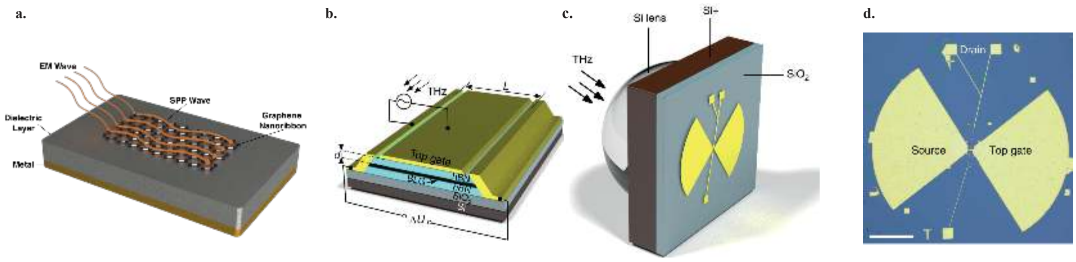

Figure 2.6: (a) Conceptual design of a graphene nanoribbon-based plasmonic antenna for THz communication. (b, c, d) Graphene-based THz detector [6]: (b) Schematics of the bilayer graphene FET architecture used in the THz detector. (c) 3D rendering of the THz detector with a broadband bow-tie antenna and hemispherical silicon lens, enabling modulation of the gate-to-source voltage. (d) Optical micrograph of the detector.

graphene's tunable surface conductivity [229]. Moreover, the ease of integrating graphene-based THz components with each other, as exemplified by integrated modulators and detectors, could facilitate low-power, on-chip THz Tx/Rxs, highly sought after for standalone IoBNT applications. Additionally, graphene's low electronic noise temperature makes it suitable for physiological environments, preventing performance degradation in THz Tx/Rx devices [230].

Graphene's support for tunable surface plasmon polaritons (SPPs) at THz frequencies offers great potential for realizing micro/nanoscale THz Tx/Rxs. Confinement of THz waves in a sub-wavelength scale in the SPP mode enables high-order miniaturization [229] due to the smaller wavelength of SPP waves compared to EM waves, resulting from the lower propagation speed of SPP waves on graphene [231]. Despite offering high miniaturization, plasmonic antennas based on pure graphene exhibit low radiation efficiency [232]. Radiation efficiency can be improved by employing substrate materials with a higher dielectric constant or increasing the number of graphene layers, as demonstrated by hybrid graphene-dielectric structures [233] and few-layer graphene stacks [234]. However, this compromises the level of miniaturization [233]. Consequently, further research is necessary to address the trade-off between miniaturization and radiation efficiency.

The utilization of graphene SPPs enables frequency-reconfigurable THz plasmonic antennas [232] and modulators [67, 144], paving the way for efficient, integrated on-chip all-graphene THz Tx/Rxs [66] along with on-chip plasmonic THz signal sources [235], and detectors [6] as exemplified by the THz plasmonic components shown in Fig. 2.6. The frequency-reconfigurability of graphene sheets is achieved by varying the chemical potential (Fermi level) of graphene, typically via electric field application. Altering the chemical potential allows control of graphene surface conductivity, thus affecting the propagation constant and resonance frequency of graphene SPPs. For example, increasing the chemical potential shifts the resonant frequency upwards, resulting in higher radiation efficiency [236]. However, it should be noted that electronic reconfigurability is adversely affected by high chemical potentials [228].

Several GRM-based configurations have been reported in the literature that can simultaneously provide high radiation efficiency and frequency reconfigurability, such as tunable THz metamaterials comprising metallic resonance structures with embedded graphene [237], and multiple graphene sheets controlled by different bias voltages [238]. Nevertheless, the feasibility of these configurations for IoBNT applications must be evaluated in terms of miniaturization. Additionally, complex physiological environments with various co-existing molecules can present significant challenges for the reliable operation of plasmonic Tx/Rx components. Specifically, the adsorption of interfering molecules on the graphene surface can alter its refractive index, subsequently affecting the propagation characteristics of the SPPs [85]. Therefore, a comprehensive analysis of interfering molecular interactions with graphene under different physiological conditions is required to assess their impact on graphene's reconfigurability.

2.3.3 Transceivers for Ultrasonic Nanocommunications

Ultrasonic nanocommunications utilizing high-frequency acoustic waves (above 20 kHz) represents a promising approach for IoBNT, particularly in intra-body applications [239]. Acoustic communications has certain advantages over EM-based communications in water-dense media. For example, sound is often preferred for underwater communication as RF waves experience significant absorption losses. Therefore, acoustic communication within the body, where water is the primary constituent, may also be advantageous.

Moreover, ultrasonic nanocommunications has the potential to support high data rates in intra-body applications. In one study, researchers experimentally demonstrated ultrasonic propagation through a tissue-mimicking environment, achieving data rates up to 700 kbps with a $40\mu m$ transmit power [240]. However, ultrasonic Tx/Rxs must be tailored for IoBNT in several aspects, including size, robustness, and biocompatibility. This is because BNTs have micro/nanoscale dimensions, propagation in biological environments with numerous obstacles requires robustness, and transmission in biological tissues must adhere to safety limits concerning acoustic pressure and power. To meet these requirements, directional transmission at high frequencies (around hundreds of MHz) is necessary for *in vivo* communications [239]. Additionally, wideband ultrasonic nanocommunications employing short pulses with low duty cycles can provide compatibility with IoBNT by reducing thermal and mechanical effects on tissues and offering robustness against the multipath fading caused by obstacles inside the body [240].

The primary component in ultrasonic communications is the ultrasonic transducer, which emits and detects ultrasound waves. Conventional ultrasonic transducers typically rely on the piezoelectric effect, converting mechanical vibrations to electrical signals and vice versa. However, these transducers often operate only near their resonance frequency and allow only limited miniaturization due to performance and fabrication constraints [241]. Alternatively, optoacoustic generation of acoustic waves is a powerful method for generating high-frequency, wideband ultrasound. Using light-absorbing nanomaterials providing efficient light-to-ultrasound conversion, such as GRMs and CNTs, miniaturized ultrasonic transmitters can be developed. These transmitters can be integrated with wideband sensitive, all-optical detectors, such as optical interferometric detectors, enabling the implementation of all-optical, wideband, high-frequency ultrasound transducers with strong miniaturization potential [241].

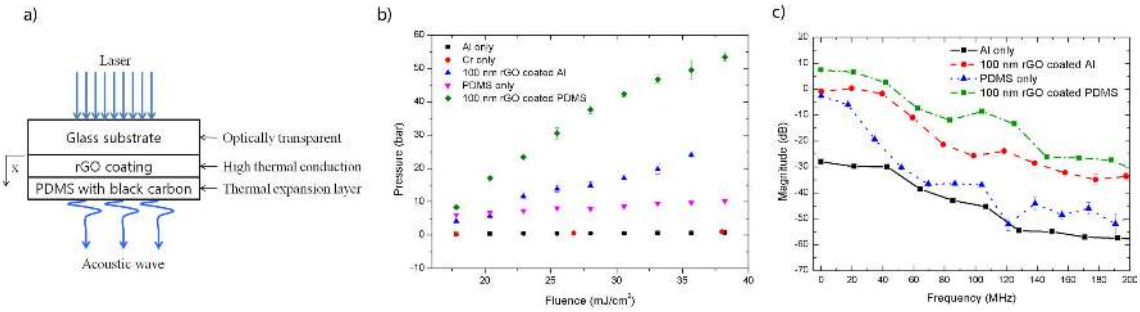

Figure 2.7: Optoacoustic ultrasound transmitter based on rGO-coated PDMS film [7]: (a) Schematic representation of the film. (b) Maximum pressure of ultrasonic waves from different samples at varying fluences. (c) Frequency spectra of ultrasonic waves observed for different samples. Reproduced from S. H. Lee et al, "Reduced graphene oxide coated polydimethylsiloxane film as an optoacoustic transmitter for high pressure and high frequency ultrasound generation," Applied Physics Letters, vol. 106, no. 8, p. 081911, 2015, with the permission of AIP Publishing.

The photoacoustic effect describes the generation of sound waves via modulated optical waves. The absorbed light causes the material to heat up, leading to sound emission via thermoelastic expansion. As a result, wideband ultrasound can be generated using short laser pulses on light-absorbing materials. For *in vivo* ultrasonic transmitters, efficient light-to-sound conversion is crucial to achieve adequate acoustic pressure, considering the limited laser pulse energy to avoid harmful biological effects. Conversion efficiency mainly depends on the absorbing material, which should ideally possess high optical absorption capacity, high thermal conductivity, and low heat capacity [242]. Carbon-based nanomaterials, such as GRMs and CNTs, with their exceptional photothermal properties and wideband light absorption capability, are well-suited for efficient photoacoustic conversion. Both rGO and CNT have been extensively explored for optoacoustic ultrasound generation [7]. In biological environments, rGO is favored over CNT due to its larger surface area and improved dispersibility [243].

Enhancing photoacoustic conversion efficiency is commonly achieved through engineering composite nanomaterials. For instance, rGO can be combined with metallic materials, such as gold nanoparticles (AuNPs), to improve its light-absorbing capability [244]. Additionally, rGO can be mixed with metals and polymers acting as thermal expansion layer, such as aluminum (Al) and polydimethylsiloxane (PDMS), for enhanced thermoelastic expansion and increased acoustic pressure [174, 7]. Comparatively, rGO-PDMS ultrasound transmitters exhibit higher photoacoustic pressure than rGO-Al, as PDMS has greater thermoelastic expansion than Al [7], as demonstrated in Fig. 2.7. Optimizing composite material properties for maximum sound pressure requires considering certain trade-offs. For examples, while rGO's light absorptivity increases with its thickness [174], the bandwidth of the generated ultrasonic pulses decreases with the thickness of the composite [245].

Piezoelectric detectors are commonly used for detecting ultrasonic signals in optoacoustic imaging. However, these detectors have an inherently narrow operation frequency, and their sensitivity decreases as the detector size is reduced [241]. In contrast, optical interferometric resonators are not size-dependent and can be miniaturized. All-optical generation and detection of ultrasound can enable on-chip integrated optical ultrasonic Tx/Rx, a direction further motivated by advancements in nanolaser technology, such as plasmonic nanolasers [246]. Nevertheless, fabricating on-chip integrated plasmonic nanolasers presents significant challenges, including the need for electrical pumping without harming the biological environment. To address this issue, it is crucial to lower the pumping threshold and maintain high efficiency [247].

2.3.4 Multi-modal Transceivers for IoBNT

As discussed in previous sections, GRMs can enable the reliable and information-efficient transduction of diverse communication modalities into the electrical domain and vice versa. This inter-modality transduction property of graphene can be harnessed to develop Tx/Rxs capable of seamlessly interfacing heterogeneous networks within IoBNT, and connecting IoBNT with the conventional communication networks.

We recently introduced a device concept called *universal transceivers* [169], characterized by *multi-modality* (in communication and energy harvesting), *modularity*, *tunability*, and *scalability* (to micro/nanoscales). Universal Tx/Rx architectures possessing these attributes can address the major inter-operability challenges in realizing the emerging *Internet of Everything (IoE)* paradigm. This paradigm has the potential to revolutionize our interaction with the physical world [169] by integrating various Internet of Things (IoT) technologies and applications, including IoBNT.

However, device complexity poses a significant challenge for the physical implementation of universal Tx/Rxs, as each communication modality adds to the overall hardware complexity. Direct inter-modality transduction without conversion to the electrical domain, where signals are processed, can considerably reduce device complexity. For example, molecule-sensitive graphene field-effect transistors (GFETs) capable of simultaneously sensing molecules and modulating the output RF signal have been reported [56]. GRMs with multi-functional capabilities in other forms also show promise in addressing device complexity, as demonstrated by a multi-functional graphene-based modulator combining storage and transduction capabilities [55].

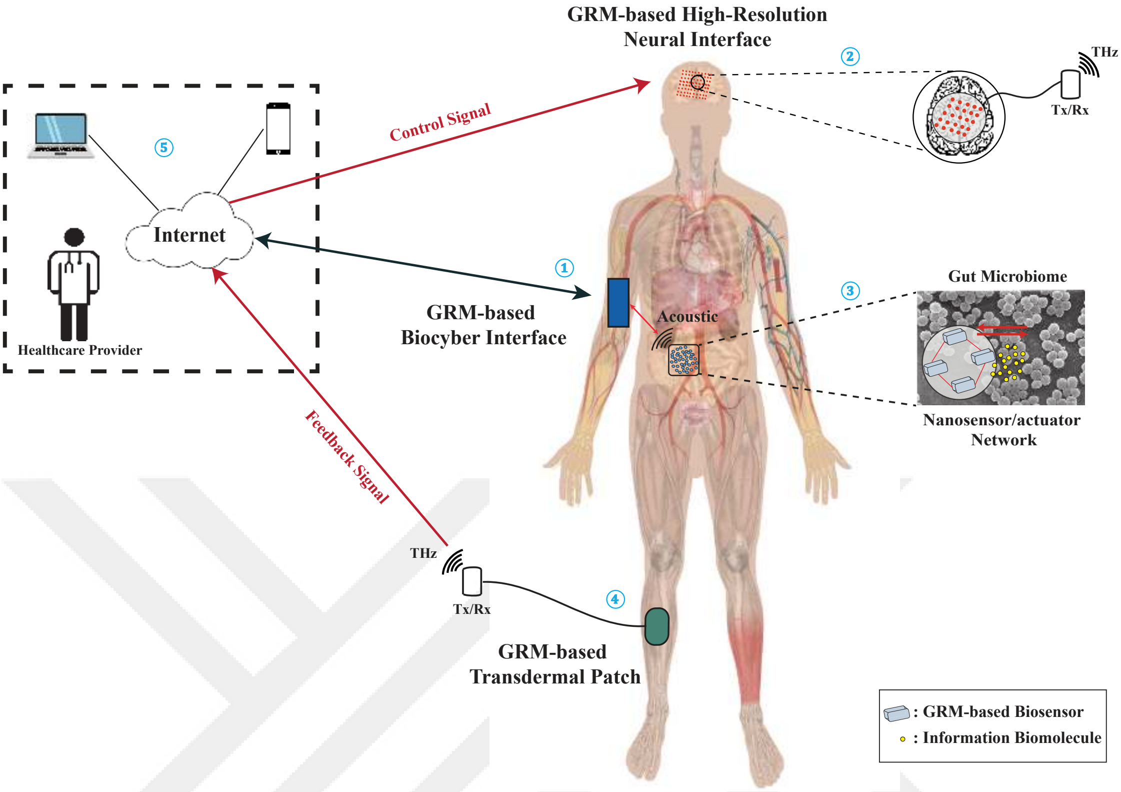

Figure 2.8: An IoBNT architecture with GRM-based bio-cyber interfaces facilitating bi-directional communication between intrabody nanonetworks and conventional networks: (1) GRM-based bio-cyber interface enabling bi-directional communication between the Internet and intra-body networks. (2) GRM-based high-resolution neural interface connecting to external networks via THz signals. (3) Nanosensor/actuator network monitoring and controlling gut microbiome composition, connected to a bio-cyber interface through acoustic signals. (4) GRM-based transdermal patch providing sensory feedback to (2) via the Internet by converting biochemical signals to THz signals and transmitting them to the Internet infrastructure for further processing. (5) The cyber domain of the Internet.

2.4 GRM-based Bio-cyber Interfaces

Realizing the envisioned IoBNT applications often necessitates bridging the gap between bio-nano networks, which typically operate in the biochemical domain (e.g., intra-body), and conventional networks that primarily rely on electromagnetic signal exchange. The disparities between these heterogeneous networks in terms of communication media, modality, and compatible device technologies require sophisticated interfaces capable of seamlessly interconnecting these networks by overcoming interoperability challenges (Fig. 2.8). These so-called bio-cyber interfaces have been the focus of extensive research, with various innovative methods proposed in the IoBNT context, including those based on optogenetics [113], THz control of protein conformations [248], stimuli-responsive hydrogels [5], redox electrochemisty [53], and biosensing [222, 249]. These methods offer uni-directional or bi-directional bio-cyber interfacing with varying spatiotemporal resolution. In this section, we provide a brief overview of IoBNT bio-cyber interfacing technologies where GRMs can provide unique advantages.

2.4.1 GRM-based Biosensors for IoBNT

Depending on the specific IoBNT application, biosensors can serve as bio-cyber interfaces, converting molecular signals into electrical or other signal forms that can be processed and transmitted over conventional communication networks. The use of biosensors as bio-cyber interfaces within IoBNT applications, however, presents challenges related to size, energy consumption, biocompatibility, and the establishment of reliable bi-directional communication.

A wide array of IoBNT applications require interfacing with living systems and tissues, which necessitates biosensors at the micro/nanoscale and demands high-level biocompatibility. This is crucial for preventing toxic and adverse effects on living cells and biochemical processes therein, while also ensuring the proper operation of biosensors without performance degradation [250, 251].

The performance of a biosensor is directly related to its transduction process. Reliable and information-efficient inter-modality transduction (e.g., biochemical signals to electrical signals) is required to eliminate processing delays and information loss. Ensuring information-efficient and rapid transduction is particularly critical for healthcare applications of IoBNT, such as early diagnosis and treatment of diseases.

Biosensing is one of the areas where GRMs excel due to their biocompatibility, flexibility, high charge carrier mobility, and unique 2D structure with a significantly high surface-to-volume ratio, leading to exceptional sensitivity [252, 253, 254, 68, 255]. Their capacity to be functionalized with a diverse array of bio-recognition elements, such as proteins, enzymes, and DNA/RNA aptamers, makes them versatile platforms for selective interfacing with various biochemical systems and signals. Notably, aptamer-functionalized graphene sensors have demonstrated real-time monitoring of cytokines in human biofluid, achieving highly sensitive detection of disease biomarkers [256]. Furthermore, GRM-based biosensors can transduce biochemical signals into a broad range of signal forms, such as electrical, optical, RF/microwave/THz electromagnetic signals [57, 169], making them ideal candidates for addressing bio-cyber interfacing challenges in IoBNT.

FET-based biosensors, also known as bioFETs, represent a widely adopted architecture for GRM-based biosensors due to their inherent signal amplification capability. In bioFETs, the GRM-based transduction channel of the transistor is in direct contact with the biochemical environment, with biorecognition elements, i.e., receptors, serving as the gate electrode. An example application of GRM-based bioFETs is wearable contact lens sensors (Fig. 2.9), which detect glucose concentration in tears and wirelessly transmit data to a mobile device for blood glucose level estimation. [8]. Exploiting correlations between biomarker levels in blood and those in bodily fluids, e.g., tears, saliva, and sweat, that are easily accessible by wearable GRM-based biosensors is crucial for bio-cyber interfacing in IoBNT applications, where the molecular signals generated by intra-body MC networks can be detected non-invasively [257].

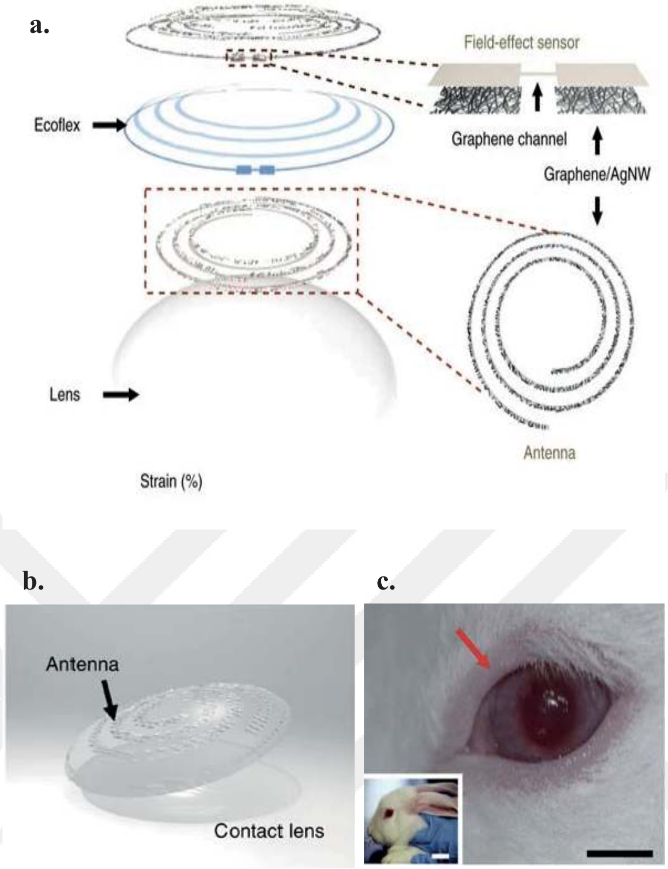

Figure 2.9: GRM-based wearable smart contact lens [8]: (a) GRM-based wearable contact lens sensor integrating a glucose sensor and an intraocular pressure sensor. (b) Illustration of the transparent glucose sensor on the contact lens. (c) GRM-based wireless sensor integrated onto a rabbit's eye. Joohee Kim, Nature communications, 8, 14997 (2017), 2017; licensed under a Creative Commons Attribution (CC BY) license.

Biodegradable biosensors and patches have been developed to collect data before harmlessly decomposing into environmentally benign byproducts. The unique properties of GRMs, combined with their ability to degrade naturally over time, enable the development of these versatile and biocompatible biosensors and patches, capable of detecting various physical, chemical, or biological signals [258]. For instance, researchers have introduced GRM-based waterborne biodegradable nanocomposites, which not only have excellent physical properties, but also can be completely degraded through a simple enzymatic reaction [259]. Through the application of these nanocomposites, the design and production of GRM-based biodegradable sensors and patches become possible, which holds considerable importance for bio-cyber interfacing in IoBNT.

In conclusion, the advancements in GRM-based biosensors hold great potential for addressing the challenges associated with bio-cyber interfacing in IoBNT applications. These cutting-edge biosensors offer unprecedented sensitivity, versatility, and biocompatibility, opening new avenues for IoBNT applications in healthcare and beyond.

2.4.2 GRM-based Neural Interfaces for IoBNT

The nervous system is the most advanced and complex human-body network [260] with the intricacies of many of its signaling pathways yet to be unfolded. It is a very large-scale network distributed throughout the body for transferring external stimuli to the brain and *vice versa*. The nervous system utilizes electrical and chemical signals to transfer information among its constituents, standing as a multimodal and natural communication infrastructure for artificial IoBNT networks. In that regard, bi-directional interfacing with the nervous system is essential to enable many of the foreseen IoBNT applications.

One promising target for IoBNT applications is the bi-directional gut-brain axis, which connects the gut microbiota with the central nervous system. The electrochemical signaling pathways in this axis play a significant role in numerous neurological disorders, such as autism and depression, as well as digestive conditions, e.g., irritable bowel syndrome [261, 262, 263, 264]. Implementing an IoBNT system capable of bi-directional communication with the gut-brain axis through bio-cyber interfaces could facilitate monitoring and controlling gut-brain signaling for early diagnosis and treatment of associated diseases. Moreover, IoBNT networks interfacing with the nervous system could be employed to reestablish disrupted neural signaling between the brain and muscles in spinal cord injuries, ultimately restoring motor functions in paralyzed patients [38].

Interfacing with the nervous system is conventionally realized via electrical stimulation of the neurons and transduction of dynamic electrochemical neural activities into electrical signals [265, 266, 267]. Achieving high spatio-temporal resolution neural interfaces remains a significant challenge due to the complex anatomy of nervous tissues and intricate interconnections among neurons, leading to considerable noise and interference. These challenges are currently being addressed with advanced nanomaterials and flexible electronic technologies.

Exceptional physicochemical properties of GRMs, such as extraordinary charge carrier mobility, electrochemical stability, mechanical flexibility, miniaturization capacity, and transparency make them ideal for addressing the aforementioned challenges in neural interface design [268, 269, 270]. GRM-based neural interfaces enable unprecedented access to the spatio-temporal dynamics of neural activity, facilitating remote monitoring and control of the nervous system. For instance, transparent graphene electrode arrays allow high-resolution visualization of cells during neural imaging and recording. In [271], the authors propose using transparent graphene micro-electrodes to develop a compact closed-loop system for optogenetic stimulation, selectively exciting and inhibiting genetically targeted cells through photons. This optical control of genetically engineered cells enables external activation of light-sensitive ion channels, further modulating the release of specific information molecules, such as neurotransmitters, neuropeptides and ions. Beyond monitoring and controlling the nervous system's electrical activity, GRM-based neural interfaces also create opportunities for *in situ* biosensing and smart drug delivery applications. Real-time detection of neurotransmitters and neuromodulators, e.g., serotonin, and monitoring ion channel activity can enable early diagnosis of neural disorders and the release of therapeutic molecules based on biosensing readouts [268].

In conclusion, GRM-based interfacing holds immense potential as a bridge between communication engineering and life sciences, paving the way for the development of future IoBNT-based diagnosis and treatment applications for communication-related neural disorders.

2.4.3 GRM-based Drug Delivery Systems for IoBNT

Stimuli-response smart drug delivery systems hold significant potential for informing the design of bio-cyber interfaces in IoBNT applications. These advanced technologies can precisely modulate molecule release rates in response to time-varying external stimuli, such as electrical, optical, and magnetic signals. This capability enables seamless interfacing between conventional communication networks and bio-nano networks that interact through molecular communications.

GRMs have emerged as valuable components in the development of stimuli-responsive drug delivery systems. Their unique properties, such as hydrophilicity, high surface area, and ability to form composites, make them ideal candidates for this purpose. Specifically, GO composites with various types of nanoparticles have been widely explored for their capacity to respond to near-infrared (NIR) light and magnetic-field stimuli for controlled molecule release [272]. These composites exhibit excellent biocompatibility, stability, and tunable physicochemical properties, leading to highly effective and targeted drug delivery systems.

Another promising application of GRMs in drug delivery is the development of electro-responsive hydrogels [273]. These hydrogels, when combined with graphene, can exhibit enhanced drug release performance by providing reliable and precise control over molecule release through the magnitude, duration, and frequency of the applied field. Although activating drug delivery devices via an electrical field may cause resistive heating problems; the incorporation of pristine graphene with an electro-sensitive hydrogel matrix mitigates this issue. This combination results in a mechanically and chemically stable interface, suitable for triggering drug release through electrical fields [274].

Further advances in GRM-based drug delivery systems could lead to more sophisticated and responsive bio-cyber interface designs for IoBNT applications. For instance, integrating multi-stimuli responsive components, such as thermo-responsive polymers, could enable even more precise control over drug release profiles, increasing the bandwidth of transmitted molecular signals. Additionally, combining GRMs with other nanomaterials, such as gold nanoparticles or quantum dots, can facilitate multi-modal drug delivery systems that simultaneously support imaging, sensing, and therapeutic functions, enabling bi-directional bio-cyber interfaces for IoBNT.

2.5 GRM-based Micro/Nanoscale Energy Harvesting and Storage

Ensuring uninterrupted sensing, computation, and data communication at the micro/nanoscale requires efficient utilization of limited energy resources and the adoption of self-sustaining strategies, such as energy harvesting (EH), to fulfill the stringent requirements of IoBNT applications. However, the projected scale and capabilities of the components required for this purpose present challenges to existing technologies, prompting the development of novel and unconventional solutions. GRMs have recently garnered significant interest in this field due to their exceptional properties. In this section, we examine the potential of GRMs in advancing micro/nanoscale energy harvesting and storage technologies, which will ensure the perpetual operation of IoBNT applications.

2.5.1 GRM-based Micro/Nanoscale Energy Harvesting for IoBNT

A critical challenge in realizing IoBNT applications is continuous power provisioning [3], where a self-sustaining strategy could be optimal. For micro/nanoscale devices, nanomaterial-based energy generators (or *nanogenerators*) have emerged as a key element due to their ability to convert various ambient energy resources, such as motion, light, flow, and heat, into utilizable power. GRMs have been widely adopted in the development of nanogenerators (Fig. 2.10) due to their excellent electrical and mechanical properties. Below, we summarize the typical energy sources harnessed by GRM-based nanogenerators for powering IoBNT applications.

EH from Motion

In IoBNT applications, motion-based kinetic or mechanical energy can be harvested from vibrations and pressure/stress-strain variations in and around the body through piezoelectric or triboelectric nanogenerators. Yet, this process is not always straightforward. Creating electrical voltage at nanoscales using vibrations is an issue since the nano-mechanical devices rarely have a high enough resonant frequency to harvest the required energy. However, research showed that the intrinsic mechanical nonlinearity of strained nanostructured graphene could overcome this issue by acting like a double-well system when pressed [275], thereby enabling nonlinear EH at nanoscales based on piezoelectric effect.

GRMs have also been employed in triboelectric nanogenerators (TENGs) that capitalize on mechanical energy. *Triboelectricity* is based on the principle of contact electrification between two sheets of dissimilar materials and the resulting electrostatic induction between them [276]. Stretchable crumpled graphene has proven highly effective in enhancing the output performance of TENGs through the modification of surface nanostructures [277]. Similarly, ultra-thin GRM-based TENGs have been developed to extract human skin-generated electricity via contact with clothing or the body [278]. Owing to their flexibility, conductivity, and transparency [279], GRM-based TENGs have found extensive applications in wearable electronics, hinting at their potential for use in IoBNT applications as integrated components within BNTs.

EH from Flow

GRMs can also be used to harvest fluid-based flow energy for powering IoBNT applications. For example, in [280], researchers utilized 2D nanofluidic GO to create an ultra-thin osmotic power source, which was coupled with a TENG to form a self-charged conformable triboiontronic device. Another study focusing on fluid flow considered the most prominent source of power for in vivo applications, i.e., blood circulation, and used monolayer-graphene single microelectrodes to harvest energy and measure the blood flow rate at the same time [281]. The monolayer graphene was also used in [282], where a droplet of sea water or ionic solution was moved over a strip of it to create electricity. Hybrid nanogenerators that simultaneously exploit water droplet movements and sunlight have also been developed using monolayer graphene films [283]. Other research has explored the role of the substrate in

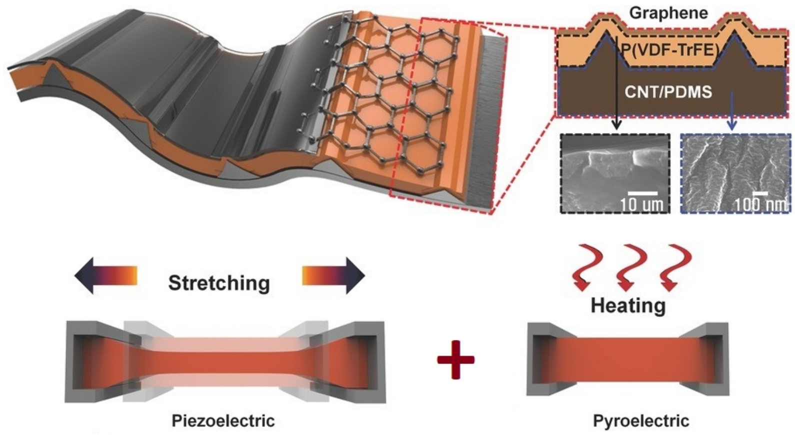

Figure 2.10: Illustration of a GRM-based hybrid nanogenerator, simultaneously converting kinetic and thermal energy into electricity [9]. Reproduced with permission from Ju-Hyuck Lee et al, Advanced Materials 26, 5 (2014). Copyright 2014 Wiley Online Library.

electricity generation with graphene-piezoelectric material heterostructures [284]. A systematic evaluation of various factors, such as graphene dimensions, materials and preparation methods, substrates, solutions, and energy outputs for ionic and non-ionic fluids, can be found in [285].

Air/wind flow can also be harnessed as an energy source for IoBNT. In [286], a rotating TENG based on GO-filled polyvinylidene fluoride films was developed to harvest energy from airflow. In contrast to studies where GRMs constitute the harvester or part of it, some research focuses on using graphene to enhance the performance of existing harvesters. For example, wind turbine blades coated with GO and epoxy nanocomposites demonstrated reduced lighting damages and increased energy harvesting efficiency [287]. Despite being implemented at macroscale, this example showcases the potential of GRMs in addressing real-world challenges, which could be adapted for micro/nanoscale IoBNT through miniaturization [169].

EH from Light

GRMs have also been extensively employed in photovoltaic devices, such as solar cells, to harvest energy from sunlight or artificial light resources [288]. In solar cells, GRMs can be used as electron and hole transport materials, buffer layers, and window or/and counter electrodes to enhance certain capabilities. One study presented a power system with series-connected organic photovoltaic cells and graphene supercapacitors on the same substrate, achieving a $\approx$5V open-circuit voltage suitable for flexible applications [289]. Different from the conventional photovoltaic cells utilizing the visible light frequency range for EH, [290] designed a graphene-based nanoscale antenna harvesting energy in the ultraviolet spectrum, showing promising results for the aerospace industry. With light being abundant both outdoors and indoors, GRM-based photovoltaic nanogenerators could support airborne IoBNT applications.

EH from Heat

Temperature gradients in the vicinity of BNTs can also be harnessed as an energy source through thermoelectric or pyroelectric nanogenerators. *Thermoelectricity* (or the Seebeck effect) is the generation of electrical energy due to a thermal difference between two dissimilar electrical conductors [291]. One study developed a thermoelectric nanogenerator integrated with a graphene-based light-driven actuator, providing self-powered sensing capabilities [292]. Another generator used form-stable phase change materials (PCMs) supported by rGO aerogels, with graphene nanoplatelet (GNP) fillers enhancing thermal conductivity [291]. Similarly, in [293], a flexible, conformal, and reconfigurable thin-film thermoelectric generator based on rGO-CNT composites was developed, achieving a promising thermovoltage level suitable for low-energy applications, such as bio-integrated systems. However, ensuring the bio-compatibility and durability of the employed materials is crucial, particularly for systems operating *in vivo*.

EH from Sound

Sound-based energy harvesting presents a viable option for powering IoBNT applications, with ambient acoustic vibrations and ultrasonic signals being potential energy sources. In one study, researchers leveraged GO to fabricate an acoustic nanogenerator that achieved high conversion efficiency from sound to electricity [294]. Another study introduced a stretchable, transparent nanogenerator by utilizing a polymeric piezoelectric material encapsulated between graphene electrodes, which exhibited remarkable sensitivity to various sound frequencies and amplitudes [295]. These advances indicate that GRM-based acoustic nanogenerators hold significant potential for IoBNT applications, particularly those employing liquid-borne MC in complex *in vivo* and *in vitro* environments, such as underwater scenarios, where conventional energy sources may be impractical or inefficient.

Hybrid EH

While EH offers promising capabilities for BNTs, the low power density and inherent intermittency of available sources present challenges. These limitations, often due to uncontrollable factors suggest that relying on a single energy source may be insufficient for consistent operation in dynamic environments. Consequently, there is growing interest in hybrid EH approaches, which exploit multiple energy sources concurrently to boost overall energy output and enable uninterrupted functionality.

Hybridization of energy sources is a well-established research area in the EH domain [296], with numerous implementations at macroscale. Leveraging this accumulated knowledge, recent developments have extended hybrid EH approaches to micro/nanoscales through the use of GRM-based hybrid nanogenerators. For instance, [283] developed a 2D monolayer graphene film-based hybrid nanogenerator capable of harvesting energy from both sunlight and water flow simultaneously. Another study introduced a highly stretchable hybrid nanogenerator based on graphene nanosheets, which combined piezoelectric and pyroelectric properties to simultaneously harvest thermal and kinetic energy [9]. These advancements demonstrated that concurrently utilizing multiple energy sources in a complementary manner can mitigate the uncertainties associated with EH, thus paving the way for self-sustaining IoBNT applications in dynamic environments.

However, further exploration is needed to address unique challenges and requirements arising from source hybridization, such as complexity, interoperability, and modularity. Given the existing solutions and growing research activity in this area, it is anticipated that GRM-enhanced (hybrid) nanogenerators will play a pivotal role in advancing IoBNT applications across diverse fields, including healthcare, biomedical engineering, aeronautics, automotive, aerospace, and beyond.

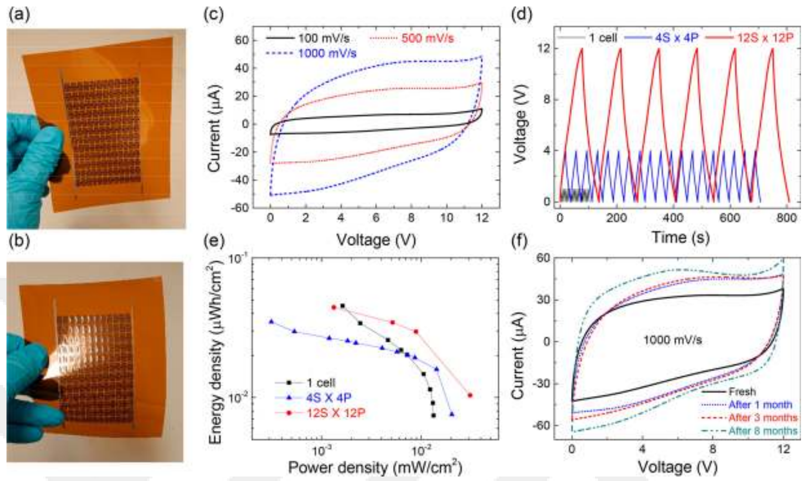

Figure 2.11: Large-scale integration of fully inkjet-printed flexible MSCs on Kapton [10]: (a-b) Photographic images of MSC arrays from different perspectives. (c) Cyclic voltammetry (CV) profiles at different scan rates, captured one month post-fabrication. (f) CV profiles at various time intervals following fabrication, illustrating long-term stability. (d) Galvanostatic charge/discharge (GCD) curves, demonstrating ideal capacitive performance. (e) Areal energy density versus power density plot, demonstrating that large-scale MSCs deliver heightened power density. Reproduced with permission from ACS Nano 11, 8 (2017). Copyright 2017 American Chemical Society.

2.5.2 GRM-based Micro/Nanoscale Energy Storage for IoBNT

In an ideal EH system, the harvested power should instantaneously match the power consumption, allowing the load or device to connect directly to the harvester without the need for intermediate components, such as storage. This concept known as *power-neutral* operation [130], is often impractical due to the intrinsic characteristics of EH, such as uncontrollability, unpredictability, volatility [297]. As ambient energy sources are often unstable and intermittent, energy-harvesting BNTs require energy accumulation during periods of ample energy in a capacitor or battery-like storage. This stored energy is then used during periods of scarce energy to ensure continuous communications, a process referred to as *energy-neutral* operation [131].

The growing demand for micro/nano storage components in microelectronic applications has led to the development of on-chip integrable solutions, such as the complementary micro-batteries (MBs) and micro-supercapacitors (MSCs). MBs typically exhibit high energy density, short lifetimes (typically < 1000 cycles [298]) and low power density. In contrast, MSCs usually possess long lifetimes (over 10^5 cycles [299]), fast charge/discharge rate, high power density, but low energy density compared to MBs. However, the short lifetimes of MBs can pose significant challenges in operating regions where battery replacement or maintenance is not feasible, such as within the body.

In addition to energy and power performance, the flexibility and compactness of energy storage components are crucial for seamless integration. Planar MCSs, such as interdigital in-plane MSCs, hold great potential for combining these attributes. For example, graphene-based planar MSCs on various substrates demonstrate remarkable scalability and integrability through various printing techniques [10, 300], as shown in Fig. 2.11. Moreover, as Wu *et al.* demonstrated, graphene-based in-plane MSCs, fabricated on flexible substrates via plasma-etching, can achieve high energy densities comparable to those of lithium-ion thin-film batteries while maintaining high power densities [11].

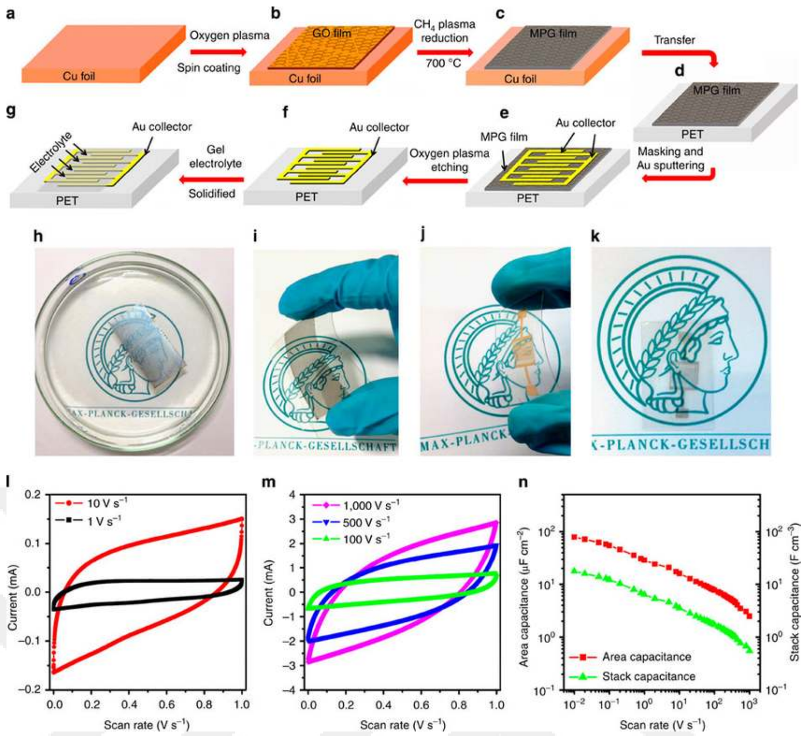

Figure 2.12: (a-g) Schematic illustration of the fabrication process for flexible rGO-based MSC on a PET substrate, involving plasma reduction and oxygen plasma etching [11]. (h-k) Optical images depicting (h) the rGO film on a PMMA substrate, (i) the rGO film on a PET substrate, (j) the rGO-MSC-PET device with gold current collectors, and (k) the rGO-MSC-PET device without gold current collectors, illustrating the device's flexibility. (l-n) CV curves of the rGO-MSC-PET device at various scan rates, showcasing high power performance, and areal capacitance measurements, indicating high energy performance. Zhong Shuai Wu et al, Nature Communications, 4, 2487 (2013), 2013; licensed under a Creative Commons Attribution (CC BY) license.

MSCs typically operate based on two principles: electrostatic double-layer MSCs, which store energy through ion adsorption at the interface between the electrode material (e.g., graphene) and the electrolyte (liquid or solid-state); pseudo-MSCs, which store energy via fast reversible redox reactions between the electrode material (e.g., pseudocapacitive materials like metal oxides) and the electrolyte; and hybrid MSCs, which combine both mechanisms for rapid charge storage and high charge capacity.

GRMs, such as graphene and rGO, are among the most widely-used active materials for planar MSC electrodes due to their favorable properties. These materials offer a combination of high specific surface area, excellent electrical conductivity, electrochemical stability, mechanical strength, and ultra-thin flexible structure, resulting in several beneficial outcomes. The high specific surface area of GRMs provides numerous electroactive sites, allowing for a large electrode-electrolyte interface for high-charge storage capacity [11]. The high electrical conductivity of GRMs facilitates electron transport, leading to high power density [11]. The electrochemical stability of GRMs ensures their ability to withstand numerous charge-discharge cycles without significant degradation, which is crucial for the long-term and reliable operation of the MSCs [301]. Moreover, GRMs exhibit remarkable mechanical strength, allowing for the fabrication of robust planar MSC electrodes, which is important for lifespan [302]. Additionally, the ultra-thin and flexible structure of GRMs enables the fabrication of compact and bendable MSC electrodes [302], allowing for integration into miniaturized devices and flexible and wearable electronics. Thanks to their chemical reactivity, GRMs can also undergo chemical reactions, such as reduction, oxidation, and functionalization [303]. The ability to be both reduced and oxidized allows GRMs' electronic properties and surface chemistry to change.

Flexible graphene-based MSCs can achieve high energy and power densities, remarkable cycling stability, and mechanical robustness by leveraging these properties, as demonstrated in [11]. In this study, GO films were reduced using methane-plasma treatment at 700°C, which repaired GO defects, and gold current collectors were deposited to maximize the accessible surface area of graphene, resulting in high conductivity (Fig. 2.12).

However, graphene's large specific surface area does not always translate to high capacitance, as van der Waals forces can cause graphene sheets to restack and reduce ion accessible surface area. Strategies for enhancing the energy performance of graphene-based MSCs primarily involve utilizing graphene composites and heterostructures. For instance, CNTs have been employed as nano-spacers between rGO sheets to mitigate restacking [304]. Heterostructure films that combine graphene's high conductivity with the high capacity of pseudocapacitive materials have been considered to achieve high power and energy performance simulatenaously [305]. However, optimizing the electrochemical performance of heterostructures remains challenging, as the principles governing ion and electrical transport in such architectures are not yet fully understood [306]. Moreover, it is essential to optimize the fabrication methods for graphene-based planar MSCs, as the performance of the resulting components is closely tied to the manufacturing process.

2.6 Discussion on Material Challenges

GRMs hold immense promise for facilitating the practical implementation of core IoBNT components and enhancing their performance and functionality. However, realizing this potential necessitates overcoming several material challenges inherent to GRMs, particularly in terms of reproducibility, biocompatibility, and device performance. In this section, we explore these challenges from a material science perspective, while also providing insights into potential solutions and ongoing research efforts in the field.

IoBNT applications typically encompass a vast number of BNTs [3]. When implemented with GRMs, this raises concerns regarding device ***heterogeneity*** in terms of performance due to existing reproducibility issues associated with GRM-based devices. The delicate and non-standardized GRM synthesis and processing methods challenge the attainment of consistent properties and functionality among the fabricated devices. Therefore, to enhance reproducibility of GRM-based BNTs and IoBNT applications, it is imperative to standardize the GRM synthesis and processing techniques. In the case of graphene, CVD is regarded as the most promising technique for producing large-area, high-quality graphene films with high electrical and thermal conductivity, as well as good structural and mechanical properties [307]. The CVD process typically involves growing graphene films on conductive metallic substrates such as copper or nickel, necessitating the transfer of graphene onto other substrates for practical device implementations. However, the graphene transfer process, particularly the wet transfer method, often subjects the graphene sample to various chemicals, resulting in the formation of defects and impurities that can stochastically alter the material properties. Hence, direct growth of graphene on the target substrate is preferable to circumvent the need for a transfer process. However, the high temperatures (> 1000 C°) required for graphene synthesis via CVD can damage many types of substrates, complicating direct growth on such materials. Researchers are actively exploring low-temperature, transfer-free methods to address this challenge [308].

IoBNT applications often involve integrating BNTs with complex and dynamic biological systems. Achieving this integration demands a deep understanding of the specific biological processes and tissues that interact with the devices. Additionally, it requires the development of technologies and techniques that can effectively interface with these biological systems without causing any local or systemic toxic or adverse effects. However, the ***biocompatibility*** of GRMs has not yet reached a consensus, as the literature presents conflicting reports [309]. These discrepancies regarding the biocompatibility of GRMs can be attributed to variations in material properties influenced by factors such as the specific form of graphene employed, thickness, lateral dimensions, surface chemistry, as well as the particular biological system being studied. As a result, it is crucial to explore the relationship between the physical and chemical properties of distinct graphene forms and the corresponding response elicited by the biological systems in question. A comprehensive understanding of these relationships will be instrumental in assessing the biocompatibility of GRMs and advancing their use in the development of BNTs and IoBNT applications.

Integrating GRMs with other materials like semiconductors and insulators is essential for developing ***multifunctional*** BNTs for IoBNT applications. However, this integration entails significant challenges pertaining to material compatibility, interface engineering, and fabrication processes. Discrepancies in thermal expansion coefficients, lattice constants, and chemical reactivity among different materials may induce structural defects and impair performance [310]. Achieving high-quality interfaces between different materials is crucial for efficient charge and energy transfer in BNT implementations [311]. Fabrication processes must be carefully designed and optimized to ensure that the integration of disparate materials does not compromise the unique properties of GRMs or other materials involved, that are core to the functionality of IoBNT.

Alongside GRMs, a diverse family of 2D layered materials has emerged with significant potential for IoBNT applications. This array of materials spans a large range of exceptional properties, with some behaving as insulators, metals, or even topological insulators [312]. Layered heterostructures that combine these diverse materials with GRMs offer novel device concepts and functionalities for IoBNTs [313, 314]. Prominent examples within this broad and continuously expanding family include h-BN, transition metal dichalcogenides (TMDs), and black phosphorus [315]. For example, h-BN is a wide-bandgap insulator that can be integrated with graphene to enhance the capabilities of GRM-based devices by providing an atomically smooth substrate that preserves the outstanding electronic properties of graphene [186]. TMDs, such as MoS_2, WS_2, and WSe_2, possess direct band gaps in the visible to near-infrared region, enabling their potential use in optoelectronic, e.g., optical bio-cyber interfaces, and photovoltaic, e.g., energy harvesting, applications within the IoBNT framework [316]. Black phosphorus, with its widely tunable band gap, holds promise for use in electronic and optoelectronic BNTs [317]. Recent explorations into a new class of 2D nanomaterials, known as MXenes, also show promising potential for IoBNT applications. MXenes, composed of early transition metals and carbon and/or nitrogen, possess metallic conductivity and hydrophilic surfaces, making them attractive for various applications, including biosensing [318]. Thus, while GRMs remain a core focus, the application of other 2D nanomaterials and their layered heterostructures with GRMs can offer extended opportunities for IoBNT.

In addition to the general challenges associated with the reproducibility and biocompatibility of GRMs, specific obstacles may emerge in the context of IoBNT components, namely micro/nano transceivers, bio-cyber interfaces, and energy harvesting/storage units. For example, GRM-based THz detectors, which are integral components of micro/nano transceivers for THz-band EM nanocommunications, commonly display low responsivity and slow operation. This is primarily due to the limited interaction between EM waves and graphene at THz frequencies, along with the inadequate absorption of EM radiation resulting from the small-scale nature of these components. To attain satisfactory responsivity, excessive bias voltages are often necessary, which is not a practical solution. Plasmonic graphene detectors can offer enhanced responsivity by augmenting light-graphene interaction via subwavelength confinement of light. However, significant potential remains for further enhancement. In this pursuit, researchers are exploring the integration of graphene with various materials and the incorporation of these composites into metamaterial structures. Despite the abundance of theoretical research in this domain, experimental demonstrations have been relatively scarce, mainly due to the reliance on sophisticated micro/nanofabrication techniques, such as patterning. Nonetheless, ongoing research efforts continue to explore and address these challenges [319].

While GRMs offer great potential for enabling bio-cyber interfaces in IoBNT applications thanks to their flexibility and sensitivity, certain challenges persist. These include ensuring the chemical and structural integrity of GRM-based interfaces, as well as their long-term operational stability [320, 321]. For both *in vitro* and *in vivo* IoBNT applications, maintaining the homogeneity of GRMs in terms of size, thickness, and the number of surface functional groups is crucial. Inhomogeneities in GRM structure can directly impact surface functionalization efficiency, performance evaluation, biocompatibility, and reproducibility of the resulting devices. The development of application-specific bio-functionalization methods for GRM-based bio-cyber interfaces remains a significant challenge, as it is essential to maintain the stability of these devices without altering the structure and function of biomolecules and GRMs [322, 273].

Similar challenges are encountered in GRM-based EH at nanoscale. For the effective creation and mass production of nanoscale energy harvesters using GRMs, research must focus on advanced fabrication technologies that are precise, high-resolution, scalable, and cost-effective [323, 324]. Various microfabrication techniques can be employed to fabricate microelectrodes for integration into energy harvesting BNTs. However, consistent and accurate preparation of these devices, particularly for electrode arrays, is crucial for enhancing the energy density of GRM-based nanoscale energy harvesters. Stability of the active material, adhesion between the electrode material and electrolyte, and appropriate packaging are also essential factors to consider for the development of power provisioning techniques for BNTs and IoBNT applications based on GRMs.

Specifically, TENGs, which may power IoBNT applications, face numerous challenges, including the development of efficient and scalable methods for producing large quantities of high-quality graphene [325, 326]. Understanding the fundamental mechanisms behind triboelectrification and charge transfer in GRMs could aid in enhancing the energy conversion efficiency of TENGs. Additionally, concerns regarding the long-term stability and performance of graphene-based TENG systems under different environmental conditions must be addressed.

In summary, standardizing GRM synthesis and processing techniques, as well as exploring low-temperature, transfer-free methods, will play a crucial role in enhancing the reproducibility of GRM-based devices. A comprehensive understanding of the relationship between GRM properties and biological responses will be instrumental in assessing biocompatibility and furthering their use in the development of BNTs. The integration of GRMs with other materials to create multifunctional BNTs demands careful consideration of material compatibility, interface engineering, and fabrication processes. Addressing these material challenges and optimizing fabrication processes, researchers can unlock the full potential of GRMs in IoBNT applications.

2.7 Conclusions and Future Outlook

In this chapter, we have explored the potential of GRMs and GRM-based technologies to advance the emerging IoBNT paradigm, which particularly aims to extend human connectivity to biological environments. These environments present unique challenges, including the scale of communicating entities and the diverse forms of information exchange. Despite these challenges, we have argued that GRMs, with their remarkable properties, hold great promise for addressing these issues and enabling the development of key IoBNT components. Our discussion centered on practical transceivers of unconventional communication techniques for IoBNT applications, with a focus on GRM-based architectures capable of emitting and detecting unconventional signal forms, such as molecular and very high frequency EM signals. Examples include graphene bioFET-based MC receivers, graphene nanoporous membranes for MC transmitters, graphene plasmonic THz radiators/detectors, and GRM-based optoacoustic ultrasonic sources. Moreover, we assessed the potential of existing GRM-based bio-interfacing technologies to inform the design of sophisticated bio-cyber interfaces tailored for IoBNT applications. These technologies include biosensors, neural interfaces, and stimuli-responsive drug delivery devices. We also examined the current capabilities and limitations of GRM technologies for energy harvesting from relevant ambient sources and storing energy to provide uninterrupted power to both artificial and biological devices, i.e., BNTs, within the IoBNT ecosystem. By harnessing the exceptional properties of GRMs, the IoBNT paradigm can transform our understanding of, and interactions with biological systems, fostering unprecedented advancements in healthcare, environmental monitoring, and a myriad of other fields.

Although IoBNT is currently in the research phase, it presents substantial market opportunities across various sectors, particularly in healthcare. The envisioned capabilities of networked BNTs to collectively gather health-critical data at unprecedented resolution, as well as to continuously process the collected data in distributed manner and share them with end-users offers transformative possibilities for personalized medicine. When integrated emerging technologies such as digital twin, virtual reality, and machine learning, the power of IoBNT can be significantly amplified, expanding its reach beyond the realm of healthcare towards agriculture, environmental monitoring and manufacturing applications. Market reports project that the estimated market size for the Internet of Nano Things (IoNT), a broader technological concept encompassing IoBNT, is anticipated to reach USD 55.31 billion by 2028 [327]. To fully harness the market potential, addressing the key challenges mentioned is imperative. One of the most significant of these challenges is bridging the gap between the electronics and biological domains. This necessitates expanding the understanding of biological systems, and the development of high resolution and reliable sensors, interfaces and communication transceivers, where GRMs can play a significant role and accelerate the commercialization of IoBNT applications as discussed throughout the chapter. An important aspect to consider for large-scale commercialization is the symbiotic relationship of IoBNT with next-generation wireless networking technologies, such as 6G networks. Key components of IoBNT, including molecular communications, have been already forecasted to be integral components of these emerging network standards [328, 329]. However, the incorporation of such innovative technologies into the wider communication technology landscape underscores the crucial need for standardization for IoBNT technologies. Moreover, cultivating collaboration and establishing robust partnerships among researchers across diverse disciplines, including synthetic biology, nanotechnology, communication engineering, and philosophy of science, is of utmost significance for the advancement of IoBNT [208]. This collaborative approach should also involve active engagement from industry stakeholders, healthcare providers, regulatory agencies, and policymakers, as they contribute valuable perspectives and expertise to interdisciplinary research endeavors. Such collaborative endeavors can drive the formulation of standardized protocols, regulatory frameworks, and best practices, thus accelerating the widespread adoption of IoBNT technologies in real-world applications.

Part II

Physical Layer Techniques for Practical Molecular Communication Systems

Chapter 3

FREQUENCY-DOMAIN DETECTION FOR MOLECULAR COMMUNICATIONS

3.1 Introduction

Using molecules for encoding and transmitting information, namely, Molecular Communications (MC), is the nature's method of interconnecting biological entities, such as natural cells. The engineering of this unconventional mode of communication has the potential to broaden our connectivity to synthetic *bio-nano things*, including nanobiosensors and artificial cells. This potential gave rise to the emergence of the *Internet of Bio-Nano Things (IoBNT)*, a novel networking framework holding the promise for transformative healthcare and environmental applications [172, 330].

MC differs significantly from conventional electromagnetic communication methods and requires unique transceiver designs as well as novel modulation, coding, and detection techniques tailored to the dynamic, nonlinear, and complex channel characteristics typical of biochemical environments. The development of MC receivers (MC-Rxs) and detection methods has received notable attention in the MC literature. Yet, due to the ease of modeling, most of the early work focused on passive Rx architectures that are physically detached from the MC channel, rendering them of limited practical relevance [5]. A growing trend in MC research involves the development of more practical MC-Rxs that incorporate ligand receptors on their surface as selective bio-recognition elements, mirroring the sensing and communication mechanisms of biological cells. A notable example, practically realized in [4], utilizes biosensor field-effect transistors (bioFETs). In this architecture, ligand-receptor (LR) interactions are translated into electrical signals through field-effect, enabling the decoding of the transmitted information.

LR interactions are crucial for the sensing and communication functions of natural cells. However, the selectivity of biological receptors for their target ligands is not perfect. This so-called LR promiscuity leads to cross-talk with non-target molecules co-existing in the biochemical environment [331]. Natural cells typically manage this cross-talk using several mechanisms involving intracellular chemical reaction networks, multi-state receptor dynamics, and kinetic proofreading [45]. The problem of molecular interference is similarly encountered in abiotic MC-Rxs employing ligand receptors. However, the lack of inherent molecular mechanisms to mitigate this interference underscores the need to devise effective detection techniques for these systems.

In the earlier work on biosynthetic MC-Rxs, the molecular interference problem was addressed using time-domain detection (TDD) methods. These methods rely on diverse ligand-receptor binding statistics, obtained by tracking individual receptor binding states, such as the bound/unbound durations and the entire binding trajectory of individual receptors [332]. Additionally, channel sensing techniques capable of detecting the concentration of multiple ligand types simultaneously, thereby mitigating interference [45] were devised. With the synthetic biology approach, altering natural gene circuits in living cells, such as bacteria, or bottom-up creating synthetic ones can enable the implementation of biosynthetic MC-Rxs. These biosynthetic MC-Rxs, with biologically derived receptors, can monitor individual receptor states, as their natural counterparts. One of the key selective-sensing mechanisms in natural cells, kinetic proofreading, can also be adapted in biosynthetic MC-Rxs to estimate the type of the ligand binding to the receptor. This estimation involves intracellular signal processing based on chemical reaction networks, as detailed in [45, 332]. However, TDD techniques for biosynthetic MC-Rxs are not applicable to biosensor-based MC-Rxs, as these systems lack mechanisms inherent in biosynthetic MC-Rxs for tracking individual receptor binding states. In biosensor-based MC-Rxs, the observable variable is the variation of the electrical output of the bioFET channel, which results from the combined electric field effect of receptor-bound ligands and does not reveal information regarding the binding states of individual receptors.

Consequently, decoding information from the electrical output of biosensor-based MC-Rx becomes challenging, particularly in the absence of additional data on interference concentration statistics. Moreover, the impact of molecular interference is more pronounced when the receiver operates close to saturation, i.e., when vast majority of receptors occupied by information and interfering molecules, diminishing the receiver's sensitivity to changes in the concentration of information-carrying molecules. Therefore, there is a need for reliable detection techniques specifically designed to address molecular interference in biosensor-based MC-Rxs.

This chapter introduces a novel frequency-domain detection (FDD) technique that enables distinguishing different ligand types interacting with biosensor-based MC-Rxs having cross-reactive receptors. This method employs the power spectral density (PSD) of time-domain samples collected from the electrical output of the biosensor-based MC-Rx. The noise in this output includes binding noise, which results from the combined effects of ligand binding and unbinding fluctuations at the receptors. The distinct characteristics of different LR interactions are reflected in the PSD of the binding noise, which can be formulated as a function of ligand concentrations and their respective reaction rates. FDD utilizes this property to extract the concentration of information-carrying and interferer molecules effective on the MC-Rx and then decode the transmitted symbol.

More spesifically, stochastic and reversible LR interactions can be represented through a one-step binding/unbinding model, where the state transition rates are determined by the binding and unbinding rates for the LR pair [333]. Although various types of ligands can interact with the same kind of receptors, these interactions often have different binding and unbinding rates. These differences in reaction rates are manifested in distinct characteristic frequencies f_c, which are also dependent on the concentrations of the involved ligands. The characteristic frequency of the LR pair appears as a cut-off frequency in the Lorentzian-shaped PSD of the binding noise. When multiple types of ligands interact with the receptors, the PSD can be represented as the superposition of the Lorentzian-shaped PSDs. In such a scenario, the characteristic frequencies that define the shape of the binding noise PSD contain information on both reaction rates and the concentrations of the different ligands.

To our knowledge, the FDD method introduced in this chapter represents a novel approach for biosensor-based MC-Rxs. This method overcomes the limitations of existing detection methods in the time domain, particularly their inability to distinguish between information-carrying and interfering ligands. To evaluate the performance of the FDD method, we derived the theoretical bit error probability (BEP) and conducted a comparative analysis with a TDD method, a well-known detection strategy based on a single sample from the peak of the received signal. To validate the accuracy of our analytical results, we employed a particle-based stochastic simulator, enabling the simulation of LR interactions on the surface of the MC-Rx in a microfluidic channel. While the FDD method requires more computational resources than TDD, simulation results indicate that it is a promising detection strategy for biosensor-based MC-Rxs, particularly in high-interference scenarios where TDD methods significantly underperform.

3.2 System Model

We consider an MC system consisting of an MC-Tx, an MC-Rx and a three-dimensional microfluidic channel with a rectangular cross-section where molecules undergo diffusion and flow. As illustrated in Fig. 4.1(a), MC-Tx is located at the channel inlet ($x = 0$), and MC-Rx is positioned at the channel floor, centered at $x = x_R$. The system is defined with the following features and assumptions:

- MC-Tx encodes information using binary concentration shift keying (CSK) modulation by releasing a certain number of information molecules corresponding to each bit, denoted as $N_{m|s}$, at the beginning of each signaling interval. Here, m denotes the information-carrying molecules, and s denotes the transmitted bit, where $s \in \{0, 1\}$. MC-Tx releases molecules instantaneously and uniformly along the channel cross-section, propagating through a unidirectional fluid flow along the x axis.

- The signaling interval is long enough to neglect inter-symbol interference (ISI).

- MC-Rx incorporates the graphene bioFET architecture illustrated in Fig. 4.1(b). This architecture is based on a graphene transducer channel functionalized with uniform receptors that reversibly bind to specific targets, allowing continuous and label-free sensing. By harnessing graphene's exceptional electrical, mechanical, and biochemical properties, including high charge carrier mobility, atomic thickness, and a two-dimensional geometry combined with the signal amplification capacity of the bioFET configuration, the system enables highly sensitive detection across a wide spectrum of biomolecules [?]. A recent milestone in this technology is the first successful demonstration of micro/nanoscale MC-Rx based on graphene bioFET using single-stranded DNA molecules as information carriers and their complementary strands as receptors on the graphene surface [4].

- Two different types of ligands are present in the channel: information molecules and interfering molecules. Information molecules have the capability to undergo reversible reactions with receptors on the MC-Rx. Similarly, interfering molecules can also react with MC-Rx receptors, but at different reaction rates compared to information molecules. The concentration of interfering molecules in the vicinity of MC-Rx during the sampling interval, denoted as c_i, follows a log-normal distribution with mean μ_{c_i} and variance $\sigma_{c_i}^2$. This statistical model is widely used in the literature to characterize the natural variability observed in biological systems [334].

- The MC-Rx has the knowledge of the number of transmitted information molecules corresponding to bits $s = 0$ and $s = 1$, denoted as $N_{m|s}$. It also has the knowledge of the binding/unbinding rates of information molecules (k_m^-/k_m^+) and interference molecules (k_i^-/k_i^+).

Ligand transport in the microfluidic channel follows advection-diffusion processes. Considering the instantaneous release of information molecules from MC-Tx and assuming that ligand-receptor reactions have a negligible effect on the ligand

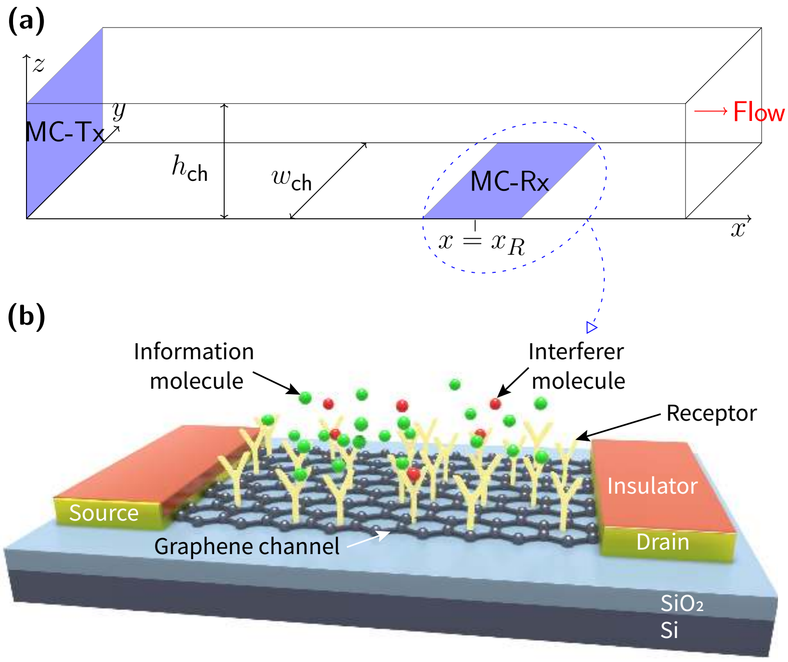

Figure 3.1: A three-dimensional illustration (a) the microfluidic MC channel, including the positions of the MC-Tx and MC-Rx, and (b) the detailed view of the graphene bioFET-based MC-Rx exposed to information and interferer molecules.

concentration in the channel, the ligand concentration over space and time can be described as follows [335]:

$$c_{m|s}(x,t) = \frac{N_{m|s}}{A_{ch}\sqrt{4\pi Dt}} \exp\left(-\frac{(x-ut)^2}{4Dt}\right), \tag{3.1}$$

where $A_{ch} = h_{ch}w_{ch}$ is the channel cross-sectional area, with h_{ch} being the channel height and w_{ch} as the channel width. The constant fluid flow velocity along the x-axis is denoted by u and D stands for the effective diffusion coefficient. In the case of rectangular cross-section channels, the effective diffusion coefficient D is expressed in terms of the intrinsic ligand diffusion coefficient D_0 as follows [336]:

$$D = \left(1 + \frac{8.5u^2h_{ch}^2w_{ch}^2}{210D_0^2(h_{ch}^2 + 2.4h_{ch}w_{ch} + w_{ch}^2)}\right)D_0. \tag{3.2}$$

The peak of the ligand concentration profile reaches the MC-Rx's center position

x_R at time $t_D = \frac{x_R}{u}$. Due to the low-pass filtering characteristics of the MC channel induced by the advection diffusion, the ligand concentration at the Rx position varies slowly. This allows the LR reactions to quickly reach equilibrium within a narrow time window centered around t_D [336, 335], where the MC-Rx can collect samples from the received signal. The information molecule concentration within the sampling window can be expressed as

$$c_{m|s}(x_R, t_D) = \frac{N_{m|s}}{A_{ch}\sqrt{4\pi D t_D}}. \tag{3.3}$$

Given that the transmitted bit is s, the probability of the bound state of a single receptor at the sampling time in the presence interference can be written as

$$p_{b|s} = \frac{c_{m|s}/K_{D_m} + c_i/K_{D_i}}{1 + c_{m|s}/K_{D_m} + c_i/K_{D_i}}, \tag{3.4}$$

where $K_{D_m} = k_m^-/k_m^+$ and $K_{D_i} = k_i^-/k_i^+$ are the dissociation constant of information and interference molecules, respectively [45].

The total number of receptors in the bound state at the sampling time, denoted as $N_{b|s}$, follows a Binomial distribution, i.e., $N_{b|s} \sim \text{Binomial}(N_r, p_{b|s})$, where N_r represents the number of independent surface receptors [249]. Considering that the interference concentration follows a log-normal distribution, by applying the total law of expectation, we can obtain the mean of the number of bound receptors sampled as follows:

$$\mu_{N_{b|s}} = \int_0^\infty N_r p_{b|s}(c_i) f(c_i) \mathrm{d}c_i, \tag{3.5}$$

where $p_{b|s}(c_i) = \dfrac{c_{m|s}/K_{D_m} + c_i/K_{D_i}}{1 + c_{m|s}/K_{D_m} + c_i/K_{D_i}}$, and $f(\cdot)$ is the probability density function of log-normal distribution. Similarly, by applying the law of total variance, we can determine the variance of the total number of bound receptors as follows:

$$\sigma^2_{N_{b|s}} = \left(\int_0^\infty N_r \left(1 - p_{b|s}(c_i)\right) p_{b|s}(c_i) f(c_i) \mathrm{d}c_i + \int_0^\infty \left(p_{b|s}(c_i) N_r\right)^2 f(c_i) \mathrm{d}c_i \right) - \mu^2_{N_{b|s}} + \sigma^2_f. \tag{3.6}$$

In the case of a large number of receptors, the distribution of $N_{b|s}$ can be approximated by a Gaussian distribution, expressed as $N_{b|s} \sim \mathcal{N}(\mu_{N_{b|s}}, \sigma^2_{N_{b|s}})$ [249].

The binding of charged ligands to the receptors results in an effective charge on the graphene channel through the electric field effect. This effect can be described by the equation $Q_{Gr|s} = N_{b|s} q_{eff} N_{e^-}$. In this context, N_{e^-} refers to the number of free electrons per ligand molecule. q_{eff} represents the mean effective charge of a single electron in a bound ligand in the presence of ionic screening, namely Debye screening. The expression for q_{eff} is given by $q_{eff} = q \times \exp\left(-\frac{r}{\lambda_D}\right)$, where q is the elementary charge, r is the effective length of a surface receptor, and λ_D is the Debye length. The Debye length, λ_D, is expressed by $\lambda_D = \sqrt{(\epsilon \kappa_B T)/(2 N_A q^2 c_{ion})}$, where ϵ represents the permittivity of the medium, T is the temperature, κ_B stands for Boltzmann's constant, N_A is Avogadro's constant, and c_{ion} denotes the ionic concentration of the medium [249].

Accordingly, the mean surface potential due to the bound ligands can be expressed as

$$\Psi_{Gr|s} = \frac{Q_{Gr|s}}{C_G}, \tag{3.7}$$

where $C_G = \left(\frac{1}{C_{Gr}} + \frac{1}{C_Q}\right)^{-1}$ is the total gate capacitance of the bioFET. C_{Gr} is the electrical double-layer capacitance between the graphene and electrolyte channel and is defined by $C_{Gr} = A_{Gr}\epsilon/\lambda_D$. In this expression, A_{Gr} is the area of the graphene surface exposed to the electrolyte. Additionally, C_Q represents the quantum capacitance and is obtained as $C_Q = c_q \times A_{Gr}$, where c_q is the quantum capacitance of graphene per unit area [4].

The change in the output current resulting from bound molecules at the sampling time can be formulated as $\Delta I_{b|s} = g \times \Psi_{Gr|s}$, where g is the transconductance of the bioFET. Using the Gaussian approximation for the distribution of the number of bound receptors, $N_{b|s}$, and considering the linearity of the transduction process, the change in the output current due to bound molecules, $\Delta I_{b|s}$, can also be approximated as following a Gaussian distribution, i.e., $\Delta I_{b|s} \sim \mathcal{N}(\zeta \mu_{N_{b|s}}, \zeta^2 \sigma^2_{N_{b|s}})$, where the parameter ζ is defined as $\zeta = \frac{q_{eff} N_e - g}{C_G}$.

In low-dimensional semiconductor materials such as graphene, another factor adding to the variability in the overall output current is $1/f$ noise. According to the widely-used charge-noise model for graphene FETs [337], the power spectral density of $1/f$ noise is described by

$$S_f(f) = \frac{S_{f_{1Hz}}}{f^{\beta}}, \tag{3.8}$$

where $S_{f_{1Hz}}$ is the noise power at 1 Hz, and β is an empirically determined noise exponent with a typical range of $0.8 \leq \beta \leq 1.2$. As discussed in [249], $1/f$ noise can be approximated as white noise within physically relevant observation windows. Accordingly, the variance of $1/f$ noise can be formulated as

$$\sigma_f^2 = \int_0^{f_L} S_f(f_L)\, \mathrm{d}f + \int_{f_L}^{f_H} S_f(f)\, \mathrm{d}f, \tag{3.9}$$

where f_L represents the lower frequency limit of the observation window, below which the noise power is considered constant, and f_H is the upper frequency limit, beyond which the noise power is considered negligible.

Considering that the output current is influenced by the sum of two additive stationary noise processes, specifically binding noise and 1/f noise, each following independent Gaussian statistics, the overall noise process affecting the output current is also Gaussian [249]. Therefore, the mean and variance of the change in the output current are expressed as follows:

$$\begin{aligned} \mu_{\Delta I_s} &= \zeta \mu_{N_{b|s}}, \\ \sigma^2_{\Delta I_s} &= \zeta^2 \sigma^2_{N_{b|s}} + \sigma_f^2. \end{aligned} \tag{3.10}$$

In (3.10), $\mu_{\Delta I_s}$ denotes the expected change in the output current, and $\sigma^2_{\Delta I_s}$ represents its variance, both conditioned on the transmitted bit s.

3.3 *Time-Domain Detection*

The MC-Rx uses maximum likelihood (ML) detection for TDD, employing the decision threshold γ_{td} as expressed by

$$\Delta I \underset{\hat{s}=0}{\overset{\hat{s}=1}{\gtrless}} \gamma_{td}, \tag{3.11}$$

where ΔI is the sample taken from the output current at the sampling time.

Given that MC-Rx has no knowledge of the interferer concentration statistics, it determines the ML decision threshold for TDD based solely on the received information molecule concentration statistics, ignoring the interferer [332]. In this case, the probability of the receptor in a bound state is given by $\tilde{p}_{b|s} = \dfrac{c_{m|s}/K_{D_m}}{1 + c_{m|s}/K_{D_m}}$. Consequently, the mean and variance of the number of bound receptors are obtained as $\tilde{\mu}_{N_{b|s}} = \tilde{p}_{b|s} N_r$ and $\tilde{\sigma}^2_{N_{b|s}} = \tilde{p}_{b|s}(1 - \tilde{p}_{b|s}) N_r$ respectively. The mean and variance of the resulting change in the output current are $\tilde{\mu}_{\Delta I_s} = \zeta \tilde{\mu}_{N_{b|s}}$, and $\tilde{\sigma}^2_{\Delta I_s} = \zeta^2 \tilde{\sigma}^2_{N_{b|s}} + \sigma^2_f$, respectively. The decision threshold is then obtained as

$$\begin{aligned}\gamma_{td} = \frac{1}{\tilde{\sigma}^2_{\Delta I_1} - \tilde{\sigma}^2_{\Delta I_0}} \Big(&\tilde{\sigma}^2_{\Delta I_1} \tilde{\mu}_{\Delta I_0} - \tilde{\sigma}^2_{\Delta I_0} \tilde{\mu}_{\Delta I_1} + \tilde{\sigma}_{\Delta I_1} \tilde{\sigma}_{\Delta I_0} \\ &\times \sqrt{(\tilde{\mu}_{\Delta I_1} - \tilde{\mu}_{\Delta I_0})^2 + 2(\tilde{\sigma}^2_{\Delta I_1} - \tilde{\sigma}^2_{\Delta I_0}) \ln(\tilde{\sigma}_{\Delta I_1}/\tilde{\sigma}_{\Delta I_0})} \Big),\end{aligned} \tag{3.12}$$

where $\tilde{\mu}_{\Delta I_0}$ and $\tilde{\mu}_{\Delta I_1}$ are the mean changes in the output current corresponding to the transmitted bits $s = 0$ and $s = 1$, respectively, and $\tilde{\sigma}^2_{\Delta I_0}$ and $\tilde{\sigma}^2_{\Delta I_1}$ are the respective variances.

Therefore, given the decision threshold γ_{td}, the BEP for TDD is formulated as detailed in [332]:

$$P_e^{TDD} = \frac{1}{4} \operatorname{erfc}\left(\frac{\gamma_{td} - \mu_{\Delta I_0}}{\sqrt{2\sigma^2_{\Delta I_0}}} \right) + \frac{1}{4} \operatorname{erfc}\left(\frac{\mu_{\Delta I_1} - \gamma_{td}}{\sqrt{2\sigma^2_{\Delta I_1}}} \right), \tag{3.13}$$

where $\mu_{\Delta I_0}$ and $\mu_{\Delta I_1}$ represent the expected changes in the output current for the transmitted bits $s = 0$ and $s = 1$ respectively, while $\sigma^2_{\Delta I_0}$ and $\sigma^2_{\Delta I_1}$ represent the corresponding variances. Note that these means and variances are determined using (3.10), which takes into account the presence of both information and interference molecules in the channel.

3.4 Frequency-domain Detection

This section introduces the FDD method, utilizing the overall noise PSD, which comprises binding noise and $1/f$ noise PSD inherent in the output current of the MC-Rx. The aim is to estimate the received information molecule concentration, c_m, for use in symbol decision. In particular, the FDD method uses the theoretical and observed noise PSD, where the observed PSD is the periodogram of the noise generated from time domain samples of the output current of the MC-Rx. In the following, we describe the theoretical model for the noise PSD and then detail the parameter estimation and symbol detection procedures.

3.4.1 Theoretical Model of Binding Noise PSD

In this section, we detail the theoretical model of the binding noise PSD for a pair of information and interfering molecules, denoted as $\boldsymbol{\lambda} = [c_m, c_i]$.

The ligand-receptor binding process is represented by a three-state reaction model with receptors in the unbound state (R), receptors bound with information molecules (RM) and receptors bound with interference molecules (RI). The corresponding state occupation probabilities are denoted as p_R, p_{RM} and p_{RI}, respectively [333].

$$
\begin{aligned}
R + M &\underset{k_m^+}{\overset{k_m^-}{\rightleftharpoons}} RM \\
R + I &\underset{k_i^+}{\overset{k_i^-}{\rightleftharpoons}} RI.
\end{aligned}
\tag{3.14}
$$

The chemical master equations for the system are expressed in matrix form as follows:

$$\begin{bmatrix} \frac{\mathrm{d}p_{RM}}{\mathrm{d}t} \\ \frac{\mathrm{d}p_{RI}}{\mathrm{d}t} \\ \frac{\mathrm{d}p_{R}}{\mathrm{d}t} \end{bmatrix} = \begin{bmatrix} -k_m^- & 0 & k_m^+ c_m \\ 0 & -k_i^- & k_i^+ c_i \\ k_m^- & k_i^- & -k_m^+ c_m - k_i^+ c_i \end{bmatrix} \begin{bmatrix} p_{RM} \\ p_{RI} \\ p_R \end{bmatrix}. \tag{3.15}$$

In (3.15), the matrix incorporating reaction rates and concentrations, has a rank of two as we can express the probability of one state in terms of the others: $p_R = 1 - p_{RM} - p_{RI}$. Consequently, by setting the left-hand side in (3.15) to zero, the equilibrium state probabilities can be determined as follows:

$$p_{RM}^0 = \frac{c_m/K_{D_m}}{1 + \frac{c_m}{K_{D_m}} + \frac{c_i}{K_{D_i}}}, \quad p_{RI}^0 = \frac{c_i/K_{D_i}}{1 + \frac{c_m}{K_{D_m}} + \frac{c_i}{K_{D_i}}}, \tag{3.16}$$

and $p_R^0 = 1 - (p_{RM}^0 + p_{RI}^0)$. The state occupation probabilities can be expressed in terms of the equilibrium state probability and the fluctuations around this probability [333, 338]:

$$p_j(t) = p_j^0 + \Delta p_j(t), \quad j \in \{RM, RI, R\}. \tag{3.17}$$

We define a column vector $\mathbf{p}(t)$ containing the state occupation probabilities as $\mathbf{p}(t) = [p_{RM}(t); p_{RI}(t); p_R(t)]$ and its reduced form as $\mathbf{p}'(t) = [p_{RM}(t); p_{RI}(t)]$. The relation between $\Delta\mathbf{p}'(t)$ and $\Delta\mathbf{p}(t)$ is given by

$$\Delta\mathbf{p}(t) = \mathbf{R}\Delta\mathbf{p}'(t), \tag{3.18}$$

where $\mathbf{R}$ is the transformation matrix [333]. By substituting (3.17) into (3.15) and applying Taylor's expansion, the state probability fluctuations can be expressed as follows [333]:

$$\frac{\mathrm{d}\Delta\mathbf{p}'(t)}{\mathrm{d}t} = \mathbf{\Omega}\Delta\mathbf{p}'(t), \tag{3.19}$$

where, the matrix $\boldsymbol{\Omega}$ is defined as

$$\boldsymbol{\Omega} = \begin{bmatrix} -k_m^+ c_m - k_m^- & -k_m^+ \\ -k_i^+ c_i & -k_i^+ c_i - k_i^- \end{bmatrix}. \tag{3.20}$$

The fluctuation in the output current of the MC-Rx due to stochastic binding reactions, denoted as $\Delta I_b(t)$, is then derived as

$$\Delta I_b(t) = \frac{q_{eff}\ g}{C_G}\ \mathbf{z}^T \mathbf{R} \Delta \mathbf{p}'(t) \tag{3.21}$$

where $\mathbf{z} = \left[N_{e^-}; N_{e^-}; 0\right]$ is the column vector containing the number of elementary charges corresponding to each state.

Since $\Delta I_b(t)$ is a stationary process, the theoretical binding noise PSD can be obtained by setting $t = 0$ in the following expression [333]:

$$\begin{aligned} S_b(f) &= 2\ \mathcal{F}\{\mathbb{E}[\Delta I_b(t)\Delta I_b(t+\tau)]\} \\ &= 2\ \mathcal{F}\{\mathbb{E}[\Delta I_b(0)\Delta I_b(\tau)]\} \\ &= 4N_r \left(\frac{q_{eff} g}{C_G}\right)^2 \mathbf{z}^T \mathbf{R} \Gamma \left(\mathrm{Re}\{(j2\pi f \mathbf{I}_{2\times 2} - \boldsymbol{\Omega})^{-1}\}\right)^T \mathbf{R}^T \mathbf{z}. \end{aligned} \tag{3.22}$$

In (3.22), $\mathcal{F}\{\cdot\}$ denotes the Fourier transform, $\mathbb{E}[.]$ stands for the expectation, $\mathbf{I}_{2\times 2}$ is the 2 by 2 identity matrix, and Γ is the matrix containing the expected state probabilities, defined as follows [333]:

$$\Gamma = \begin{bmatrix} p_{RM}^0 (1 - p_{RM}^0) & -p_{RM}^0 p_{RI}^0 \\ -p_{RM}^0 p_{RI}^0 & p_{RI}^0 (1 - p_{RI}^0) \end{bmatrix}. \tag{3.23}$$

As a result, the overall noise PSD affecting the output current of the MC-Rx can be written as

$$S(f) = S_b(f) + S_f(f), \tag{3.24}$$

where $S_f(f)$ is the $1/f$ noise PSD expressed by (3.8).

3.4.2 Maximum Likelihood Estimation of PSD Parameters

This section details the ML estimation of the unknown parameter values, namely received information and interference molecule concentrations, $\boldsymbol{\lambda} = [c_m, c_i]$, from the noise PSD. The detector uses the estimated information molecule concentration, $\hat{c}_m$, for symbol decision, as described in Section 3.4.3.

The estimation method relies on several underlying assumptions. First, the overall noise process, which includes binding noise and $1/f$ noise, is assumed to be stationary, zero-mean, and characterized by a single-sided spectrum. The MC-Rx is equipped with the theoretical model of the noise PSD expressed by (3.22) and (3.24). Furthermore, the MC-Rx has the knowledge of the binding/unbinding rates of information and interference molecules, along with the number of information molecules transmitted for bits $s = 0$ and $s = 1$ as explained in Section 3.2.

The MC-Rx estimates steady concentrations of information and interference molecules by sampling the output current ΔI_b within a predefined sampling window. The concentrations of information and interference molecules within this window are considered constant, adhering to the equilibrium assumption discussed in Section 3.2 [249]. In the sampling window, a single realization of the interferer concentration c_i is considered, following a log-normal distribution as detailed in Section 3.2. The mean value of ΔI_b is discarded to isolate the noise before further processing.

ML estimate of $\boldsymbol{\lambda} = [c_m, c_i]$ is realized using the observed noise PSD generated from time-domain noise samples and the parametric model of the noise PSD expressed by (3.24). The observed noise PSD is assumed to be generated using the periodogram method.

The MC-Rx takes N noise samples for each transmitted symbol, denoted as $\boldsymbol{x} = (x_1, x_2, ..., x_N)$, sampled with a period of Δt. Therefore, the sampling duration per symbol, representing the length of the sampling window, is $T_d = N\Delta t$. The periodogram for the sampled noise can be computed using the Discrete Fourier Transform (DFT) of the samples $\boldsymbol{x}$. Considering even N, the periodogram values can be expressed as follows:

$$Y_k = \frac{2\Delta t}{N}|X_k|^2,$$

where $k = 1, ..., N/2 - 1$, and $|X_k|$ represents the DFT components of $\boldsymbol{x}$.

For a stochastic time series of length N, the random variable $W_k = \frac{2Y_k}{S(f_k)}$ follows chi-squared distribution χ^2. Here, $S(f_k)$, described by (3.24), represents the true noise PSD at frequency f_k, where $f_k = \frac{k}{N\Delta t}$ and $k = 1, ..., N/2 - 1$. Note that the chi-square distribution with two degrees of freedom is an exponential distribution [339]. As a result, the periodogram values exhibit an exponential distribution about the true PSD. This distribution is defined by the following probability expression associated with the model PSD value at a given frequency:

$$p(Y_k|S(f_k)) = \frac{1}{S(f_k)}\mathrm{e}^{-\frac{Y_k}{S(f_k)}}, \tag{3.25}$$

where $S(f_k)$ equals to expected value of $S(f)$ at the frequency f_k. [339].

Using (4.7), the likelihood of observing a specific pair of information and interferer concentrations, $\boldsymbol{\lambda} = [c_m, c_i]$, can be expressed as follows:

$$\mathcal{L}(\boldsymbol{\lambda}) = \prod_{k=1}^{N/2-1} p(Y_k|S(f_k, \boldsymbol{\lambda})) = \prod_{k=1}^{N/2-1} \frac{1}{S(f_k, \boldsymbol{\lambda})}\mathrm{e}^{-\frac{Y_k}{S(f_k,\boldsymbol{\lambda})}}. \tag{3.26}$$

We use the Whittle approximation to express the log-likelihood, as it serves as a good approximation to the exact likelihood asymptotically while providing computational efficiency. Specifically, to calculate the Whittle likelihood, $O(N \log N)$ computations are required compared to $O(N^2)$ for the exact likelihood [339, 340]. Thus, the quasi-log-likelihood can be written as follows:

$$\ln \mathcal{L}(\boldsymbol{\lambda}) = -\sum_{k=1}^{N/2-1} \left(\frac{Y_k}{S(f_k, \boldsymbol{\lambda})} + \ln S(f_k, \boldsymbol{\lambda})\right). \tag{3.27}$$

The ML estimator determines the optimal value of $\boldsymbol{\lambda}$, denoted as $\hat{\boldsymbol{\lambda}}$, which maximizes the log-likelihood function $\ln \mathcal{L}(\boldsymbol{\lambda})$ as given by (4.8). This maximization is equivalent to minimizing the negative log-likelihood, $l = -\ln \mathcal{L}(\boldsymbol{\lambda})$ [341]. Consequently, $\hat{\boldsymbol{\lambda}}$ is obtained by solving the following minimization problem:

$$\hat{\boldsymbol{\lambda}} = \arg\min_{\boldsymbol{\lambda}}\{l\}. \tag{3.28}$$

(3.28) can be solved using numerical methods such as the Newton-Raphson method, which enables efficient convergence to the ML estimate within a few numbers of iterations. For the FDD technique, the computational complexity for evaluating the Whittle likelihood is $O(N \log N)$, in addition to the calculations required for the numerical estimation. In contrast, the TDD strategy involves acquiring a single time sample from the MC-Rx output and applying a thresholding operation to decide the received symbol.

3.4.3 Symbol Detection

The ML estimator introduced in the previous section is asymptotically unbiased and exhibits asymptotic normality. Therefore, the relation $\mathbb{E}[\hat{\boldsymbol{\lambda}}] = \boldsymbol{\lambda}$ holds [342]. The variance of the estimated parameters can be obtained from the diagonal elements of the inverse Fisher Information Matrix (FIM), which is denoted as $\mathbf{F}(\boldsymbol{\lambda})$:

$$\sigma^2_{\hat{\lambda}_i} = (\mathbf{F}(\boldsymbol{\lambda}))^{-1}_{(ii)}, \quad \mathbf{F}(\boldsymbol{\lambda})_{(ij)} = \mathbb{E}\left(\frac{\partial^2 l}{\partial \lambda_i \partial \lambda_j}\right), \tag{3.29}$$

where the expectation is taken with respect to the probability distribution of the observed spectrum $p(Y_1, Y_2, ..., Y_N)$.

By substituting $l = -\ln \mathcal{L}(\boldsymbol{\lambda})$ into (4.9), the FIM can be elaborated as follows:

$$\mathbf{F}_{(ij)} = \mathbb{E}\left(\sum_{k=1}^{N/2-1} \frac{S(f_k) - Y_k}{S^2(f_k)} \frac{\partial^2 S}{\partial \lambda_i \partial \lambda_j} + \frac{2Y_k - S(f_k)}{S^3(f_k)} \frac{\partial S}{\partial \lambda_i} \frac{\partial S}{\partial \lambda_j}\right). \tag{3.30}$$

Given that $S(f)$ is a slowly varying function, it is unnecessary to calculate the individual periodogram values in (3.30), since the periodogram values can be smoothed by summing over frequency, as described by

$$\sum_{n=1}^{N/2-1} Y_k \phi(f_k) \simeq \sum_{n=1}^{N/2-1} S(f_k)\phi(f_k), \tag{3.31}$$

where $\phi(f_k)$ is any smooth function as detailed in [343, 342].

Following (3.31), the FIM defined by (3.30) can be simplified to the following expression

$$\mathbf{F}_{(ij)} \simeq \sum_{k=1}^{N/2-1} \frac{1}{S^2(f_k)} \frac{\partial S}{\partial \lambda_i} \frac{\partial S}{\partial \lambda_j}, \tag{3.32}$$

where the derivatives are evaluated at the true value of the parameters. Additionally, (3.32) can be approximated as an integral, as suggested by [342, 343] as follows:

$$\mathbf{F}_{(ij)} \simeq \frac{N\Delta t}{2} \int_0^{\frac{1}{2\Delta t}} \frac{1}{S^2(f)} \frac{\partial S}{\partial \lambda_i} \frac{\partial S}{\partial \lambda_j} \mathrm{d}f. \tag{3.33}$$

(4.10) is a good approximation when a large number of time samples are taken by the MC-Rx, allowing to approximate the periodogram values as a Gaussian distribution by the Central Limit Theorem [344].

The MC-Rx determines the transmitted bit by applying the ML decision rule to the estimated information molecule concentration, $\hat{c}_m$. Since the MC-Rx lacks knowledge of the interfering molecule concentration, it calculates the bit decision threshold γ_{fd} under the assumption of an interference-free channel. Therefore, the computation of the γ_{fd} decision threshold relies on the following noise PSD model that accounts for only one type of molecule in the channel, i.e., the information molecule:

$$\tilde{S}(f, c_m) = 4N_r\zeta^2 \frac{1}{2\pi f + 1/\tau_m} \tilde{p}_b(1 - \tilde{p}_b) + S_f(f), \tag{3.34}$$

Algorithm 1 Frequency Domain Detection

function FREQUENCYDETECTION($Y[k], N, \Delta t, \gamma_{fd}$)
  Find initial guess: $\boldsymbol{\lambda}^0 \leftarrow [c_m^0, c_i^0]$
  $f_k \leftarrow \frac{k}{N\Delta t}$ for $k = 1, \ldots, N/2 - 1$
  Use Newton's method on WHITTLE($Y[k], f_k, \boldsymbol{\lambda}$) with initial guess $\boldsymbol{\lambda}^0$ to find optimal $\boldsymbol{\lambda}^* = [c_m^*, c_i^*]$.
  $\hat{c}_m \leftarrow c_m^*$
  if $\hat{c}_m > \gamma_{fd}$
    Estimated bit: $\hat{s} \leftarrow 1$
  else
    Estimated bit: $\hat{s} \leftarrow 0$
  end if
  return $\hat{s}$
end function
function WHITTLE($Y[k], f_k, \boldsymbol{\lambda}$)
  $l \leftarrow \sum_{k=1}^{N/2-1} \frac{Y_k}{S(f_k,\boldsymbol{\lambda})} + \ln S(f_k, \boldsymbol{\lambda})$
  return l
end function

where $\tau_m = 1/(c_m k_m^+ + k_m^-)$ and $\tilde{p}_b = \dfrac{c_m}{K_{D_m} + c_m}$. Evaluating (3.32) with the noise PSD model given in (4.11) and considering a single unknown parameter $\boldsymbol{\lambda} = [c_m]$, the variance of the estimated information molecule concentration for the transmitted bit $s \in \{0, 1\}$ is determined as follows [332]:

$$\tilde{\sigma}^2_{\hat{c}_{m|s}} = \frac{1}{\frac{N\Delta t}{2} \int_0^{\frac{1}{2\Delta t}} \frac{1}{\tilde{S}^2(f, c_{m|s})} \left(\frac{\partial \tilde{S}}{\partial c_m} \right)^2 \Big|_{c_m = c_{m|s}} \mathrm{d}f}. \tag{3.35}$$

Note that $\tilde{\sigma}^2_{\hat{c}_{m|s}}$ is not the actual asymptotic variance, as the c_m estimate of MC-Rx is based on the noise PSD model described in (3.24). Using (3.35), the decision threshold for FDD is determined by the following equation:

$$\begin{aligned} \gamma_{fd} = \frac{1}{\tilde{\sigma}^2_{\hat{c}_{m|1}} - \tilde{\sigma}^2_{\hat{c}_{m|0}}} \Bigg(& \tilde{\sigma}^2_{\hat{c}_{m|1}} c_{m|0} - \tilde{\sigma}^2_{\hat{c}_{m|0}} c_{m|1} + \tilde{\sigma}_{\hat{c}_{m|1}} \tilde{\sigma}_{\hat{c}_{m|0}} \\ & \times \sqrt{(c_{m|1} - c_{m|0})^2 + 2(\tilde{\sigma}^2_{\hat{c}_{m|1}} - \tilde{\sigma}^2_{\hat{c}_{m|0}}) \ln\Big(\tilde{\sigma}_{\hat{c}_{m|1}} / \tilde{\sigma}_{\hat{c}_{m|0}} \Big)} \Bigg), \end{aligned} \tag{3.36}$$

where $c_{m|s}$ is the expected value of the estimated information molecule concentration, corresponding to the transmitted bit $s \in \{0, 1\}$.

Algorithm 1 presents the FDD method, detailing the functions used to solve the estimation problem formulated by (3.28) and to detect the transmitted bit. On line 2, the algorithm determines the initial guesses for the concentration values $[c_m^0, c_i^0]$ by sweeping over the range of sparse concentration values and selecting those minimizing the function $\textsc{Whittle}(Y[k], f_k, \boldsymbol{\lambda})$. On line 3 of the algorithm, f_k is assigned to represent the frequencies corresponding to available periodogram values. Line 4 then applies the Newton-Raphson method to solve the estimation problem outlined in (3.28) numerically by using the Whittle likelihood function $\textsc{Whittle}(Y[k], f_k, \boldsymbol{\lambda})$ and the initial guesses for molecule concentrations, denoted as $[c_m^0, c_i^0]$. After determining the optimal parameter set $\boldsymbol{\lambda}^*$, lines 6-11 perform the thresholding operation on the estimated information molecule concentration, $\hat{c}_m$, to decide the transmitted bit.

3.4.4 Asymptotic Bit Error Probability

To calculate the BEP for FDD, we need the actual variance of the estimated concentration of information molecules, denoted as $\sigma^2_{\hat{c}_{m|s}}$. Using the noise PSD model described in (3.24), which takes into account the presence of information and interference molecules in the channel, we can calculate the FIM for the two unknown parameters $\boldsymbol{\lambda} = [c_m, c_i]$ via (3.32). Accordingly, the respective variance for the transmitted bit s is determined from the FIM, denoted as $\mathbf{F}_s$, as follows:

$$\sigma^2_{\hat{c}_{m|s}} = (\mathbf{F}_s(\boldsymbol{\lambda}))^{-1}_{(11)}, \tag{3.37}$$

where $s \in \{0,1\}$ and the elements of the FIM $\mathbf{F}_s$ are

$$\begin{aligned}
&\mathbf{F}_{s(11)} = \\
&\frac{N\Delta t}{2}\int_0^{\frac{1}{2\Delta t}} \frac{1}{S^2(f,(c_{m|s},\mu_{c_i}))}\left(\frac{\partial S}{\partial c_m}\right)^2\Big|_{\substack{c_m=c_{m|s}\\ c_i=\mu_{c_i}}}\mathrm{d}f \\
&\mathbf{F}_{s(22)} = \\
&\frac{N\Delta t}{2}\int_0^{\frac{1}{2\Delta t}} \frac{1}{S^2(f,(c_{m|s},\mu_{c_i}))}\left(\frac{\partial S}{\partial c_i}\right)^2\Big|_{\substack{c_m=c_{m|s}\\ c_i=\mu_{c_i}}}\mathrm{d}f, \\
&\mathbf{F}_{s(12),(21)} = \\
&\frac{N\Delta t}{2}\int_0^{\frac{1}{2\Delta t}} \frac{1}{S^2(f,(c_{m|s},\mu_{c_i}))}\left(\frac{\partial S}{\partial c_m}\right)\left(\frac{\partial S}{\partial c_i}\right)\Big|_{\substack{c_m=c_{m|s}\\ c_i=\mu_{c_i}}}\mathrm{d}f.
\end{aligned} \tag{3.38}$$

As a result, BEP for FDD is obtained as follows:

$$P_e^{FDD} = \frac{1}{4}\,\mathrm{erfc}\left(\frac{\gamma_{fd} - c_{m|0}}{\sqrt{2\sigma^2_{\hat{c}_{m|0}}}}\right) + \frac{1}{4}\,\mathrm{erfc}\left(\frac{c_{m|1} - \gamma_{fd}}{\sqrt{2\sigma^2_{\hat{c}_{m|1}}}}\right). \tag{3.39}$$

Note that (3.39) represents an asymptotic BEP derived under the Gaussian distribution assumption discussed in Sec. 3.4.3.

3.5 Simulation of the System

In this section, we detailed the simulation process used to validate our FDD technique. Specifically, we conducted Monte Carlo simulations to compare the theoretical results obtained by the analytical expressions derived in Sections 3.3 and 3.4 and the results obtained through particle-based stochastic simulations. For the latter, we used Smoldyn [345]. The simulation algorithms were implemented in MATLAB, and parallelized CPU cores were used for reasonable computation times.

3.5.1 Particle-based Stochastic Simulations

We used the open-source particle-based spatial stochastic simulator, *Smoldyn*, to simulate the system. Its capability to capture stochastic events at a molecular

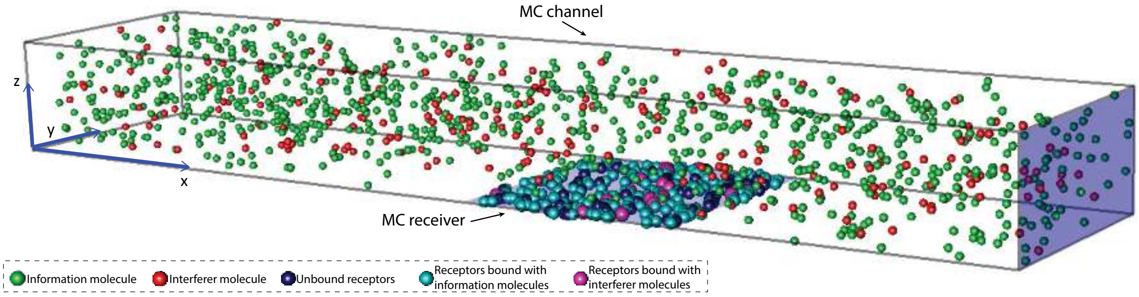

Figure 3.2: Snapshot of the Smoldyn simulation illustrating the MC system. The parameters have been adjusted for illustrative purposes. Thus, this representation is not to scale.

level, such as diffusion and receptor binding/unbinding, fits our purpose [345]. As illustrated in Fig. 3.2, we created a straight microfluidic channel with a rectangular cross-section. The receptors are located in a specific region on the channel bed, indicating the position of the MC-Rx.

3.5.2 Simulation parameters

The simulation time step is an important parameter that affects the accuracy of Smoldyn. Using shorter time steps generally leads to higher accuracy but slower simulations. When choosing the time step, one consideration is to ensure it is significantly shorter than the characteristic time scale of any reaction in the system. For the reactions described by (3.14), the characteristic times or time constants can be obtained from the matrix $\mathbf{\Omega}$ defined by (3.20), as follows:

$$\tau_{c_{1,2}} = -1/\lambda_{c_{1,2}}, \tag{3.40}$$

where $\lambda_{c_{1,2}}$ corresponds to the eigenvalues of $\mathbf{\Omega}$. These time constants only depend on the kinetics of the reactions and the concentrations of the information and interferer molecules. Therefore, given the transmitted bit s, the characteristic times (3.40) can be expanded as

$$\tau_{c_{1,2|s}} = \frac{2}{\left[\frac{1}{\tau_{m|s}} + \frac{1}{\tau_i} \pm \sqrt{\left(\frac{1}{\tau_{m|s}} - \frac{1}{\tau_i}\right)^2 + 4k_m^+ c_{m|s} k_i^+ c_i}\right]}, \tag{3.41}$$

where $\tau_{m|s} = 1/(c_{m|s}k_m^+ + k_m^-), \tau_i = 1/(c_i k_i^+ + k_i^-)$ correspond to the characteristic times of the independent reactions $R + M \underset{k_m^+}{\overset{k_m^-}{\rightleftharpoons}} RM$ and $R + I \underset{k_i^+}{\overset{k_i^-}{\rightleftharpoons}} RI$ respectively.

Considering the system parameters summarized in Table 3.1, we have chosen the simulation time step as $\Delta t_s = 0.0025$ s. This choice represents a good compromise between accuracy and total execution time. Further reducing the time step can significantly increase the simulation time, posing a challenge for repeated experiments.

The noise PSD, given by equations (3.22)-(3.24), can be described as a superposition of Lorentzian spectral profiles. The corner frequencies of these Lorentzian profiles are defined by the characteristic frequencies, which can be expressed in terms of characteristic times as $f_{c_{1,2|s}} = 1/(2\pi\tau_{c_{1,2|s}})$. When these frequencies are not masked, they can be identified by locating the peaks of the noise PSD multiplied by the corresponding frequency, as illustrated in Fig. 3.3a. Since the PSD exhibits a profile defined by its characteristic frequencies, which contain information about the equilibrium concentration of the information molecules within the sampling window, it is crucial to resolve these characteristic frequencies to extract the relevant information accurately. In this regard, the sampling period Δt is a relevant parameter. The maximum observable frequency can be determined by $f_{c_{\max}} = \frac{1}{2\Delta t}$. When a characteristic frequency exceeds this limit, certain portion of the information can be lost.

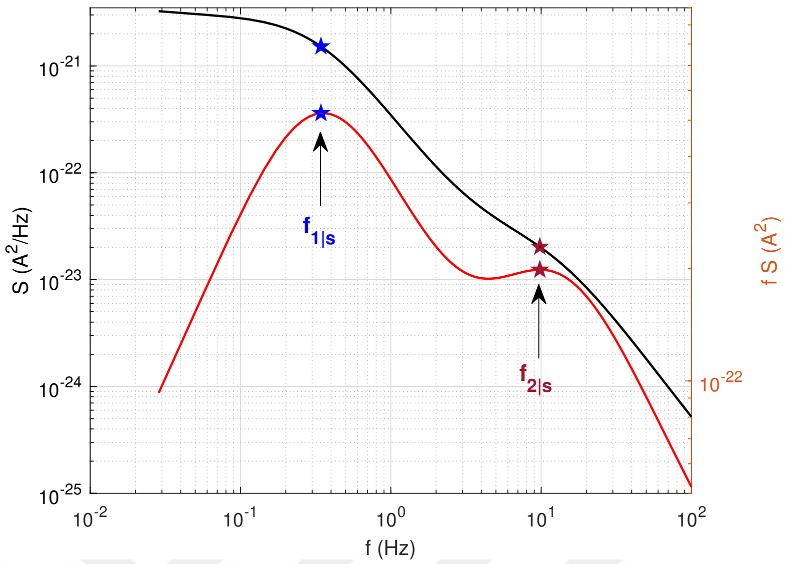

(a)

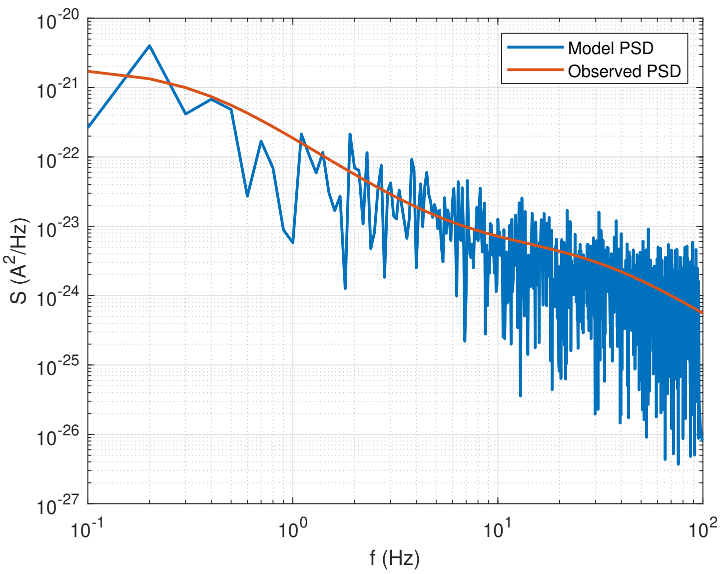

(b)

Figure 3.3: (a) Characteristic frequencies highlighted on the graph of the S multiplied by frequency f, where S is the theoretical PSD of noise. (b) Model PSD generated with estimated molecule concentrations and the observed PSD (periodogram) generated with the Smoldyn data.

Algorithm 2 Monte Carlo Simulation

Initialize: TDD error $e_t \leftarrow 0$, FDD error $e_f \leftarrow 0$

Generate a *bitstream* consisting of K bits

Find decision threshold for TDD γ_{td}

Find decision threshold for FDD γ_{fd}

for each bit s in *bitstream* **do**

  Compute information concentrations $c_{m|s}$ with (4.2)

  Generate interferer concentration $c_i \sim \log \mathcal{N}(\mu_{c_i}, \sigma_{c_i}^2)$

  Run Smoldyn. Wait until equilibrium.

  Record N samples from the number of bound receptors $n_B[k]$ for $k = 1, \ldots, N$ with sampling period Δt

  Generate $1/f$ noise samples in the time domain $n_{1/f}[k]$ for $k = 1, \ldots, N$

  Convert to electrical output $I_b[k] \leftarrow n_{1/f}[k] + \zeta n_B[k]$ for $k = 1, \ldots, N$

  Take one sample, denoted as ΔI, from $I_b[k]$

  $\hat{s}_t \leftarrow \textsc{TimeDetection}(\gamma_{td}, \Delta I)$

  If $\hat{s}_t \neq s$, increment e_t by 1.

  Isolate the noise, denoted as $\Delta I_b[k]$, from $I_b[k]$

  Apply low pass filter to $\Delta I_b[k]$ to obtain $\Delta I_{b_f}[k]$

  Compute the periodogram $Y[m]$ for $\Delta I_{b_f}[k]$, for $m = 1, \ldots, \frac{N}{2} - 1$ and sampling period Δt

  $\hat{s_f} \leftarrow \textsc{FrequencyDetection}(Y[m], N, \Delta t, \gamma_{fd})$

  If $\hat{s_f} \neq s$, increment e_f by 1.

end for

Compute BEP for TDD: $P_e^{TDD} \leftarrow e_t/K$

Compute BEP for FDD: $P_e^{FDD} \leftarrow e_f/K$

function $\textsc{TimeDetection}(\gamma_{td}, \Delta I)$

  if $\Delta I > \gamma_{td}$

    Estimated bit: $\hat{s} \leftarrow 1$

  else

    Estimated bit: $\hat{s} \leftarrow 0$

  end if

  return $\hat{s}$

end function

3.5.3 Monte Carlo Simulation

The Monte Carlo algorithm used to validate the BEP performance of FDD is described in Algorithm 2. In each iteration (line 6-19), representing the transmission of a random bit s in the microfluidic channel, the procedure is as follows.

Based on the equilibrium assumption explained in Sec. 3.2, the information molecule concentration $c_{m|s}$ and interferer concentration c_i are assumed to remain constant within the sampling window. Therefore, the information concentration $c_{m|s}$ corresponding the generated bit s and the interferer concentration c_i generated from a log-normal distribution represent the concentrations at the sampling time. In Smoldyn simulations, interference molecules are initially placed uniformly randomly throughout the microfluidic channel at a given concentration c_i. With the initial concentration values, the Smoldyn simulation is run for a time duration sufficient for the binding reactions to reach equilibrium. Once equilibrium is attained, time samples are taken from the output of the Smoldyn simulation (line 9), where the output corresponds to the number of bound receptors. The collected time samples of number of bound receptors are then scaled and combined with 1/f noise to simulate the transduction process of the bioFET, resulting in the electrical output denoted as $I_b[k]$.

To simulate the 1/f noise in the time domain, we employed the FIR filtering method described in [346], which involves filtering white Gaussian noise in the frequency domain using an FIR filter with a 1/f passband and subsequently performing an inverse Fourier transform to obtain the 1/f noise sequence. The approximate noise variance σ_f^2 is computed based on the expression given in Equation (3.9), with the parameter values specified in Table 3.1.

As stated in line 12, a single sample is taken from the middle of the electrical output $I_b[k]$ for TDD. For FDD, the base signal is removed from the electrical output $I_b[k]$ to isolate the noise component, $\Delta I_b[k]$. Additionally, considering that samples are taken within a finite sampling window, distortions near the Nyquist frequency in the PSD are inevitable due to the aliasing. Therefore, a low-pass filter with a passband near the Nyquist frequency is applied to the sampled noise to mitigate this distortion, as outlined in line 16. This filtering step helps reduce outliers that could affect the accuracy of the MLE. Then, periodogram PSD is computed using an N-point FFT of the filtered noise samples. No further processing is performed on the noise signal or the estimated PSD before the MLE to avoid introducing statistical distortion, which can result in erroneous parameter predictions. Finally, the MLE is performed by MATLAB's *fminunc* solver [347], which uses the quasi-Newton algorithm. The solver can find the solution within a few iterations in this specific scenario. Finally, BEP for TDD and FDD are computed as described by line 20-21.

Fig. 3.3b depicts the model noise PSD generated using the MLE estimated information and interferer concentration pair, $[\hat{c}_{m|s}, \hat{c}_i]$, and the periodogram estimate of the observed noise PSD obtained by using the data from the Smoldyn.

3.6 Performance Evaluation

In this section, we analyze the performance of FDD and TDD in terms of BEP. The default values of the system parameters are given in Table 3.1, with the reaction rates adopted from [332]. Unless stated otherwise, the default parameter values are used in the rest of the chapter.

It can be observed that the simulation results can deviate from the theoretical results due to the inherent nature of Monte Carlo simulations. Especially when dealing with stochastic concentration values, Monte Carlo simulations can require a large number of iterations to converge, potentially leading to excessive simulation times when using Smoldyn. Therefore, to maintain a compromise between convergence and simulation times, we chose moderate number of iterations (1000) for the Monte Carlo simulations.

Table 3.1: Default Values of System Parameters

Temperature (T)	300K
Microfluidic channel height (h_{ch}), width (l_{ch})	5 μm, 10 μm
Average flow velocity (u)	10 μm/s
Distance of Rx's center position to Tx (x_R)	1mm
Ionic concentration of medium (c_{ion})	30 mol/m^3
Relative permittivity of medium (ϵ/ϵ_0)	80
Intrinsic diffusion coefficient (D_0)	2×10^{-11} m^2/s
Binding rate of information and interferer molecules (k_m^+, k_i^+)	4×10^{-17} m^3/s
Unbinding rate of information molecules (k_m^-)	2 s^{-1}
Unbinding rate of interferers (k_i^-)	8 s^{-1}
Average # of electrons in a ligand (N_{e^-})	3
Number of independent receptors (N_r)	120
Length of a surface receptor (r)	2 nm
Transconductance of graphene bioFET (g)	1.9044×10^{-4} A/V
Width of graphene in transistor (l_{gr})	10μm
Quant. capacitance of graphene per unit area (c_q)	2×10^{-2} F m^{-2}
# of transmitted ligands for $s = 0, 1$ ($N_{m\|s}$)	$[1, 5] \times 10^3$
# of noise samples (N)	700
Sampling period (Δt)	0.005 s
Mean interference to information concentration ratio ($\gamma = \mu_{c_i}/c_{m\|s=1}$)	0.7
Interference mean/std ratio (μ_{c_i}/σ_{c_i})	10
Power of $1/f$ noise at 1 Hz ($S_{f_{1Hz}}$)	10^{-23} A^2/Hz
Noise exponent for 1/f noise (β)	1
Lower frequency limit for 1/f noise (f_L)	10^{-8}
Upper frequency limit for 1/f noise (f_H)	10^7

3.6.1 Effect of Interference on BEP

In the initial analysis, we examine the impact of interference strength on the BEP performance of both TDD and FDD. To investigate this, we introduce a tuning parameter γ, which determines the mean interferer concentration μ_{c_i} as $\mu_{c_i} = \gamma \cdot c_{m|s=1}$. The results, as depicted in Fig. 3.4a, show that FDD outperforms TDD, except in

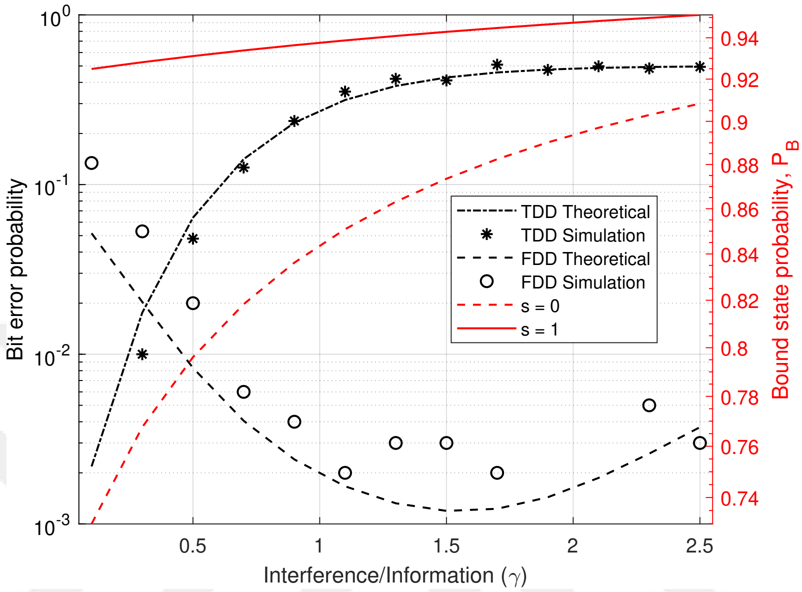

(a)

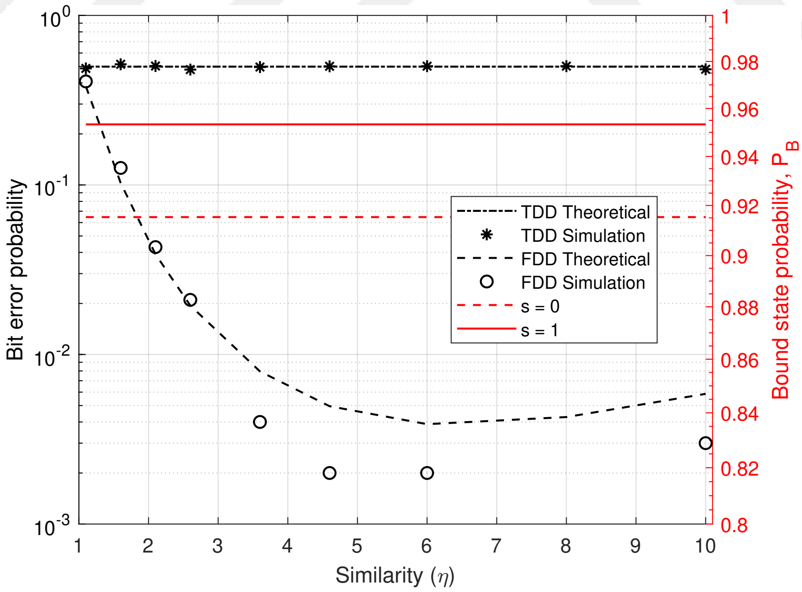

(b)

Figure 3.4: BEP for varying (a) information to interference ratio γ and (b) similarity η.

cases where the interferer concentration is significantly lower than the concentration of information molecules as shown in Fig. 3.4a. As the interferer concentration increases, the performance of TDD deteriorates. This degradation occurs because the increasing number of bound receptors becomes occupied by the interfering molecules, leading to saturation of the receiver, thereby causing increase in the error probability. On the other hand, the performance of FDD improves with increasing interferer concentration up to a certain point, after which it starts to degrade. Considering that the characteristic frequencies are influenced by both the concentration and affinities of the molecules, the effect of interference is initially indistinguishable in the PSD. This is because the concentration of interfering molecules is initially lower, which results in the individual Lorentzian PSD attributed to interfering molecules being overshadowed by that of the information-carrying molecules. However, as the concentration of interfering molecules increases, its impact on the combined PSD becomes more pronounced, allowing for a more accurate estimation of concentrations and, consequently, reduced error probabilities. Nevertheless, beyond a particular concentration of interfering molecules, the Lorentzian PSD attributed to the information-carrying molecules is overshadowed, increasing error probabilities.

3.6.2 Effect of Similarity on BEP

We also consider the effect of the affinity ratio between the information and interferer molecules, which we refer as the similarity parameter and define as $\eta = \frac{K_{D_i}}{K_{D_m}}$. To observe the direct effect of the similarity, we keep the bound state probabilities constant by scaling the mean interferer concentration, μ_{c_i}, by η. As expected, TDD is not affected by the similarity parameter, as shown in Figure 3.4b. This occurs because the TDD method relies on the total bound state probability p_{b_s}, which remains constant in this case, thereby not affected by changes in similarity. On the other hand, BEP for FDD exhibits an interesting behavior. BEP improves as the similarity parameter η increases, indicating that the information and interfering molecules become dissimilar. However, beyond a specific value of the similarity parameter, BEP starts to degrade. This trend can be explained as follows: When the similarity parameter η is low, indicating high similarity between the information and interfering molecules, FDD cannot distinguish between these two types of molecules based on their affinities. This is because any noticeable distinction is not reflected in the spectrum. For example, when the similarity parameter η is close to 1, the noise PSD appears as a single Lorentzian profile, thereby obscuring the Lorentzian profile associated with the reaction $R+M \underset{k_m^+}{\overset{k_m^-}{\rightleftharpoons}} RM$ in the spectrum. As the similarity increases, it becomes more visible that PSD is the superposition of two Lorentzian profiles, and the characteristic frequencies $f_{c_{1|s}}$ and $f_{c_{2|s}}$ are more distinguishable. However, once the similarity goes beyond the point where $f_{c_{1|s}}$ and $f_{c_{2|s}}$ are most distinguishable, the PSD becomes less informative about the concentration of information $c_{m|s}$. This occurs because interference becomes the dominant factor on the profile of the PSD, and the variations in $c_{m|s}$ have a lesser impact on the PSD. As a result, the PSD becomes less informative about the information concentration, $c_{m|s}$, increasing the error probability.

3.6.3 Effect of Number of Samples on BEP

The BEP performance is further analyzed for the number of time samples N. As depicted in Fig. 3.5a, it is observed that the performance of FDD improves as the number of samples increases. This outcome aligns with expectations, as a larger number of samples leads to a decrease in the variance of the estimated information molecule concentration, $\sigma^2_{\hat{c}_{m|s}}$. The reduction in variance results in more accurate estimation as the error on the estimated parameter follows $\sigma_{\hat{c}_{m|s}} \propto \sqrt{(\mathbf{F}_s)^{-1}_{(11)}/N}$. Consequently, more samples lead to a decrease in the BEP. On the other hand, the performance of TDD remains unaffected by the number of samples, as the receiver only takes one sample, typically from the middle of the signal within the sampling window.

3.6.4 Effect of 1/f Noise on BEP

We also simulated the BEP performance of FDD and TDD under varying $1/f$ noise power (at 1 Hz), as depicted in Fig. 3.5b. To better observe the performance trend,

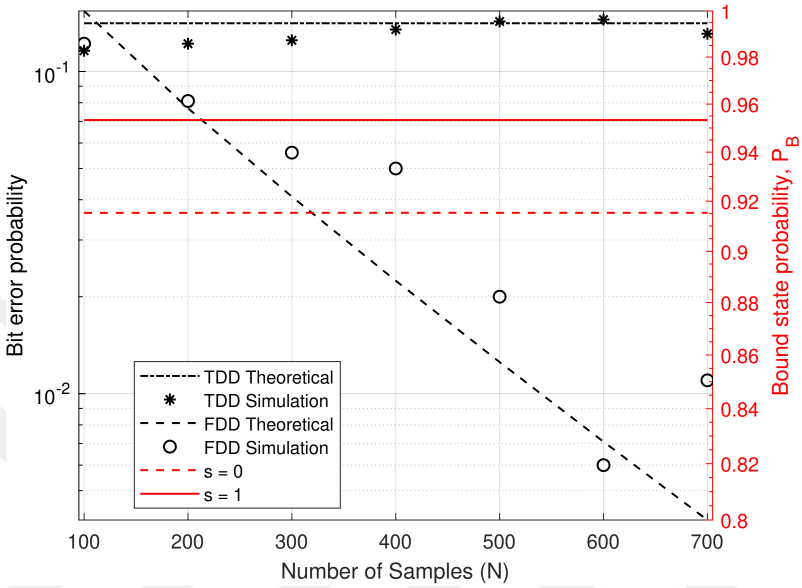

(a)

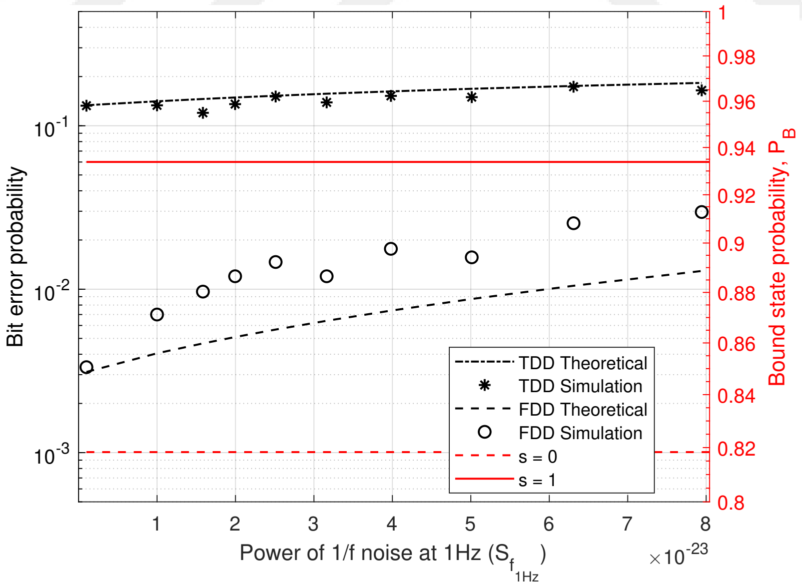

(b)

Figure 3.5: BEP for varying (a) number of samples (b) power of 1/f noise at 1 Hz.

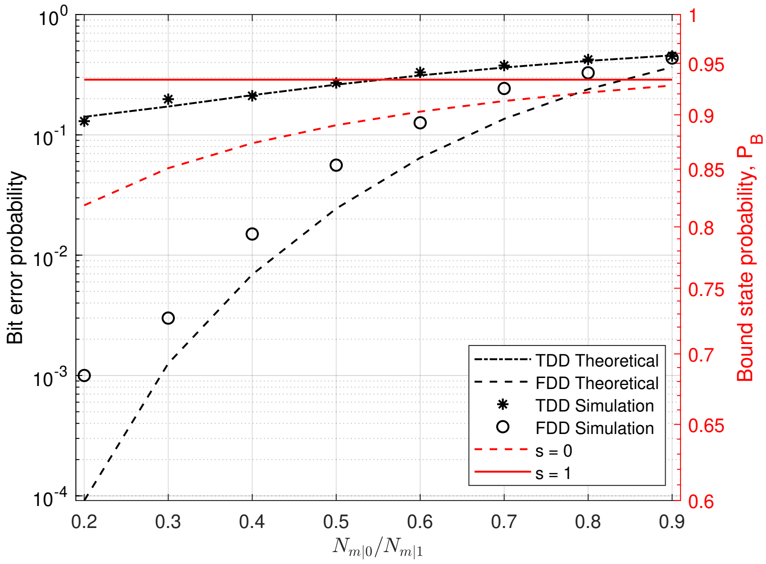

(a)

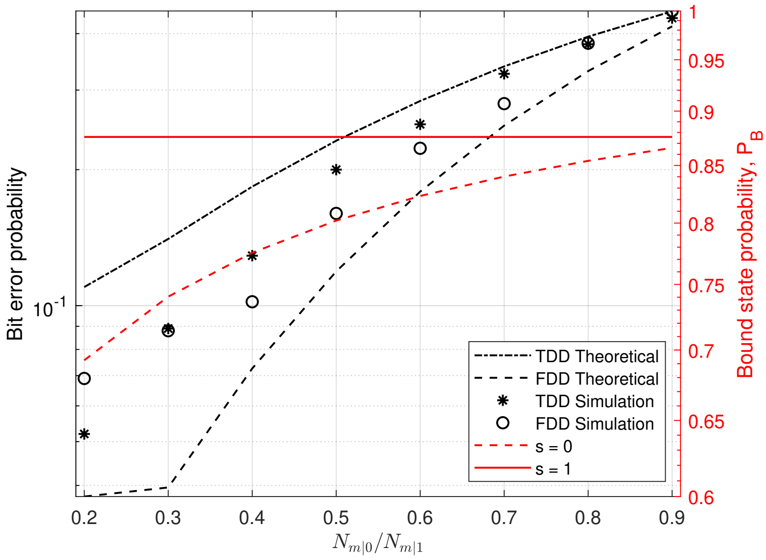

(b)

Figure 3.6: BEP for varying bit-0/bit-1 concentration ratio when the MC-Rx is (a) near saturation, and (b) in a non-saturation state.

a similarity value of $\eta = 3$ is chosen for this case. The results show that 1/f noise affects the performance of both TDD and FDD. Additionally, it can be observed that the performance of FDD is more sensitive to changes in the 1/f noise levels compared to TDD. Since 1/f noise is directly additive across the entire spectrum, increasing the 1/f noise level reduces the FDD performance by potentially masking critical frequencies under the background 1/f noise.

3.6.5 Effect of Bit-0/Bit-1 Concentration Ratio on BEP

We further explored the impact of the ratio of concentrations for bit-0 and bit-1, denoted as $N_{m|0}/N_{m|1}$, on the BEP. As depicted in Fig. 3.6a, it becomes apparent that the detection performances of both TDD and FDD methods experience a decline when the concentration values become closer.

In Fig.3.6a, the MC-Rx is observed in near saturation, implying a high level of receptor occupancy. Comparing the performance in Fig.3.6a with the result shown in Fig.3.6b, which corresponds to a case of lower bound state probabilities, a noticeable performance decline can be observed in the latter.

These results suggest that the FDD method is more effective when the receptor occupancy at the MC-Rx is higher. This property could be advantageous, as it aligns more closely with the typical conditions encountered in MC, wherein the receiver is commonly expected to operate near saturation most of the time due to the remaining molecules from previous transmissions or interferers.

3.6.6 Effect of Transmitter-Receiver Distance on BEP

As the distance between the MC-Tx and the MC-Rx ($d = x_R$) varies, the BEP performance of FDD and TDD exhibit different behaviors, as shown in Fig. 3.7a. Increasing the value of d from 0.5 mm to 3 mm leads to a significant degradation in the BEP performance of the FDD and a slight improvement in that of the TDD. These trends are related to the varying concentration of information molecules at the MC-Rx's location. At small distances, information molecule concentration is significantly higher but decreases as the distance increases, following an attenuation proportional to $\sqrt{d}$ [249]. As the information molecule concentration at the location of the MC-Rx is getting lower with the distance, the Lorentzian noise PSD profile associated with information molecules can become obscured under the influence of interference molecules or 1/f noise. This effect is the cause of the observed degradation in the BEP of FDD, as we also discussed while analyzing the effect of interference.

In contrast, TDD's performance shows a marginal improvement at longer distances. At small distances, the MC-Rx is prone to saturation due to high ligand concentrations, which reduces its sensitivity to varying information molecule concentration levels corresponding to different symbols, thus reducing its ability to distinguish distinct symbols with TDD. Therefore, increasing the distance improves the performance of TDD when the MC-Rx is saturated or near saturation.

3.6.7 Effect of Surface Receptor Length on BEP

The surface receptor length, represented as r, is an important parameter affecting the sensitivity of a bioFET-based MC-Rx [249]. Therefore, we investigated the effect of r on the BEP performance of FDD and TDD given a Debye length (λ_D) of 1.77 nm, corresponding to the default system parameters in Table 3.1. When r exceeds λ_D, the sensitivity of the MC-Rx to ligands decreases exponentially due to the screening effect, weakening the response as this effect strengthens. As shown in Fig. 3.7b, the BEP performance for both FDD and TDD deteriorates as r increases from 1 nm to 9 nm (corresponding to $\sim 3-26$ nucleobases in a single stranded DNA receptor). While FDD improves the detection sensitivity compared to TDD, for example, when the MC-Rx is saturated and less sensitive to ligand concentration changes, characteristic frequencies containing concentration information can still be recognized in the noise spectra [348]. However, the results also show that beyond $r = 3$ nm, there is a significant decrease in the BEP values for both methods. Therefore, choosing a surface receptor length comparable to the Debye length is essential for optimal MC-Rx design.

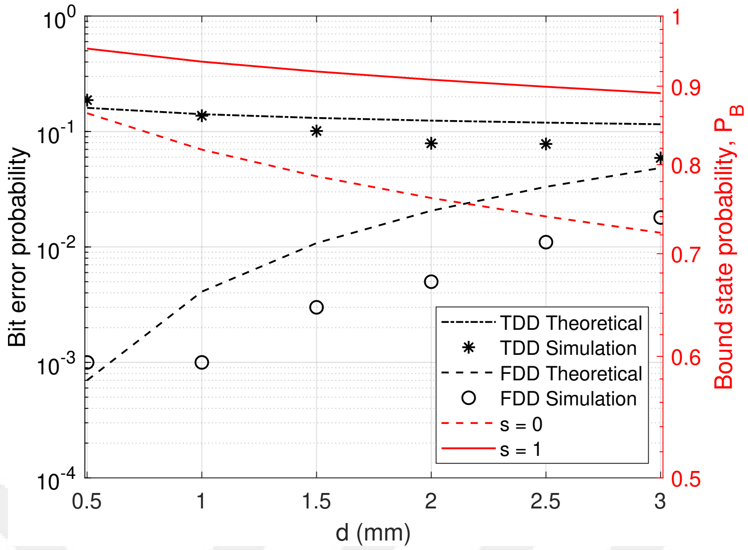

(a)

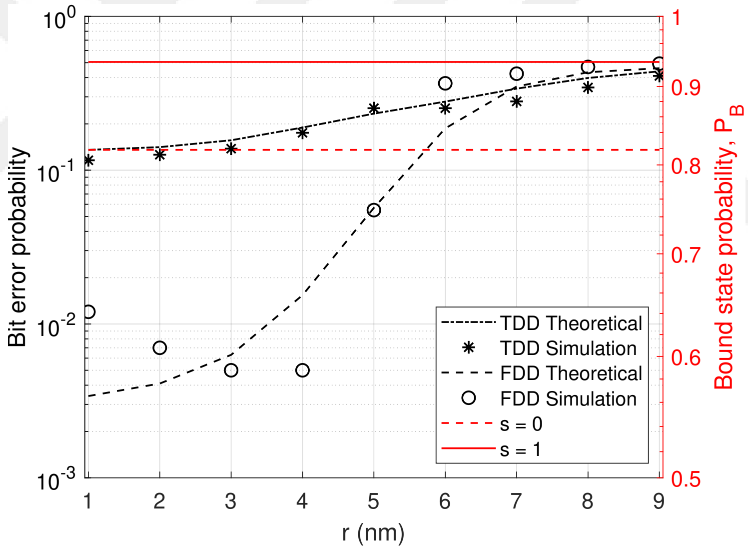

(b)

Figure 3.7: BEP for varying (a) transmitter-receiver distance d and (b) receptor length r.

3.6.8 Effect of Multiple Types of Interferers on BEP

We further analyze the BEP performance under varying receptor-ligand affinities in the scenario involving multiple interfering molecules that can interact with MC-Rx receptors. For this analysis, we employed the generalized binding noise PSD model, as detailed in Sec. 3.7. The scenario considered includes three distinct types of ligands: information molecules (L_1) and two types of interference molecules (L_2, L_3). In our simulations, both types of interferers had equilibrium concentrations sampled from independent lognormal distributions with means equal to ($\gamma \cdot c_{1|s=1}$), each having the same mean-to-standard deviation ratio. Here, $c_{1|s=1}$ represents the concentration of information molecules given the transmitted bit is $s = 1$. The interference to information concentration ratio (γ), the concentration of information molecules for bits $s = 0$ and $s = 1$, and the mean/std ratio for the lognormal distributions were set according to the default values in Table 3.1. Additionally, the binding rates for all ligand types were set to the default values given in Table 3.1. The unbinding rates were determined by the following relation: $k_2^- = \nu \cdot k_1^-$ and $k_3^- = \nu \cdot k_2^-$, where k_1^-, k_2^-, and k_3^- are the unbinding rates for the ligand types L_1, L_2, and L_3, respectively, and ν is the selectivity factor defined for modulating the receptor selectivity to different type of ligands.

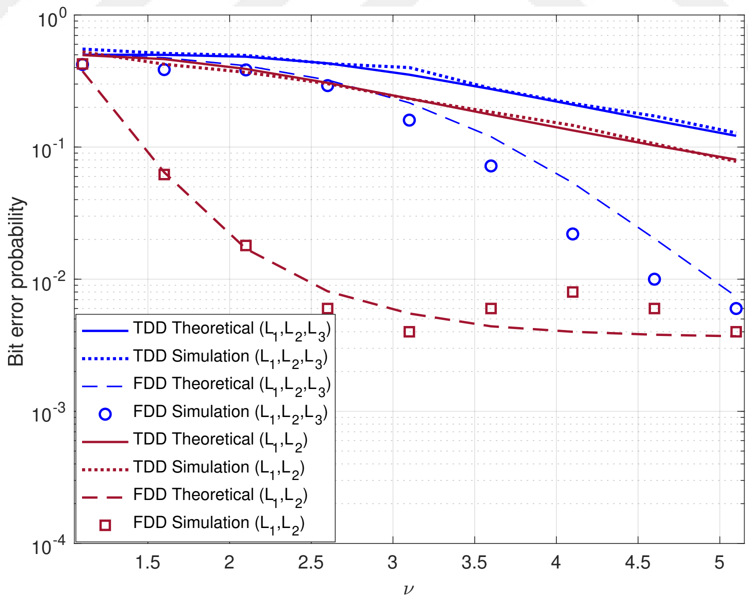

Figure 3.8: BEP performance under different ligand-receptor affinities, modulated by the factor ν, in scenarios involving (i) a single interferer type (L_2) and (ii) multiple interferer types (L_2, L_3) in the channel.

As shown in Fig. 3.8, FDD exhibits poorer BEP performance with multiple interferers compared to the case of a single interferer. The interfering ligand L_3 exhibits lower binding affinities than the information-carrying ligand L_1 and the interfering ligand L_2, which becomes more pronounced as ν increases. With increasing ν, which indicates increasing dissimilarity, the second interfering molecules L_3 are less likely to bind to receptors, and their influence on the spectra diminishes. As a result, the multi-interferer scenario resembles the single-interferer case, as clear from the results.

Regarding TDD, it clearly performs worse in the multi-interferer scenario than in the single-interferer case. TDD is non-selective regarding interferer types. Adding another type of interferer leads to an overall increase in interferer concentration in the channel, which deteriorates the detection performance compared to the single interferer scenario, where the overall interferer concentration is lower. On the other hand, the performance of TDD generally improves with increasing ν. As ν increases, the receptors are less likely to be occupied by interferers since a higher ν value indicates a lower binding affinity between the interferer molecule and the receptor.

3.7 Conclusion

We introduced a frequency-domain detection method for bioFET-based MC receiver architectures. The method exploits receptor cross-reactivity towards various ligand types and utilizes the output noise PSD for detecting the transmitted bits. Considering a microfluidic channel with stochastic molecular interference, we derived BEP for frequency-domain and one-shot time-domain detection methods. Through particle-based spatial stochastic simulations, we validated our theoretical BEP derivations. Our analysis revealed that the proposed frequency-domain detection method provides a significant performance improvement over the time-domain detection method, particularly under high interference conditions in the MC channel. The effectiveness of frequency domain detection is particularly relevant in practical MC scenarios where receivers operate close to saturation due to accumulating residual molecules from previous transmissions or cross-talk.

General Model of Binding Noise PSD

For the scenarios where the channel contains $M-1$ distinct ligand types $\{L_1, ..., L_{M-1}\}$ reacting with MC-Rx receptors, the binding noise model can be extended as detailed in [333]. In such a case, M potential states exist and $M-1$ possible reactions occur as described by the reaction model:

$$R + L_j \underset{k_j^-}{\overset{k_j^+}{\rightleftharpoons}} RL_j, \tag{3.42}$$

where k_j^+ is the binding rate and k_j^- is the unbinding rate for the jth ligand type, where $j \in \{1, ..., M-1\}$.

The chemical master equations for the system in matrix form are expressed as:

$$\frac{\mathrm{d}\mathbf{p}(t)}{\mathrm{d}t} = \mathbf{G}\mathbf{p}(t), \tag{3.43}$$

where $\mathbf{p}(t)$ is the vector containing state probabilities, defined as

$$\mathbf{p}(t) = \begin{pmatrix} p_{RL_1}(t) \\ p_{RL_2}(t) \\ \vdots \\ p_{RL_{M-1}}(t) \\ p_R(t) \end{pmatrix}$$

and the matrix $\mathbf{G}$ is

$$\mathbf{G} = \begin{bmatrix} -k_1^- & 0 & \cdots & 0 & 0 & k_1^+ c_1 \\ 0 & -k_2^- & \cdots & 0 & 0 & k_2^+ c_2 \\ \vdots & \vdots & \ddots & \vdots & \vdots & \vdots \\ 0 & 0 & \cdots & -k_{M-2}^- & 0 & k_{M-2}^+ c_{M-2} \\ 0 & 0 & \cdots & 0 & -k_{M-1}^- & k_{M-1}^+ c_{M-1} \\ k_1^- & k_2^- & \cdots & k_{M-2}^- & k_{M-1}^- & -\sum_{l=1}^{M-1} k_l^+ c_l \end{bmatrix},$$

where c_j is the concentration of the jth ligand type. The equilibrium state probabilities can be expressed as

$$p^0_{RL_j} = \frac{\frac{c_j}{K_{D_j}}}{1 + \sum_{l=1}^{M-1} \frac{c_l}{K_{D_l}}} \quad \text{for} \quad j = 1, \dots, M-1, \tag{3.44}$$

and $p^0_R = 1 - \sum_{l=1}^{M-1} p^0_{RL_l}$, where $K_{D_j} = \frac{k_j^-}{k_j^+}$ is the dissociation constant for the jth ligand type. The state probabilities are defined in relation to equilibrium probabilities and the fluctuations around these equilibrium probabilities as follows [333]:

$$p_{RL_j}(t) = p^0_{RL_j} + \Delta p_{RL_j}(t), \quad j = 1, ..., M-1 \tag{3.45}$$

Therefore, (4.4) can be reformulated as

$$\frac{\mathrm{d}\Delta\mathbf{p}'(t)}{\mathrm{d}t} = \mathbf{\Omega}\Delta\mathbf{p}'(t), \tag{3.46}$$

where $\Delta\mathbf{p}'(t)$ is a column vector comprising the state fluctuations for all states except the last one. The matrix $\mathbf{\Omega}$ is defined as $\mathbf{\Omega} = \mathbf{TGR}$, with the matrices $\mathbf{T}$ and $\mathbf{R}$ being defined as follows [333]:

$$\mathbf{T} = \begin{bmatrix} 1 & 0 & \cdots & 0 & 0 \\ 0 & 1 & \cdots & 0 & 0 \\ \vdots & \vdots & \ddots & \vdots & \vdots \\ 0 & 0 & \cdots & 1 & 0 \end{bmatrix} \quad \mathbf{R} = \begin{bmatrix} 1 & 0 & \cdots & 0 \\ 0 & 1 & \cdots & 0 \\ \vdots & \vdots & \ddots & \vdots \\ 0 & 0 & \cdots & 1 \\ -1 & -1 & \cdots & -1 \end{bmatrix}.$$

The binding noise PSD is then given as [333]:

$$S_b(f) = 4N_r \left(\frac{q_{eff}g}{C_G}\right)^2 \mathbf{z}^T\mathbf{R}\mathbf{\Gamma}\left(\mathrm{Re}\{(j2\pi f\mathbf{I} - \mathbf{\Omega})^{-1}\}\right)^T \mathbf{R}^T\mathbf{z}. \tag{3.47}$$

where $\mathbf{I}$ is $(M-1)$ by $(M-1)$ identity matrix, and the matrix $\mathbf{\Gamma}$ is defined as $\mathbf{\Gamma} = \mathbb{E}[\mathbf{\Delta p}'(0)\mathbf{\Delta p}'^{\mathrm{T}}(0)]$.

Chapter 4

PERFORMANCE ANALYSIS OF MOLECULAR COMMUNICATION WITH CROSS-REACTIVE RECEPTORS

4.1 Introduction

Molecular Communications (MC) is founded on encoding and transmitting information via molecules, mirroring the communication systems observed in biological cells. MC is a promising approach to realizing the Internet of Bio-Nano Things (IoBNT). This transformative networking framework combines biological entities and artificial micro/nano-scale devices, known as Bio-Nano Things (BNTs), also integrated with conventional communication networks to enable innovative biomedical and environmental applications.

Unlike conventional electromagnetic communication methods, MC necessitates specialized transceiver designs and new modulation, coding, and detection approaches tailored to the dynamic and complex nature of biochemical environments. Initial MC research predominantly focused on passive receiver architectures. While more straightforward to model, these architectures were limited in practical application due to their lack of direct interaction with the MC channel. Recent trends in MC research have shifted toward developing more practical MC receivers (MC-Rxs), such as those that incorporate ligand receptors on their surfaces. These receptors act as selective bio-recognition elements, reflecting the communication and sensing mechanisms of biological cells. A significant development in this area is the introduction of biosensor field-effect transistors (bioFETs), which convert ligand-receptor interactions into electrical signals for information decoding.

Ligand-receptor interactions, essential for natural cell sensing and communication functions, are not perfectly selective. This imperfect selectivity, known as LR promiscuity, leads to cross-talk with non-target molecules. Natural cells mitigate this cross-talk through various intracellular mechanisms. In contrast, abiotic MC-Rxs using ligand receptors face similar challenges, highlighting the need for effective detection methods. In the previous chapter, a novel frequency-domain detection (FDD) to tackle the background interference challenge has been introduced. This method enables distinguishing different ligand types in biosensor-based MC-Rxs with cross-reactive receptors. This chapter aims to extend the performance analysis to the symbol error probability (SEP) and channel capacity in MC systems using bioFET-based receivers with cross-reactive receptors. This analysis explores the impact of different system parameters on SEP and channel capacity, improving our understanding of the potential and limitations of biosensor-based MC-Rxs in practical applications.

The rest of the chapter is organized as follows. Section 4.2 provides an overview of the system model, while Section 4.3 include the derivation and the analysis of SEP for FDD. Next, Section 4.4 involves the analysis of the end to end MC channel with respect to different parameters including background noise level and the similarity in the affinities of the ligands. Finally, Section 4.5 summarizes our conclusions.

4.2 System Model

We consider an MC system comprising an MC Transmitter (MC-Tx), an MC Receiver (MC-Rx), and a three-dimensional microfluidic channel with a rectangular cross-section, where molecules experience diffusion and flow. The MC-Tx is situated at the channel inlet (at $x = 0$), while the MC-Rx is located on the channel floor, centered at $x = x_R$.

The system operates under the following assumptions, unless specified otherwise: The MC-Tx employs M-ary Concentration Shift Keying (M-CSK) modulation for information encoding, releasing a specific number of information molecules, denoted as N_m for each symbol m, where $m \in \{0, ..., M-1\}$, at the start of each signaling interval of duration T_s. Molecule release by the MC-Tx is instantaneous and uniform across the channel cross-section, and molecules propagate via unidirectional fluid flow along the x axis. The signaling interval T_s is sufficiently long to minimize Inter-Symbol Interference (ISI).

The MC-Rx incorporates a graphene bioFET architecture, as depicted in Fig. 4.1. This design features a graphene transducer channel, uniformly functionalized with receptors that reversibly bind to specific targets, enabling continuous and label-free sensing [4]. The MC-Rx has the knowledge of the number of information molecules transmitted corresponding to each symbol m, N_m, and the binding/unbinding rates of ligands. It employs a frequency-domain detection method for decoding symbols.

4.2.1 Channel Model

In the microfluidic channel, the transport of ligands is governed by advection-diffusion mechanisms. Given that information molecules are released instantaneously from the MC-Tx, and assuming the impact of ligand-receptor reactions on the overall ligand concentration within the channel is minimal, the spatial and temporal distribution of ligand concentration can be modeled as described in the following equation [335]:

$$c_m(x,t) = \frac{N_m}{A_{ch}\sqrt{4\pi D t}} \exp\left(-\frac{(x-ut)^2}{4Dt}\right), \tag{4.1}$$

where $A_{ch} = h_{ch} w_{ch}$ is the channel cross-sectional area, with h_{ch} being the channel height and w_{ch} as the channel width. The constant fluid flow velocity along the x-axis is denoted by u and D stands for the effective diffusion coefficient.

The peak concentration of the ligand reaches the central position of the MC-Rx, denoted as x_R, at time t_p, which is calculated as $t_p = \frac{x_R}{u}$. The advection-diffusion process imparts a low-pass filter effect on the MC channel, resulting in a slowly variation ligand concentration at the Rx's location. Consequently, Ligand-Receptor (LR) reactions are able to attain equilibrium rapidly within a short time frame around t_p [336, 335]. During this period, the MC-Rx samples the received signal to be used in decoding the transmitted symbol. The expression for the ligand concentration in this sampling interval is as follows:

$$c_m(x_R, t_p) = \frac{N_m}{A_{ch}\sqrt{4\pi D t_p}}. \tag{4.2}$$

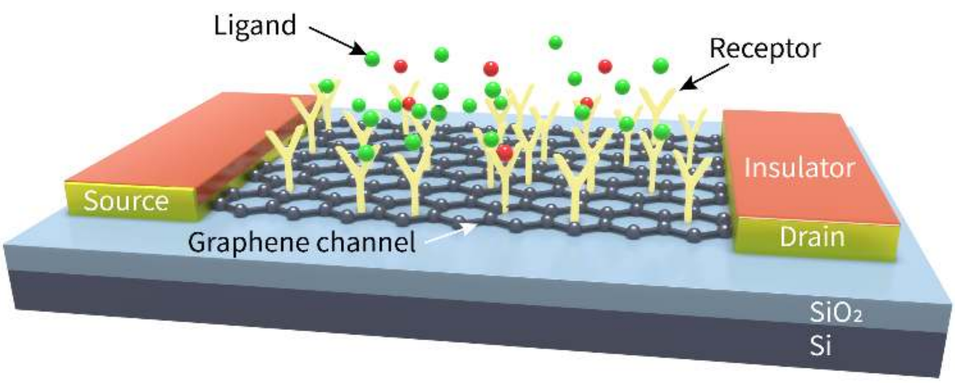

Figure 4.1: A detailed view of the graphene bioFET-based MC-Rx exposed to ligands.

4.2.2 Reception Model

The MC-Rx employs the FDD method relying on the noise PSD of its electrical output. This output noise includes both binding noise and the inherent $1/f$ noise. Specifically, FDD compares the theoretical noise PSD with the observed PSD, where the latter is derived from the periodogram based on time-domain samples of the MC-Rx's output current. The general model for the binding noise PSD is outlined as follows:

Considering $\Lambda - 1$ distinct types of ligands $\{L_1, ..., L_{\Lambda-1}\}$ that interact with the receptors of the MC-Rx, the binding noise model can be characterized as detailed in [333]. In this scenario, there are Λ potential states, each associated with a state probability $p_j(t)$. Furthermore, $\Lambda - 1$ possible reactions take place, which are described by the following reaction model:

$$R + L_j \underset{k_j^-}{\overset{k_j^+}{\rightleftharpoons}} RL_j, \tag{4.3}$$

where k_j^+ is the binding rate and k_j^- is the unbinding rate for the jth ligand type, where $j \in \{1, ..., \Lambda - 1\}$.

The chemical master equations for the system in matrix form are expressed as:

$$\frac{\mathrm{d}\mathbf{p}(t)}{\mathrm{d}t} = \mathbf{G}\mathbf{p}(t), \tag{4.4}$$

where $\mathbf{p}(t)$ is the vector containing state probabilities, $p_j(t)$. The matrix $\mathbf{G}$ is

$$\mathbf{G} = \begin{bmatrix} -k_1^- & 0 & \cdots & 0 & 0 & k_1^+ c_1 \\ 0 & -k_2^- & \cdots & 0 & 0 & k_2^+ c_2 \\ \vdots & \vdots & \ddots & \vdots & \vdots & \vdots \\ 0 & 0 & \cdots & -k_{\Lambda-2}^- & 0 & k_{\Lambda-2}^+ c_{\Lambda-2} \\ 0 & 0 & \cdots & 0 & -k_{\Lambda-1}^- & k_{\Lambda-1}^+ c_{\Lambda-1} \\ k_1^- & k_2^- & \cdots & k_{\Lambda-2}^- & k_{\Lambda-1}^- & -\sum_{l=1}^{\Lambda-1} k_l^+ c_l \end{bmatrix},$$

where, c_j represents the concentration of the jth ligand type. The probabilities of the system being in equilibrium states, denoted as $p_i^0(t)$, are derived by equating the left-hand side of (4.4) to zero, i.e., $\mathbf{G}\boldsymbol{p(t)} = 0$. Around these equilibrium states, the state probabilities exhibit fluctuations. These fluctuations can be described using the following expression, as detailed in [333]:

$$\frac{\mathrm{d}\Delta\mathbf{p}'(t)}{\mathrm{d}t} = \boldsymbol{\Omega}\Delta\mathbf{p}'(t), \tag{4.5}$$

where $\Delta\mathbf{p}'(t)$ represents a column vector comprising the state fluctuations for all states except the last one. The matrix $\boldsymbol{\Omega}$ is defined as $\boldsymbol{\Omega} = \mathbf{TGR}$, with the individual matrices are defined as follows [333, 349]: $\mathbf{T} = \begin{bmatrix} \mathbf{I} \\ \mathbf{0} \end{bmatrix}$ and $\mathbf{R} = \begin{bmatrix} \mathbf{I} \\ -\mathbf{1}^T \end{bmatrix}$, where $\mathbf{I}$ is the identity matrix of size $(\Lambda - 1) \times (\Lambda - 1)$, $\mathbf{0}$ is the column vector of length

$(\Lambda - 1)$ containing all zeros, and $-\mathbf{1}^T$ is the all -1 row vector of length $(\Lambda - 1)$.

The theoretical PSD of the binding noise fluctuations can be obtained as follows [333]:

$$S_b(f) = 4N_r(\rho)^2 \mathbf{z}^T \mathbf{R}\boldsymbol{\Gamma} \left(\mathrm{Re}\{(j2\pi f \mathbf{I} - \boldsymbol{\Omega})^{-1}\}\right)^T \mathbf{R}^T \mathbf{z}. \tag{4.6}$$

where $\mathbf{I}$ is $(\Lambda - 1)$ by $(\Lambda - 1)$ identity matrix, and the matrix $\boldsymbol{\Gamma}$ is defined as $\boldsymbol{\Gamma} = \mathbb{E}[\boldsymbol{\Delta}\mathbf{p}'(0)\boldsymbol{\Delta}\mathbf{p}'^{\mathrm{T}}(0)]$ is the matrix containing the expected state probabilities [333]. The theoretical PSD of the noise in the output current can be expressed as $S(f) = S_b(f) + S_f(f)$, where $S_f(f)$ is the PSD of the $1/f$ noise and defined as $\frac{S_{f_{1Hz}}}{f^\beta}$, with β is being the noise exponent [337, 249].

The parameter ρ in equation (4.6) characterizes the linear transduction process and is defined as $\rho = \frac{q_{eff} N_{e^-} g}{C_G}$. In this equation, g represents the transconductance of the bioFET, N_{e^-} is the number of free electrons per ligand molecule, and q_{eff} denotes the mean effective charge of a single electron in a bound ligand under Debye screening ($q_{\text{eff}} = q \exp\left(-\frac{r}{\lambda_D}\right)$). The elementary charge is denoted as q, r is the effective length of a surface receptor, and λ_D is the Debye length, calculated as $\lambda_D = \sqrt{\frac{\epsilon \kappa_B T}{2 N_A q^2 c_{\text{ion}}}}$. Here, ϵ represents the medium's permittivity, T is the temperature, κ_B is Boltzmann's constant, N_A is Avogadro's constant, and c_{ion} is the ionic concentration of the medium [249]. Furthermore, the total gate capacitance of the bioFET, C_G, is given by $C_G = \left(C_{G_r} + \frac{1}{C_Q}\right)^{-1}$. C_{G_r} represents the electrical double-layer capacitance between graphene and the electrolyte channel, A_{Gr} is the graphene's exposed surface area to the electrolyte, and $C_Q = c_q \times A_{Gr}$ represents the quantum capacitance, with c_q being the graphene's quantum capacitance per unit area [4].

4.2.3 Maximum Likelihood Estimation of Ligand Concentrations

The Maximum Likelihood Estimation (MLE) for unknown ligand concentrations $\boldsymbol{\theta}$ relies on the observed noise PSD obtained from time-domain noise samples and the parametric model for the noise PSD detailed in Sec.4.2.2. The observed noise PSD is generated using the periodogram method. For each transmitted symbol, N

noise samples $\boldsymbol{x} = (x_1, x_2, ..., x_N)$ are collected at intervals of Δt. The periodogram values Y_k are computed using the Discrete Fourier Transform (DFT) and exhibit an exponential distribution around the true PSD, as expressed by

$$p(Y_k|S(f_k,\theta)) = \frac{1}{S(f_k,\theta)} \mathrm{e}^{-\frac{Y_k}{S(f_k,\theta)}}, \tag{4.7}$$

following that $\mathbb{E}[S(f_k,\theta)] = S(f_k,\theta)$ is also expectation value at f_k [339]. Assuming the independence of each frequency bin, the quasi-log likelihood can be written as follows:

$$\ln \mathcal{L}(\boldsymbol{\theta}) = -\sum_{k=1}^{N/2-1} \left(\frac{Y_k}{S(f_k,\boldsymbol{\theta})} + \ln S(f_k,\boldsymbol{\theta}) \right). \tag{4.8}$$

The ML estimator, denoted as $\hat{\boldsymbol{\theta}}$, is employed to find the optimal value of $\boldsymbol{\theta}$ by maximizing the log-likelihood function defined in equation (4.8). This maximization is equivalent to minimizing the negative log-likelihood, represented as $l = -\ln \mathcal{L}(\boldsymbol{\lambda})$ [341]. Consequently, $\hat{\boldsymbol{\theta}}$ is obtained by solving the minimization problem $\hat{\boldsymbol{\lambda}} = \arg\min_{\boldsymbol{\theta}}\{l\}$, which can be solved using numerical methods.

The ML estimator described is asymptotically unbiased, implying that $\hat{\boldsymbol{\theta}}$ asymptotically follows a multinormal distribution with $\mathbb{E}[\hat{\boldsymbol{\theta}}] = \boldsymbol{\theta}$. Furthermore, the variance of the estimated parameters corresponds to the diagonal elements of the inverse Fisher information matrix (FIM) $\mathbf{F}(\boldsymbol{\theta})$ [342]:

$$\sigma^2_{\hat{\theta}_i} = (\mathbf{F}(\boldsymbol{\theta}))^{-1}_{(ii)}, \quad \mathbf{F}(\boldsymbol{\theta})_{(ij)} = -\mathbb{E}\left(\frac{\partial^2 \ln \mathcal{L}(\boldsymbol{\theta})}{\partial\theta_i \partial\theta_j} \right). \tag{4.9}$$

which can be further simplied to the following expression for a large number of samples such that periodogram values can be approximated as Gaussian by the central limit theorem [344]. :

$$\mathbf{F}_{(ij)} \simeq \frac{N\Delta t}{2} \int_0^{\frac{1}{2\Delta t}} \frac{1}{S^2(f)} \frac{\partial S}{\partial \theta_i} \frac{\partial S}{\partial \theta_j} \mathrm{d}f. \tag{4.10}$$

After estimating the ligand concentrations, the MC-Rx employs ML detection rule on the estimated concentrations to decode the transmitted symbol.

4.3 Symbol Error Probability for M-CSK

In this section, we derive the SEP for M-CSK and analyze the SEP performance in the presence of stochastic background molecular noise and ISI.

4.3.1 Symbol Error Probability in M-CSK Under Stochastic Noise

In this section, we consider SEP performance of M-CSK when stochastic background noise exist in the channel. In such a case, two different types of ligands interacts with the MC-Rx's receptors, namely, information and interfering ligands. That is, information molecules undergo reversible reactions with receptors on the MC-Rx. Similarly, interfering molecules can also react with MC-Rx receptors, but at different reaction rates compared to information molecules. For the simulations, in the sampling window, a single realization of the interferer concentration c_i is considered, following a log-normal distribution with mean μ_{c_i} and the variance $\sigma^2_{c_i}$. This statistical model is widely used in the literature to characterize the natural variability observed in biological systems [334]. The signaling interval is assumed to be long enough to neglect inter-symbol interference (ISI) in this case.

Since the MC-Rx lacks knowledge of the interfering molecule concentration, it calculates the symbol decision threshold γ_{fd} by neglecting the interference. Therefore, the computation of the ML decision threshold γ_{fd} relies on the following noise PSD model that accounts for only one type of molecule in the channel, i.e., the information molecule:

$$\tilde{S}(f, c_m) = 4N_r\zeta^2 \frac{1}{2\pi f + 1/\tau_m}\tilde{p}_b(1 - \tilde{p}_b) + S_f(f), \tag{4.11}$$

where $\tau_m = 1/(c_m k_m^+ + k_m^-)$ and $\tilde{p}_b = \dfrac{c_m}{K_{D_m} + c_m}$. For a single unknown parameter $\theta = c_m$, while c_m denoting the information ligand concentration corresponding to the transmitted symbol $m \in \{0, ..., M-1\}$ during the sampling window, the variance of the estimated ligand concentration, denoted as $\hat{c_m}$ is obtained from the Fisher information as $\tilde{\sigma}^2_{\hat{c}_m} = 1/\mathbf{F}(c_m)$.

The decision threshold for M-CSK modulation is determined with the ML decision rule using the following relation [332]:

$$\begin{aligned}\gamma_m =& \\ &\frac{1}{\tilde{\sigma}^2_{\hat{c}_m} - \tilde{\sigma}^2_{\hat{c}_{m-1}}}\Bigg(\tilde{\sigma}^2_{\hat{c}_m}\mu_{\hat{c}_{m-1}} - \tilde{\sigma}^2_{\hat{c}_{m-1}}\mu_{\hat{c}_m} + \tilde{\sigma}_{\hat{c}_m}\tilde{\sigma}_{\hat{c}_{m-1}} \\ &\times \sqrt{(\mu_{\hat{c}_m} - \mu_{\hat{c}_{m-1}})^2 + 2(\tilde{\sigma}^2_{\hat{c}_m} - \tilde{\sigma}^2_{\hat{c}_{m-1}})\ln\bigg(\frac{\tilde{\sigma}_{\hat{c}_m}}{\tilde{\sigma}_{\hat{c}_{m-1}}}\bigg)}\Bigg), \\ & m = 1, ..., M-1,\end{aligned} \tag{4.12}$$

where μ_{c_m} is the expected value of the estimated information molecule concentration, corresponding to the transmitted symbol $m \in \{0, 1, ..., M-1\}$. Note that the expected value of the estimated parameters are corresponds to their true values in

Table 4.1: Default Values of System Parameters

Interference to information ratio (γ)	0.5
Similarity (ν)	4
Diffusion coefficient (D)	2.2065×10^{-11} m^2/s
Temperature (T)	300 K
Microfluidic channel height (h_{ch}), width (w_{ch})	5 μm, 10 μm
Average flow velocity (u)	10 μm/s
Distance of Rx's center position to Tx (x_R)	1 mm
Ionic concentration of medium (c_{ion})	30 mol/m^3
Relative permittivity of medium (ϵ/ϵ_0)	80
Binding rate of information and interferer molecules (k_m^+, k_i^+)	4×10^{-17} m^3/s
Unbinding rate of information molecules (k_m^-)	2 s^{-1}
Average # of electrons in a ligand (N_{e^-})	3
Number of independent receptors (N_r)	500
Effective length of a surface receptor (r)	2 nm
Transconductance of graphene bioFET (g)	1.9044×10^{-4} A/V
Width of graphene in transistor (l_{gr})	10μm
Quant. capacitance of graphene per unit area (c_q)	2×10^{-2} F m^{-2}
# of noise samples (N)	700
Sampling period (Δt)	0.005 s
Interference mean/std ratio (μ_{c_i}/σ_{c_i})	10
Power of 1/f noise at 1 Hz ($S_{f_{1Hz}}$)	10^{-23} A^2/Hz
Noise exponent for 1/f noise (β)	1

this setting, e.g., $\mu_{c_m} = c_m$.

To calculate the SEP, we need the actual asymptotic variance of the estimated concentration of information molecules, denoted as $\sigma^2_{\hat{c}_m}$, which is related to the FIM for the two unknown parameters $\boldsymbol{\theta} = [c_m, c_i]$, as $\sigma^2_{\hat{c}_m} = (\mathbf{F}(c_m, c_i))^{-1}_{(11)}$. The SEP for MCSK is then obtained as [249]:

$$P_e = \frac{1}{2M}\Bigg[\text{erfc}\left(\frac{\gamma_1 - \mu_{c_0}}{\sigma_{\hat{c}_0}\sqrt{2}}\right) + \text{erfc}\left(\frac{\mu_{c_{M-1}} - \gamma_{M-1}}{\sigma_{\hat{c}_{M-1}}\sqrt{2}}\right) + \sum_{m=1}^{M-2}\left(\text{erfc}\left(\frac{\mu_{c_m} - \gamma_m}{\sigma_{\hat{c}_m}\sqrt{2}}\right) + \text{erfc}\left(\frac{\gamma_{m+1} - \mu_{c_m}}{\sigma_{\hat{c}_m}\sqrt{2}}\right)\right)\Bigg], \tag{4.13}$$

where $m \in \{0, 1, ..., M-1\}$.

Regarding SEP simulations, for the constellation design, we followed the approach described in [249]. Accordingly, the number of ligands released for the symbol m is determined by the relation $N_m = (m+1)(K/M)^\alpha$ [249], where the default values are $K = 1 \times 10^4$ and $\alpha = 2$. The maximum ligand concentration in the constellation is then obtained as $c_m^{\max} = N_{M-1}/(A_{ch}\sqrt{4\pi Dt})$. The default value of system parameters are shown in Table 4.1.

SEP of MCSK for varying interference to information ratio

In the first analysis of SEP, we considered the effect varying interference to information ratio, which is defined as $\gamma = c_m^{\max}/\mu_{c_i}$ with $c_m^{\max}$ being the maximum information ligand concentration in the constellation. We also define a parameter denoted as ν, with the default value of 4, to modulate the similarity between the affinities of the information and interferer molecules. While the binding rates are the same for both molecule types, their unbinding rates are determined by the relation $k_i^- = \nu k_m^-$, where k_i^- and k_m^- are unbinding rates of interferer and information molecules, respectively. As shown in Fig. 4.2a, in general, with higher order modulation, SEP performance degrades. Regarding the impact of the interference level, SEP performance improves with increasing interference level until a certain level, then it starts to degrade. When the MC-Rx initially is not saturated, the noise

PSD is sensitive to changes in the ligand concentration, leading the higher Fisher information and improved ligand concentration estimation performance. However, after certain interference level, the MC-Rx is getting close saturation, which results in degraded detection performance.

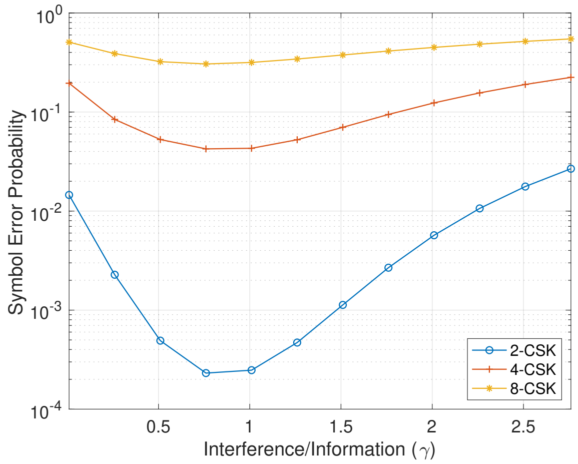

(a)

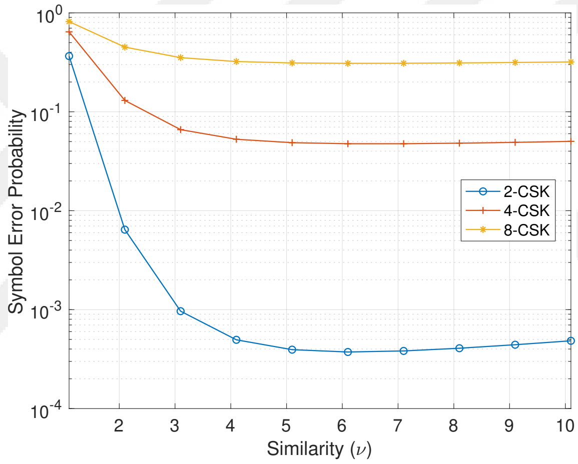

(b)

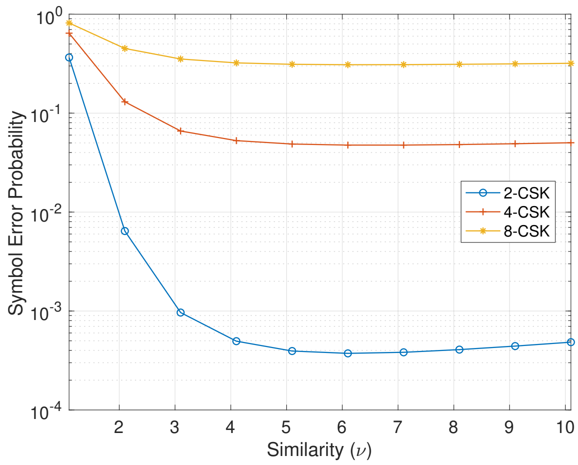

(c)

Figure 4.2: SEP in M-CSK under background interference for varying (a) ratio between interference and information ligand concentrations at sampling time γ (b) similarity in the binding affinities of information and interferer ligands (c) maximum ligand concentration $c_m^{\max}$.

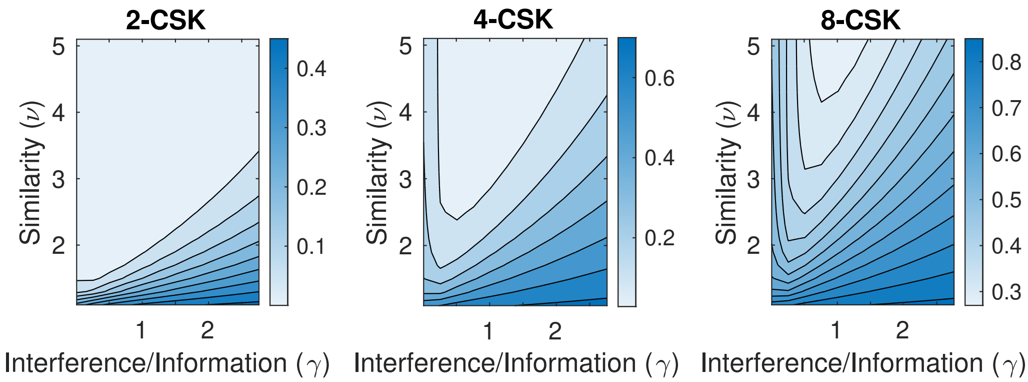

Figure 4.3: SEP in 2-CSK, 4-CSK and 8-CSK for varying interference and similarity levels.

SEP of MCSK for varying similarity values

We also considered the similarity between the affinities of the information and interferer molecules. As shown in Fig. 4.2b, with increasing ν, indicating the binding affinities of the information and interferer ligands are becoming dissimilar, SEP improves. When the binding affinities of information and interferer molecules are similar which is in case of low ν values, the existence of interferer molecules do not lead any meaninful distinction reflected in the noise PSD, degradeing the detection performance of the MC-Rx. With increasing ν, the MC-Rx is more likely to distinguishing the type of ligands from the noise PSD, which improves the detection performance. Also, Fig. 4.3 demonstrate the combined effect of similarity and the interference level on SEP. As clear from the result, in higher order modulations, the SEP performance is worse in most of the case compared to the lower order modulations.

SEP of MCSK for varying maximum information molecule concentration

Fig. 4.2c illustrates that increasing $c_m^{\max}$ results in a SEP trend similar to that caused by increasing background interference. This similarity is due to the same underlying cause: saturation at the MC-Rx, which is driven by information molecules when $c_m^{\max}$ increases and by interferer molecules in the case of increased background interference.

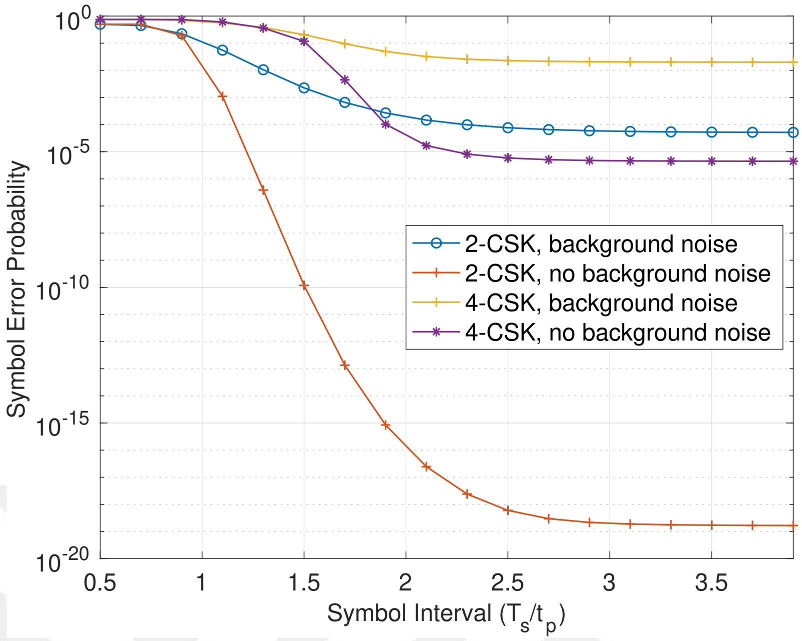

Figure 4.4: SEP performance for 2-CSK for varying symbol interval T_s/t_p with respect to peak time t_p.

4.3.2 SEP in MCSK Under Intersymbol Interference and Background Interference

In this section, we consider the effect of ISI on the SEP performance of MCSK. Considering (4.1), the MC channel impulse response can be expressed as follows:

$$h(x,t) = \frac{1}{A_{ch}\sqrt{4\pi Dt}} \exp\left(-\frac{(x-ut)^2}{4Dt}\right). \tag{4.14}$$

When ISI occurs, the information ligand concentration within the sampling window for ith transmitted symbol, is expressed as follows [350]:

$$c_m^i = N_m^i h(x_R, t_p) + \sum_{j=i-I}^{i-1} N_m^j h(x_R, t_p + (i-j)T_s) \tag{4.15}$$

where $m \in \{0, ..., M-1\}$, T_s is the symbol interval, I is the ISI length. The expected ISI affecting the ith transmitted symbol is estimated by the following expression [350]:

$$\omega_i = \sum_{m=0}^{M-1} (p_m N_m) \sum_{j=i-I}^{i-1} h(x_R, t_d + (i-j)T_s) \tag{4.16}$$

where p_m denotes the symbol probabilities, which are assumed equiprobable.

To assess the impact of ISI, the diffusion coefficient is set at $D = 1 \times 10^{-9}$ and the constant K at $K = 1 \times 10^5$. Fig. 4.4 displays the SEP for varying symbol intervals using both 2-CSK and 4-CSK modulation schemes. The symbol interval T_s is considered in relation to the peak time of the information molecule concentration profile t_p. During a brief period centered around t_p, the MC-Rx samples from the bioFET's electrical output. The findings reveal that for a low symbol interval T_s relative to t_p (i.e., $T_s/t_p < 1$), ISI significantly affects performance, hindering the MC-Rx's ability to detect symbols. As the ratio T_s/t_p increases, SEP performance improves. Beyond certain T_s/t_p values, ISI's impact diminishes, and SEP converges. It is evident that the presence of both ISI and background interference degrades SEP performance more than ISI alone.

4.4 Capacity Analysis

In this section, we analyze the information capacity for the end to end channel by utilizing the established relationship between Fisher Information and mutual information.

The information capacity, C^*, can be expressed as [351]:

$$C^* = \max_{\pi(\theta)} I(\theta, \hat{\theta}), \tag{4.17}$$

where θ is the input corresponding to the information-carrying ligand concentration, and $\hat{\theta}$ is the estimated value of it, and $\pi(\theta)$ denotes the optimal input distribution. This ultimately yields the asymptotic expression for a scalar input θ [352, 353, 351]:

$$C^* = \log_2 \left((2\pi e)^{-1/2} \int_\theta \sqrt{\mathbf{F}(\theta)} \mathrm{d}\theta \right), \tag{4.18}$$

where $\mathbf{F}(\theta)$ is the Fisher information. Then, the asymptotically optimal input distribution is described by Jeffreys' prior as $\pi^*(\theta) \propto \sqrt{\mathbf{F}(\theta)}$ [352].

4.4.1 CSK Modulation Under Background Noise

In CSK, symbols are represented through distinct concentration levels of single type of ligands, leading unidimensional input denoted as c_m. On the other hand, when single type of interferer molecules exist in the channel, the Fisher information can be represented by the matrix $\mathbf{F}(c_m, c_i)$, where c_i is the interferer concentration level during the sampling window. On the other hand, the information molecule concentration c_m is the variable is the main of interest. To estimate the information capacity in case of the background noise, we assume that the variable c_i is known ($c_i = \mu_{c_i}$) and defined a reference prior as detailed in [354, 355]:

$$\pi^*(c_m|c_i) \propto \sqrt{\mathbf{F}_{11}(c_m, c_i)}. \tag{4.19}$$

Hence, the information capacity can be estimated by the following equation:

$$C^* = \log_2 \left((2\pi e)^{-1/2} \int_0^{c_m^{\max}} \sqrt{\mathbf{F}_{11}(c_m, c_i)} \mathrm{d}c_m \right). \tag{4.20}$$

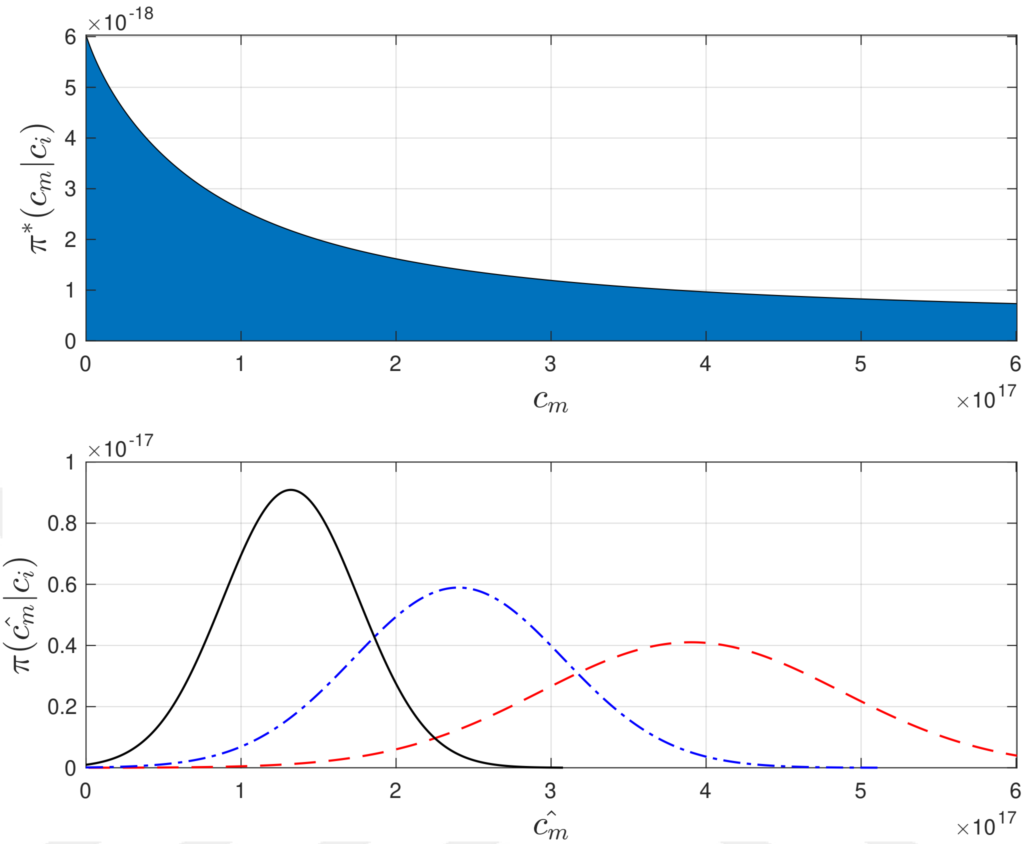

Figure 4.5: Optimal input distribution (above) and the distribution of the estimated inputs, i.e., information-carrying ligand concentrations, corresponding to Gaussian PDFs (below) given the mean interferer ligand concentration, i.e., $\mu_{c_i}/c_m^{\max} = 0.5$.

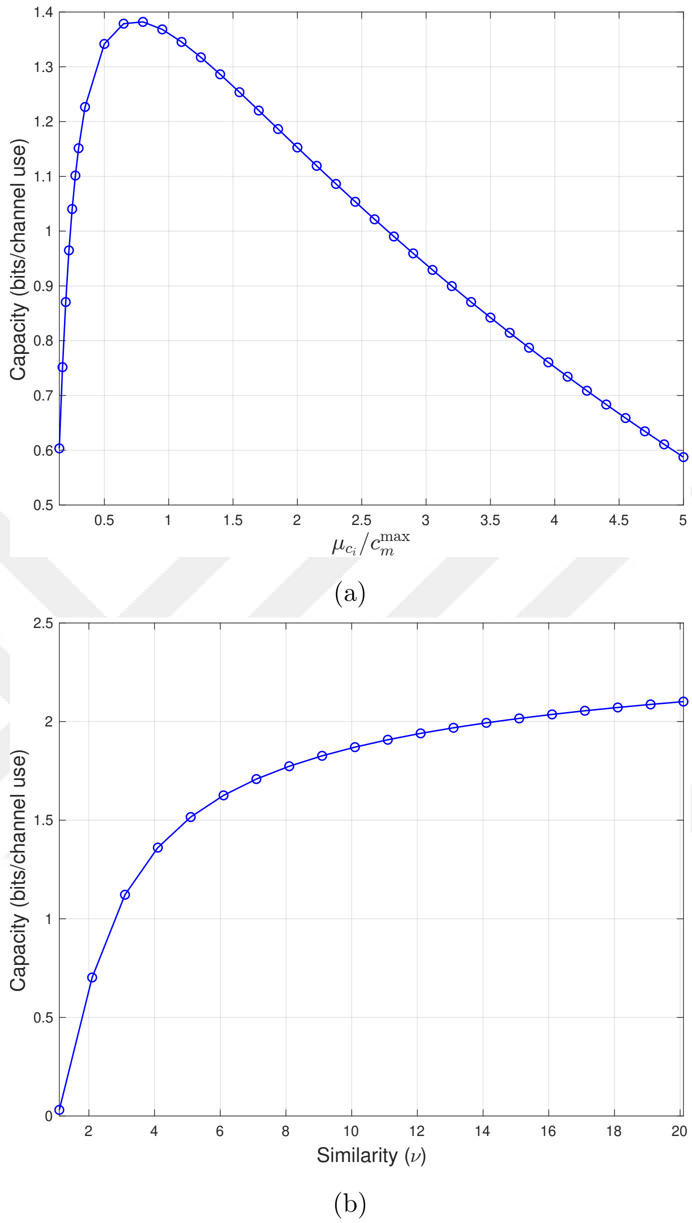

Figure 4.6: Capacity for CSK under background noise for (a) varying background noise level (b) varying similarity between the binding affinities of the information and interferer molecules.

Fig. 4.5 presents the asymptotic input distribution when the interferer concentration is $\mu_{c_i}/c_m^{\max} = 0.5$ and the maximum number of information molecules released by the transmitter is $N_m^{\max} = 5 \times 10^3$. In this scenario, our results indicate that lower information concentrations (c_m) require more precise estimation, while higher input concentrations can be estimated with relatively less precision for best information capacity.

In our initial analysis, we evaluated the information capacity under varying $\mu_{c_i}/c_m^{\max}$ ratios, as illustrated in Fig. 4.6a. The result shows that capacity initially increases and then decreases with rising levels of background interference. Up to certain levels of interference, the MC-Rx more accurately estimates the concentration of information molecules. Beyond these levels, however, the MC-Rx's ability to discern the concentration of information molecules weakens, as discussed in Sec. 4.3. This leads to a decrease in information capacity.

We also simulated the capacity for increasing ν, which indicate a growing dissimilarity in the binding affinities of the information and interferer ligands. The binding rates for both types of ligands are kept constant, as outlined in the default values in Table 3.1. Fig. 4.6b shows that an increase in the dissimilarity of the binding affinities of these ligands leads to an enhancement in the capacity.

4.4.2 Multi-dimensional Inputs

In this section, we consider a multi-dimensional input where symbols are encoded into both the concentration and types of molecules simultaneously. In this case, the multi-dimensional input composed of various ligand concentrations $\boldsymbol{\theta} = (\theta_1, \theta_2, ..., \theta_k)$, respective to a distinct type of ligand. Accordingly, the MC transmitter releases different types of molecules instantaneously at the start of the symbol interval, each with unique binding affinities and concentrations θ_k. The MC-Rx estimates the concentrations of each ligand type based on samples from the output noise PSD. The elements of the Fisher information matrix are thus calculated using (4.10). In this case, the capacity is obtained by the following expression as described in [352]:

$$C^* = \log_2 \left((2\pi e)^{-k/2} \int_{\boldsymbol{\theta}} \sqrt{|\mathbf{F}(\boldsymbol{\theta})|} \mathrm{d}\boldsymbol{\theta} \right), \tag{4.21}$$

where $|\cdot|$ represents the determinant of a matrix, and k is the dimensionality of the input. The optimal input distribution is described by Jeffreys' prior, as $\pi^*(\boldsymbol{\theta}) \propto \sqrt{|\mathbf{F}(\boldsymbol{\theta})|}$ [352].

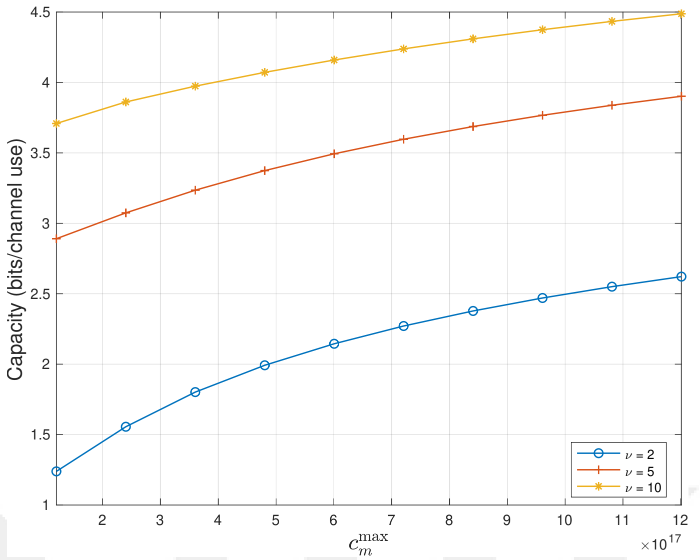

Figure 4.7: Capacity for multi-dimensional input, namely both concentration and type are used in the modulation.

In the analysis, we assume the MC channel is free from background interference and each ligand type has identical diffusion coefficient. Fig. 4.7 displays the capacity for various values of the maximum ligand concentration, assumed to be the same across all ligand types. In this analysis, we considers that two types of information-carrying ligands are employed. The results show that an increase in the maximum ligand concentration leads to improved capacity. Furthermore, a greater dissimilarity in the binding affinities of the ligands also contributes to an enhancement in information capacity.

4.5 Conclusion

This chapter considers the performance of molecular communication via bioFET-based receivers with cross-reactive receptors. Despite the challenges posed by the limited selectivity of the receptors and the resulting interference in signal decoding, FDD techniques can be an effective solution to this problem. FDD enhances the ability to decode signals in the presence of cross-reactive receptors by effectively exploiting the distinct reaction properties of different ligands. The analysis of symbol error probability and channel capacity in this chapter further highlights the potential of biosensor-based MC systems.

Part III

Enabling Terahertz Communication in the IoE: Physical Layer Solutions and Applications

Chapter 5

TERAHERTZ-BAND INTERSATELLITE COMMUNICATION LINKS

5.1 Introduction

More than 14 years passed between the launch of the first ever satellite, Sputnik 1, and demonstration of the first intersatellite communications link (ISL) in January 1975 by the radio amateurs within AMSAT. AMSAT/ OSCAR- 7 sent a signal to AMSAT/ OSCAR- 6 at a frequency of 432.15 MHz and these were repeated back to Earth at 145.95 and 29.50 MHz, respectively. The National Aeronautics and Space Administration established an ISL in the April of the same year between the low- Earth orbit (LEO) satellite GEOS-3 and ATS- 6. Although the possible use of optical beams for ISL was first mentioned in 1945 by Arthur C. Clarke, due to the unavailability of necessary components, the first optical ISL could only be established in November 2001 between ARTEMIS of the European Space Agency and French SPOT-4.

There are many criteria that need to be considered when designing an ISL system. For a microwave system, the main performance criterion, data rate, is directly proportional to the available bandwidth; thus, higher frequency bands are preferred over the lower ones. Higher frequency also translates to lower antenna diameters since effective aperture area of an antenna is directly proportional to the square of the wavelength of the transmitted wave. Smaller antennas are advantageous in terms of weight and cost too. Atmospheric attenuation is also considered during the ISL design: Frequency bands with high atmospheric attenuation are preferable since it helps ISL to be isolated from any possible interference from the Earth. Iridium and teledesic systems are two LEO constellations that are employed in microwave

ISLs.

Optical ISL systems necessitate different selection criteria compared to legacy microwave technologies. The selection of laser source depends on many parameters including output power, operating temperature, and lifetime. On the receiver (RX) side, direct or heterodyne detection can be chosen. Acquisition and tracking are part of the design issue considering the very narrow beamwidths over very long distances. Due to the advantages in size, power requirement, and data rate compared to the microwave ISL systems, optical technologies are currently the choice and many laser communication terminals are currently used in satellites including NFIRE and TerraSAR- X.

Due to the fact that components required for possible ISLs in the THz band (0.3–1 THz) were not available at the time when the performance of microwave technologies became insufficient and optical components started to provide necessary performance to realize ISLs, research was focused optical links completely by- passing the THz band. On account of the advancements in THz technologies since the beginning of 1980s, it is now possible to manufacture transceivers (TRXs) working at the frequency range of 2–3 THz. This means that it is now possible to overcome many shortcomings of the microwave systems compared to the optical systems, and competitive ISL systems that use electromagnetic (EM) radiation can be assembled.

In line with these, in this chapter first a review on the development of ISL technologies, namely microwave and optical solutions, is presented. State- of- the-art technologies are then compared in terms of their suitability for ISL adoption using many criteria including size, power consumption, and data rate. Then, keeping in mind that THz band is left out of discussion for ISL without even really being considered, a THz band ISL system is proposed in light of the developments that occurred in the area during the last decade, by also considering the "NR above 52.6 GHz" and "nonterrestrial networks" study items of the future Release 17 of the 3rd Generation Partnership Project (3GPP). Subsequently, link budgets for a typical usage scenario are calculated, helping to explain the propagation mechanisms. The chapter concludes by setting the directions for future research and challenges they may face.

5.2 Intersatellite Communication Links

Satellites can be classified into 3 categories based on the orbit altitude: Geostationary Earth orbit (GEO) satellites operating at 35786 km, medium Earth orbit (MEO) satellites operating at the orbits between 2000 and 35786 km, and LEO satellites with the orbit altitude varying between 400 and 2000 km. GEO satellites have been widely used for satellite communications since they can provide wide coverage and consequently minimal handoff. On the other hand, GEO satellites have the longest propagation latency compared to LEO and MEO; thus, they are not suitable for applications requiring low delay. Recent trends show that there is an increasing interest in LEO constellations, which can provide high throughput, and lower latency and launching cost. Multiple companies such as SpaceX, OneWeb and Amazon are currently working on or planning construction of LEO satellite constellations for broadband Internet connectivity, or scientific or military purposes. SpaceX aims to deploy thousands of small LEO satellites to build the Starlink. Due to lower altitude, much more LEO satellites are required for global coverage compared to GEO. Several disadvantages arise from deploying high number of satellites including larger Doppler spread and transmission loss due to frequent handoff [356]. MEO satellites constellation, which is exemplified by O3b, also appeals interest owing to its unique characteristics in terms of constellation size and latency. Satellite miniaturization is another aspect of the "New Space Era" [357]. Contrast to costly traditional GEO, MEO and LEO satellites, low cost cube-, micro-, and nano-satellites with short deployment cycles have been emerged [358]. These satellites can pave the way for new paradigms including Internet of Space Things (IoST).

Existing missions use X- ($8-12$ GHz), K_u- ($12-18$ GHz) and K_a-bands ($27-40$ GHz). Currently V- ($40-75$ GHz) and W-bands ($75-110$ GHz) are being considered for high throughput satellite links; however, it is apparent that increasing demand for the spectrum usage requires the employment of even higher bands of the spectrum. Thus, a paradigm shift is needed for the next generation space services.

5.3 Terahertz Band Communications

Different application areas of THz communication have been examined in various studies. The application areas covered include Internet of Nano-Things (IoNT) [359], Internet of Things (IoT) [360, 361], vehicular networks [362], nanocommunication and nanonetworking [363], THz communication networks [364, 365] and space-based THz systems [366]. In [359], a reference architecture for IoNT paradigm and communication challenges for THz nanonetworks are discussed. Early examinations on and the opportunities and challenges of the utilization of the THz band for IoT usage models are illustrated in [360, 361]. Research challenges in THz communication and the opportunities that THz band can offer for vehicular networks operating over beyond the fifth generation (5G) of mobile telecommunication systems are discussed in [362]. THz band nanocommunication and nanonetworking are detailed in [363] by identifying applications of THz nanonetworks, challenges and reviewing different aspects including channel models and experimentation tools. The novel applications of THz communications and challenges are surveyed in [364, 365]. In [367, 368], overviews for device technologies and channel models for THz communication are given together with technical issues that need to be addressed. In [369], an overview of device and antenna technologies is given, and standardization activities are discussed. Standardization activities are also discussed in [370] along with novel applications for THz communication and research challenges. In addition to opportunities for vehicular networks, a number of opportunities by means of THz wireless communication including hybrid-optical communication links, THz-based data centers with superior performance, and deployment of femtocells for mobile heterogeneous networks are detailed in [371, 372, 373]. An in-depth survey of THz medium access protocols is presented in [1]. Summaries of THz-enabled wireless systems, scenarios, applications, and challenges for the deployment of beyond 5G mobile systems are presented in [374, 375]. The state-of-the-art in THz signal generation and channel modeling is presented in [376], as well as a comparison with the other wireless technologies, THz standardization activities, and possible appli-

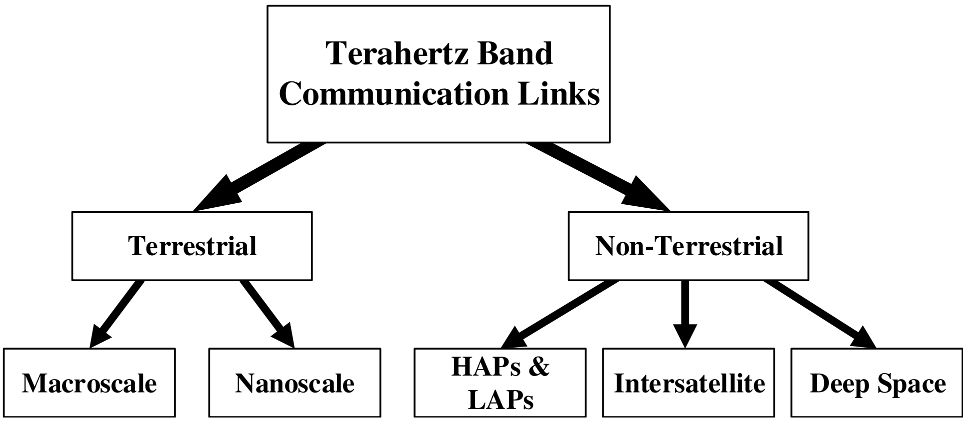

Figure 5.1: Classification of THz links.

cations of THz communications. Various modulation schemes are analyzed for THz band communication over systems simulating real world devices, and optimum modulation and physical layer (PHY) parameters in terms of energy consumption are published in [?, 377]. The current state in THz communications concerning THz channel, devices, and space-based systems from the perspective of device technology is summarized in [366]. However, very few studies covering the THz band ISLs are available in the literature. In [358], the authors propose a new CubeSat design with multi-band radios and briefly study link budget for LEO constellation of CubeSats. In [378], the feasibility of THz band for intersatellite communications is studied. In [379, 380], the authors examine the viability of using $0.75 - 10$ THz among ISLs.

THz band communication links, as illustrated in Fig. 5.1, can be classified into 2 categories: Terrestrial and non-terrestrial links. Terrestrial links comprise macroscale and nanoscale links. Non-terrestrial links are further classified into ISLs, deep space links and satellite/airborne platform links, i.e. high altitude and low altitude platforms (HAPs & LAPs) such as aircraft, unmanned aerial vehicles (UAVs), and high altitude balloons (HABs). In the following sections, we compare THz band communications with the other state-of-the-art technologies and identify further benefits of using THz band for ISLs.

5.3.1 Comparison with Other Technologies

THz communication has several key advantages over millimeter wave (mmWave) and free-space optical communication (FSO), which are summarized in Table 5.1.

Millimeter Wave Band Communication

MmWave band covers the frequencies from 30 to 300 GHz. MmWave wireless communication can offer multi gigabit-per-second (Gbps) data rates and enable many applications including vehicular and short-range wireless communications, and high-quality data streaming. Due to strong molecular absorption at frequencies around 60, 120 and 180 GHz, several special bands are chosen for utilization, namely 35, 94, 140 and 220 GHz, where the attenuation is relatively small [381, 382]. However, mmWave band communication cannot provide data rates as high as THz band communication, which can offer data rates on the orders of terabit-per-second (Tbps) owing to the extremely large bandwidth available.

THz communication has other advantages over mmWave communication apart from its higher bandwidth. Another advantage is THz links are inherently more directional compared to mmWave links because THz waves experience less free-space diffraction due to their shorter wavelengths [383, 384]. For space applications, especially for autonomous missions, security is essential. High directionality also provides securer communication compared to mmWave communication since it is harder to detect THz beams. This significantly reduces the possibility of eavesdropping. Finally, THz frequency band is still largely not regulated whereas $275 - 300$ GHz is allocated for mobile communications [385, 386].

Free-Space Optical Communication

FSO systems operate at infrared ($10 - 430$ THz), visible light ($430 - 790$ THz) and ultraviolet ($0.79 - 30$ PHz) spectra. Considering the well-known fact that information capacity increases with the bandwidth, FSO can enable high capacity links via high bandwidths. To illustrate, allowable bandwidth is on the order of hundreds of

Table 5.1: Comparison of Different Technologies [1]

Parameter	**mmWave**	**Terahertz**	**FSO**
Frequency range	30 – 300 GHz	0.3 – 10 THz	0.01 – 30 PHz
Data rate (Gbps)	$< 10^2$	$\in [10^2, 10^3)$	$\in [10^2, 10^3)$
Transmission range	Short	Short	Short
Power consumption	Medium	Low	High
Weather conditions	Robust	Robust	Sensitive
Security	Medium	High	High
System size	Large	Small	Bulky

THz in a typical optical communication link [387]. Moreover, highly directional and narrow beams reduce the probability of eavesdropping; thus, provide highly secure communication. Although FSO can provide high bandwidth and secure links, it has many disadvantages too. FSO links heavily depend on the atmospheric conditions such as fog, pollution, dust, rain, and snow. Variations of temperature and pressure of the atmosphere, i.e. atmospheric turbulence, also impacts the propagation of optical waves. In optical communication, very narrow beams are used. As the communication distance increases, beam alignment issue becomes critical to maintain reliable communication between the transmitter (TX) and RX. Since THz waves are longer than optical wavelengths, THz communication is advantageous over FSO in terms of tolerance for beam alignment. Moreover, THz communication is also favorable in terms of power and weight requirements, which are inherently large for laser-based systems [388]. Furthermore, relative position of the Sun to the laser TX and RX can degrade the system performance by increasing the solar background radiation. In case of superior solar conjunction, which occurs when the Sun, Earth and planet considered are aligned, optical communication is not possible. Lastly, due to the safety limits for eye, at certain wavelengths laser power level is limited to relatively low values, which limits the transmission range and data rates.

5.4 Terahertz Band Intersatellite Links

THz band communication is beneficial in space compared to existing radio frequency technologies in terms of data rate, size, interference and security. Higher data rates on the order of hundreds of Gbps is achievable owing to the available ultra-wide bandwidth. The space applications are expected to have low complexity designs because of the size restrictions. At the THz frequencies, antenna size is significantly small. Moreover, using simple modulation and coding schemes in THz communication, complexity can be further reduced, and high data rates can be supported for satellites and spacecrafts. THz band antennas inherently have high directivity; hence, the interference between the satellites is relatively small. Very narrow THz beams reduce the probability of eavesdropping too.

THz band communications can pave the way for new opportunities in space by enabling huge bandwidths. In terrestrial networks, EM waves at the frequencies above 300 GHz experience high gaseous attenuations due to the molecular absorption loss caused mainly by the water vapor, oxygen and pressure-induced nitrogen found in the atmosphere. Conversely, the effect of molecular absorption in the space and higher layers of the Earth's atmosphere is absent due to the lack of these absorbing molecules. So, THz band communication can potentially be employed in the links among LEO, MEO, GEO and high Earth orbit (HEO) satellites.

5.4.1 Link Budget Analysis

Investigating the link performance is critical regarding the feasibility of THz links. In this respect, research efforts focused on the link budget analysis of ground-to-satellite and intersatellite links. In [389], a ground-to-geostationary satellite link has been modelled. The authors report that based on their analyses, THz systems are superior to the optical communication when fog, cloud cover or clear-air turbulence exists. In [390], link budgets of both intersatellite (GEO-to-LEO) and GEO satellite-to-Earth station systems have been considered. The results suggest that due to the absence of water vapor, high carrier frequencies (f_c) above 300 GHz can be employed in ISLs. In [391], the authors propose a THz satellite communication system with massive antenna array to be located at Tanggula, Tibet, where the precipitable water density is low. The link budget analysis in this study shows that 1 Tbps can be achieved in the low-THz band ($0.275 - 0.37$ THz). In [358], another link budget analysis for CubeSats, which are 10 cm^3 miniaturized satellites with a mass of up to 1.33 kg, that operate ISLs at mmWave and THz bands is also simulated.

In this section, we first consider the propagation of THz waves in ISLs and then conduct link budget analyses for GEO-to-GEO and LEO CubeSat ISLs to examine the feasibility of THz ISLs.

Terahertz Propagation in Space

The propagation of THz EM waves in ISLs suffers from several types of attenuation and noise sources, which are described in this section.

Loss in Terahertz Frequencies

The propagation of THz waves can be described by the familiar Friis' transmission equation as follows [392]

$$P_{rx}\ [dB] = P_{tx}\ [dB] + G_{tx}\ [dB] + G_{rx}\ [dB] - A_{tot}\ [dB] \tag{5.1}$$

where P_{rx}, P_{tx}, G_{tx}, G_{rx} and A_{tot} are the received signal power, transmitted signal power, TX antenna gain, RX antenna gain and total path loss, respectively.

Spreading loss $A_{spread}(f)$, molecular absorption loss $A_{abs}(f)$, and scattering loss $A_{sca}(f)$ are the 3 main contributors of the total path loss $A_{tot}(f)$ in THz frequencies [**?**, 393]. Therefore, the total path loss in dB is given by

$$A_{tot}(f)\ [dB] = A_{spread}(f)\ [dB] + A_{abs}(f)\ [dB] + A_{sca}(f)\ [dB]. \tag{5.2}$$

Spreading loss describes the attenuation caused by the expansion of the wave through the propagation medium. It can be expressed, in dB, as

$$A_{spread}(f)\ [dB] = 20 \log \left(\frac{4\pi f d}{c} \right) \tag{5.3}$$

where c is the speed of light and d is the distance in m. Considering that the GEO-to-GEO and GEO-to-LEO link distances are on the orders of 10^4 km, the spreading loss is substantial [394].

Molecular absorption loss occurs when a part of the wave energy is transformed into the internal energy of molecules in the propagation environment by molecule vibration. Water vapor molecules are the main sources of molecular absorption in the Earth's atmosphere. Above 300 GHz molecular absorption is highly strong, such that the band above 300 GHz is not feasible for use in terrestrial systems. On the other hand, most of the satellites occupy the two outermost layers of Earth's atmosphere, i.e. the thermosphere and exosphere. LEO satellites inhabit the thermosphere, MEO and HEO satellites operate at the exosphere, and GEO satellites revolve at an altitude of $35,786$ km, where the atmosphere does not exist. Water vapor density is very low in the thermosphere and exosphere too. Therefore, the molecular absorption loss is negligible regarding the propagation of EM waves within ISLs. This means that higher frequencies that are not feasible for use in terrestrial networks can be employed in ISLs, which paves the way for the opportunity of performing communication in ISLs at extremely high data rates thru the available huge bandwidths.

Scattering loss occurs when the propagating EM wave is redirected into one or several paths away from the intended path, hence decreasing the received signal energy. Depending on the diameter of the atmospheric scattering particles, examples for which are gases, aerosols, hydrosols, and hydrometeors such as haze, cloud, fog, rain, snow and hail, THz waves can be affected by 3 types of scattering: Rayleigh, Mie, and, wavelength independent. Rayleigh scattering occurs when the wavelength of the EM wave is much longer than the diameter of the scattering particles and due to polar molecules of atmospheric gases. Mie scattering is generated if the sizes of the scattering particles are comparable to the wavelength of the EM wave. Otherwise, wavelength independent scattering, which is modelled by diffraction theory, is produced [387]. The amount of signal strength loss on account of Rayleigh scattering is insignificant in the THz band [395]. Regarding ISLs, we consider the layers of the Earth's atmosphere where the air molecule density is very low, namely the thermosphere and exosphere. Therefore, the effect of scattering due to atmospheric particles can be neglected for ISLs.

System Noise: The system noise power at the RX terminals is contributed by the antenna and RX noises [396]. Antenna noise depends on the frequency and direction where the antenna is pointed. For instance, if the antenna is aimed to the sky, antenna temperature is mainly contributed by the sky noise, also termed as the background noise, and extraterrestrial noise called the cosmic microwave background radiation, which is bounded by 2.725 K [397]. The sky noise is contributed by the temperature of the atmosphere, which acts as an absorbing medium [398]. Furthermore, RX noise temperature, which is caused by thermal noise in the RX components, contributes to the overall system temperature. Thus, system noise power at the RX terminals is given by

$$P_n = kT_{sys}B \tag{5.4}$$

where k is Boltzmann's constant (1.38×10^{-23} J/K), T_{sys} is the effective system noise temperature and B is the bandwidth. The effective system noise temperature at the RX terminals can be expressed as

$$T_{sys} = T_{ant} + T_{rec} \tag{5.5}$$

where T_{ant} is the antenna temperature and T_{rec} is the temperature at the RX.

Geostationary Earth Orbit-to-Geostationary Earth Orbit Links

In this section, the link budget analysis of a typical GEO-to-GEO ISL at the THz band is examined. The distance between GEO satellites is taken to be 83043 km [394]. Moreover, the effect of the Sun is assumed to be absent. As described in [389], the spectrum is separated into 6 bands from which we consider only the center frequencies (f_{cen}) of the Bands B (186 – 327 GHz), C (327 – 555 GHz) and D (567 – 747 GHz). We set the link budget to ensure a signal-to-noise ratio (SNR) of

Table 5.2: GEO-to-GEO Communications Link Case for an SNR of 10 dB

	Band B	**Band C**	**Band D**
f_{cen} (GHz)	225	350	675
P_{rx} (dBm)	-59.1	-58.3	-58.3
T_{rec} (°K)	3000	3600	3600
T_{ant} (°K)	0.6	0.6	0.7
B (GHz)	3	3	3
P_n (dBm)	-69.1	-68.3	-68.3

Table 5.3: GEO-to-GEO Communications Link Budget for an SNR of 10 dB

	Band B	**Band C**	**Band D**
f_{cen} (GHz)	225	350	675
P_{tx} (dBm)	10	10	0
G_{tx} (dBi)	88	92	95
G_{rx} (dBi)	80.8	81.5	94.2
A_{tot} (dB)	237.9	241.7	247.4

10 dB at the RX. SNR can be expressed in dB as follows

$$(SNR)\ [dB] = (P_{tx} + G_{tx} + G_{rx} - A_{tot}) - P_n. \tag{5.6}$$

Table 5.2 shows the necessary received power for an SNR of 10 dB at different frequency bands, whereas Table 5.3 presents the corresponding link budget to obtain such a received power. The results suggest that high gain transmit and receive antennas are required for GEO-to-GEO links. Moreover, the gains of the transmit and receive antennas need to increase with the rising f_c. Finally, due to the absence of molecular absorption, path loss is the main impairment regarding the EM wave propagation.

Low Earth Orbit CubeSat Links

In this section, we conduct a link budget analysis for ISLs between LEO CubeSats operating at THz frequencies. In [358], the authors propose a CubeSat design with reconfigurable multi-band radios covering mmWave, THz and optical frequencies.

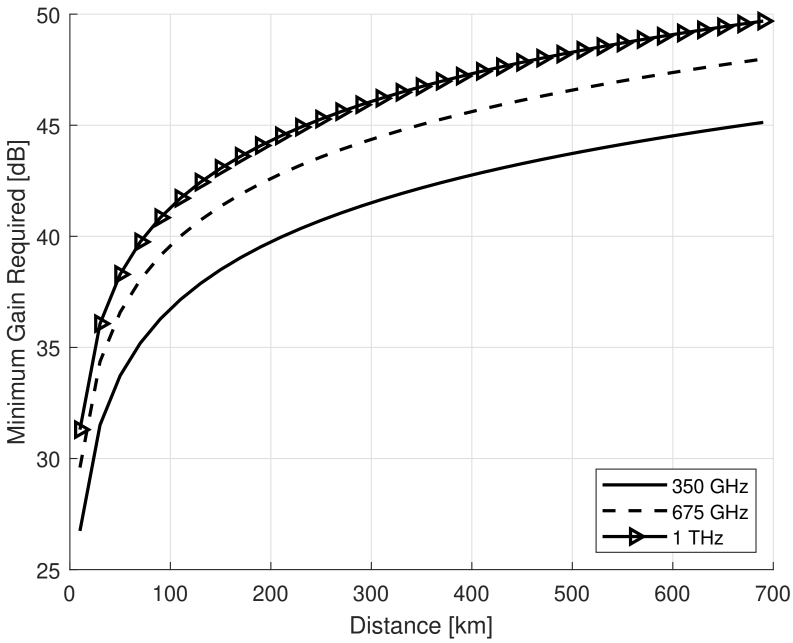

Figure 5.2: Minimum gain required.

In line with this study, we consider the analysis of THz ISLs at the frequencies 0.35, 0.675 and 1 THz. The bandwidth, temperature and transmit power are taken to be 0.5 GHz, 1500 K and 10 W, respectively [358]. The simulation results shown in figures below illustrate the minimum gains required at the TX and RX, and beamwidth required at the RX to obtain 10 dB SNR. Fig. 6.6a demonstrates that minimum antenna gain is less than 50 dB up to an f_c of 1 THz, which is potentially achievable by ultra-massive multiple input multiple output (UM MIMO) antennas. As expected, increasing transmission distance results in higher required antenna gain. Required beamwidth to obtain 10 dB SNR at the RX ranges from 0.6° to 8.3°, as presented in Fig. 6.6b. Narrower beamwidth means highly directional antenna, which can lead to outages due to relative motion. Mitigation techniques are needed for this challenge, including fast antenna beam alignment and faster handover management techniques [399]. Moreover, gain required at the RX and TX increases by 5 dB as the bandwidth is doubled, as displayed in Fig. 6.6c.

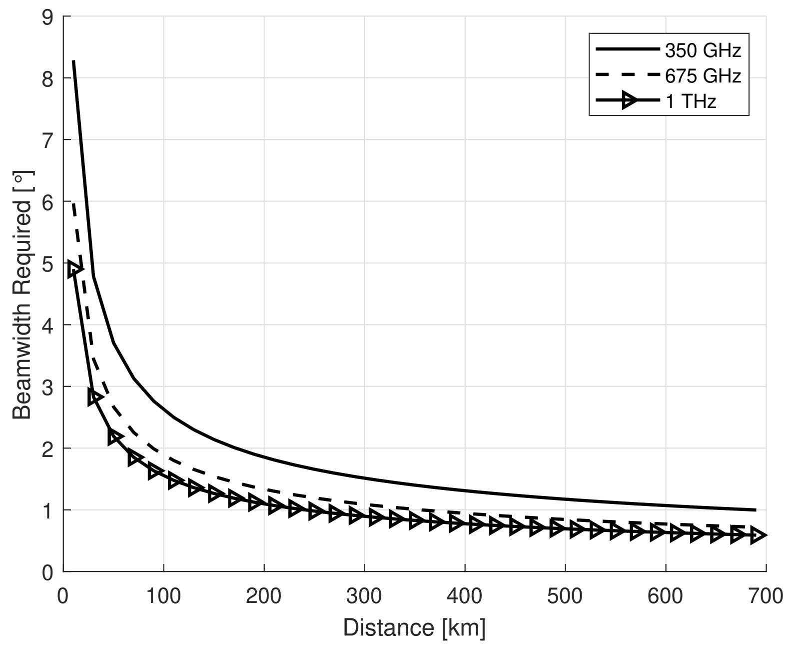

Figure 5.3: Beamwidth required.

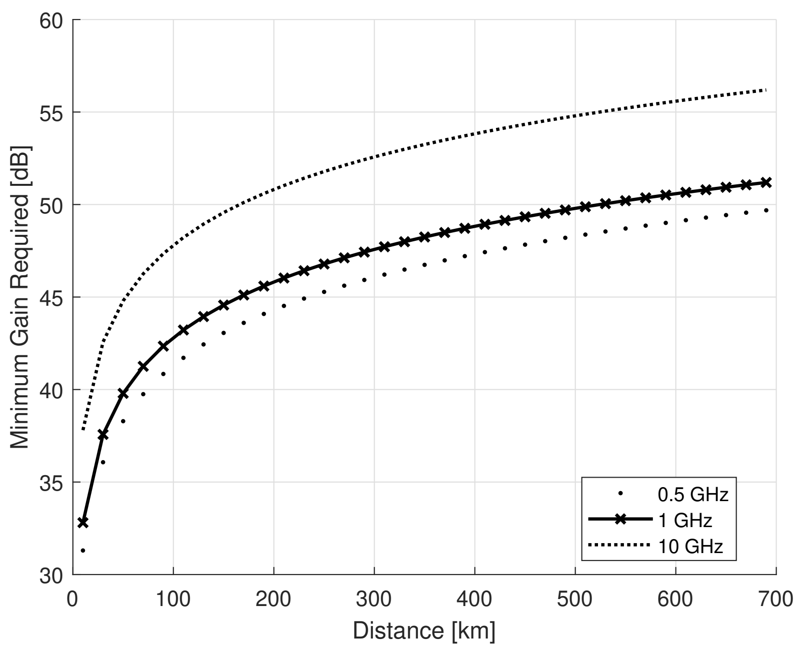

Figure 5.4: Minimum gain required for several bandwidths, $f_c = 1$ THz.

5.5 Future Research Directions

In this section, we discuss the future research directions, namely THz UM MIMO, 5G satellite networks, IoST, airborne military and defense applications, and the major challenges ISL encounters.

5.5.1 Terahertz Ultra-Massive Multiple Input Multiple Output

EM waves experience high spreading loss and the transmission power of TRXs is limited in THz frequencies. These impairments limit the transmission distance into a few tens of meters. Thus, highly directional antennas with high gains are required to increase the transmission distance. To combat the distance problem, the concept of UM MIMO communication in the THz band, which leverages many nanoantennas, has been introduced. As an enabling technology, plasmonic nanoantennas have been proposed. It has been estimated that using graphene-based plasmonic antenna arrays, thousands of antennas can be embedded in a few mm^2. On the other hand, the fabrication of nanoantenna arrays and PHY design still poses challenges for this concept [400].

5.5.2 5G and Beyond 5G Satellite Networks

IoT is a vital part of the 5G systems. The need for Internet provisioning to rural and remote areas, and ubiquitous coverage for mission critical applications focus the attention on satellites, which are also recognized as a part of 5G connectivity. The future Release 17 of the 3GPP also considers satellite networks as a study item under "Non-Terrestrial Networks", which proposes satellite systems as either a stand-alone solution or a part of 5G connectivity. This creates the opportunity to integrate the terrestrial and satellite networks. Challenges faced by traditional satellite networks such as latency and cost per data rate are expected to be overcome by 5G systems. Thus, satellites are envisioned to provide backhaul connectivity for the IoT [401]. Yet, there are still challenges such as high path losses, delays, and Doppler shifts [402] that need to be addressed to realize satellite-based new radio platforms. 5G communication systems have service requirements including enhanced mobile broadband (eMBB), massive machine-type communications (mMTC) and ultra-reliable low-latency communications (URLLC). eMBB service's use cases include backhauling, which is an emergent need in disaster areas where large amount of bandwidth is abruptly demanded. mMTC and URLLC can pave the way for plethora of IoT applications. However, terrestrial infrastructure has certain limitations including coverage to ensure full network utilization. Hence, satellites, being able to provide ubiquitous coverage to rural and remote areas such as oceans and deserts, will be integrated to both 5G and beyond 5G networks. Satellite networks can enhance network reliability for especially mission critical applications and moving platforms such as trains and planes, and enable service scalability by their broadcasting and multicasting capabilities [357].

5.5.3 Internet of Space Things

An LEO satellite constellation-based IoT system, which can enable the IoST concept, for the ubiquitous coverage of the Earth's remote areas has been proposed in [403]. However, traditional satellites suffer from several limitations such as long development time and high cost. Considering these drawbacks, another IoST concept that relies on CubeSats has been introduced in [404]. The CubeSat design proposed in [358] also supports wireless communication at the THz frequency band. IoST can be used as an alternative backhaul to terrestrial infrastructure or employed in monitoring activities and aerial reconnaissance. Yet, several challenges in the placement of the hubs and resource allocation need to be overcome.

5.5.4 Hybrid Space-Air Network

Space networks containing GEO, MEO or LEO satellites can also be integrated into air networks comprising UAVs and HAPs such as HABs. Hybrid network, which is illustrated in Fig. 5.5, can pave the way for many applications including Earth observation and secure military missions. In [405], a space-based network architecture containing hybrid links between spacecraft and satellites for Earth observation pur-

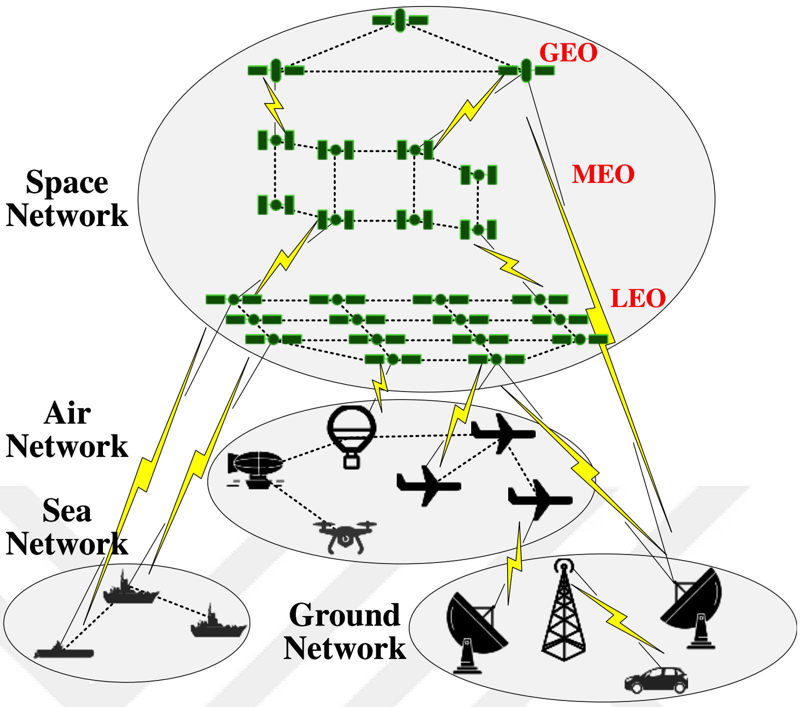

Figure 5.5: Hybrid space-air-sea-ground network.

poses has been discussed. In these links, THz communication can also be employed. For military functions such as reconnaissance, surveillance and patrol, UAV and HABs are being used. Many single UAV networks, which are already in service for almost 30 years, use satellite communications [406]. High atmospheric attenuation can create an advantage regarding secure communication links for these military and defense applications. THz waves of orbital links cannot penetrate the troposphere so that interception or disruption of the airborne links, such as satellites-to-HAB or UAVs, from the ground is not possible [388]. Moreover, terrestrial spectral noise will be minimal since THz waves from the Earth cannot penetrate space too. These eliminate the chances of interference, jamming and eavesdropping.

5.6 Challenges

In addition to the characteristic challenges of THz communication, the challenges in THz ISLs include the following subjects.

5.6.1 High Path Loss

High propagation loss is a major limitation for the THz communications. Due to higher f_c, amplified spreading loss restricts the THz communication into few tens of meters. To overcome this limitation for terrestrial networks, the authors in [407] introduce several solutions including distance-aware PHY design by considering the strong relationship between the distance and transmission windows, UM MIMO communications to augment the communication distance and reflectarrays to enhance signal coverage when line-of-sight is not available. Moreover, software defined metamaterials controlling the propagation environment for terrestrial networks have been proposed to overcome the distance limitation in the THz band [408]. Yet, further research on the methods for combating high spreading loss is still necessary regarding ISLs. Another possible solution is benefiting from the radio astronomy implementations where large aperture THz optics are employed, two exemplary systems of which are the 12.5 m Atacama Large Millimeter/Submillimeter Array (ALMA) in San Pedro de Atacama, Chile and 3.5 m Herschel Space Observatory. The authors in [389] have shown that data rates of more than 1 Tbps is possible for a ground-to-GEO satellite link, where the ground station is in the dry regions of Earth. They have further shown that aircraft and balloons with smaller apertures can even exceed 1 Tbps.

5.6.2 Interference

Earth exploration-satellite service (EESS) and radio astronomy service (RAS) use several bands in the $275 - 1000$ GHz range. The International Telecommunication Union (ITU) identifies $275 - 1000$ GHz to be potentially used by active communication services, even though this spectrum is still largely unregulated. On other hand, to protect the activities of the scientific community investigating space science from the interference of active services, current ITU Radio Regulations identify several frequency bands between $275 - 1000$ GHz for passive service applications, as detailed in the footnote 5.565. In this respect, standardization efforts are focusing on spectrum sharing studies between THz communications and passive services. Since the telescopes of RAS are located in remote areas such as the peaks of high mountains, these sharing studies are targeted to EESS in the $275-450$ GHz frequency band. EESS consists of geostationary and non-geostationary orbit satellites with down-looking antennas [409]. Thus, the interference from fixed communication services can be substantial. Preliminary simulation results reveal that the following bands can be shared between EESS and fixed services: $275-296$, $306-313$, $319-333$ and $354-450$ GHz [410]. Regarding THz ISLs, the interference from both EESS and RAS can be critical. Therefore, further studies are required to identify the bands that can be shared by THz ISLs and passive services.

5.6.3 Space Debris

Space debris refers to human-made objects that are present in the Earth orbit and mostly nonfunctional. It is a threat to both satellites and space missions, and pose a challenge for THz communication. Reflection and scatterings result in non-line-of-sight (NLoS) communication paths. Due to space debris, multipath components can be observed at the RX. As of February 2020, 34 thousand objects larger than 10 cm, 900 thousand objects between 1 and 10 cm, and 128 million objects ranging from greater than 0.1 to 1 cm are estimated to be in the Earth orbit [411]. Thus, geometric scattering occurs due to these objects. In [378], the author simulates the effect of space debris on the EM wave propagation in THz ISLs for a simple network topology, and shows that space debris can result in intersymbol interference. On the other hand, strong scattering effect of space debris can also be used to compensate the losses at RX, since any of the NLoS paths may behave as the dominant path in THz frequencies [412].

5.6.4 Doppler Spread

Relative movement between a TX and RX results in Doppler shift in the f_c of the received signal. If the RX is moving towards the TX with a speed of v, the maximum Doppler shift is calculated by $f_D = v/\lambda$, where $\lambda = c/f_c$ is the signal wavelength. If the relative speeds of satellites are high, the impact of the Doppler shift on the

THz ISLs can be severe. At 300 GHz f_c, the Doppler spread reaches 10 MHz for a v of 10 km/s, whereas the coherence time, in which the channel impulse response remains unvaried, is 0.018 μs [413]. The symbol period can be chosen to be less than the coherence time to prevent fast fading or the bandwidth can be adjusted accordingly. In any case, the Doppler shift should be estimated and compensated at the RX. However, Doppler shift estimation approaches for traditional wireless systems do not produce satisfactory performance for the high-speed systems with high f_c [414]. Therefore, new estimation methods and compensation techniques are needed for satellite systems operating at THz frequencies.

5.6.5 Device Linearity

System linearity is an important criterion to support a wide range of power levels in satellite communications. Due to only newly emergent THz device technologies, the state-of-the-art THz TRXs based on complementary metal oxide semiconductor (CMOS) have several drawbacks including non-linearity of devices. CMOS technology is preferred because it can offer low-cost solutions. However, high frequency operation is still a challenge for CMOS devices. Linear amplification is possible up to only about 300 GHz [415]. Since the cut-off frequency for transistor or maximum oscillation frequency is higher than the target frequency, the non-linearity of devices has to be utilized at THz frequencies, yet optimizing these devices increases the complexity of the designs [416]. Moreover, it degrades the power efficiency. Higher order modulations such as quadrature amplitude modulation also necessitate linearity.

5.7 Conclusions

THz band can pave the way for new opportunities by enabling huge bandwidth regarding THz ISLs. Satellite networks, which are one of the study items of 3GPP, can be employed as a part of 5G connectivity to provide ubiquitous coverage. Moreover, the constellation of small satellites with THz communication capability can enable the IoST concept. Large aperture THz optics such as the ALMA in San Pedro de Atacama, Chile are already being used by radio astronomy, which has the potential to drive THz ISLs. On the other hand, there are major challenges that need to be addressed such as high-power TXs to overcome the high spreading loss occurring between satellites.

Chapter 6

TERAHERTZ WIRELESS COMMUNICATIONS IN SPACE

6.1 Introduction

The start of a *New Space Era* has led to a paradigm shift in the space industry. An increasing number of private companies with space missions have emerged, and spacecraft are getting smaller and easily deployable with the help of enabling technologies. Moreover, the non-terrestrial networks are also recognized by the future release 17 of the 3rd Generation Partnership Project (3GPP) to be studied under the study item "Non-Terrestrial Networks". Vertical networks are expected to be integrated into the next generation 5G and beyond networks. This can lead to many novel paradigms including the Internet of Space Things (IoST) [404]. Therefore, available bandwidths are getting congested. National Aeronautics and Space Administration (NASA) estimates that the growth factor of deep space communication capability should be at least 10 to meet the growing demand in the next three decades [417]. Therefore, high data rate communication technologies are required. Free space optical (FSO) communication has been envisioned for space applications. However, optical communication highly depends on atmospheric conditions such as fog, cloud, and haze where optical links experience strong attenuation [387]. Moreover, FSO is costly, and beam alignment problems pose several additional challenges. Terahertz band (0.1-10 THz) wireless communications, which can enable high data rates on the order of Terabits per second, is an alternative to FSO.

The advantages of FSO such as large bandwidth, high data rate, high security, no spectrum licensing are of growing interest. NASA's demonstration in 2013 called Lunar Laser Communication Demonstration proved that high downlink and uplink transmission rates from lunar orbit to Earth are possible via optical links and NASA will further conduct Deep Space Optical Communications demonstration as a part of Psyche mission to show that higher data rates, 10-100 times of the current state of the art, are attainable via optical wireless communications [418]. The European Data Relay Satellite System (EDRS) also employs optical inter-satellite links, which can reach a data rate of 1.8 Gbps for a transmission distance up to 45000 km [419]. Apart from institutional projects, the companies such as SpaceX and Google aim to use optical communications for space-to-space or air-to-air links of their projects under development. Despite its advantages, FSO communications have still several challenges. Regarding space links, due to high transmission distances Effective Isotropic Radiated Power (EIRP) must be high. This can be enabled by large aperture transmitting optics, which result in narrow-beam divergence ($\propto \lambda/D$, where λ is the wavelength and D is the diameter of aperture). Thus, a deviation of the optical beam from the target results in an outage. Considering the same transmitting antenna size, THz systems have looser beam pointing requirements compared to FSO links, since we consider larger wavelengths.

FSO communications are also highly affected by atmospheric conditions such as clouds, haze, fog, and atmospheric turbulence. For instance, when visibility is less than 50 m when dense fog exists, attenuation can be as high as 350 dB/km, which limits transmission [387]. In case of fog with the same visibility, there are several windows in the THz band where the attenuation is below 100 dB/km [420]. Compared to FSO, THz communications are more robust to weather effects in general. Although the attenuation in THz links for long-distance communication is still a challenge to be addressed, there are promising solutions such as large THz antenna arrays enabling extremely high gains. Moreover, THz waves are not affected by turbulence-induced scintillation, which is observed as intensity fluctuations at the signal, as much as FSO links [421, 387].

THz band communication links can be classified into two as terrestrial and non-terrestrial networks as shown in Fig. 6.1. Terrestrial networks comprise macroscale and nano-scale links. In this study, we consider non-terrestrial network components

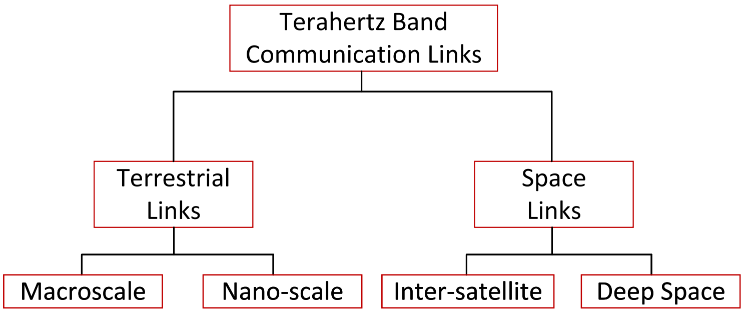

Figure 6.1: Classification of THz links [12].

ground/space and space links consisting of inter-satellite and deep space communication links. We aim to identify the challenges related to THz space links and discuss the possible solutions. The realization of THz space links poses several challenges. The spreading loss due to the expansion of propagating electromagnetic waves is increasing drastically with the frequency. This limits the communication distance to few meters on Earth due to immature THz source technology, which can enable transmit power on the order of milliwatts. Moreover, strong molecular absorption results in high atmospheric attenuation in Earth-to-space links; thus, limits the utilization of the high THz band. Artificial satellites occupy higher atmospheric layers of Earth or deep space where the air molecules are scarce or none. Therefore, THz inter-satellite links do not experience significant atmospheric attenuation. Regarding another terrestrial planet Mars, atmospheric attenuation is expected to be low compared to Earth because water molecules, which are the primary source of atmospheric attenuation, are scarce in the Mars atmosphere. These create an opportunity of utilizing the high THz band, consequently providing high data rates. In line with this, later we simulate the transmittance of Mars's atmosphere in clear and dusty atmospheric conditions using an accurate radiative transfer tool called Planetary Spectrum Generator (PSG) to show the availability of a large bandwidth for Mars communication.

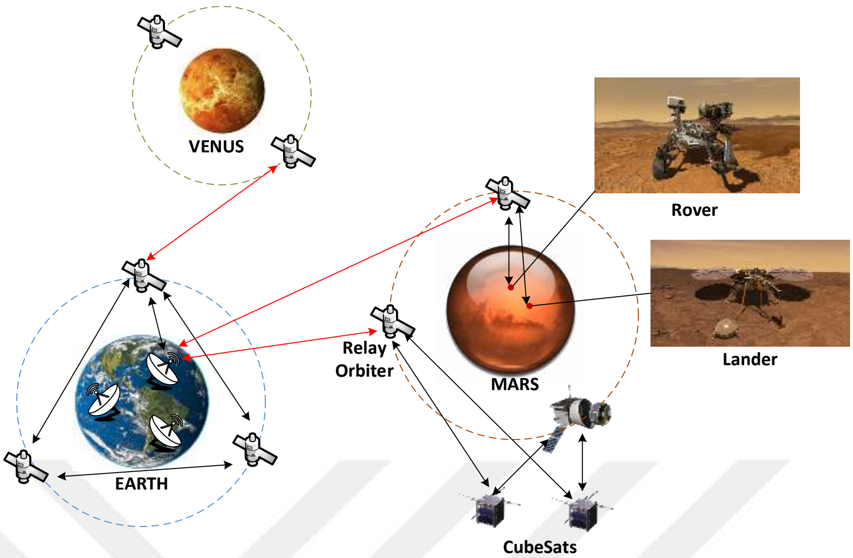

Figure 6.2: Interplanetary communications: Black arrows (THz links), red arrows (FSO links).

6.2 Applications

Utilizing THz space links can pave the way for novel applications, some of which are discussed as follows.

6.2.1 Earth Observation

Earth observation using artificial satellites began with the launch of Sputnik 1 by the former Soviet Union in 1957. Since then, many Earth observation satellites have been launched. Most of these satellites occupy Low Earth Orbits (LEO) and transmit a large amount of data to Earth daily. Recently, an increasing number of LEO satellites are being launched so that the bandwidth used is getting congested. To reduce the transmission delays and support the transmission of a large amount of sensing data to Earth, technologies supporting high data rates are required. FSO communications, providing connectivity within a few kilometers using laser beams, have been proposed as a viable solution [422]. For instance, EDRS employs FSO communications between LEO satellites collecting Earth observation data and GEO satellite relaying data to Earth. However, with the start of a New Space Era, satellites are getting miniaturized, and deploying many small satellites, e.g., CubeSats, is preferred [357]. The power and size requirements of FSO systems far exceed the limitations of cube/micro/nano-satellites. On the other hand, building THz transceivers with a large number of antenna arrays, i.e., phased Multiple-Input and Multiple-Output (MIMO) arrays, in a small footprint, is possible thanks to novel materials such as graphene [169]. Thus, for long-distance and high-data-rate near-Earth transmission, THz communications can be leveraged in the future. Large THz arrays are also advantages over FSO links in terms of beam-alignment, e.g., they can provide automatic alignment by their scanning ability [143]. However, there exist issues to realize such THz transceivers. The main impediments include the lack of practical THz signal sources and detectors, implementation and optimization of antenna arrays [143].

6.2.2 Interplanetary communications by hybrid THz/FSO links

Current state-of-the-art communication technologies used are not able to support high data rate interplanetary communications as a part of space information networks, which can result in numerous applications including space observation, Internet of Things (IoT), and maritime monitoring. To illustrate, Mars Reconnaissance Orbiter employs X-band (8-12 GHz) and Ka-band (26.5-40 GHz) to communicate with the NASA Deep Space Network, which comprises deep space communication facilities for commanding and tracking spacecraft. The data rate is between 0.5 and 4 megabits per second [423]. The services such as live video feeding, high-resolution scientific data streaming, virtual reality for controlling rovers and other machines, and real-time data transmission will require much higher data rates. Although latency is still an issue, these services can be enabled by hybrid THz/FSO links as a part of space information networks. In case of an outage due to beam pointing errors or strong atmospheric attenuation, THz links can be used as a backup [424] since THz links are more robust to weather conditions and pointing errors.

THz communication capability can be integrated into FSO communication ar-

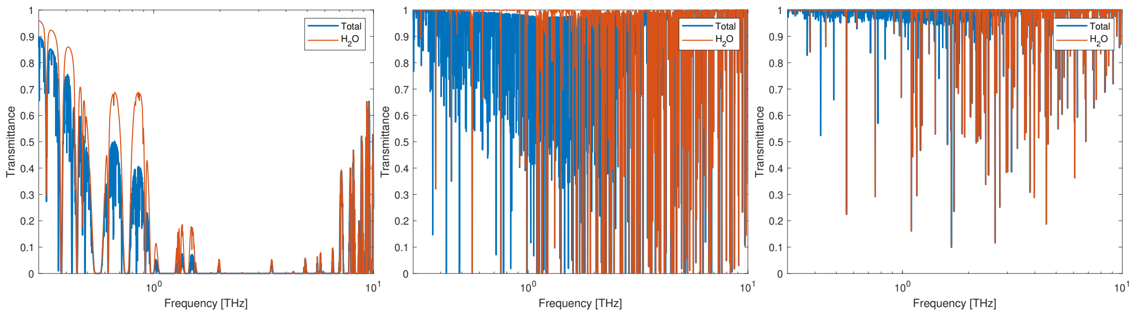

(a) Altitude = 0 km. (b) Altitude =16km. (c) Altitude =35km.

Figure 6.3: The transmittance of Earth-space links at several altitudes from one of the driest locations of the Earth, i.e., ALMA, denoting the fraction of EM radiation after experiencing molecular absorption. The zenith angle is 35°.

chitecture to support high data rates and can lead to novel applications such as space exploration. For instance, Mars rovers communicate with Earth through relay orbiters since the availability of orbiters is much longer than that of rovers. A Mars rover can communicate with a relay orbiter through THz links and the relay orbiter relays messages using FSO links because THz communications are more robust compared to FSO in ground/space links. CubeSats are being used in interplanetary missions during mission-critical events, which are exemplified by Mars Cube One (MarCO). CubeSats can be equipped with THz transceivers in the future so that they can communicate with the landing spacecraft using low latency THz links and, to relay information to Earth using FSO links.

6.3 Challenges and Solutions

In this section, we discuss the several challenges THz space links encounter. These challenges include molecular absorption and spreading loss, interference to passive services. We also discuss the potential directions to address these challenges.

6.3.1 Molecular Absorption Loss

Molecular absorption loss, which occurs when the part of wave energy is transformed into molecular energy due to the vibration of molecules, is one of the main impediments affecting Earth-space THz links. Water vapor molecules, which are scarce in the atmosphere of Mars, are the primary sources of molecular absorption on Earth in THz frequencies [425]. Inter-satellite THz links among Low Earth Orbits (LEO), Medium Earth Orbits (MEO), and Geosynchronous Orbit (GEO) satellites are not affected by molecular absorption loss because they operate at the altitudes where water vapor is almost none. To combat the high atmospheric attenuation on Earth, several approaches have been proposed. In the following section we give an overview of these approaches.

Dry ground sites

Atmospheric Precipitable Water Vapor (PWV) is the primary cause of strong atmospheric attenuation at THz frequencies. Considering ground-based telescopes of THz radio astronomy such as Atacama Large Millimeter/Submillimeter Array (ALMA) located at a high and dry plateau of Chile and Combined Array for Research in Millimeter-Wave Astronomy (CARMA) which was operating in the United States, Suen *et al.* identified the locations on Earth with lowest water vapor [425]. Dry sites for radio astronomy as well as satellite communications include Antarctica, Greenland, the Atacama Desert, and the Tibetan Plateau. Numerous dry sites that can provide acceptable performance have been identified in the United States and Europe as well. Suen *et al.* further investigated the performance of a THz ground to geostationary satellite links [389]. They have shown that utilizing radio astronomy platforms with large aperture antenna arrays, which are located at dry sites of Earth, for satellite communications 1 terabit/second link performance can be exceeded in clear atmosphere conditions [389]. In [391], the authors show that 1 terabit/second is attainable in the low THz band for ground/satellite links utilizing massive antenna arrays and establishing the ground stations at Tanggula, Tibet, where PWV is very low.

High and low altitude platforms

To combat high atmospheric attenuation in ground/satellite THz links, placing transceivers on airborne platforms has been proposed in [389, 426]. High and low altitude platforms such as aerostats, aircraft, and high altitude balloons can be employed for transceiver placement. These platforms need a lower aperture diameter compared to ground-based transceivers and can also offer performances comparable to ground-based platforms with large apertures since they operate at the altitudes where water vapor density is low [389]. In Fig. 6.3, Earth-space link transmittances for various altitude levels in a dry location of Chile, which are simulated in the Planetary Spectrum Generator (PSG) [427], is depicted. According to this, numerous bands, which are not feasible to use at sea level, are available for use at high altitudes.

Hybrid ground/satellite links

Placing ground stations only at dry locations can limit the potential of THz communication. Akyildiz *et al.* propose ground-satellite links enabled by microwave (e.g., X band (8-12 GHz), Ku band (12-18 GHz, Ka-band (26.5-40 GHz)), and mmWave/THz bands for small satellites called CubeSats in [358]. If a ground/satellite link is not suitable for transmission at THz frequencies, mmWave and microwave bands can be utilized. The idea is based on sending a pilot signal to obtain the availability of the link according to some criteria (e.g., Line of Sight (LOS) and weather conditions). The analysis in [358] shows that even with a relatively high water vapor density, data rates on the order of tens of Gbps can be achieved.

6.3.2 Spreading loss

As an Electromagnetic (EM) wave propagates through a medium it expands and this leads to a loss called spreading loss. Spreading loss is one of the significant challenges limiting communication to short distances at THz frequencies because free space path loss increases with the frequency in a quadratic relation according to Friis' law. Regarding space links, we consider the distances at least on the order of thousands of kilometers. On the other hand, transmit power in THz frequencies is on the order of milliwatts due to immature THz source technology, which is also called the THz gap. Thus, high gain antennas with high directivity are required for THz space links. Several approaches for combating the problem of high propagation loss have been proposed in the literature [407]. Some of these solutions apply to indoor and nano-scale communications such as intelligent surfaces controlling the behavior of an EM wave [428] and graphene plasmonic nano-antennas [173]. In the following section, we discuss the potential solutions for THz space links.

Radio astronomy optics

Large aperture THz optics, which are exemplified by ALMA comprising 54 reflector antennas with 12 meter diameter and 12 smaller antennas with a 7 meter dish diameter, are already being used by radio astronomy. In line with this, one approach is employing large aperture THz ground stations and airborne stations with smaller apertures [389]. Large apertures can provide high gain; however, one drawback is that the construction cost increases with the diameter [426].

Reflect-arrays

Reflect-array antennas are being used by the systems such as satellite communications, radars and deep-space communication links [429]. Traditional aperture antennas can provide high gain but they are not as electronically flexible as phased arrays. However, the implementation cost of phased arrays is high. Reflect-arrays offering high gain, low cost, ease of manufacturing as well as electronic flexibility are a compromise between aperture antennas and phased arrays. To illustrate, the MarCO spacecraft communicated with Earth at a distance of 160 million km on X-band via a high-gain reflect-array antenna with small volume [430]. Operating frequencies of reflect-array antennas are now shifting towards THz frequencies [431]. Thus, they offer the potential to be employed in THz space links. On the other hand, enabling technologies need to be studied because RF and MEMS technologies such as semiconductor diodes and MEMS lumped elements do not apply to the THz band due to loss and size constraints [228].

Ultra-massive MIMO

The concept of Ultra-Massive Multiple Input Multiple Output (UM-MIMO) has been introduced in [141] for combating the distance problem in THz communications. According to this concept, using novel materials such as graphene to build antennas with a number of antenna elements in a small footprint is possible. Utilizing both space and frequency, the coverage range can be increased. However, the realization of this concept poses several challenges [141]. The performance of UM-MIMO depends on the THz channel; thus, accurate THz channel models are required. Moreover, to control arrays, dynamic beam-forming algorithms are needed [358]. Moreover, the performance of THz MIMO links can also be affected by the frequency-dependent diffraction of THz waves, which arises from the divergence of THz beams from their modulation side-bands. This results in degraded bit-error-rate performance due to the detection of unwanted spectrum information. Thus, novel detection and demodulation methods are required in this direction [142].

6.3.3 Spectrum sharing

Spectrum beyond 275 GHz is not largely regulated in the Radio Regulations (RR). Footnote 5.565 of RR identifies numerous frequency bands in the range from 275 GHz to 1000 GHz that are used by passive services, namely Radio Astronomy Services (RAS), Earth Exploration Satellite Services (EESS), and Space Research Service, and states that the activity of these services must be protected from harmful interference of active services until the frequency allocation is established [432]. Active and passive services will coexist on the spectrum. Current spectrum sharing studies, which aim to identify the bands where the coexistence of active and passive services is possible, mainly focus on the interference to EESS [410] because RAS telescopes are located in high dry mountains. However, coexistence studies should cover both RAS and EESS because both can be affected by THz ground/satellite

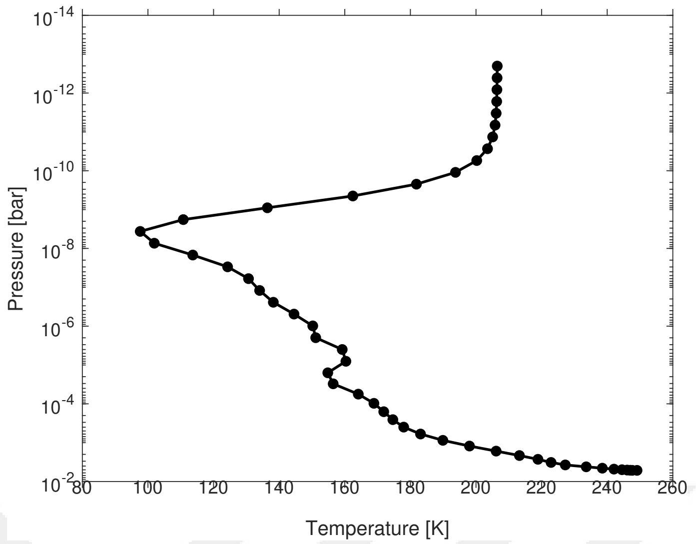

Figure 6.4: Pressure vs temperature.

and inter-satellite links.

6.4 Terahertz Mars-Space Links

Preparing Mars for human exploration is one of the targets of current missions on Mars. Thus, communication among human explorers, remote-controlled vehicles, space instruments, or any other space entities will be an essential part of Mars missions soon. Water vapor molecules and oxygen are scarce in the Mars atmosphere. Thus, the effect of molecular absorption is less compared to Earth. However, Mars's atmosphere can pose other challenges due to scattering aerosols such as seasonal dust storms, limiting reliable communication.

6.4.1 The Planetary Spectrum Generator

The PSG is an online radiative-transfer suite, which can generate planetary spectra of planets and other planetary objects [427]. PSG uses several radiative transfers and scattering models, and databases including spectroscopic (e.g., high-resolution transmission database (HITRAN)) and climatological databases (e.g., Mars Climate Database (MCD)).

Table 6.1: Vertical profile of Mars atmosphere

Gas	**Symbol**	**Composition**
Carbon Dioxide	CO_2	95.717%
Nitrogen	N_2	1.991%
Oxygen	O_2	0.152%
Carbon Monoxide	CO	818.452 ppm
Water Vapor	H_2O	194.232 ppm
Ozone	O_3	4.750 ppb
Column	-	1.947e+27 m-2
Col mass	-	1.408e+2 kg/m2

We use the module of PSG extracting atmospheric profile MCD. The model of the Mars atmosphere comprises 49 layers up to 257.90 km. PSG further extracts information of pressure and temperature, and profiles of atmospheric gases, scattering particle sizes from MCD [427]. The pressure and temperature profile used is shown in Fig. 6.4. The surface temperature is 279.48 K and the surface pressure is 5.1666 mbar. Regarding the geometry, we have used the looking-up mode, in which the zenith path is considered while integrating radiative transfer. We consider the location with the longitude of 175.5 and the latitude of -14.8 (Mars Exploration Rover A landing site). The zenith angle is 25.045 and the azimuth angle is 297.909 in the simulations. Mars date considered is 2018/05/07.

6.4.2 Zenith transmittance

For a clear Mars atmosphere, the zenith transmittance of a Mars-space link is shown in Fig. 6.5. When the altitude is 0 km, it can be observed that in the $0.3 - 10$ THz band, transmittance values are greater than 0.9. There are numerous sharp decreases in the band ($1 - 10$ THz). At the altitude of 30 km, the whole band is available except for sharp decreases in the transmittance, since molecular absorption is not so effective at high altitudes due to the very low abundance of molecules.

Dust storms are an important phenomenon of Mars. They can be classified as local ($< 2000\text{km}^2$), regional ($> 2000\text{km}^2$) and planet-encircling [433]. Global dust storms occur in the southern spring and summer seasons of Mars. Dust devils are

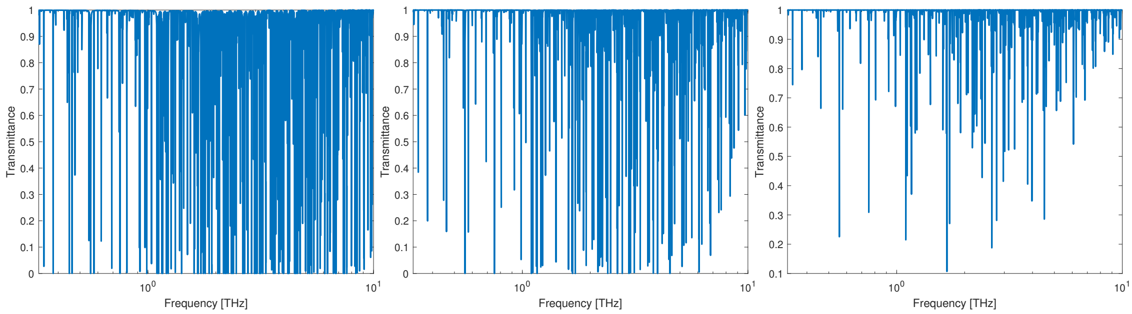

(a) Altitude = 0 km. (b) Altitude =16km. (c) Altitude =30km.

Figure 6.5: Zenith transmittance of clear Mars atmosphere for various altitudes.

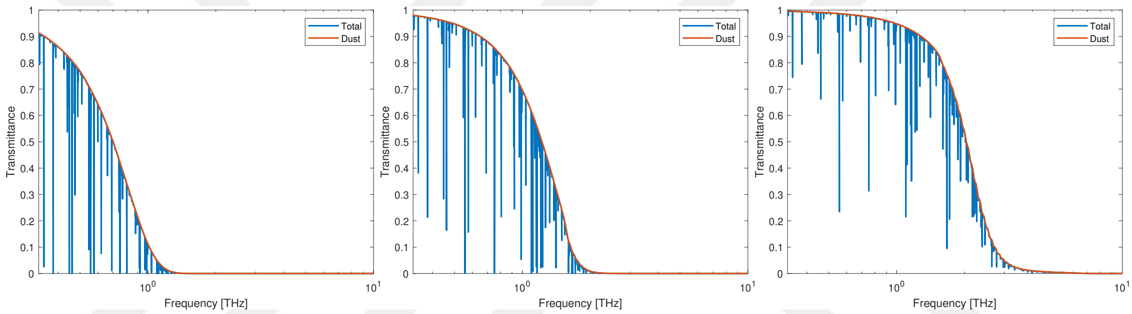

(a) Altitude = 0 km. (b) Altitude =16km. (c) Altitude =30km.

Figure 6.6: Zenith transmittance of Mars atmosphere during a local dust storm for various altitudes ($r_{eff} = 1.5\mu m$).

common phenomena seen both on Earth and Mars. They inject a high amount of dust into the atmosphere. During Mars southern spring and summer 0.9 to 2.9×10^{11} kg/km^2 dust devil flux is estimated in [434]. The amount of dust injected into the atmosphere in local and regional dust storms is also reported comparable to dust devils. Accordingly, in a local storm the abundance of dust in the atmosphere can be calculated as 0.145×10^6kg/m^2 (for 2000km^2 area) for the worst case. Mean or effective radius r_{eff} is another important parameter to examine the effect of dust on the scattering. We assume the abundance of dust is 0.145×10^6kg/m^2 in every 49 layers of the atmosphere. According to observation of Mars atmosphere, r_{eff} varies between $1.5\mu m$ and $1.6\mu m$ [435]. Thus, we consider the effect of a local dust storm on THz-band transmission in a Mars-space link at various altitudes for $r_{eff} = 1.6\mu$m.

The results in Fig. 6.6 show that even in a heavy dust storm, transmittance values are close to 0.9 in the low THz band when the altitude is 0, which is the worst case. When the altitude is increased, transmittance values are higher than 0.9 up to 1 THz.

6.5 Conclusion

THz space links can pave the way for services including live video feeding, high-resolution imagery, and virtual reality from space. Apart from its inherent challenges such as molecular absorption loss, THz band communications pose other challenges due to developing THz source and antenna technologies. Therefore, in this study, we discuss the major challenges of THz space links, namely molecular absorption loss, spreading loss, and interference from RAS and EESS. The possible solutions for ground/space links are locating ground stations to high and dry locations, and multiband antennas. Regarding spreading loss, large aperture antennas can be used for ground stations benefiting from radio astronomy optics. Reflect-arrays and UM-MIMO are other solutions.

Chapter 7

CONCLUSION

This thesis delved into the emerging IoE framework, a revolutionary paradigm in ICT that extends human connectivity beyond traditional boundaries. The IoE envisions a comprehensive network architecture mirroring the intricate interconnected systems in nature, integrating a diverse array of ICT technologies across various scales and environments. While this advancement offers numerous opportunities, it also presents significant challenges, particularly in aligning communication technologies with the IoE's intricate and dynamic nature. The thesis examined these challenges and proposed solutions at the physical layer/device level, essential for realizing the IoE. It specifically focused on two unconventional communication paradigms: Molecular communications and Terahertz-band communications. These paradigms are pivotal for surpassing the limitations of existing networks and are crucial in making the IoE a reality. A comprehensive exploration of the challenges and potential solutions associated with these unconventional communication methods was conducted. The thesis introduced the concept of a universal IoE transceiver, a novel device designed to integrate heterogeneous networks within the IoE framework. It discussed transceiver architectures based on graphene and related materials, which show promise for unconventional communication modalities, particularly in the context of the Internet of Bio-Nano Things (IoBNT), an emerging subset of the IoE. Furthermore, the thesis delved into advanced physical layer techniques for practical MC systems and explored effective solutions for facilitating THz-band communication in space. These investigations shed light on the practical aspects of implementing these communication paradigms in real-world IoE scenarios.

The detailed conclusions drawn from the chapters are summarized as follows:

Chapter 1 - Universal Transceivers for the IoE: In this chapter, we introduced the concept of universal IoE transceiver that defines the transceiver architectures, which possess multi-modality in communication and energy harvesting, modularity, tunability, and scalability. Through several practical cases involving also non-conventional communication modalities, e.g., molecular, THz-band communications, which will be relevant in the upcoming IoE landscape, we argued that such universal transceivers that can be scaled down to micro/nanoscales could address the unique IoE challenges, such as interoperability, ubiquitous connectivity, energy efficiency, and miniaturization, and could open up further opportunities in diversifying the IoE applications. Along this direction, key physical layer challenges are outlined with potential solutions, which are centered around the use of novel nanomaterials, such as graphene, that manifest unique electrical, optical, mechanical and biochemical properties.

Chapter 2 - Graphene and Related Materials for the Internet of Bio-Nano Things: In this chapter, we have explored the potential of GRMs and GRM-based technologies to advance the emerging IoBNT paradigm, which particularly aims to extend human connectivity to biological environments. These environments present unique challenges, including the scale of communicating entities and the diverse forms of information exchange. Despite these challenges, we have argued that GRMs, with their remarkable properties, hold great promise for addressing these issues and enabling the development of key IoBNT components. Our discussion centered on practical transceivers of unconventional communication techniques for IoBNT applications, with a focus on GRM-based architectures capable of emitting and detecting unconventional signal forms, such as molecular and very high frequency EM signals. Examples include graphene bioFET-based MC receivers, graphene nanoporous membranes for MC transmitters, graphene plasmonic THz radiators/detectors, and GRM-based optoacoustic ultrasonic sources. Moreover, we assessed the potential of existing GRM-based bio-interfacing technologies to inform the design of sophisticated bio-cyber interfaces tailored for IoBNT applications.

These technologies include biosensors, neural interfaces, and stimuli-responsive drug delivery devices. We also examined the current capabilities and limitations of GRM technologies for energy harvesting from relevant ambient sources and storing energy to provide uninterrupted power to both artificial and biological devices, i.e., BNTs, within the IoBNT ecosystem. By harnessing the exceptional properties of GRMs, the IoBNT paradigm can transform our understanding of, and interactions with biological systems, fostering unprecedented advancements in healthcare, environmental monitoring, and a myriad of other fields.

Chapter 3 - Frequency-Domain Detection for Molecular Communication: In this chapter, we introduced a frequency-domain detection method for bioFET-based MC receiver architectures. The method exploits receptor cross-reactivity towards various ligand types and utilizes the output noise PSD for detecting the transmitted bits. Considering a microfluidic channel with stochastic molecular interference, we derived BEP for frequency-domain and one-shot time-domain detection methods. Through particle-based spatial stochastic simulations, we validated our theoretical BEP derivations. Our analysis revealed that the proposed frequency-domain detection method provides a significant performance improvement over the time-domain detection method, particularly under high interference conditions in the MC channel. The effectiveness of frequency domain detection is particularly relevant in practical MC scenarios where receivers operate close to saturation due to accumulating residual molecules from previous transmissions or cross-talk.

Chapter 4 - Performance Analysis of Molecular Communication with Cross-Reactive Receptors: This chapter considers the performance of molecular communication via bioFET-based receivers with cross-reactive receptors. Despite the challenges posed by the limited selectivity of the receptors and the resulting interference in signal decoding, FDD techniques can be an effective solution to this problem. FDD enhances the ability to decode signals in the presence of cross-reactive receptors by effectively exploiting the distinct reaction properties of different ligands. The analysis of symbol error probability and channel capacity in this chapter further highlights the potential of biosensor-based MC systems.

Chapter 5 - Terahertz-Band Intersatellite Communication Links: THz band can pave the way for new opportunities by enabling huge bandwidth regarding THz ISLs. Satellite networks, which are one of the study items of 3GPP, can be employed as a part of 5G connectivity to provide ubiquitous coverage. Moreover, the constellation of small satellites with THz communication capability can enable the IoST concept. Large aperture THz optics such as the ALMA in San Pedro de Atacama, Chile are already being used by radio astronomy, which has the potential to drive THz ISLs. On the other hand, there are major challenges that need to be addressed such as high-power TXs to overcome the high spreading loss occurring between satellites.

Chapter 6 - Terahertz Wireless Communications in Space: THz space links can pave the way for services including live video feeding, high-resolution imagery, and virtual reality from space. Apart from its inherent challenges such as molecular absorption loss, THz band communications pose other challenges due to developing THz source and antenna technologies. Therefore, in this chapter, we discuss the major challenges of THz space links, namely molecular absorption loss, spreading loss, and interference from RAS and EESS. The possible solutions for ground/space links are locating ground stations to high and dry locations, and multiband antennas. Regarding spreading loss, large aperture antennas can be used for ground stations benefiting from radio astronomy optics. Reflect-arrays and UM-MIMO are other solutions.

BIBLIOGRAPHY

[1] S. Ghafoor, N. Boujnah, M. H. Rehmani, and A. Davy, "Mac protocols for terahertz communication: A comprehensive survey," *arXiv preprint arXiv:1904.11441v2*, 2019.

[2] M. Kuscu, H. Ramezani, E. Dinc, S. Akhavan, and O. B. Akan, "Fabrication and microfluidic analysis of graphene-based molecular communication receiver for internet of nano things (iont)," *Scientific Reports*, vol. In Press, 2021.

[3] M. Kuscu and B. D. Unluturk, "Internet of bio-nano things: A review of applications, enabling technologies and key challenges," *arXiv preprint arXiv:2112.09249*, 2021.

[4] M. Kuscu, H. Ramezani, E. Dinc, S. Akhavan, and O. B. Akan, "Fabrication and microfluidic analysis of graphene-based molecular communication receiver for internet of nano things (iont)," *Scientific reports*, vol. 11, no. 1, pp. 1–20, 2021.

[5] M. Kuscu, E. Dinc, B. A. Bilgin, H. Ramezani, and O. B. Akan, "Transmitter and receiver architectures for molecular communications: A survey on physical design with modulation, coding, and detection techniques," *Proceedings of the IEEE*, vol. 107, no. 7, pp. 1302–1341, 2019.

[6] D. A. Bandurin, D. Svintsov, I. Gayduchenko, S. G. Xu, A. Principi, M. Moskotin, I. Tretyakov, D. Yagodkin, S. Zhukov, T. Taniguchi *et al.*, "Resonant terahertz detection using graphene plasmons," *Nature communications*, vol. 9, no. 1, pp. 1–8, 2018.

[7] S. H. Lee, Y. Lee, and J. J. Yoh, "Reduced graphene oxide coated polydimethylsiloxane film as an optoacoustic transmitter for high pressure and high frequency ultrasound generation," *Applied Physics Letters*, vol. 106, no. 8, p. 081911, 2015.

[8] J. Kim, M. Kim, M.-S. Lee, K. Kim, S. Ji, Y.-T. Kim, J. Park, K. Na, K.-H. Bae, H. Kyun Kim *et al.*, "Wearable smart sensor systems integrated on soft contact lenses for wireless ocular diagnostics," *Nature communications*, vol. 8, no. 1, pp. 1–8, 2017.

[9] J.-H. Lee, K. Y. Lee, M. K. Gupta, T. Y. Kim, D.-Y. Lee, J. Oh, C. Ryu, W. J. Yoo, C.-Y. Kang, S.-J. Yoon *et al.*, "Highly stretchable piezoelectric-pyroelectric hybrid nanogenerator," *Advanced Materials*, vol. 26, no. 5, pp. 765–769, 2014.

[10] J. Li, S. Sollami Delekta, P. Zhang, S. Yang, M. R. Lohe, X. Zhuang, X. Feng, and M. Ostling, "Scalable fabrication and integration of graphene microsupercapacitors through full inkjet printing," *ACS nano*, vol. 11, no. 8, pp. 8249–8256, 2017.

[11] Z.-S. Wu, K. Parvez, X. Feng, and K. Müllen, "Graphene-based in-plane micro-supercapacitors with high power and energy densities," *Nature communications*, vol. 4, no. 1, pp. 1–8, 2013.

[12] M. Civas, T. Yilmaz, and O. B. Akan, "Terahertz band intersatellite communication links," in *Next Generation Wireless Terahertz Communication Networks*. CRC Press, pp. 337–354.

[13] I. F. Akyildiz, A. Kak, and S. Nie, "6g and beyond: The future of wireless communications systems," *IEEE Access*, vol. 8, pp. 133 995–134 030, 2020.

[14] I. F. Akyildiz, M. Pierobon, and S. Balasubramaniam, "Moving forward with molecular communication: From theory to human health applications [point of view]," *Proceedings of the IEEE*, vol. 107, no. 5, pp. 858–865, 2019.

[15] A. Song, M. Stojanovic, and M. Chitre, "Editorial underwater acoustic communications: Where we stand and what is next?" *IEEE Journal of Oceanic Engineering*, vol. 44, no. 1, 2019.

[16] O. B. Akan, O. Cetinkaya, C. Koca, and M. Ozger, "Internet of hybrid energy harvesting things," *IEEE Internet of Things Journal*, vol. 5, no. 2, pp. 736–746, 2018.

[17] T. Long, M. Ozger, O. Cetinkaya, and O. B. Akan, "Energy neutral internet of drones," *IEEE Communications Magazine*, vol. 56, no. 1, pp. 22–28, 2018.

[18] P. Kamalinejad, C. Mahapatra, Z. Sheng, S. Mirabbasi, V. C. Leung, and Y. L. Guan, "Wireless energy harvesting for the internet of things," *IEEE Communications Magazine*, vol. 53, no. 6, pp. 102–108, 2015.

[19] E. Dinc, M. Kuscu, B. A. Bilgin, and O. B. Akan, "Internet of everything: A unifying framework beyond internet of things," in *Harnessing the Internet of Everything (IoE) for Accelerated Innovation Opportunities*. IGI Global, 2019, pp. 1–30.

[20] I. F. Akyildiz, M. Pierobon, S. Balasubramaniam, and Y. Koucheryavy, "The internet of bio-nano things," *IEEE Communications Magazine*, vol. 53, no. 3, pp. 32–40, 2015.

[21] S. Basagni, V. Di Valerio, P. Gjanci, and C. Petrioli, "Marlin-q: Multi-modal communications for reliable and low-latency underwater data delivery," *Ad Hoc Networks*, vol. 82, pp. 134–145, 2019.

[22] Z. Zhao, C. Liu, W. Qu, and T. Yu, "An energy efficiency multi-level transmission strategy based on underwater multimodal communication in uwsns," in *IEEE INFOCOM 2020-IEEE Conference on Computer Communications*. IEEE, 2020, pp. 1579–1587.

[23] F. Campagnaro, P. Casari, M. Zorzi, and R. Diamant, "Optimal transmission scheduling in small multimodal underwater networks," *IEEE Wireless Communications Letters*, vol. 8, no. 2, pp. 368–371, 2018.

[24] S. Guoqiang, C. Yanming, Z. Chao, and Z. Yanxu, "Design and implementation of a smart iot gateway," in *2013 IEEE International Conference on Green Computing and Communications and IEEE Internet of Things and IEEE Cyber, Physical and Social Computing*. IEEE, 2013, pp. 720–723.

[25] A. Zalonis, A. Polydoros *et al.*, "Flexible-radio: A general framework with phy-layer algorithm-design insights," in *EUROCON 2005-The International Conference on" Computer as a Tool"*, vol. 1. IEEE, 2005, pp. 120–123.

[26] H. Arslan, *Cognitive radio, software defined radio, and adaptive wireless systems*. Springer, 2007.

[27] O. Cetinkaya, M. Ozger, and O. Akan, "Internet of energy harvesting cognitive radios," *Towards Cognitive IoT Networks*, pp. 125–150, 2020.

[28] M. Kuscu and O. B. Akan, "Modeling and analysis of sinw biofet as molecular antenna for bio-cyber interfaces towards the internet of bio-nanothings," in *2015 IEEE 2nd World Forum on Internet of Things (WF-IoT)*. IEEE, 2015, pp. 669–674.

[29] Y. Koucheryavy, A. Yastrebova, D. P. Martins, and S. Balasubramaniam, "A review on bio-cyber interfaces for intrabody molecular communications systems," *arXiv preprint arXiv:2104.14944*, 2021.

[30] T. Nakano, S. Kobayashi, T. Suda, Y. Okaie, Y. Hiraoka, and T. Haraguchi, "Externally controllable molecular communication," *IEEE Journal on Selected Areas in Communications*, vol. 32, no. 12, pp. 2417–2431, 2014.

[31] J. A. Foster and K.-A. M. Neufeld, "Gut–brain axis: how the microbiome influences anxiety and depression," *Trends in neurosciences*, vol. 36, no. 5, pp. 305–312, 2013.

[32] M. G. Schöner, R. Simon, and C. R. Schöner, "Acoustic communication in plant–animal interactions," *Current Opinion in Plant Biology*, vol. 32, pp. 88–95, 2016.

[33] P. Harkes, J. J. M. Van Steenbrugge, S. J. J. Van Den Elsen, A. K. A. Suleiman, J. J. De Haan, M. H. M. Holterman, and J. Helder, "Shifts in the active rhizobiome paralleling low meloidogyne chitwoodi densities in fields under prolonged organic soil management," *Frontiers in plant science*, vol. 10, p. 1697, 2020.

[34] O. Cetinkaya and G. V. Merrett, "Efficient deployment of uav-powered sensors for optimal coverage and connectivity," in *2020 IEEE Wireless Communications and Networking Conference (WCNC)*. IEEE, 2020, pp. 1–6.

[35] O. Cetinkaya, D. Balsamo, and G. V. Merrett, "Internet of mimo things: Uav-assisted wireless-powered networks for future smart cities," *IEEE Internet of Things Magazine*, vol. 3, no. 1, pp. 8–13, 2020.

[36] T. Khan, M. Civas, O. Cetinkaya, N. A. Abbasi, and O. B. Akan, "Nanosensor networks for smart health care," in *Nanosensors for Smart Cities*. Elsevier, 2020, pp. 387–403.

[37] C. Grau, R. Ginhoux, A. Riera, T. L. Nguyen, H. Chauvat, M. Berg, J. L. Amengual, A. Pascual-Leone, and G. Ruffini, "Conscious brain-to-brain communication in humans using non-invasive technologies," *PloS one*, vol. 9, no. 8, p. e105225, 2014.

[38] O. B. Akan, H. Ramezani, M. Civas, O. Cetinkaya, B. A. Bilgin, and N. A. Abbasi, "Information and communication theoretical understanding and treatment of spinal cord injuries: State-of-the-art and research challenges," *IEEE Reviews in Biomedical Engineering*, 2021.

[39] H. Kaushal and G. Kaddoum, "Free space optical communication: challenges and mitigation techniques," *arXiv preprint arXiv:1506.04836*, 2015.

[40] A. Eslami, S. Vangala, and H. Pishro-Nik, "Hybrid channel codes for efficient fso/rf communication systems," *IEEE Transactions on Communications*, vol. 58, no. 10, pp. 2926–2938, 2010.

[41] W. Guo, I. Atthanayake, and P. Thomas, "Vertical underwater molecular communications via buoyancy: Gaussian velocity distribution of signal," in *ICC 2020-2020 IEEE International Conference on Communications (ICC)*. IEEE, 2020, pp. 1–6.

[42] J. Famaey, R. Berkvens, G. Ergeerts, E. De Poorter, F. Van den Abeele, T. Bolckmans, J. Hoebeke, and M. Weyn, "Flexible multimodal sub-gigahertz communication for heterogeneous internet of things applications," *IEEE Communications Magazine*, vol. 56, no. 7, pp. 146–153, 2018.

[43] S. S. Basu, J. Haxhibeqiri, M. Baert, B. Moons, and J. Hoebeke, "An energy-efficient multi-modal iot system leveraging nb-iot and ble," in *2020 IEEE International Conference on Internet of Things and Intelligence System (IoTaIS)*. IEEE, 2021, pp. 30–36.

[44] E. Dinc and O. B. Akan, "Theoretical limits on multiuser molecular communication in internet of nano-bio things," *IEEE transactions on nanobioscience*, vol. 16, no. 4, pp. 266–270, 2017.

[45] M. Kuscu and O. B. Akan, "Channel sensing in molecular communications with single type of ligand receptors," *IEEE Transactions on Communications*, vol. 67, no. 10, pp. 6868–6884, 2019.

[46] L. Lin, C. Yang, M. Ma, S. Ma, and H. Yan, "A clock synchronization method for molecular nanomachines in bionanosensor networks," *IEEE Sensors Journal*, vol. 16, no. 19, pp. 7194–7203, 2016.

[47] V. Jamali, A. Ahmadzadeh, and R. Schober, "Symbol synchronization for diffusive molecular communication systems," in *2017 IEEE International Conference on Communications (ICC)*. IEEE, 2017, pp. 1–7.

[48] S. Han, R. Chen, Y. Noh, and M. Gerla, "Real-time video streaming from mobile underwater sensors," in *Proceedings of the International Conference on Underwater Networks & Systems*, 2014, pp. 1–8.

[49] R. K. Gupta, Q. Shi, L. Dhakar, T. Wang, C. H. Heng, and C. Lee, "Broadband energy harvester using non-linear polymer spring and electromagnetic/triboelectric hybrid mechanism," *Scientific reports*, vol. 7, no. 1, pp. 1–13, 2017.

[50] M.-L. Seol, J.-W. Han, S.-J. Park, S.-B. Jeon, and Y.-K. Choi, "Hybrid energy harvester with simultaneous triboelectric and electromagnetic generation from an embedded floating oscillator in a single package," *Nano Energy*, vol. 23, pp. 50–59, 2016.

[51] Y. Liu, C.-Y. Tsao, E. Kim, T. Tschirhart, J. L. Terrell, W. E. Bentley, and G. F. Payne, "Using a redox modality to connect synthetic biology to electronics: Hydrogel-based chemo-electro signal transduction for molecular communication," *Advanced healthcare materials*, vol. 6, no. 1, p. 1600908, 2017.

[52] L. Grebenstein, J. Kirchner, R. S. Peixoto, W. Zimmermann, F. Irnstorfer, W. Wicke, A. Ahmadzadeh, V. Jamali, G. Fischer, R. Weigel *et al.*, "Biological optical-to-chemical signal conversion interface: A small-scale modulator for molecular communications," *IEEE transactions on nanobioscience*, vol. 18, no. 1, pp. 31–42, 2018.

[53] E. VanArsdale, J. Pitzer, G. F. Payne, and W. E. Bentley, "Redox electrochemistry to interrogate and control biomolecular communication," *Iscience*, vol. 23, no. 9, p. 101545, 2020.

[54] T. A. Dixon, T. C. Williams, and I. S. Pretorius, "Sensing the future of bio-informational engineering," *Nature Communications*, vol. 12, no. 1, pp. 1–12, 2021.

[55] H. Huang, L. Tao, F. Liu, L. Ji, Y. Hu, M. M.-C. Cheng, P.-Y. Chen, and D. Akinwande, "Chemical-sensitive graphene modulator with a memory effect for internet-of-things applications," *Microsystems & nanoengineering*, vol. 2, no. 1, p. 025021, 2016.

[56] M. Hajizadegan, M. Sakhdari, L. Zhu, Q. Cui, H. Huang, M. M. Cheng, J. C. Hung, and P.-Y. Chen, "Graphene sensing modulator: Toward low-noise, self-powered wireless microsensors," *IEEE Sensors Journal*, vol. 17, no. 22, pp. 7239–7247, 2017.

[57] A. C. Ferrari, F. Bonaccorso, V. Fal'Ko, K. S. Novoselov, S. Roche, P. Bøggild, S. Borini, F. H. Koppens, V. Palermo, N. Pugno *et al.*, "Science and technology roadmap for graphene, related two-dimensional crystals, and hybrid systems," *Nanoscale*, vol. 7, no. 11, pp. 4598–4810, 2015.

[58] Q. Zhou, J. Zheng, S. Onishi, M. Crommie, and A. K. Zettl, "Graphene electrostatic microphone and ultrasonic radio," *Proceedings of the National Academy of Sciences*, vol. 112, no. 29, pp. 8942–8946, 2015.

[59] Q. Zhou and A. Zettl, "Electrostatic graphene loudspeaker," *Applied Physics Letters*, vol. 102, no. 22, p. 223109, 2013.

[60] S. Xu, B. Man, S. Jiang, C. Chen, C. Yang, M. Liu, X. Gao, Z. Sun, and C. Zhang, "Flexible and transparent graphene-based loudspeakers," *Applied Physics Letters*, vol. 102, no. 15, p. 151902, 2013.

[61] T. Tu, Z.-Y. Ju, Y.-T. Li, G.-Y. Gou, Y. Tian, F. Wu, Z.-Y. Yan, H.-F. Liu, T.-Z. Yang, Y. Yang *et al.*, "A novel thermal acoustic device based on vertical graphene film," *AIP Advances*, vol. 9, no. 7, p. 075302, 2019.

[62] M. Romagnoli, V. Sorianello, M. Midrio, F. H. Koppens, C. Huyghebaert, D. Neumaier, P. Galli, W. Templ, A. D'Errico, and A. C. Ferrari, "Graphene-based integrated photonics for next-generation datacom and telecom," *Nature Reviews Materials*, vol. 3, no. 10, pp. 392–414, 2018.

[63] J. S. Gomez-Diaz and J. Perruisseau-Carrier, "Microwave to thz properties of graphene and potential antenna applications," in *2012 International Symposium on Antennas and Propagation (ISAP)*. IEEE, 2012, pp. 239–242.

[64] X. Huang, T. Leng, K. H. Chang, J. C. Chen, K. S. Novoselov, and Z. Hu, "Graphene radio frequency and microwave passive components for low cost wearable electronics," *2D Materials*, vol. 3, no. 2, 2016.

[65] S. Liu, C. Zhang, M. Hu, X. Chen, P. Zhang, S. Gong, T. Zhao, and R. Zhong, "Coherent and tunable terahertz radiation from graphene surface plasmon polaritons excited by an electron beam," *Applied Physics Letters*, vol. 104, no. 20, p. 201104, 2014.

[66] J. M. Jornet and I. F. Akyildiz, "Graphene-based plasmonic nano-transceiver for terahertz band communication," in *The 8th European conference on antennas and propagation (EuCAP 2014)*. IEEE, 2014, pp. 492–496.

[67] P. K. Singh, G. Aizin, N. Thawdar, M. Medley, and J. M. Jornet, "Graphene-based plasmonic phase modulator for terahertz-band communication," in *2016 10th European Conference on Antennas and Propagation (EuCAP)*. IEEE, 2016, pp. 1–5.

[68] S. Szunerits and R. Boukherroub, "Graphene-based biosensors," *Interface focus*, vol. 8, no. 3, p. 20160132, 2018.

[69] D. K. H. Tsang, T. J. Lieberthal, C. Watts, I. E. Dunlop, S. Ramadan, E. Armando, and N. Klein, "Chemically functionalised graphene fet biosensor for the label-free sensing of exosomes," *Scientific reports*, vol. 9, no. 1, pp. 1–10, 2019.

[70] M. I. Walker, K. Ubych, V. Saraswat, E. A. Chalklen, P. Braeuninger-Weimer, S. Caneva, R. S. Weatherup, S. Hofmann, and U. F. Keyser, "Extrinsic cation selectivity of 2d membranes," *ACS nano*, vol. 11, no. 2, pp. 1340–1346, 2017.

[71] S. Manzeli, D. Ovchinnikov, D. Pasquier, O. V. Yazyev, and A. Kis, "2d transition metal dichalcogenides," *Nature Reviews Materials*, vol. 2, no. 8, pp. 1–15, 2017.

[72] D. Sarkar, W. Liu, X. Xie, A. C. Anselmo, S. Mitragotri, and K. Banerjee, "Mos2 field-effect transistor for next-generation label-free biosensors," *ACS nano*, vol. 8, no. 4, pp. 3992–4003, 2014.

[73] O. Lopez-Sanchez, D. Lembke, M. Kayci, A. Radenovic, and A. Kis, "Ultrasensitive photodetectors based on monolayer mos 2," *Nature nanotechnology*, vol. 8, no. 7, pp. 497–501, 2013.

[74] B. Li, S. Zu, J. Zhou, Q. Jiang, B. Du, H. Shan, Y. Luo, Z. Liu, X. Zhu, and Z. Fang, "Single-nanoparticle plasmonic electro-optic modulator based on mos2 monolayers," *ACS nano*, vol. 11, no. 10, pp. 9720–9727, 2017.

[75] Z. Sun, A. Martinez, and F. Wang, "Optical modulators with 2d layered materials," *Nature Photonics*, vol. 10, no. 4, pp. 227–238, 2016.

[76] Y. Zhou, M. Zhang, Z. Guo, L. Miao, S.-T. Han, Z. Wang, X. Zhang, H. Zhang, and Z. Peng, "Recent advances in black phosphorus-based photonics, electronics, sensors and energy devices," *Materials Horizons*, vol. 4, no. 6, pp. 997–1019, 2017.

[77] D. Purdie, N. Pugno, T. Taniguchi, K. Watanabe, A. Ferrari, and A. Lombardo, "Cleaning interfaces in layered materials heterostructures," *Nature communications*, vol. 9, no. 1, pp. 1–12, 2018.

[78] T. Mueller, F. Xia, and P. Avouris, "Graphene photodetectors for high-speed optical communications," *Nature photonics*, vol. 4, no. 5, pp. 297–301, 2010.

[79] M. Mittendorff, S. Winnerl, J. Kamann, J. Eroms, D. Weiss, H. Schneider, and M. Helm, "Ultrafast graphene-based broadband thz detector," *Applied Physics Letters*, vol. 103, no. 2, p. 021113, 2013.

[80] S. Kovalev, H. A. Hafez, K.-J. Tielrooij, J.-C. Deinert, I. Ilyakov, N. Awari, D. Alcaraz, K. Soundarapandian, D. Saleta, S. Germanskiy *et al.*, "Electrical tunability of terahertz nonlinearity in graphene," *Science advances*, vol. 7, no. 15, p. eabf9809, 2021.

[81] W. Yuan and G. Shi, "Graphene-based gas sensors," *Journal of Materials Chemistry A*, vol. 1, no. 35, pp. 10 078–10 091, 2013.

[82] T.-S. Dinh Le, J. An, Y. Huang, Q. Vo, J. Boonruangkan, T. Tran, S.-W. Kim, G. Sun, and Y.-J. Kim, "Ultrasensitive anti-interference voice recognition by bio-inspired skin-attachable self-cleaning acoustic sensors," *ACS nano*, vol. 13, no. 11, pp. 13 293–13 303, 2019.

[83] K. Yang, D. Bi, Y. Deng, R. Zhang, M. M. U. Rahman, N. A. Ali, M. A. Imran, J. M. Jornet, Q. H. Abbasi, and A. Alomainy, "A comprehensive survey on hybrid communication in context of molecular communication and terahertz communication for body-centric nanonetworks," *IEEE Transactions on Molecular, Biological and Multi-Scale Communications*, vol. 6, no. 2, pp. 107–133, 2020.

[84] S. P. Singh, S. Singh, W. Guo, S. Mishra, and S. Kumar, "Radiation absorption noise for molecular information transfer," *IEEE Access*, vol. 8, pp. 6379–6387, 2020.

[85] D. Rodrigo, O. Limaj, D. Janner, D. Etezadi, F. J. G. De Abajo, V. Pruneri, and H. Altug, "Mid-infrared plasmonic biosensing with graphene," *Science*, vol. 349, no. 6244, pp. 165–168, 2015.

[86] X. Gao, L. Cheng, W. Jiang, X.-K. Li, and F. Xing, "Graphene and its derivatives-based optical sensors," *Frontiers in Chemistry*, vol. 9, p. 5, 2021.

[87] H. Jayakumar, K. Lee, W. S. Lee, A. Raha, Y. Kim, and V. Raghunathan, "Powering the internet of things," in *Proceedings of the 2014 international symposium on Low power electronics and design*, 2014, pp. 375–380.

[88] O. Cetinkaya and O. B. Akan, "Electric-field energy harvesting from lighting elements for battery-less internet of things," *IEEE Access*, vol. 5, pp. 7423–7434, 2017.

[89] ——, "Electric-field energy harvesting in wireless networks," *IEEE Wireless Communications*, vol. 24, no. 2, pp. 34–41, 2017.

[90] E. B. Pehlivanoglu, M. Ozger, O. Cetinkaya, and O. B. Akan, "Harvesting-throughput trade-off for wireless-powered smart grid iot applications: An experimental study," in *2018 IEEE International Conference on Communications (ICC)*. IEEE, 2018, pp. 1–6.

[91] C. Dagdeviren, Z. Li, and Z. L. Wang, "Energy harvesting from the animal/human body for self-powered electronics," *Annual review of biomedical engineering*, vol. 19, pp. 85–108, 2017.

[92] V. Leonov, "Thermoelectric energy harvesting of human body heat for wearable sensors," *IEEE Sensors Journal*, vol. 13, no. 6, pp. 2284–2291, 2013.

[93] M. Amin Karami and D. J. Inman, "Powering pacemakers from heartbeat vibrations using linear and nonlinear energy harvesters," *Applied Physics Letters*, vol. 100, no. 4, p. 042901, 2012.

[94] Q. Zheng, B. Shi, F. Fan, X. Wang, L. Yan, W. Yuan, S. Wang, H. Liu, Z. Li, and Z. L. Wang, "In vivo powering of pacemaker by breathing-driven implanted triboelectric nanogenerator," *Advanced materials*, vol. 26, no. 33, pp. 5851–5856, 2014.

[95] W. Jia, G. Valdés-Ramírez, A. J. Bandodkar, J. R. Windmiller, and J. Wang, "Epidermal biofuel cells: energy harvesting from human perspiration," *Angewandte Chemie International Edition*, vol. 52, no. 28, pp. 7233–7236, 2013.

[96] B. Shi, Z. Li, and Y. Fan, "Implantable energy-harvesting devices," *Advanced Materials*, vol. 30, no. 44, p. 1801511, 2018.

[97] Z. L. Wang and W. Wu, "Nanotechnology-enabled energy harvesting for self-powered micro-/nanosystems," *Angewandte Chemie International Edition*, vol. 51, no. 47, pp. 11 700–11 721, 2012.

[98] I. F. Akyildiz and J. M. Jornet, "Electromagnetic wireless nanosensor networks," *Nano Communication Networks*, vol. 1, no. 1, pp. 3–19, 2010.

[99] M. Wagih, O. Cetinkaya, B. Zaghari, A. S. Weddell, and S. Beeby, "Real-world performance of sub-1 ghz and 2.4 ghz textile antennas for rf-powered body area networks," *IEEE Access*, vol. 8, pp. 133 746–133 756, 2020.

[100] K. Agarwal, R. Jegadeesan, Y.-X. Guo, and N. V. Thakor, "Wireless power transfer strategies for implantable bioelectronics," *IEEE reviews in biomedical engineering*, vol. 10, pp. 136–161, 2017.

[101] J. S. Ho, A. J. Yeh, E. Neofytou, S. Kim, Y. Tanabe, B. Patlolla, R. E. Beygui, and A. S. Poon, "Wireless power transfer to deep-tissue microimplants," *Proceedings of the National Academy of Sciences*, vol. 111, no. 22, pp. 7974–7979, 2014.

[102] S. R. Khan, S. K. Pavuluri, G. Cummins, and M. P. Desmulliez, "Wireless power transfer techniques for implantable medical devices: A review," *Sensors*, vol. 20, no. 12, p. 3487, 2020.

[103] M. Manoufali, K. Bialkowski, B. J. Mohammed, P. C. Mills, and A. Abbosh, "Near-field inductive-coupling link to power a three-dimensional millimeter-size antenna for brain implantable medical devices," *IEEE Transactions on Biomedical Engineering*, vol. 65, no. 1, pp. 4–14, 2017.

[104] Z. Rong, M. S. Leeson, M. D. Higgins, and Y. Lu, "Nano-rectenna powered body-centric nano-networks in the terahertz band," *Healthcare technology letters*, vol. 5, no. 4, pp. 113–117, 2018.

[105] L. Feng, A. Ali, M. Iqbal, F. Ali, I. Raza, M. H. Siddiqi, M. Shafiq, and S. A. Hussain, "Dynamic wireless information and power transfer scheme for nano-empowered vehicular networks," *IEEE Transactions on Intelligent Transportation Systems*, 2020.

[106] Z. Rong, M. S. Leeson, M. D. Higgins, and Y. Lu, "Simultaneous wireless information and power transfer for af relaying nanonetworks in the terahertz band," *Nano Communication Networks*, vol. 14, pp. 1–8, 2017.

[107] W. Guo, Y. Deng, H. B. Yilmaz, N. Farsad, M. Elkashlan, A. Eckford, A. Nallanathan, and C.-B. Chae, "Smiet: Simultaneous molecular information and energy transfer," *IEEE Wireless Communications*, vol. 25, no. 1, pp. 106–113, 2017.

[108] Y. Deng, W. Guo, A. Noel, A. Nallanathan, and M. Elkashlan, "Enabling energy efficient molecular communication via molecule energy transfer," *IEEE Communications Letters*, vol. 21, no. 2, pp. 254–257, 2016.

[109] T. Maleki, N. Cao, S. H. Song, C. Kao, S.-C. Ko, and B. Ziaie, "An ultrasonically powered implantable micro-oxygen generator (imog)," *IEEE transactions on Biomedical Engineering*, vol. 58, no. 11, pp. 3104–3111, 2011.

[110] P. J. Larson and B. C. Towe, "Miniature ultrasonically powered wireless nerve cuff stimulator," in *2011 5th International IEEE/EMBS Conference on Neural Engineering*. IEEE, 2011, pp. 265–268.

[111] M. Donohoe, S. Balasubramaniam, B. Jennings, and J. M. Jornet, "Powering in-body nanosensors with ultrasounds," *IEEE Transactions on Nanotechnology*, vol. 15, no. 2, pp. 151–154, 2015.

[112] M. Donohoe, B. Jennings, J. M. Jornet, and S. Balasubramaniam, "Nanodevice arrays for peripheral nerve fascicle activation using ultrasound energy-harvesting," *IEEE Transactions on Nanotechnology*, vol. 16, no. 6, pp. 919–930, 2017.

[113] S. Balasubramaniam, S. A. Wirdatmadja, M. T. Barros, Y. Koucheryavy, M. Stachowiak, and J. M. Jornet, "Wireless communications for optogenetics-based brain stimulation: Present technology and future challenges," *IEEE Communications Magazine*, vol. 56, no. 7, pp. 218–224, 2018.

[114] O. Cetinkaya, E. Dinc, C. Koca, G. V. Merrett, and O. B. Akan, "Energy-neutral wireless-powered networks," *IEEE Wireless Communications Letters*, vol. 8, no. 5, pp. 1373–1376, 2019.

[115] T. Yucek and H. Arslan, "A survey of spectrum sensing algorithms for cognitive radio applications," *IEEE communications surveys & tutorials*, vol. 11, no. 1, pp. 116–130, 2009.

[116] M. Ozger, O. Cetinkaya, and O. B. Akan, "Energy harvesting cognitive radio networking for iot-enabled smart grid," *Mobile Networks and Applications*, vol. 23, no. 4, pp. 956–966, 2018.

[117] C. Gong and Z. Xu, "Temporal spectrum sensing for optical wireless scattering communications," *Journal of Lightwave Technology*, vol. 33, no. 18, pp. 3890–3900, 2015.

[118] X. Liu, C. Gong, and Z. Xu, "Sequential detection for optical wireless scattering communication," *Journal of Optical Communications and Networking*, vol. 9, no. 9, pp. D86–D95, 2017.

[119] S. Arya and Y. H. Chung, "Spectrum sensing for optical wireless scattering communications over málaga fading-a cooperative approach with hard decision fusion," *IEEE Transactions on Communications*, vol. 69, no. 7, pp. 4615–4631, 2021.

[120] N. Baldo, P. Casari, and M. Zorzi, "Cognitive spectrum access for underwater acoustic communications," in *ICC Workshops-2008 IEEE International Conference on Communications Workshops.* IEEE, 2008, pp. 518–523.

[121] A. O. Bicen, A. B. Sahin, and O. B. Akan, "Spectrum-aware underwater networks: Cognitive acoustic communications," *IEEE Vehicular Technology Magazine*, vol. 7, no. 2, pp. 34–40, 2012.

[122] Y. A. Eldemerdash, O. A. Dobre, and M. Öner, "Signal identification for multiple-antenna wireless systems: Achievements and challenges," *IEEE Communications Surveys & Tutorials*, vol. 18, no. 3, pp. 1524–1551, 2016.

[123] S. Zheng, S. Chen, P. Qi, H. Zhou, and X. Yang, "Spectrum sensing based on deep learning classification for cognitive radios," *China Communications*, vol. 17, no. 2, pp. 138–148, 2020.

[124] K. Tekbıyık, Ö. Akbunar, A. R. Ekti, A. Görçin, G. K. Kurt, and K. A. Qaraqe, "Spectrum sensing and signal identification with deep learning based on spectral correlation function," *arXiv preprint arXiv:2003.08359*, 2020.

[125] H. Sun, W.-Y. Chiu, J. Jiang, A. Nallanathan, and H. V. Poor, "Wideband spectrum sensing with sub-nyquist sampling in cognitive radios," *IEEE Transactions on Signal Processing*, vol. 60, no. 11, pp. 6068–6073, 2012.

[126] A. Brighente, M. Cerutti, M. Nicoli, S. Tomasin, and U. Spagnolini, "Estimation of wideband dynamic mmwave and thz channels for 5g systems and beyond," *IEEE Journal on Selected Areas in Communications*, vol. 38, no. 9, pp. 2026–2040, 2020.

[127] B. Hamdaoui, B. Khalfi, and N. Zorba, "Dynamic spectrum sharing in the age of millimeter-wave spectrum access," *IEEE Network*, vol. 34, no. 5, pp. 164–170, 2020.

[128] Y. Luo, L. Pu, M. Zuba, Z. Peng, and J.-H. Cui, "Challenges and opportunities of underwater cognitive acoustic networks," *IEEE Transactions on Emerging Topics in Computing*, vol. 2, no. 2, pp. 198–211, 2014.

[129] E. Longman, O. Cetinkaya, M. El-Hajjar, and G. V. Merrett, "Wake-up radio-enabled intermittently-powered devices for mesh networking: A power analysis," in *2021 IEEE 18th Annual Consumer Communications & Networking Conference (CCNC)*. IEEE, 2021, pp. 1–6.

[130] S. T. Sliper, O. Cetinkaya, A. S. Weddell, B. Al-Hashimi, and G. V. Merrett, "Energy-driven computing," *Philosophical Transactions of the Royal Society A*, vol. 378, no. 2164, p. 20190158, 2020.

[131] D. Balsamo, O. Cetinkaya, A. R. Arreola, S. C. Wong, G. V. Merrett, and A. S. Weddell, "A control flow for transiently powered energy harvesting sensor systems," *IEEE Sensors Journal*, vol. 20, no. 18, pp. 10 687–10 695, 2020.

[132] N. Islam, S. Pal, S. Balasubramaniam, and S. Misra, "Energy-aware tracking of mobile targets by bacterial nanonetworks," *IEEE Transactions on Mobile Computing*, 2020.

[133] H. G. Bafghi, A. Gohari, M. Mirmohseni, G. Aminian, and M. Nasiri-Kenari, "Diffusion-based molecular communication with limited molecule production rate," *IEEE Transactions on Molecular, Biological and Multi-Scale Communications*, vol. 4, no. 2, pp. 61–72, 2018.

[134] V. Musa, G. Piro, L. A. Grieco, and G. Boggia, "A lean control theoretic approach to energy-harvesting in diffusion-based molecular communications," *IEEE Communications Letters*, vol. 24, no. 5, pp. 981–985, 2020.

[135] A. S. Weddell, M. Magno, G. V. Merrett, D. Brunelli, B. M. Al-Hashimi, and L. Benini, "A survey of multi-source energy harvesting systems," in *2013 Design, Automation & Test in Europe Conference & Exhibition (DATE)*. IEEE, 2013, pp. 905–908.

[136] P. M. Conn, *Pulsatility in neuroendocrine systems*. Academic Press, 2013.

[137] S. Dang, O. Amin, B. Shihada, and M.-S. Alouini, "What should 6g be?" *Nature Electronics*, vol. 3, no. 1, pp. 20–29, 2020.

[138] M.-Y. Li, S.-K. Su, H.-S. P. Wong, and L.-J. Li, "How 2d semiconductors could extend moore's law," 2019.

[139] D. Neumaier, S. Pindl, and M. C. Lemme, "Integrating graphene into semiconductor fabrication lines," *Nature materials*, vol. 18, no. 6, pp. 525–529, 2019.

[140] Z. Xu, X. Dong, and J. Bornemann, "Design of a reconfigurable mimo system for thz communications based on graphene antennas," *IEEE Transactions on Terahertz science and technology*, vol. 4, no. 5, pp. 609–617, 2014.

[141] I. F. Akyildiz and J. M. Jornet, "Realizing ultra-massive mimo (1024× 1024) communication in the (0.06–10) terahertz band," *Nano Communication Networks*, vol. 8, pp. 46–54, 2016.

[142] J. Ma, N. J. Karl, S. Bretin, G. Ducournau, and D. M. Mittleman, "Frequency-division multiplexer and demultiplexer for terahertz wireless links," *Nature communications*, vol. 8, no. 1, pp. 1–8, 2017.

[143] K. Sengupta, T. Nagatsuma, and D. M. Mittleman, "Terahertz integrated electronic and hybrid electronic–photonic systems," *Nature Electronics*, vol. 1, no. 12, pp. 622–635, 2018.

[144] M. Nafari, G. R. Aizin, and J. M. Jornet, "Plasmonic hemt terahertz transmitter based on the dyakonov-shur instability: Performance analysis and impact of nonideal boundaries," *Physical Review Applied*, vol. 10, no. 6, p. 064025, 2018.

[145] F. Bianco, D. Perenzoni, D. Convertino, S. De Bonis, D. Spirito, M. Perenzoni, C. Coletti, M. Vitiello, and A. Tredicucci, "Terahertz detection by epitaxial-graphene field-effect-transistors on silicon carbide," *Applied Physics Letters*, vol. 107, no. 13, p. 131104, 2015.

[146] Q. Xu, B. Schmidt, S. Pradhan, and M. Lipson, "Micrometre-scale silicon electro-optic modulator," *nature*, vol. 435, no. 7040, pp. 325–327, 2005.

[147] K. J. Vahala, "Optical microcavities," *nature*, vol. 424, no. 6950, pp. 839–846, 2003.

[148] M. Cohen, R. Shavit, and Z. Zalevsky, "Enabling high efficiency nanoplasmonics with novel nanoantenna architectures," *Scientific reports*, vol. 5, no. 1, pp. 1–9, 2015.

[149] Y.-J. Lu, J. Kim, H.-Y. Chen, C. Wu, N. Dabidian, C. E. Sanders, C.-Y. Wang, M.-Y. Lu, B.-H. Li, X. Qiu *et al.*, "Plasmonic nanolaser using epitaxially grown silver film," *science*, vol. 337, no. 6093, pp. 450–453, 2012.

[150] M. Klein, B. H. Badada, R. Binder, A. Alfrey, M. McKie, M. R. Koehler, D. G. Mandrus, T. Taniguchi, K. Watanabe, B. J. LeRoy *et al.*, "2d semiconductor nonlinear plasmonic modulators," *Nature communications*, vol. 10, no. 1, pp. 1–7, 2019.

[151] S. Yu, X. Wu, Y. Wang, X. Guo, and L. Tong, "2d materials for optical modulation: challenges and opportunities," *Advanced Materials*, vol. 29, no. 14, p. 1606128, 2017.

[152] C. Haffner, W. Heni, Y. Fedoryshyn, J. Niegemann, A. Melikyan, D. L. Elder, B. Baeuerle, Y. Salamin, A. Josten, U. Koch *et al.*, "All-plasmonic mach–zehnder modulator enabling optical high-speed communication at the microscale," *Nature Photonics*, vol. 9, no. 8, pp. 525–528, 2015.

[153] R. B. Schoch, J. Han, and P. Renaud, "Transport phenomena in nanofluidics," *Reviews of modern physics*, vol. 80, no. 3, p. 839, 2008.

[154] J. Li and D. J. Mooney, "Designing hydrogels for controlled drug delivery," *Nature Reviews Materials*, vol. 1, no. 12, pp. 1–17, 2016.

[155] Q. Shi, H. Liu, D. Tang, Y. Li, X. Li, and F. Xu, "Bioactuators based on stimulus-responsive hydrogels and their emerging biomedical applications," *NPG Asia Materials*, vol. 11, no. 1, pp. 1–21, 2019.

[156] M. Schroter, M. Claus, P. Sakalas, M. Haferlach, and D. Wang, "Carbon nanotube fet technology for radio-frequency electronics: State-of-the-art overview," *IEEE Journal of the Electron Devices Society*, vol. 1, no. 1, pp. 9–20, 2013.

[157] K. Jensen, J. Weldon, H. Garcia, and A. Zettl, "Nanotube radio," *Nano letters*, vol. 7, no. 11, pp. 3508–3511, 2007.

[158] C. Rutherglen and P. Burke, "Carbon nanotube radio," *Nano letters*, vol. 7, no. 11, pp. 3296–3299, 2007.

[159] P. Burke and C. Rutherglen, "Towards a single-chip, implantable rfid system: is a single-cell radio possible?" *Biomedical microdevices*, vol. 12, no. 4, pp. 589–596, 2010.

[160] P. J. Burke, S. Li, and Z. Yu, "Quantitative theory of nanowire and nanotube antenna performance," *IEEE transactions on nanotechnology*, vol. 5, no. 4, pp. 314–334, 2006.

[161] C. Rutherglen, D. Jain, and P. Burke, "Nanotube electronics for radiofrequency applications," *Nature nanotechnology*, vol. 4, no. 12, pp. 811–819, 2009.

[162] T. Nan, H. Lin, Y. Gao, A. Matyushov, G. Yu, H. Chen, N. Sun, S. Wei, Z. Wang, M. Li *et al.*, "Acoustically actuated ultra-compact nems magnetoelectric antennas," *Nature communications*, vol. 8, no. 1, pp. 1–8, 2017.

[163] H. Chen, X. Liang, C. Dong, Y. He, N. Sun, M. Zaeimbashi, Y. He, Y. Gao, P. V. Parimi, H. Lin *et al.*, "Ultra-compact mechanical antennas," *Applied Physics Letters*, vol. 117, no. 17, p. 170501, 2020.

[164] H. Lin, M. Zaeimbashi, N. Sun, X. Liang, H. Chen, C. Dong, A. Matyushov, X. Wang, Y. Guo, Y. Gao *et al.*, “Nems magnetoelectric antennas for biomedical application,” in *2018 IEEE International Microwave Biomedical Conference (IMBioC)*. IEEE, 2018, pp. 13–15.

[165] H. Tian, Y. Yang, C. Li, W.-T. Mi, M. A. Mohammad, and T.-L. Ren, “A flexible, transparent and ultrathin single-layer graphene earphone,” *RSC Advances*, vol. 5, no. 22, pp. 17 366–17 371, 2015.

[166] J. S. Bunch, A. M. Van Der Zande, S. S. Verbridge, I. W. Frank, D. M. Tanenbaum, J. M. Parpia, H. G. Craighead, and P. L. McEuen, “Electromechanical resonators from graphene sheets,” *Science*, vol. 315, no. 5811, pp. 490–493, 2007.

[167] A. K. Al-Mashaal, G. S. Wood, A. Torin, E. Mastropaolo, M. J. Newton, and R. Cheung, “Tunable graphene-polymer resonators for audio frequency sensing applications,” *IEEE Sensors Journal*, vol. 19, no. 2, pp. 465–473, 2018.

[168] D. Todorović, A. Matković, M. Milićević, D. Jovanović, R. Gajić, I. Salom, and M. Spasenović, “Multilayer graphene condenser microphone,” *2D Materials*, vol. 2, no. 4, p. 045013, 2015.

[169] M. Civas, O. Cetinkaya, M. Kuscu, and O. B. Akan, “Universal transceivers: Opportunities and future directions for the internet of everything (ioe),” *arXiv preprint arXiv:2107.01028*, 2021.

[170] O. B. Akan, E. Dinc, M. Kuscu, O. Cetinkaya, and B. A. Bilgin, “Internet of everything (ioe)–from molecules to the universe,” *arXiv preprint arXiv:2301.03374*, 2022.

[171] S. Mann, “Life as a nanoscale phenomenon,” *Angewandte Chemie International Edition*, vol. 47, no. 29, pp. 5306–5320, 2008.

[172] O. B. Akan, H. Ramezani, T. Khan, N. A. Abbasi, and M. Kuscu, “Fundamentals of molecular information and communication science,” *Proc. IEEE*, vol. 105, no. 2, pp. 306–318, 2016.

[173] M. Tamagnone, J. Gomez-Diaz, J. R. Mosig, and J. Perruisseau-Carrier, “Reconfigurable terahertz plasmonic antenna concept using a graphene stack,” *Applied Physics Letters*, vol. 101, no. 21, p. 214102, 2012.

[174] S. Hwan Lee, M.-a. Park, J. J. Yoh, H. Song, E. Yun Jang, Y. Hyup Kim, S. Kang, and Y. Seop Yoon, “Reduced graphene oxide coated thin aluminum film as an optoacoustic transmitter for high pressure and high frequency ultrasound generation,” *Applied Physics Letters*, vol. 101, no. 24, p. 241909, 2012.

[175] D. Kwong Hong Tsang, T. J. Lieberthal, C. Watts, I. E. Dunlop, S. Ramadan, A. E. del Rio Hernandez, and N. Klein, "Chemically functionalised graphene fet biosensor for the label-free sensing of exosomes," *Scientific reports*, vol. 9, no. 1, pp. 1–10, 2019.

[176] C. L. Weaver, J. M. LaRosa, X. Luo, and X. T. Cui, "Electrically controlled drug delivery from graphene oxide nanocomposite films," *ACS nano*, vol. 8, no. 2, pp. 1834–1843, 2014.

[177] K. S. Novoselov, A. K. Geim, S. V. Morozov, D. Jiang, Y. Zhang, S. V. Dubonos, I. V. Grigorieva, and A. A. Firsov, "Electric Field Effect in Atomically Thin Carbon Films," *Science*, vol. 306, no. 5696, pp. 666–669, Oct. 2004. [Online]. Available: https://www.science.org/doi/10.1126/science.1102896

[178] Z. Zhen and H. Zhu, "Structure and Properties of Graphene," in *Graphene*. Elsevier, 2018, pp. 1–12. [Online]. Available: https://linkinghub.elsevier.com/retrieve/pii/B978012812651600001X

[179] L. Liao, H. Peng, and Z. Liu, "Chemistry Makes Graphene beyond Graphene," *Journal of the American Chemical Society*, vol. 136, no. 35, pp. 12 194–12 200, Sep. 2014. [Online]. Available: https://pubs.acs.org/doi/10.1021/ja5048297

[180] A. Kovtun, E. Treossi, N. Mirotta, A. Scidà, A. Liscio, M. Christian, F. Valorosi, A. Boschi, R. J. Young, C. Galiotis *et al.*, "Benchmarking of graphene-based materials: real commercial products versus ideal graphene," *2D Materials*, vol. 6, no. 2, p. 025006, 2019.

[181] D. Li and R. B. Kaner, "Graphene-Based Materials," *Science*, vol. 320, no. 5880, pp. 1170–1171, May 2008. [Online]. Available: https://www.science.org/doi/10.1126/science.1158180

[182] F. Afshari and M. Ghaffarian, "Electronic properties of zigzag and armchair graphene nanoribbons in the external electric and magnetic fields," *Physica E: Low-dimensional Systems and Nanostructures*, vol. 89, pp. 86–92, May 2017. [Online]. Available: https://linkinghub.elsevier.com/retrieve/pii/S1386947717301182

[183] A. C. Neto, F. Guinea, N. M. Peres, K. S. Novoselov, and A. K. Geim, "The electronic properties of graphene," *Reviews of modern physics*, vol. 81, no. 1, p. 109, 2009.

[184] R. M. Westervelt, "Graphene Nanoelectronics," *Science*, vol. 320, no. 5874, pp. 324–325, Apr. 2008. [Online]. Available: https://www.science.org/doi/10.1126/science.1156936

[185] J.-H. Chen, C. Jang, S. Xiao, M. Ishigami, and M. S. Fuhrer, "Intrinsic and extrinsic performance limits of graphene devices on sio 2," *Nature nanotechnology*, vol. 3, no. 4, pp. 206–209, 2008.

[186] J. Wang, F. Ma, W. Liang, and M. Sun, "Electrical properties and applications of graphene, hexagonal boron nitride (h-bn), and graphene/h-bn heterostructures," *Materials Today Physics*, vol. 2, pp. 6–34, 2017.

[187] F. Yavari and N. Koratkar, "Graphene-Based Chemical Sensors," *The Journal of Physical Chemistry Letters*, vol. 3, no. 13, pp. 1746–1753, Jul. 2012. [Online]. Available: https://pubs.acs.org/doi/10.1021/jz300358t

[188] D. Kireev, K. Sel, B. Ibrahim, N. Kumar, A. Akbari, R. Jafari, and D. Akinwande, "Continuous cuffless monitoring of arterial blood pressure via graphene bioimpedance tattoos," *Nature Nanotechnology*, vol. 17, no. 8, pp. 864–870, 2022.

[189] A. Fabbro, D. Scaini, V. Leon, E. Vázquez, G. Cellot, G. Privitera, L. Lombardi, F. Torrisi, F. Tomarchio, F. Bonaccorso *et al.*, "Graphene-based interfaces do not alter target nerve cells," *ACS nano*, vol. 10, no. 1, pp. 615–623, 2016.

[190] W.-S. Kuo, N.-H. Tai, and T.-W. Chang, "Deformation and fracture in graphene nanosheets," *Composites Part A: Applied Science and Manufacturing*, vol. 51, pp. 56–61, Aug. 2013. [Online]. Available: https://linkinghub.elsevier.com/retrieve/pii/S1359835X13001024

[191] H. Chen, M. B. Müller, K. J. Gilmore, G. G. Wallace, and D. Li, "Mechanically Strong, Electrically Conductive, and Biocompatible Graphene Paper," *Advanced Materials*, vol. 20, no. 18, pp. 3557–3561, Jul. 2008. [Online]. Available: https://onlinelibrary.wiley.com/doi/10.1002/adma.200800757

[192] S. Park, N. Mohanty, J. W. Suk, A. Nagaraja, J. An, R. D. Piner, W. Cai, D. R. Dreyer, V. Berry, and R. S. Ruoff, "Biocompatible, Robust Free-Standing Paper Composed of a TWEEN/Graphene Composite," *Advanced Materials*, vol. 22, no. 15, pp. 1736–1740, Apr. 2010. [Online]. Available: https://onlinelibrary.wiley.com/doi/10.1002/adma.200903611

[193] K. Yang, J. Wan, S. Zhang, Y. Zhang, S.-T. Lee, and Z. Liu, "*In Vivo* Pharmacokinetics, Long-Term Biodistribution, and Toxicology of PEGylated Graphene in Mice," *ACS Nano*, vol. 5, no. 1, pp. 516–522, Jan. 2011. [Online]. Available: https://pubs.acs.org/doi/10.1021/nn1024303

[194] R. R. Nair, P. Blake, A. N. Grigorenko, K. S. Novoselov, T. J. Booth, T. Stauber, N. M. R. Peres, and A. K. Geim, "Fine

Structure Constant Defines Visual Transparency of Graphene," *Science*, vol. 320, no. 5881, pp. 1308–1308, Jun. 2008. [Online]. Available: https://www.science.org/doi/10.1126/science.1156965

[195] K. S. Novoselov, A. K. Geim, S. V. Morozov, D. Jiang, M. I. Katsnelson, I. V. Grigorieva, S. V. Dubonos, and A. A. Firsov, "Two-dimensional gas of massless Dirac fermions in graphene," *Nature*, vol. 438, no. 7065, pp. 197–200, Nov. 2005. [Online]. Available: http://www.nature.com/articles/nature04233

[196] F. Wang, Y. Zhang, C. Tian, C. Girit, A. Zettl, M. Crommie, and Y. R. Shen, "Gate-Variable Optical Transitions in Graphene," *Science*, vol. 320, no. 5873, pp. 206–209, Apr. 2008. [Online]. Available: https://www.science.org/doi/10.1126/science.1152793

[197] F. H. L. Koppens, D. E. Chang, and F. J. García de Abajo, "Graphene Plasmonics: A Platform for Strong Light–Matter Interactions," *Nano Letters*, vol. 11, no. 8, pp. 3370–3377, Aug. 2011. [Online]. Available: https://pubs.acs.org/doi/10.1021/nl201771h

[198] H. Yan, F. Xia, W. Zhu, M. Freitag, C. Dimitrakopoulos, A. A. Bol, G. Tulevski, and P. Avouris, "Infrared Spectroscopy of Wafer-Scale Graphene," *ACS Nano*, vol. 5, no. 12, pp. 9854–9860, Dec. 2011. [Online]. Available: https://pubs.acs.org/doi/10.1021/nn203506n

[199] L. J. Cote, F. Kim, and J. Huang, "LangmuirBlodgett Assembly of Graphite Oxide Single Layers," *Journal of the American Chemical Society*, vol. 131, no. 3, pp. 1043–1049, Jan. 2009. [Online]. Available: https://pubs.acs.org/doi/10.1021/ja806262m

[200] M. Monajjemi, "Liquid-phase exfoliation (LPE) of graphite towards graphene: An ab initio study," *Journal of Molecular Liquids*, vol. 230, pp. 461–472, Mar. 2017. [Online]. Available: https://linkinghub.elsevier.com/retrieve/pii/S016773221630633X

[201] Y.-S. Li, J.-L. Liao, S.-Y. Wang, and W.-H. Chiang, "Intercalation-assisted longitudinal unzipping of carbon nanotubes for green and scalable synthesis of graphene nanoribbons," *Scientific Reports*, vol. 6, no. 1, p. 22755, Sep. 2016. [Online]. Available: http://www.nature.com/articles/srep22755

[202] L. Jiao, L. Zhang, X. Wang, G. Diankov, and H. Dai, "Narrow graphene nanoribbons from carbon nanotubes," *Nature*, vol. 458, no. 7240, pp. 877–880, Apr. 2009. [Online]. Available: http://www.nature.com/articles/nature07919

[203] K. Kim, A. Sussman, and A. Zettl, "Graphene Nanoribbons Obtained by Electrically Unwrapping Carbon Nanotubes," *ACS Nano*, vol. 4, no. 3, pp.

1362–1366, Mar. 2010. [Online]. Available: https://pubs.acs.org/doi/10.1021/nn901782g

[204] A. L. Higginbotham, D. V. Kosynkin, A. Sinitskii, Z. Sun, and J. M. Tour, "Lower-Defect Graphene Oxide Nanoribbons from Multiwalled Carbon Nanotubes," *ACS Nano*, vol. 4, no. 4, pp. 2059–2069, Apr. 2010. [Online]. Available: https://pubs.acs.org/doi/10.1021/nn100118m

[205] Z. Yan, Z. Peng, and J. M. Tour, "Chemical Vapor Deposition of Graphene Single Crystals," *Accounts of Chemical Research*, vol. 47, no. 4, pp. 1327–1337, Apr. 2014. [Online]. Available: https://pubs.acs.org/doi/10.1021/ar4003043

[206] G. Yazdi, T. Iakimov, and R. Yakimova, "Epitaxial Graphene on SiC: A Review of Growth and Characterization," *Crystals*, vol. 6, no. 5, p. 53, May 2016. [Online]. Available: http://www.mdpi.com/2073-4352/6/5/53

[207] B. D. Unluturk, A. O. Bicen, and I. F. Akyildiz, "Genetically engineered bacteria-based biotransceivers for molecular communication," *IEEE Transactions on Communications*, vol. 63, no. 4, pp. 1271–1281, 2015.

[208] M. Egan, M. Kuscu, M. T. Barros, M. Booth, A. Llopis-Lorente, M. Magarini, D. P. Martins, M. Schäfer, and P. Stano, "Toward interdisciplinary synergies in molecular communications: Perspectives from synthetic biology, nanotechnology, communications engineering and philosophy of science," *Life*, vol. 13, no. 1, p. 208, 2023.

[209] C. A. Söldner, E. Socher, V. Jamali, W. Wicke, A. Ahmadzadeh, H.-G. Breitinger, A. Burkovski, K. Castiglione, R. Schober, and H. Sticht, "A survey of biological building blocks for synthetic molecular communication systems," *IEEE Communications Surveys & Tutorials*, vol. 22, no. 4, pp. 2765–2800, 2020.

[210] A. Economou, C. Kokkinos, and M. Prodromidis, "Flexible plastic, paper and textile lab-on-a chip platforms for electrochemical biosensing," *Lab on a Chip*, vol. 18, no. 13, pp. 1812–1830, 2018.

[211] A. Béraud, M. Sauvage, C. M. Bazán, M. Tie, A. Bencherif, and D. Bouilly, "Graphene field-effect transistors as bioanalytical sensors: design, operation and performance," *Analyst*, vol. 146, no. 2, pp. 403–428, 2021.

[212] G. Seo, G. Lee, M. J. Kim, S.-H. Baek, M. Choi, K. B. Ku, C.-S. Lee, S. Jun, D. Park, H. G. Kim *et al.*, "Rapid detection of covid-19 causative virus (sars-cov-2) in human nasopharyngeal swab specimens using field-effect transistor-based biosensor," *ACS nano*, vol. 14, no. 4, pp. 5135–5142, 2020.

[213] K.-I. Chen, B.-R. Li, and Y.-T. Chen, "Silicon nanowire field-effect transistor-based biosensors for biomedical diagnosis and cellular recording investigation," *Nano today*, vol. 6, no. 2, pp. 131–154, 2011.

[214] M. Curreli, R. Zhang, F. N. Ishikawa, H.-K. Chang, R. J. Cote, C. Zhou, and M. E. Thompson, "Real-time, label-free detection of biological entities using nanowire-based fets," *IEEE Transactions on nanotechnology*, vol. 7, no. 6, pp. 651–667, 2008.

[215] D. P. Tran, T. T. T. Pham, B. Wolfrum, A. Offenhäusser, and B. Thierry, "Cmos-compatible silicon nanowire field-effect transistor biosensor: Technology development toward commercialization," *Materials*, vol. 11, no. 5, p. 785, 2018.

[216] Y. Huang, X. Dong, Y. Liu, L.-J. Li, and P. Chen, "Graphene-based biosensors for detection of bacteria and their metabolic activities," *Journal of Materials Chemistry*, vol. 21, no. 33, pp. 12 358–12 362, 2011.

[217] T. Bungon, C. Haslam, S. Damiati, B. O'Driscoll, T. Whitley, P. Davey, G. Siligardi, J. Charmet, and S. A. Awan, "Graphene fet sensors for alzheimer's disease protein biomarker clusterin detection," *Frontiers in Molecular Biosciences*, vol. 8, 2021.

[218] M. T. Hwang, M. Heiranian, Y. Kim, S. You, J. Leem, A. Taqieddin, V. Faramarzi, Y. Jing, I. Park, A. M. van der Zande *et al.*, "Ultrasensitive detection of nucleic acids using deformed graphene channel field effect biosensors," *Nature communications*, vol. 11, no. 1, pp. 1–11, 2020.

[219] D. De Fazio, D. G. Purdie, A. K. Ott, P. Braeuninger-Weimer, T. Khodkov, S. Goossens, T. Taniguchi, K. Watanabe, P. Livreri, F. H. Koppens *et al.*, "High-mobility, wet-transferred graphene grown by chemical vapor deposition," *ACS nano*, vol. 13, no. 8, pp. 8926–8935, 2019.

[220] X. Zhang, Q. Jing, S. Ao, G. F. Schneider, D. Kireev, Z. Zhang, and W. Fu, "Ultrasensitive field-effect biosensors enabled by the unique electronic properties of graphene," *Small*, vol. 16, no. 15, p. 1902820, 2020.

[221] S. Xu, S. Jiang, C. Zhang, W. Yue, Y. Zou, G. Wang, H. Liu, X. Zhang, M. Li, Z. Zhu *et al.*, "Ultrasensitive label-free detection of dna hybridization by sapphire-based graphene field-effect transistor biosensor," *Applied Surface Science*, vol. 427, pp. 1114–1119, 2018.

[222] M. Kuscu and O. B. Akan, "On the physical design of molecular communication receiver based on nanoscale biosensors," *IEEE Sensors Journal*, vol. 16, no. 8, pp. 2228–2243, 2016.

[223] N. Gao, W. Zhou, X. Jiang, G. Hong, T.-M. Fu, and C. M. Lieber, "General strategy for biodetection in high ionic strength solutions using transistor-based nanoelectronic sensors," *Nano letters*, vol. 15, no. 3, pp. 2143–2148, 2015.

[224] A.-I. Lazăr, K. Aghasoleimani, A. Semertsidou, J. Vyas, A.-L. Roșca, D. Ficai, and A. Ficai, "Graphene-related nanomaterials for biomedical applications," *Nanomaterials*, vol. 13, no. 6, p. 1092, 2023.

[225] L. Zhao, Y.-H. Hao, and R.-Y. Peng, "Advances in the biological effects of terahertz wave radiation," *Military Medical Research*, vol. 1, no. 1, pp. 1–4, 2014.

[226] A. Chaves, J. Azadani, H. Alsalman, D. R. da Costa, R. Frisenda, A. Chaves, S. H. Song, Y. Kim, D. He, J. Zhou *et al.*, "Bandgap engineering of two-dimensional semiconductor materials," *npj 2D Materials and Applications*, vol. 4, no. 1, pp. 1–21, 2020.

[227] C. Liu, L. Du, W. Tang, D. Wei, J. Li, L. Wang, G. Chen, X. Chen, and W. Lu, "Towards sensitive terahertz detection via thermoelectric manipulation using graphene transistors," *NPG Asia Materials*, vol. 10, no. 4, pp. 318–327, 2018.

[228] D. Correas-Serrano and J. S. Gomez-Diaz, "Graphene-based antennas for terahertz systems: A review," *arXiv preprint arXiv:1704.00371*, 2017.

[229] M. Andrello, A. Singh, N. Thawdar, and J. M. Jornet, "Dynamic beamforming algorithms for ultra-directional terahertz communication systems based on graphene-based plasmonic nano-antenna arrays," in *2018 52nd Asilomar Conference on Signals, Systems, and Computers*. IEEE, 2018, pp. 1558–1563.

[230] K. Yang, Y. Hao, A. Alomainy, Q. H. Abbasi, and K. Qaraqe, "Channel modelling of human tissues at terahertz band," in *2016 IEEE Wireless Communications and Networking Conference Workshops (WCNCW)*. IEEE, 2016, pp. 218–221.

[231] J. M. Jornet and I. F. Akyildiz, "Graphene-based nano-antennas for electromagnetic nanocommunications in the terahertz band," in *Proceedings of the Fourth European Conference on Antennas and Propagation*. IEEE, 2010, pp. 1–5.

[232] I. Akylidiz and M. Jornet, "Graphene based plasmonic nano antenna for terahertz," *IEEE Journal on Selected Areas in Communication*, vol. 1, 2013.

[233] S. E. Hosseininejad, E. Alarcón, N. Komjani, S. Abadal, M. C. Lemme, P. H. Bolívar, and A. Cabellos-Aparicio, "Surveying of pure and hybrid plasmonic structures based on graphene for terahertz antenna," in *Proceedings of the 3rd*

ACM International Conference on Nanoscale Computing and Communication, 2016, pp. 1–6.

[234] S. E. Hosseininejad, M. Neshat, R. Faraji-Dana, M. Lemme, P. Haring Bolívar, A. Cabellos-Aparicio, E. Alarcón, and S. Abadal, "Reconfigurable thz plasmonic antenna based on few-layer graphene with high radiation efficiency," *Nanomaterials*, vol. 8, no. 8, p. 577, 2018.

[235] J. Crabb, X. Cantos-Roman, G. R. Aizin, and J. M. Jornet, "An on-chip amplitude and frequency modulating graphene-based plasmonic terahertz signal nano-generator," in *Proceedings of the Eight Annual ACM International Conference on Nanoscale Computing and Communication*, 2021, pp. 1–6.

[236] E. Lallas, "Key roles of plasmonics in wireless thz nanocommunications—a survey," *Applied Sciences*, vol. 9, no. 24, p. 5488, 2019.

[237] Y. Luo, Q. Zeng, X. Yan, T. Jiang, R. Yang, J. Wang, Y. Wu, Q. Lu, and X. Zhang, "A graphene-based tunable negative refractive index metamaterial and its application in dynamic beam-tilting terahertz antenna," *Microwave and Optical Technology Letters*, vol. 61, no. 12, pp. 2766–2772, 2019.

[238] X. Zhang, R. Cunjun, J. Dai, Y. Ding, S. Ullah, and A. Kosar Fahad, "Design of a reconfigurable antenna based on graphene for terahertz communication," *International Journal of Numerical Modelling: Electronic Networks, Devices and Fields*, p. e2911, 2021.

[239] T. Hogg and R. A. Freitas Jr, "Acoustic communication for medical nanorobots," *Nano Communication Networks*, vol. 3, no. 2, pp. 83–102, 2012.

[240] G. E. Santagati and T. Melodia, "Experimental evaluation of impulsive ultrasonic intra-body communications for implantable biomedical devices," *IEEE Transactions on Mobile Computing*, vol. 16, no. 2, pp. 367–380, 2016.

[241] G. Wissmeyer, M. A. Pleitez, A. Rosenthal, and V. Ntziachristos, "Looking at sound: optoacoustics with all-optical ultrasound detection," *Light: Science & Applications*, vol. 7, no. 1, pp. 1–16, 2018.

[242] F. Giorgianni, C. Vicario, M. Shalaby, L. D. Tenuzzo, A. Marcelli, T. Zhang, K. Zhao, Y. Chen, C. Hauri, and S. Lupi, "High-efficiency and low distortion photoacoustic effect in 3d graphene sponge," *Advanced Functional Materials*, vol. 28, no. 2, p. 1702652, 2018.

[243] Q. Fu, R. Zhu, J. Song, H. Yang, and X. Chen, "Photoacoustic imaging: contrast agents and their biomedical applications," *Advanced Materials*, vol. 31, no. 6, p. 1805875, 2019.

[244] H. Moon, D. Kumar, H. Kim, C. Sim, J.-H. Chang, J.-M. Kim, H. Kim, and D.-K. Lim, "Amplified photoacoustic performance and enhanced photothermal stability of reduced graphene oxide coated gold nanorods for sensitive photoacoustic imaging," *ACS nano*, vol. 9, no. 3, pp. 2711–2719, 2015.

[245] T. Lee, H. W. Baac, Q. Li, and L. J. Guo, "Efficient photoacoustic conversion in optical nanomaterials and composites," *Advanced Optical Materials*, vol. 6, no. 24, p. 1800491, 2018.

[246] S. I. Azzam, A. V. Kildishev, R.-M. Ma, C.-Z. Ning, R. Oulton, V. M. Shalaev, M. I. Stockman, J.-L. Xu, and X. Zhang, "Ten years of spasers and plasmonic nanolasers," *Light: Science & Applications*, vol. 9, no. 1, pp. 1–21, 2020.

[247] Y. Liang, C. Li, Y.-Z. Huang, and Q. Zhang, "Plasmonic nanolasers in on-chip light sources: prospects and challenges," *ACS nano*, vol. 14, no. 11, pp. 14 375–14 390, 2020.

[248] H. Elayan, A. W. Eckford, and R. S. Adve, "Information rates of controlled protein interactions using terahertz communication," *IEEE Transactions on NanoBioscience*, vol. 20, no. 1, pp. 9–19, 2020.

[249] M. Kuscu and O. B. Akan, "Modeling and analysis of sinw fet-based molecular communication receiver," *IEEE Transactions on Communications*, vol. 64, no. 9, pp. 3708–3721, 2016.

[250] P. K. D. Pramanik, A. Solanki, A. Debnath, A. Nayyar, S. El-Sappagh, and K.-S. Kwak, "Advancing modern healthcare with nanotechnology, nanobiosensors, and internet of nano things: Taxonomies, applications, architecture, and challenges," *IEEE Access*, vol. 8, pp. 65 230–65 266, 2020.

[251] S. Syama and P. Mohanan, "Safety and biocompatibility of graphene: A new generation nanomaterial for biomedical application," *International journal of biological macromolecules*, vol. 86, pp. 546–555, 2016.

[252] N. Celik, W. Balachandran, and N. Manivannan, "Graphene-based biosensors: methods, analysis and future perspectives," *IET Circuits, Devices & Systems*, vol. 9, no. 6, pp. 434–445, 2015.

[253] C. Liao, Y. Li, and S. C. Tjong, "Graphene nanomaterials: Synthesis, biocompatibility, and cytotoxicity," *International journal of molecular sciences*, vol. 19, no. 11, p. 3564, 2018.

[254] M. Holzinger, A. Le Goff, and S. Cosnier, "Nanomaterials for biosensing applications: a review," *Frontiers in chemistry*, vol. 2, p. 63, 2014.

[255] A. M. Pinto, I. C. Goncalves, and F. D. Magalhaes, "Graphene-based materials biocompatibility: a review," *Colloids and Surfaces B: Biointerfaces*, vol. 111, pp. 188–202, 2013.

[256] Z. Wang, Z. Hao, S. Yu, C. Huang, Y. Pan, and X. Zhao, "A wearable and deformable graphene-based affinity nanosensor for monitoring of cytokines in biofluids," *Nanomaterials*, vol. 10, no. 8, p. 1503, 2020.

[257] C. W. Lee, T. H. Eom, S. H. Cho, and H. W. Jang, "Chemical sensors based on graphene and 2d graphene analogs," *Advanced Sensor Research*, p. 2200057, 2023.

[258] S. S. Sethi, M. Kovac, F. Wiesemüller, A. Miriyev, and C. M. Boutry, "Biodegradable sensors are ready to transform autonomous ecological monitoring," *Nature Ecology & Evolution*, vol. 6, no. 9, pp. 1245–1247, 2022.

[259] C. Li, J. Adamcik, and R. Mezzenga, "Biodegradable nanocomposites of amyloid fibrils and graphene with shape-memory and enzyme-sensing properties," *Nature nanotechnology*, vol. 7, no. 7, pp. 421–427, 2012.

[260] D. Malak and O. B. Akan, "Communication theoretical understanding of intra-body nervous nanonetworks," *IEEE Communications Magazine*, vol. 52, no. 4, pp. 129–135, 2014.

[261] E. A. Mayer, K. Tillisch, A. Gupta *et al.*, "Gut/brain axis and the microbiota," *The Journal of clinical investigation*, vol. 125, no. 3, pp. 926–938, 2015.

[262] J. F. Cryan, K. J. O'Riordan, C. S. Cowan, K. V. Sandhu, T. F. Bastiaanssen, M. Boehme, M. G. Codagnone, S. Cussotto, C. Fulling, A. V. Golubeva *et al.*, "The microbiota-gut-brain axis," *Physiological reviews*, 2019.

[263] S. H. Rhee, C. Pothoulakis, and E. A. Mayer, "Principles and clinical implications of the brain–gut–enteric microbiota axis," *Nature reviews Gastroenterology & hepatology*, vol. 6, no. 5, pp. 306–314, 2009.

[264] S. Grenham, G. Clarke, J. F. Cryan, and T. G. Dinan, "Brain–gut–microbe communication in health and disease," *Frontiers in physiology*, vol. 2, p. 94, 2011.

[265] M. Zhang, Z. Tang, X. Liu, and J. Van der Spiegel, "Electronic neural interfaces," *Nature Electronics*, vol. 3, no. 4, pp. 191–200, 2020.

[266] A. Jackson and J. B. Zimmermann, "Neural interfaces for the brain and spinal cord—restoring motor function," *Nature Reviews Neurology*, vol. 8, no. 12, pp. 690–699, 2012.

[267] W. M. Grill, S. E. Norman, and R. V. Bellamkonda, "Implanted neural interfaces: biochallenges and engineered solutions," *Annual review of biomedical engineering*, vol. 11, pp. 1–24, 2009.

[268] K. Kostarelos, M. Vincent, C. Hebert, and J. A. Garrido, "Graphene in the design and engineering of next-generation neural interfaces," *Advanced Materials*, vol. 29, no. 42, p. 1700909, 2017.

[269] H. Huang, S. Su, N. Wu, H. Wan, S. Wan, H. Bi, and L. Sun, "Graphene-based sensors for human health monitoring," *Frontiers in chemistry*, vol. 7, p. 399, 2019.

[270] R. Society, *iHuman: blurring lines between mind and machine*. Royal Society, 2019.

[271] X. Liu, Y. Lu, E. Iseri, Y. Shi, and D. Kuzum, "A compact closed-loop optogenetics system based on artifact-free transparent graphene electrodes," *Frontiers in neuroscience*, vol. 12, p. 132, 2018.

[272] K. Yang, L. Feng, and Z. Liu, "Stimuli responsive drug delivery systems based on nano-graphene for cancer therapy," *Advanced drug delivery reviews*, vol. 105, pp. 228–241, 2016.

[273] G. Reina, J. M. González-Domínguez, A. Criado, E. Vázquez, A. Bianco, and M. Prato, "Promises, facts and challenges for graphene in biomedical applications," *Chemical Society Reviews*, vol. 46, no. 15, pp. 4400–4416, 2017.

[274] A. Servant, V. Leon, D. Jasim, L. Methven, P. Limousin, E. V. Fernandez-Pacheco, M. Prato, and K. Kostarelos, "Graphene-based electroresponsive scaffolds as polymeric implants for on-demand drug delivery," *Advanced healthcare materials*, vol. 3, no. 8, pp. 1334–1343, 2014.

[275] M. López-Suárez, R. Rurali, L. Gammaitoni, and G. Abadal, "Nanostructured graphene for energy harvesting," *Physical Review B*, vol. 84, no. 16, p. 161401, 2011.

[276] Q. Shi, T. He, and C. Lee, "More than energy harvesting–combining triboelectric nanogenerator and flexible electronics technology for enabling novel micro-/nano-systems," *Nano Energy*, vol. 57, pp. 851–871, 2019.

[277] H. Chen, Y. Xu, J. Zhang, W. Wu, and G. Song, "Enhanced stretchable graphene-based triboelectric nanogenerator via control of surface nanostructure," *Nano Energy*, vol. 58, pp. 304–311, 2019.

[278] H. Chu, H. Jang, Y. Lee, Y. Chae, and J.-H. Ahn, "Conformal, graphene-based triboelectric nanogenerator for self-powered wearable electronics," *Nano Energy*, vol. 27, pp. 298–305, 2016.

[279] S. Kim, M. K. Gupta, K. Y. Lee, A. Sohn, T. Y. Kim, K.-S. Shin, D. Kim, S. K. Kim, K. H. Lee, H.-J. Shin *et al.*, "Transparent flexible graphene triboelectric nanogenerators," *Advanced materials*, vol. 26, no. 23, pp. 3918–3925, 2014.

[280] D. Wei, F. Yang, Z. Jiang, and Z. Wang, "Flexible iontronics based on 2d nanofluidic material."

[281] X. Zhang, E. Chia, X. Fan, and J. Ping, "Flow-sensory contact electrification of graphene," *Nature Communications*, vol. 12, no. 1, p. 1755, 2021.

[282] J. Yin, X. Li, J. Yu, Z. Zhang, J. Zhou, and W. Guo, "Generating electricity by moving a droplet of ionic liquid along graphene," *Nature nanotechnology*, vol. 9, no. 5, pp. 378–383, 2014.

[283] H. Zhong, Z. Wu, X. Li, W. Xu, S. Xu, S. Zhang, Z. Xu, H. Chen, and S. Lin, "Graphene based two dimensional hybrid nanogenerator for concurrently harvesting energy from sunlight and water flow," *Carbon*, vol. 105, pp. 199–204, 2016.

[284] H. Zhong, J. Xia, F. Wang, H. Chen, H. Wu, and S. Lin, "Graphene-piezoelectric material heterostructure for harvesting energy from water flow," *Advanced Functional Materials*, vol. 27, no. 5, p. 1604226, 2017.

[285] J. P. Tarelho, M. P. S. dos Santos, J. A. Ferreira, A. Ramos, S. Kopyl, S. O. Kim, S. Hong, and A. Kholkin, "Graphene-based materials and structures for energy harvesting with fluids–a review," *Materials Today*, vol. 21, no. 10, pp. 1019–1041, 2018.

[286] M. Wang, W. Liu, W. Song, X. Shi, W. Zhong, T. Sun, J. Wang, and Y. Tang, "Boosting wind energy harvesting of polyvinylidene fluoride via graphene oxide induced charges accumulation," *Energy Reports*, vol. 7, pp. 3156–3161, 2021.

[287] O. Vryonis, T. Andritsch, A. Vaughan, and P. Lewin, "Improved lightning protection of carbon fiber reinforced polymer wind turbine blades: epoxy/graphene oxide nanocomposites," in *2016 IEEE conference on electrical insulation and dielectric phenomena (CEIDP)*. IEEE, 2016, pp. 635–638.

[288] C. X. Guo, G. H. Guai, and C. M. Li, "Graphene based materials: enhancing solar energy harvesting," 2011.

[289] C.-T. Chien, P. Hiralal, D.-Y. Wang, I.-S. Huang, C.-C. Chen, C.-W. Chen, and G. A. Amaratunga, "Graphene-based integrated photovoltaic energy harvesting/storage device," *Small*, vol. 11, no. 24, pp. 2929–2937, 2015.

[290] A. Vakil and H. Bajwa, "Energy harvesting using graphene based antenna for uv spectrum," in *IEEE Long Island Systems, Applications and Technology (LISAT) Conference 2014*. IEEE, 2014, pp. 1–4.

[291] C. Yu and Y. S. Song, "Analysis of thermoelectric energy harvesting with graphene aerogel-supported form-stable phase change materials," *Nanomaterials*, vol. 11, no. 9, p. 2192, 2021.

[292] P. Zhou, J. Lin, W. Zhang, Z. Luo, and L. Chen, "Photo-thermoelectric generator integrated in graphene-based actuator for self-powered sensing function," *Nano Research*, pp. 1–8, 2021.

[293] T. Mehmood, J. H. Kim, D.-J. Lee, S. Dizhur, E. S. Hirst, R. M. Osgood, M. H. Sayyad, M. A. Munawar, and J. Xu, "A flexible, printable, thin-film thermoelectric generator based on reduced graphene oxide–carbon nanotubes composites," *Journal of Materials Science*, vol. 55, no. 24, pp. 10 572–10 581, 2020.

[294] R. Que, Q. Shao, Q. Li, M. Shao, S. Cai, S. Wang, and S.-T. Lee, "Flexible nanogenerators based on graphene oxide films for acoustic energy harvesting," *Angewandte Chemie*, vol. 124, no. 22, pp. 5514–5518, 2012.

[295] J.-H. Lee, K. Y. Lee, B. Kumar, N. T. Tien, N.-E. Lee, and S.-W. Kim, "Highly sensitive stretchable transparent piezoelectric nanogenerators," *Energy & Environmental Science*, vol. 6, no. 1, pp. 169–175, 2013.

[296] O. B. Akan, O. Cetinkaya, C. Koca, and M. Ozger, "Internet of hybrid energy harvesting things," *IEEE Internet of Things Journal*, vol. 5, no. 2, pp. 736–746, 2017.

[297] T. Becker, V. Borjesson, O. Cetinkaya, C. Baoxing, J. Colomer-Farrarons, D. Maeve, A. Elefsiniotis, L. Govoni, Z. Hadas, M. Hayes *et al.*, "Energy harvesting for a green internet of things," PSMA, NJ, USA, White Paper, 2021, ISBN: 978-1-7337815-2-7. [Online]. Available: https://www.psma.com/technical-forums/energy-harvesting/whitepaper

[298] A. Jetybayeva, B. Uzakbaiuly, A. Mukanova, S.-T. Myung, and Z. Bakenov, "Recent advancements in solid electrolytes integrated into all-solid-state 2d and 3d lithium-ion microbatteries," *Journal of Materials Chemistry A*, vol. 9, no. 27, pp. 15 140–15 178, 2021.

[299] N. A. Kyeremateng, T. Brousse, and D. Pech, "Microsupercapacitors as miniaturized energy-storage components for on-chip electronics," *Nature nanotechnology*, vol. 12, no. 1, pp. 7–15, 2017.

[300] X. Shi, S. Pei, F. Zhou, W. Ren, H.-M. Cheng, Z.-S. Wu, and X. Bao, "Ultrahigh-voltage integrated micro-supercapacitors with designable shapes and superior flexibility," *Energy & Environmental Science*, vol. 12, no. 5, pp. 1534–1541, 2019.

[301] M. F. El-Kady and R. B. Kaner, "Scalable fabrication of high-power graphene micro-supercapacitors for flexible and on-chip energy storage," *Nature communications*, vol. 4, no. 1, p. 1475, 2013.

[302] F. Li, J. Qu, Y. Li, J. Wang, M. Zhu, L. Liu, J. Ge, S. Duan, T. Li, V. K. Bandari *et al.*, "Stamping fabrication of flexible planar micro-supercapacitors using porous graphene inks," *Advanced Science*, vol. 7, no. 19, p. 2001561, 2020.

[303] A. Ambrosi, C. K. Chua, N. M. Latiff, A. H. Loo, C. H. A. Wong, A. Y. S. Eng, A. Bonanni, and M. Pumera, "Graphene and its electrochemistry–an update," *Chemical Society Reviews*, vol. 45, no. 9, pp. 2458–2493, 2016.

[304] M. Beidaghi and C. Wang, "Micro-supercapacitors based on interdigital electrodes of reduced graphene oxide and carbon nanotube composites with ultrahigh power handling performance," *Advanced Functional Materials*, vol. 22, no. 21, pp. 4501–4510, 2012.

[305] Z.-S. Wu, Y. Zheng, S. Zheng, S. Wang, C. Sun, K. Parvez, T. Ikeda, X. Bao, K. Müllen, and X. Feng, "Stacked-layer heterostructure films of 2d thiophene nanosheets and graphene for high-rate all-solid-state pseudocapacitors with enhanced volumetric capacitance," *Advanced materials*, vol. 29, no. 3, p. 1602960, 2017.

[306] E. Pomerantseva, F. Bonaccorso, X. Feng, Y. Cui, and Y. Gogotsi, "Energy storage: The future enabled by nanomaterials," *Science*, vol. 366, no. 6468, 2019.

[307] Y. Zhang, L. Zhang, and C. Zhou, "Review of chemical vapor deposition of graphene and related applications," *Accounts of chemical research*, vol. 46, no. 10, pp. 2329–2339, 2013.

[308] R. Vishwakarma, M. S. Rosmi, K. Takahashi, Y. Wakamatsu, Y. Yaakob, M. I. Araby, G. Kalita, M. Kitazawa, and M. Tanemura, "Transfer free graphene growth on sio2 substrate at 250 c," *Scientific reports*, vol. 7, no. 1, pp. 1–8, 2017.

[309] C. J. Bullock and C. Bussy, "Biocompatibility considerations in the design of graphene biomedical materials," *Advanced Materials Interfaces*, vol. 6, no. 11, p. 1900229, 2019.

[310] M. C. Lemme, D. Akinwande, C. Huyghebaert, and C. Stampfer, "2d materials for future heterogeneous electronics," *Nature Communications*, vol. 13, no. 1, pp. 1–5, 2022.

[311] E. Heidari, H. Dalir, F. M. Koushyar, B. M. Nouri, C. Patil, M. Miscuglio, D. Akinwande, and V. J. Sorger, "Integrated ultra-high-performance graphene optical modulator," *Nanophotonics*, vol. 11, no. 17, pp. 4011–4016, 2022.

[312] G. R. Bhimanapati, Z. Lin, V. Meunier, Y. Jung, J. Cha, S. Das, D. Xiao, Y. Son, M. S. Strano, V. R. Cooper *et al.*, "Recent advances in two-dimensional materials beyond graphene," *ACS nano*, vol. 9, no. 12, pp. 11 509–11 539, 2015.

[313] M.-Y. Li, C.-H. Chen, Y. Shi, and L.-J. Li, "Heterostructures based on two-dimensional layered materials and their potential applications," *Materials Today*, vol. 19, no. 6, pp. 322–335, 2016.

[314] N. Rohaizad, C. C. Mayorga-Martinez, M. Fojt, N. M. Latiff, and M. Pumera, "Two-dimensional materials in biomedical, biosensing and sensing applications," *Chemical Society Reviews*, vol. 50, no. 1, pp. 619–657, 2021.

[315] C. Tan, X. Cao, X.-J. Wu, Q. He, J. Yang, X. Zhang, J. Chen, W. Zhao, S. Han, G.-H. Nam *et al.*, "Recent advances in ultrathin two-dimensional nanomaterials," *Chemical reviews*, vol. 117, no. 9, pp. 6225–6331, 2017.

[316] Q. Zeng and Z. Liu, "Novel optoelectronic devices: transition-metal-dichalcogenide-based 2d heterostructures," *Advanced Electronic Materials*, vol. 4, no. 2, p. 1700335, 2018.

[317] L. Li, Y. Yu, G. J. Ye, Q. Ge, X. Ou, H. Wu, D. Feng, X. H. Chen, and Y. Zhang, "Black phosphorus field-effect transistors," *Nature nanotechnology*, vol. 9, no. 5, pp. 372–377, 2014.

[318] J. Huang, Z. Li, Y. Mao, and Z. Li, "Progress and biomedical applications of mxenes," *Nano Select*, vol. 2, no. 8, pp. 1480–1508, 2021.

[319] A. D. Squires, X. Gao, J. Du, Z. Han, D. H. Seo, J. S. Cooper, A. T. Murdock, S. K. Lam, T. Zhang, and T. van der Laan, "Electrically tuneable terahertz metasurface enabled by a graphene/gold bilayer structure," *Communications Materials*, vol. 3, no. 1, pp. 1–9, 2022.

[320] D. Bitounis, H. Ali-Boucetta, B. H. Hong, D.-H. Min, and K. Kostarelos, "Prospects and challenges of graphene in biomedical applications," *Advanced Materials*, vol. 25, no. 16, pp. 2258–2268, 2013.

[321] D. San Roman, R. Garg, and T. Cohen-Karni, "Bioelectronics with graphene nanostructures," *APL Materials*, vol. 8, no. 10, p. 100906, 2020.

[322] Z. Jiang, B. Feng, J. Xu, T. Qing, P. Zhang, and Z. Qing, "Graphene biosensors for bacterial and viral pathogens," *Biosensors and Bioelectronics*, vol. 166, p. 112471, 2020.

[323] X. Li, Y. Wang, Y. Zhao, J. Zhang, and L. Qu, "Graphene materials for miniaturized energy harvest and storage devices," *Small Structures*, vol. 3, no. 1, p. 2100124, 2022.

[324] M. Pusty and P. M. Shirage, "Insights and perspectives on graphene-pvdf based nanocomposite materials for harvesting mechanical energy," *Journal of Alloys and Compounds*, p. 164060, 2022.

[325] K. Cheng, S. Wallaert, H. Ardebili, and A. Karim, "Advanced triboelectric nanogenerators based on low-dimension carbon materials: A review," *Carbon*, 2022.

[326] F. F. Hatta, M. A. S. Mohammad Haniff, and M. A. Mohamed, "A review on applications of graphene in triboelectric nanogenerators," *International Journal of Energy Research*, vol. 46, no. 2, pp. 544–576, 2022.

[327] "Internet of nano things market size & share analysis - industry research report - growth trends," Internet Of Nano Things Market Size & Share Analysis - Industry Research Report - Growth Trends, Accessed June 18, 2023.

[328] L. Kong, L. Huang, L. Lin, Z. Zheng, Y. Li, Q. Wang, and G. Liu, "A survey for possible technologies of micro/nanomachines used for molecular communication within 6g application scenarios," *IEEE Internet of Things Journal*, 2023.

[329] C. De Alwis, A. Kalla, Q.-V. Pham, P. Kumar, K. Dev, W.-J. Hwang, and M. Liyanage, "Survey on 6g frontiers: Trends, applications, requirements, technologies and future research," *IEEE Open Journal of the Communications Society*, vol. 2, pp. 836–886, 2021.

[330] I. F. Akyildiz, M. Ghovanloo, U. Guler, T. Ozkaya-Ahmadov, A. F. Sarioglu, and B. D. Unluturk, "Panacea: An internet of bio-nanothings application for early detection and mitigation of infectious diseases," *IEEE Access*, vol. 8, pp. 140 512–140 523, 2020.

[331] T. Mora, "Physical limit to concentration sensing amid spurious ligands," *Physical review letters*, vol. 115, no. 3, p. 038102, 2015.

[332] M. Kuscu and O. B. Akan, "Detection in molecular communications with ligand receptors under molecular interference," *Digital Signal Processing*, vol. 124, p. 103186, 2022.

[333] L. J. Mele, P. Palestri, and L. Selmi, "General model and equivalent circuit for the chemical noise spectrum associated to surface charge fluctuation in potentiometric sensors," *IEEE Sensors Journal*, vol. 21, no. 5, pp. 6258–6269, 2020.

[334] E. Limpert, W. A. Stahel, and M. Abbt, "Log-normal distributions across the sciences: keys and clues: on the charms of statistics, and how mechanical models resembling gambling machines offer a link to a handy way to characterize log-normal distributions, which can provide deeper insight into variability and probability—normal or log-normal: that is the question," *BioScience*, vol. 51, no. 5, pp. 341–352, 2001.

[335] M. Kuscu and O. B. Akan, "Modeling convection-diffusion-reaction systems for microfluidic molecular communications with surface-based receivers in internet of bio-nano things," *PloS one*, vol. 13, no. 2, p. e0192202, 2018.

[336] A. O. Bicen and I. F. Akyildiz, "System-theoretic analysis and least-squares design of microfluidic channels for flow-induced molecular communication," *IEEE Transactions on Signal Processing*, vol. 61, no. 20, pp. 5000–5013, 2013.

[337] I. Heller, S. Chatoor, J. Mannik, M. A. Zevenbergen, J. B. Oostinga, A. F. Morpurgo, C. Dekker, and S. G. Lemay, "Charge noise in graphene transistors," *Nano letters*, vol. 10, no. 5, pp. 1563–1567, 2010.

[338] J. Mucksch, P. Blumhardt, M. T. Strauss, E. P. Petrov, R. Jungmann, and P. Schwille, "Quantifying reversible surface binding via surface-integrated fluorescence correlation spectroscopy," *Nano Letters*, vol. 18, no. 5, pp. 3185–3192, 2018.

[339] D. Barret and S. Vaughan, "Maximum likelihood fitting of x-ray power density spectra: application to high-frequency quasi-periodic oscillations from the neutron star x-ray binary 4u1608-522," *The Astrophysical Journal*, vol. 746, no. 2, p. 131, 2012.

[340] A. M. Sykulski, S. C. Olhede, A. P. Guillaumin, J. M. Lilly, and J. J. Early, "The debiased whittle likelihood," *Biometrika*, vol. 106, no. 2, pp. 251–266, 2019.

[341] E. R. Anderson, T. L. Duvall Jr, and S. M. Jefferies, "Modeling of solar oscillation power spectra," *The Astrophysical Journal*, vol. 364, pp. 699–705, 1990.

[342] T. Toutain and T. Appourchaux, "Maximum likelihood estimators: An application to the estimation of the precision of helioseismic measurements," *Astronomy and Astrophysics*, vol. 289, pp. 649–658, 1994.

[343] M. Levin, "Power spectrum parameter estimation," *IEEE Transactions on Information Theory*, vol. 11, no. 1, pp. 100–107, 1965.

[344] K. Libbrecht, "On the ultimate accuracy of solar oscillation frequency measurements," *The Astrophysical Journal*, vol. 387, pp. 712–714, 1992.

[345] S. S. Andrews, "Smoldyn: particle-based simulation with rule-based modeling, improved molecular interaction and a library interface," *Bioinformatics*, vol. 33, no. 5, pp. 710–717, 2017.

[346] N. J. Kasdin, "Discrete simulation of colored noise and stochastic processes and 1/f/sup/spl alpha//power law noise generation," *Proceedings of the IEEE*, vol. 83, no. 5, pp. 802–827, 1995.

[347] T. M. Inc., "Optimization toolbox version: 9.2 (r2021b)," Natick, Massachusetts, United States, 2022. [Online]. Available: https://www.mathworks.com

[348] G. Zheng, X. P. Gao, and C. M. Lieber, "Frequency domain detection of biomolecules using silicon nanowire biosensors," *Nano letters*, vol. 10, no. 8, pp. 3179–3183, 2010.

[349] F. Bettetti, L. J. Mele, and P. Palestri, "Critical overview and comparison between models for adsorption-desorption noise in bio-chemical sensors," *Applied Surface Science Advances*, vol. 18, p. 100472, 2023.

[350] M. Kuscu and O. B. Akan, "Maximum likelihood detection with ligand receptors for diffusion-based molecular communications in internet of bio-nano things," *IEEE transactions on nanobioscience*, vol. 17, no. 1, pp. 44–54, 2018.

[351] M. O. Araz, A. R. Emirdagi, M. S. Kopuzlu, and M. Kuscu, "Ratio shift keying modulation for time-varying molecular communication channels," *IEEE Transactions on NanoBioscience*, vol. 23, no. 1, pp. 176–189, 2024.

[352] T. Jetka, K. Nienałtowski, S. Filippi, M. P. Stumpf, and M. Komorowski, "An information-theoretic framework for deciphering pleiotropic and noisy biochemical signaling," *Nature communications*, vol. 9, no. 1, p. 4591, 2018.

[353] M. Komorowski and D. S. Tawfik, "The limited information capacity of cross-reactive sensors drives the evolutionary expansion of signaling," *Cell systems*, vol. 8, no. 1, pp. 76–85, 2019.

[354] J. O. Berger, B. Liseo, and R. L. Wolpert, "Integrated likelihood methods for eliminating nuisance parameters," *Statistical science*, pp. 1–22, 1999.

[355] B. Clarke and L. Wasserman, "Noninformative priors and nuisance parameters," *Journal of the American Statistical Association*, vol. 88, no. 424, pp. 1427–1432, 1993.

[356] P. Wang, J. Zhang, X. Zhang, Z. Yan, B. G. Evans, and W. Wang, "Convergence of satellite and terrestrial networks: A comprehensive survey," *IEEE Access*, 2019.

[357] O. Kodheli, E. Lagunas, N. Maturo, S. K. Sharma, B. Shankar, J. Montoya, J. Duncan, D. Spano, S. Chatzinotas, S. Kisseleff *et al.*, "Satellite communications in the new space era: A survey and future challenges," *arXiv preprint arXiv:2002.08811*, 2020.

[358] I. F. Akyildiz, J. M. Jornet, and S. Nie, "A new cubesat design with reconfigurable multi-band radios for dynamic spectrum satellite communication networks," *Ad Hoc Networks*, vol. 86, pp. 166–178, 2019.

[359] I. F. Akyildiz and J. M. Jornet, "The internet of nano-things," *IEEE Wireless Communications*, vol. 17, no. 6, pp. 58–63, 2010.

[360] T. Yilmaz, G. Gokkoca, and O. B. Akan, "Millimetre wave communication for 5g iot applications," in *Millimetre Wave Communication for 5G IoT Applications*. Springer International Publishing, 2016, pp. 37–53.

[361] T. Yilmaz and O. B. Akan, "On the use of the millimeter wave and low terahertz bands for internet of things," in *2015 IEEE 2nd World Forum on Internet of Things (WF-IoT)*, 2015, pp. 177–180.

[362] S. Mumtaz, J. M. Jornet, J. Aulin, W. H. Gerstacker, X. Dong, and B. Ai, "Terahertz communication for vehicular networks," *IEEE Transactions on Vehicular Technology*, vol. 66, no. 7, pp. 5617–5625, 2017.

[363] F. Lemic *et al.*, "Survey on terahertz nanocommunication and networking: A top-down perspective," *arXiv preprint arXiv:1909.05703v1*, 2019.

[364] I. F. Akyildiz, J. M. Jornet, and C. Han, "Terahertz band: Next frontier for wireless communications," *Physical Communication*, vol. 12, no. 0, pp. 16–32, 2014.

[365] T. Yilmaz and O. B. Akan, "State-of-the-art and research challenges for consumer wireless communications at 60 ghz," *IEEE Transactions on Consumer Electronics*, vol. 62, no. 3, pp. 216–225, 2016.

[366] J. F. O'Hara, S. Ekin, W. Choi, and I. Song, "A perspective on terahertz next-generation wireless communications," *Technologies*, vol. 7, no. 2, p. 43, 2019.

[367] S. Ho-Jin and T. Nagatsuma, "Present and future of terahertz communications," *IEEE Transactions on Terahertz Science and Technology*, vol. 1, no. 1, pp. 256–263, 2011.

[368] T. Yilmaz and O. B. Akan, "On the 5g wireless communications at the low terahertz band," *arXiv preprint arXiv:1605.02606*, 2016.

[369] A. Hirata and M. Yaita, "Ultrafast terahertz wireless communications technologies," *IEEE Transactions on Terahertz Science and Technology*, vol. 5, no. 6, pp. 1128–1132, 2015.

[370] V. Petrov, A. Pyattaev, D. Moltchanov, and Y. Koucheryavy, "Terahertz band communications: Applications, research challenges, and standardization activities," in *2016 8th International Congress on Ultra Modern Telecommunications and Control Systems and Workshops (ICUMT)*, 2016, pp. 183–190.

[371] H. Elayan, O. Amin, R. M. Shubair, and M. Alouini, "Terahertz communication: The opportunities of wireless technology beyond 5g," in *2018 International Conference on Advanced Communication Technologies and Networking (CommNet)*, 2018, pp. 1–5.

[372] S. Ahearne *et al.*, "Integrating thz wireless communication links in a data centre network," in *2019 IEEE 2nd 5G World Forum (5GWF)*, 2019, pp. 393–398.

[373] N. Boujnah, S. Ghafoor, and A. Davy, "Modeling and link quality assessment of thz network within data center," in *2019 European Conference on Networks and Communications (EuCNC)*, 2019, pp. 57–62.

[374] K. M. S. Huq, S. A. Busari, J. Rodriguez, V. Frascolla, W. Bazzi, and D. C. Sicker, "Terahertz-enabled wireless system for beyond-5g ultra-fast networks: A brief survey," *IEEE Network*, vol. 33, no. 4, pp. 89–95, 2019.

[375] T. Yilmaz and O. B. Akan, "On the use of low terahertz band for 5g indoor mobile networks," *Computers & Electrical Engineering*, vol. 48, pp. 164–173, 2015.

[376] T. Yilmaz, "On the use of low terahertz band for wireless communications," Ph.D. dissertation, Koç Univ., Istanbul, Turkey, 2018.

[377] N. Khalid, T. Yilmaz, and O. B. Akan, "Energy-efficient modulation scheme for thz-band 5g femtocell internet of things," in *2017 International Balkan Conference on Communications and Networking (BalkanCom)*, 2017.

[378] P. Hanswal, "Terahertz communication for satellite networks," Ph.D. dissertation, 2018.

[379] A. Saeed, O. Gurbuz, and M. A. Akkas, "Terahertz communications at various atmospheric altitudes," *Physical Communication*, vol. 101113, 2020.

[380] A. Saeed, O. Gurbuz, A. O. Bicen, and M. A. Akkas, "Variable-bandwidth model and capacity analysis for aerial communications in the terahertz band," *IEEE Journal on Selected Areas in Communications*, vol. 39, no. 6, pp. 1768–1784, 2021.

[381] X. W. et al., "Millimeter wave communication: A comprehensive survey," *IEEE Communications Surveys & Tutorials*, vol. 20, no. 3, pp. 1616–1653, 2018.

[382] T. Yilmaz and O. B. Akan, "Millimeter-wave communications for 5g wireless networks." CRC Press, 2016, pp. 425–440.

[383] T. Yilmaz, N. A. Abbasi, and O. B. Akan, "Millimeter-wave 5g-enabled internet of things." CRC Press, Boca Raton, FL, 2019, pp. 163–181.

[384] T. Yilmaz and O. B. Akan, "Utilizing terahertz band for local and personal area wireless communication systems," in *2014 IEEE 19th International Workshop on Computer Aided Modeling and Design of Communication Links and Networks (CAMAD)*, 2014, pp. 330–334.

[385] O. Erturk and T. Yilmaz, "A hexagonal grid based human blockage model for the 5g low terahertz band communications," in *2018 IEEE 5G World Forum (5GWF)*, 2018, pp. 395–398.

[386] T. Yilmaz, E. Fadel, and O. B. Akan, "Employing 60 ghz ism band for 5g wireless communications," in *2014 IEEE International Black Sea Conference on Communications and Networking (BlackSeaCom)*, 2014, pp. 77–82.

[387] H. Kaushal and G. Kaddoum, "Optical communication in space: challenges and mitigation techniques," *IEEE communications surveys & tutorials*, vol. 19, no. 1, pp. 57–96, 2016.

[388] I. Mehdi, J. Siles, C. P. Chen, and J. M. Jornet, “Thz technology for space communications,” in *2018 Asia-Pacific Microwave Conference (APMC)*, 2018, pp. 76–78.

[389] J. Y. Suen, M. T. Fang, S. P. Denny, and P. M. Lubin, “Modeling of terabit geostationary terahertz satellite links from globally dry locations,” *IEEE Transactions on Terahertz Science and Technology*, vol. 5, no. 2, pp. 299–313, 2015.

[390] M. Saqlain, N. M. Idrees, X. Cao, X. Gao, and X. Yu, “Feasibility analysis of opto-electronic thz earth-satellite links in the low- and mid-latitude regions,” *Applied Optics*, vol. 58, no. 25, pp. 6762–6769, 2019.

[391] R. Zhen and C. Han, “Link budget analysis for massive-antenna-array-enabled terahertz satellite communications,” *Journal of Shanghai Jiaotong University (Science)*, vol. 23, no. 1, pp. 20–27, 2018.

[392] H. T. Friis, “A note on a simple transmission formula,” *Proc. IRE*, vol. 34, no. 5, pp. 254–256, 1946.

[393] T. Yilmaz and O. B. Akan, “Attenuation constant measurements of clear glass samples at the low terahertz band,” *Electronics Letters*, 2020.

[394] “Nasa 60 ghz intersatellite communication link definition study,” National Aeronautics and Space Administration, Tech. Rep., 1986.

[395] “Recommendation itu-r p.1621-2: Propagation data required for the design of earth-space systems operating between 20 thz and 375 thz,” ITU, Geneva, CHE, Tech. Rep., 2015.

[396] C. A. Balanis, *Antenna Theory: Analysis and Design*, 4th ed. Hoboken, NJ: John Wiley & Sons, Inc., 2016.

[397] A. Straiton, “The absorption and reradiation of radio waves by oxygen and water vapor in the atmosphere,” *IEEE Transactions on Antennas and Propagation*, vol. 23, no. 4, pp. 595–597, 1975.

[398] J. Kokkoniemi, J. Lehtomaki, and M. Juntti, “A discussion on molecular absorption noise in the terahertz band,” *Nano Communication Networks*, vol. 8, pp. 35–45, 2016.

[399] R. Singh and D. Sicker, “Beyond 5g: Thz spectrum futures and implications for wireless communication,” International Telecommunications Society (ITS), Helsinki, Tech. Rep., 2019.

[400] I. F. Akyildiz and J. M. Jornet, "Realizing ultra-massive mimo (1024x1024) communication in the (0.06–10) terahertz band," *Nano Communication Networks*, vol. 8, pp. 46–54, 2016.

[401] E. Yaacoub and M.-S. Alouini, "A key 6g challenge and opportunity - connecting the remaining 4 billions: A survey on rural connectivity," *arXiv preprint*, 2019.

[402] A. Guidotti *et al.*, "Architectures and key technical challenges for 5g systems incorporating satellites," *IEEE Transactions on Vehicular Technology*, vol. 68, no. 3, pp. 2624–2639, 2019.

[403] Z. Qu, G. Zhang, H. Cao, and J. Xie, "Leo satellite constellation for internet of things," *IEEE Access*, vol. 5, pp. 18 391–18 401, 2017.

[404] I. F. Akyildiz and A. Kak, "The internet of space things/cubesats," *IEEE Network*, vol. 33, no. 5, pp. 212–218, 2019.

[405] J. Du, C. Jiang, Q. Guo, M. Guizani, and Y. Ren, "Cooperative earth observation through complex space information networks," *IEEE wireless communications*, vol. 23, no. 2, pp. 136–144, 2016.

[406] X. Cao, P. Yang, M. Alzenad, X. Xi, D. Wu, and H. Yanikomeroglu, "Airborne communication networks: A survey," *IEEE Journal on Selected Areas in Communications*, vol. 36, no. 9, pp. 1907–1926, 2018.

[407] I. F. Akyildiz, C. Han, and S. Nie, "Combating the distance problem in the millimeter wave and terahertz frequency bands," *IEEE Communications Magazine*, vol. 56, no. 6, pp. 102–108, 2018.

[408] C. Liaskos *et al.*, "Design and development of software defined metamaterials for nanonetworks," *IEEE Circuits and Systems Magazine*, vol. 15, no. 4, pp. 12–25, 2015.

[409] M. J. Marcus, "Wrc-19 issues: Agenda item 1.15 and the use of 275–450 ghz," *IEEE Wireless Communications*, vol. 23, no. 6, pp. 2–3, 2016.

[410] T. Kürner, "Regulatory aspects of thz communications and related activities towards wrc 2019."

[411] T. E. S. Agency, "Space debris by the numbers," https://www.esa.int/Safety_Security/Space_Debris/Space_debris_by_the_numbers, 2020.

[412] S. Ju *et al.*, "Scattering mechanisms and modeling for terahertz wireless communications," in *2019 IEEE International Conference on Communications (ICC)*. IEEE, 2019, pp. 1–7.

[413] T. S. Rappaport, *Wireless Communications: Principles and Practice*, 2nd ed. Upper Saddle River, NJ, USA: Prentice Hall, 2001.

[414] C. Zhang, G. Wang, M. Jia, R. He, L. Zhou, and B. Ai, "Doppler shift estimation for millimeter-wave communication systems on high-speed railways," *IEEE Access*, vol. 7, pp. 40 454–40 462, 2018.

[415] K. K. O *et al.*, "Opening terahertz for everyday applications," *IEEE Communications Magazine*, vol. 57, no. 8, pp. 70–76, 2019.

[416] S. H. Naghavi, M. T. Taba, R. Han, M. A. Aseeri, A. Cathelin, and E. Afshari, "Filling the gap with sand: When cmos reaches thz," *IEEE Solid-State Circuits Magazine*, vol. 11, no. 3, pp. 33–42, 2019.

[417] NASA. Deep space communications. [Online]. Available: https://scienceandtechnology.jpl.nasa.gov/research/research-topics-list/communications-computing-software/deep-space-communications

[418] ——. Deep space optical communications (dsoc). [Online]. Available: https://www.nasa.gov/mission_pages/tdm/dsoc

[419] ESA. European data relay satellite system (edrs) overview. [Online]. Available: https://artes.esa.int/edrs/overview

[420] T. Schneider, A. Wiatrek, S. Preußler, M. Grigat, and R.-P. Braun, "Link budget analysis for terahertz fixed wireless links," *IEEE Transactions on Terahertz Science and Technology*, vol. 2, no. 2, pp. 250–256, 2012.

[421] C. Han, Y. Wu, Z. Chen, and X. Wang, "Terahertz communications (teracom): Challenges and impact on 6g wireless systems," *arXiv preprint arXiv:1912.06040*, 2019.

[422] V. Venugopal, "The light way to go 6g," *Photonics Focus*, vol. 2, no. 1, pp. 30–33, 2021.

[423] NASA. Communications with earth. [Online]. Available: https://mars.nasa.gov/mro/mission/communications/

[424] M. A. Khalighi and M. Uysal, "Survey on free space optical communication: A communication theory perspective," *IEEE communications surveys & tutorials*, vol. 16, no. 4, pp. 2231–2258, 2014.

[425] J. Y. Suen, M. T. Fang, and P. M. Lubin, "Global distribution of water vapor and cloud cover sites for high-performance thz applications," *IEEE Transactions on Terahertz Science and Technology*, vol. 4, no. 1, pp. 86–100, 2014.

[426] J. Y. Suen, "Terabit-per-second satellite links: a path toward ubiquitous terahertz communication," *Journal of Infrared, Millimeter, and Terahertz Waves*, vol. 37, no. 7, pp. 615–639, 2016.

[427] G. L. Villanueva, M. D. Smith, S. Protopapa, S. Faggi, and A. M. Mandell, "Planetary spectrum generator: An accurate online radiative transfer suite for atmospheres, comets, small bodies and exoplanets," *Journal of Quantitative Spectroscopy and Radiative Transfer*, vol. 217, pp. 86–104, 2018.

[428] S. Nie, J. M. Jornet, and I. F. Akyildiz, "Intelligent environments based on ultra-massive mimo platforms for wireless communication in millimeter wave and terahertz bands," in *ICASSP 2019-2019 IEEE International Conference on Acoustics, Speech and Signal Processing (ICASSP).* IEEE, 2019, pp. 7849–7853.

[429] S. V. Hum and J. Perruisseau-Carrier, "Reconfigurable reflectarrays and array lenses for dynamic antenna beam control: A review," *IEEE Transactions on Antennas and Propagation*, vol. 62, no. 1, pp. 183–198, 2013.

[430] R. E. Hodges, N. Chahat, D. J. Hoppe, and J. D. Vacchione, "A deployable high-gain antenna bound for mars: Developing a new folded-panel reflectarray for the first cubesat mission to mars." *IEEE Antennas and Propagation Magazine*, vol. 59, no. 2, pp. 39–49, 2017.

[431] E. Carrasco and J. Perruisseau-Carrier, "Reflectarray antenna at terahertz using graphene," *IEEE Antennas and Wireless Propagation Letters*, vol. 12, pp. 253–256, 2013.

[432] R. Regulations, "Articles," *Edition of*, 2016.

[433] C. Ho, N. Golshan, and A. Kliore, "Radio wave propagation handbook for communication on and around mars," 2002.

[434] P. L. Whelley and R. Greeley, "The distribution of dust devil activity on mars," *Journal of Geophysical Research: Planets*, vol. 113, no. E7, 2008.

[435] M. D. Smith, "Spacecraft observations of the martian atmosphere," *Annu. Rev. Earth Planet. Sci.*, vol. 36, pp. 191–219, 2008.